AE BASED HEALTH MONITORING AND BONDED FRP PATCH REPAIR IN BRIDGE MANAGEMENT

By

Ozgur Yapar

Dissertation

Submitted to the Faculty of the

Graduate School of Vanderbilt University

in partial fulfillment of the requirements

for the degree of

DOCTOR OF PHILOSOPHY

in

Civil Engineering

May, 2015

Nashville, TN

Approved:

Professor Prodyot K. Basu

Professor Sankaran Mahadevan

Professor Caglar Oskay

Professor Eric Barth

To my Mother, Father and Sister,

For their boundless love, support and encouragement.

ACKNOWLEDGEMENTS

Foremost, I would like to express my gratitude to my advisor Prof. P.K. Basu for supporting me with his wisdom, immense knowledge and patience during this process. His skillful and unstinted guidance helped me all the time both in academic and personal matters. I also would like to thank my committee members Prof. Sankaran Mahadevan, Prof. Caglar Oskay and Prof. Eric Barth for providing me their thoughtful criticism, time and help during busy semesters.

This dissertation would not have been possible without the financial support of Tennessee Department of Transportation (TDOT), National Science Foundation (NSF) and Vanderbilt University Dissertation Enhancement Grant. I would also like to express my appreciation to Prof. Ted Bapty for his academic and financial support for this work during my association with the Vanderbilt University Institute for Software Integrated Systems.

I would like to express my sincere appreciation, especially, to Nikolas Nordendale for his help and support whenever I needed in this work. I would also like to thank Dr. David DeLapp and my fellow students Adrian Bennett, Jacob McNutt, Bethany Burkhardt, Lesa Brown and Joshua Arnold for their help throughout my research. I also owe thanks to Dassault Systèmes Simulia Corp. and my colleagues for their support, understanding and encouragement during this study.

Last, but by no means the least, I wholeheartedly thank to my family for their unbounded love and understanding. They were always supporting and encouraging me through the good times and bad.

TABLE OF CONTENTS

LIST OF TABLES

LIST OF FIGURES

CHAPTER 1

1. INTRODUCTION

1.1. Background

The transportation system of a country is the heart of its economy and the most critical link in a transportation system is the bridges. According to the National Bridge Inventory (NBI), 72,868 (12.1%) bridges were categorized as structurally deficient and 89,024 (14.8%) were categorized as functionally obsolete with a price tag of $48 billion to repair structurally deficient bridges and $91 billion to improve functionally obsolete ones. Some of these bridges were designed with older codes of practice and are considered to be inadequate (i.e. lower load carrying capacity, susceptibility to flooding etc.) for present day needs and some of them are in dilapidated condition and need to be closely monitored, inspected, or repaired.

Most of the bridges of the transportation network of US were built in the post-World War II-era fueled by the booming economy of the time. Therefore, most of these structures are approaching their 50-year theoretical design life and are not compatible with modern standards reflecting today's loading conditions. Consequently, these bridges are prone to progressive deterioration that may lead to eventual collapse, unless measures are taken to monitor such deterioration coupled with timely repair and maintenance to slow down the deterioration process and prolong bridge life. In this tight economic environment, creating an effective and cost-efficient bridge management system for health monitoring

and repairing these structures for early damage detection and collapse prevention is extremely important.

Moreover, by catching the problem early, appropriate preventive maintenance action would avoid unscheduled repairs later that are not only likely to be much more extensive and hence expensive but cause more severe financial impact in terms of cost to the owners of a bridge and lead to expensive long-term detours for the commuters. The mandated visual inspection every two years alone may not be effective in this situation and it is necessary to develop a reliable but cost-effective real-time scheme for monitoring the health of such bridge structures. Structural damage to a bridge needs to be detected at an early stage, so that necessary repairs can be undertaken in a timely manner by using inexpensive and cost-effective procedures before the damage reaches dangerous proportions. This research effort focuses on these two aspects of life extension of existing bridges.

For bridge health monitoring a number of alternative schemes can be identified. But before adopting a particular one in a given situation, it is necessary to ensure that the adopted scheme can adequately address the following aspects of bridge management.

1. Conventional periodic visual inspection of bridges may fail to reveal the existence or initiation of all the potentially critical structural damage, sometimes in hidden locations.
2. The monitoring system should be able to warn the owners and managers of a bridge in real-time about the problem(s) with structural integrity in the monitored bridge structure before assuming critical proportions, potentially saving human lives and property and minimizing disruption of traffic.

3. As far as possible, the scheme should report damage to engineers concerned autonomously. In other words, the data from structural health monitoring (SHM) system measuring bridge health should be communicated to the responsible engineer's desk without the need for personally visiting the bridge site, except in special situations.
4. Energy needs of the SHM system should be met appropriately even if no conventional power supply happens to exist at or near the bridge site.
5. Apart from reliability, cost-effectiveness is an important consideration.

Figure 1.1.1 presents the essential components of an effective bridge management system, comprising of a network of sensors, a reliable power source (if possible, untethered), a sensor data acquisition and processing system, a telemetric data communication system, and a system for interpretation and decision making (for diagnosis and prognosis).

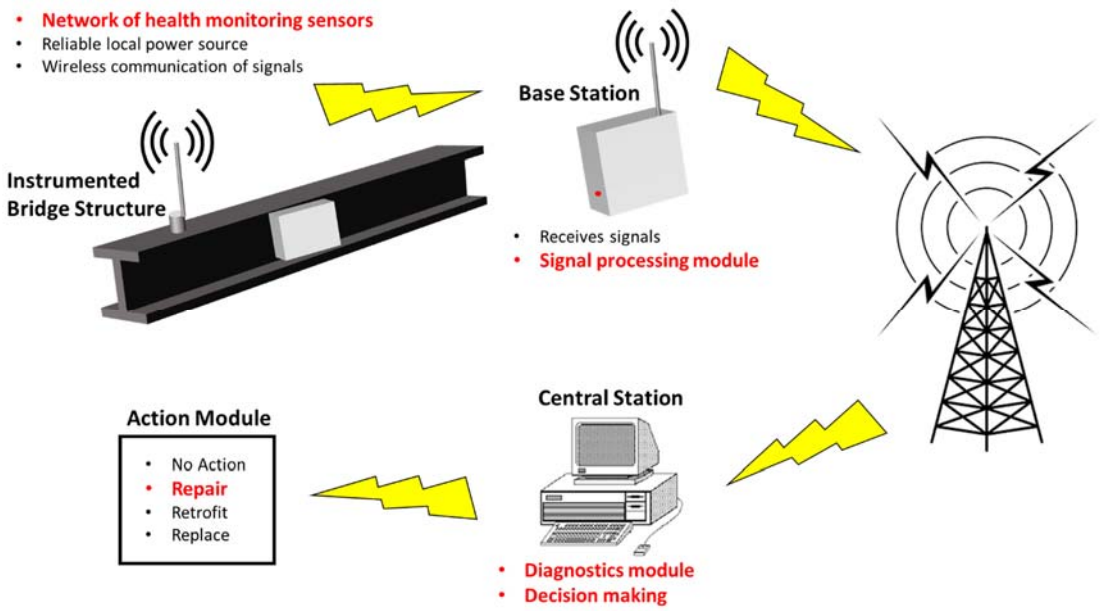

Figure 1.1.1. Essential Components of a Bridge Management System.

As per Figure 1.1.1, the focus of this research will be on the items labeled in red that is health monitoring using a network of sensors, processing of sensor data, signal characterization, detection of damage location, identification of the needs for repair, and undertaking necessary repair to prolong the life of bridge to the desired extent. In a nutshell, therefore, it involves health monitoring of an operational bridge structure to ensure its safe and satisfactory performance in real-time and enabling the condition-based timely maintenance.

1.2. State of the Art

1.2.1. Current State of the Art in Bridge Management

The most widely adopted method by NBI for structural health monitoring of bridges is visual inspection every two years. The other methods that have been tried for structural health monitoring of bridges, at least, in the context of research and development are strain gages, LVDTs, tiltmeters, ultrasound testing, fiber-optics, 3D laser scanning, GPS based systems.

The 3D laser scanning and GPS based monitoring systems provide only displacement data to the operator which makes it impossible to detect the source location of the damage accurately and are very expensive. Fiber-optics sensors are best suited for new bridges, need precise installation and also are very expensive like the other two stated methods. Additionally, such sensors are very sensitive to temperature changes which make them unsuitable in field applications like real-time SHM of bridges. In ultrasonic testing, the transducer needs to be passed over the surface of the structure, which makes the testing impossible without an onsite operator. Furthermore, the interpretation of output from

ultrasonic transducer requires very high degree of operating skill, experience and training. Consequently, the automation of a real-time SHM system based on ultrasonic testing becomes an extremely complex task. All these methods, except for fiber-optic sensors, are better suited for investigating a bridge suspected to have already undergone damage. In the case of acoustic emission (AE) technique, however, the ease of installation of the sensors and acquisition of the sensor signal data is off-set by the great difficulty in interpreting the signals in terms of damage location as well as its nature and source.

As stated above, most of the stated methods are geared towards determining the health of a bridge after the known occurrence of a damage event. However, for really effective bridge health management, there is a need for real-time monitoring its status. As mentioned above, methods based on acoustic emission measurement and fiber-optic systems are the viable alternatives. As the acoustic emission technique is better suited for this purpose and can be used on both new and existing bridges, the focus of attention of this study is on the use of this technique. In the case of bridge structures, the effort so far in this regard has rather been limited due to shortcomings in proper interpretation of the sensor signals, especially, in the case of concrete bridges. Unlike metals, acoustic signals get severely modified during propagation inside concrete due to diffusion, reflection and refraction and the non-homogenous character of the material. In this context, the separation of damage related signals from other unavoidable acoustic sources becomes a daunting task. Additionally, since significant signal parameters directly affect the speed of the acoustic waves, the detection of source of signals of interest gets highly involved. Together with the issues related to concrete material, the critical problems with the field application of the AE technique to bridges need to be addressed.

Replacement, retrofitting and repair are the three main options for bridge owners to ensure the safety of damaged bridges. As replacement and retrofitting methods are expensive, time consuming and prone to traffic rerouting and gridlocks, another focus of this research is repair. There are several conventional repair methods which need to be chosen through case-by-case consideration keeping in view the material of the bridge element to be repaired and the extent as well as nature of damage. In addition to the traditional repair techniques, the FRP composite based repair method is another option to extend the useful life of a deteriorating bridge. The focus of this research in this phase is a repair technique which will help restore the strength of a bridge in the early stages of a localized damage that could potentially assume dangerous proportions requiring extensive repair which can be expensive and time consuming. Ideally, a localized composite patch repair is expected to be quick, inexpensive, and will, most likely, not require closure of the bridge to traffic. Available FRP composite repair methods, which can be applied to bridges, are near-surface FRP, prestressed FRP, post-tensioned FRP and externally bonded FRP patch repair.

Localized FRP composite repair method is tried in this study because it is easy and quick to install and well suited for repairing local cracks, namely, the flexural and shear cracks in a bridge girder. Additionally, the labor cost is less and doesn't require closure of the bridge during repair. FRP composites are customizable with respect to shape, size, and strength and they are durable, lightweight, and have a high strength-to-weight ratio. However, the selection of the type and size of the patch material and the effect of same on the local as well as global behavior of the repaired structural element are issues of detailed investigation. Another important aspect is the selection of the composite material from

those available commercially. Fiber reinforced polymer based composites are being used by automotive, aerospace, sports equipment, etc. industries for quite some time. Naturally, therefore, these materials are available to cater, primarily, for the needs and methods followed in such industries. The application of such materials in civil infrastructure arena is relatively a new phenomenon requiring significant amount of proper adaptation. This challenge also needs to be addressed adequately in this study.

1.2.2. Acoustic Emission based SHM

Acoustic Emission measurement based technique is an emerging approach for real-time damage detection of bridges. According to ASTM, AE refers to the generation of transient elastic waves during the rapid release of energy from localized sources within a material. Dislocation movement accompanying plastic deformation and the initiation and extension of cracks in a structure under cyclic stress conditions cause the release of these emissions. Other causes of such emission could be thermal stresses, residual stress cracks induced during fabrication process, or other types of failure due to stress buildup. The AE damage detection technique relies upon surface mounted piezoelectric transducers which sense these high frequency elastic waves by conversion into electrical signals.

As an in-service bridge undergoes crack initiation or crack-growth, transient strain waves are generated from such a location due to sudden redistribution of stresses in the damaged component leading to acoustic emission. Actually, crack formation and growth involve release of energy in the form of elastic waves with spherical wave front which can be reflected at the boundaries of an instrumented structural component. Usually, the phenomenon at the source is over within a few millionths of a second. Depending upon the

material, the effects of the event may die out in micro-seconds to milliseconds. The AE sensor is essentially designed to convert dynamic excitation caused by strain waves into voltage signals, taking advantage of the properties of piezoelectric crystals like lead zirconate titanate ($PbZr_{0.52}Ti_{0.48}O_3$). Energy attenuation of the AE signal is caused by geometric spreading, material damping, and scattering due to reflections at boundaries, material inclusions, pores, etc. As a result, the AE signals detected by a sensor may be significantly different than at the source.

As shown in Figure 1.2.1, the primary components of an AE sensor are: (a) a piezoelectric crystal element (PZT), (b) two electrodes between which the PZT element is sandwiched with one electrically grounded and the other connected to a signal output socket, (c) a backing of damping material to damp out reflections and resonance conditions within the transducer, if any, (d) a coupling layer or bonding agent to enable a smooth transfer of acoustic emission signals from the structure to the sensor, and (e) a protective metal enclosure which also acts as a shield against electromagnetic interference. Sometimes, it may have a preamplifier integrated within the enclosure to amplify the strength of the voltage signal picked up by the sensor. After pre-amplification of the signals picked up by the AE sensor, it is subjected to A/D conversion before being processed in a computer for display and analysis. Appropriate analysis of records from various AE sensors enables noise elimination, identification of the nature of the source and its location. These results may be further supplemented by undertaking traditional non-destructive (ND) tests using records of ultrasonic devices, strain-gages, accelerometers, and the like.

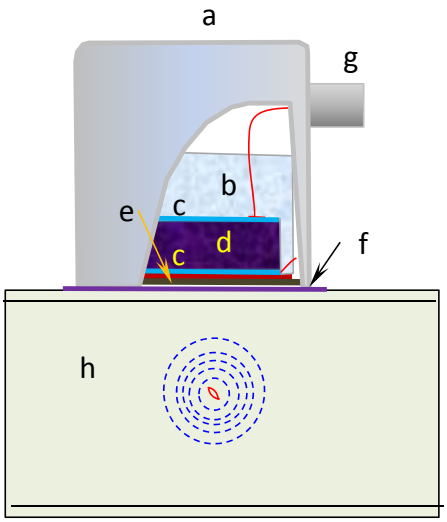

(a) Case of AE sensor
(b) Damping agent
(c) Electrode layer
(d) Piezoelectric element layer
(e) Wear plate element
(f) Coupling layer
(g) Socket for coaxial cable
(h) Monitored structure

Figure 1.2.1. Schematic view of an acoustic emission sensor.

Typically, a burst of acoustic emission signal output of a transducer rises to peak amplitude quickly, and then it gets dampened out in a relatively slower pace. An idealized acoustic emission signal can be seen in Figure 1.2.2. This signal can be generated by using Equation 1.1.1, in which V, V_0, B, t and ω are output voltage, initial signal amplitude, decay constant, time and angular frequency, respectively [1].

$$V = V_0 \times e^{(-B \cdot t) \cdot \sin \omega t} \tag{1.1.1}$$

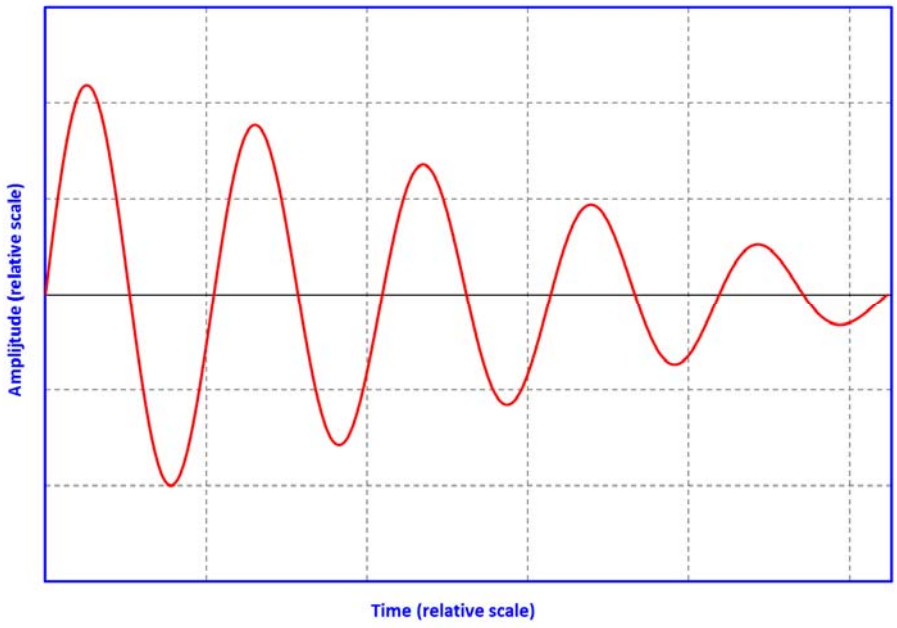

Figure 1.2.2. An idealized AE burst signal.

Acoustic emission technique is often considered to be very suitable for getting early warnings against sudden fatigue failures of structures, which is considered to be the most important contribution of the method to the industry. Under service conditions, acoustic emission testing method is very good at detecting the accumulation of micro-damage inside the structures. Because of this, the method is known for its effectiveness in fatigue damage detection.

In spite of its advantages, there are still many problems with the application of acoustic emission technique because most of the users of the method misunderstand its concepts. Although the method has been used in research studies and in the industry for quite some time, many users of the technique, including researchers, do not pay the needed attention to sensor calibration and attachment. Also, large amount of collected data is simply used as it is to explain material failure qualitatively. Sometimes, even in some

reported research work, no distinction has been made between noise and real AE signals. For this reason, a comparison of results from different published sources proved to be very difficult.

Dunegan and Harris, attempted to correlate their experimental results with the theoretical data generated by using Gilman's mobile dislocation model. As shown in Figure 1.2.3, acoustic emission count rate obtained from the experiments is plotted along with the data obtained by using theory as a function of strain. For a 7075-T6 aluminum specimen, experimental data, which is represented as dashed line, show excellent agreement with the theory as can be seen in Figure 1.2.3(a). On the other hand the theory and experimental data cannot be correlated for an iron-3% specimen, as can be seen in Figure 1.2.3(b). Although agreement between theory and experimental data in the study of Dunegen and Harris possibly happened by chance, in the republications of this figure this important aspect has not been identified.

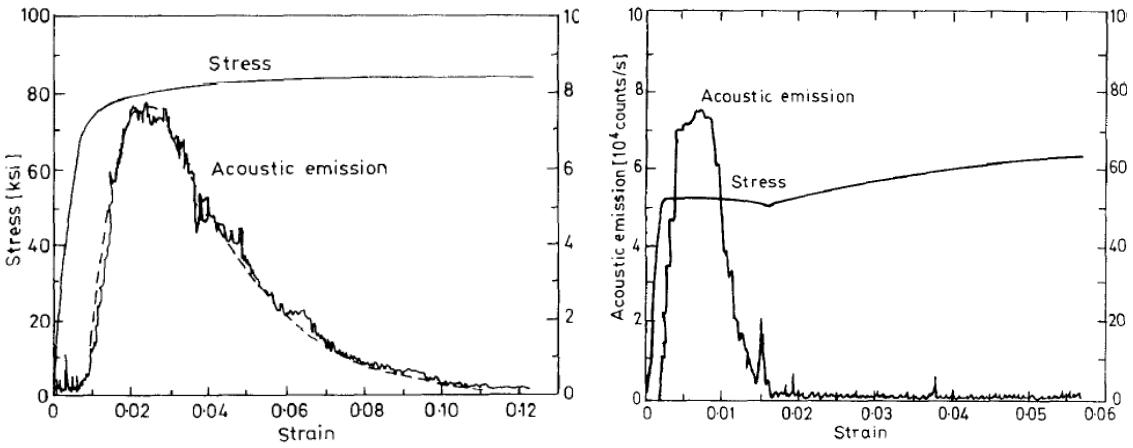

(a) 7075-T6 aluminum (b) Iron-3%

Figure 1.2.3. Acoustic emission rate and stress as a function of strain [2].

One of the main disadvantages of acoustic emission technique is its performance in a highly noisy service environment. In such conditions, signal discrimination and noise reduction becomes extremely difficult, since the acoustic emission signals by themselves are usually very weak [3].

Another disadvantage of acoustic emission technique is the modification of the generated stress waves during the propagation of the signals in the structure before they reach the sensor. Due to diffusion, reflection and refraction, waveform and the frequency characteristics of the signal gets modified, depending upon the acoustical transfer characteristics of the structure. The signals tend to undergo severe modifications as the geometry of the specimen gets more complex. This may be attributed to the different paths followed by the Rayleigh waves travelling on the surface and compression waves which may undergo repeated reflections when they hit the surface of the structure. In Figure 1.2.4 a schematic illustration of this phenomenon with respect to two simple geometries is shown.

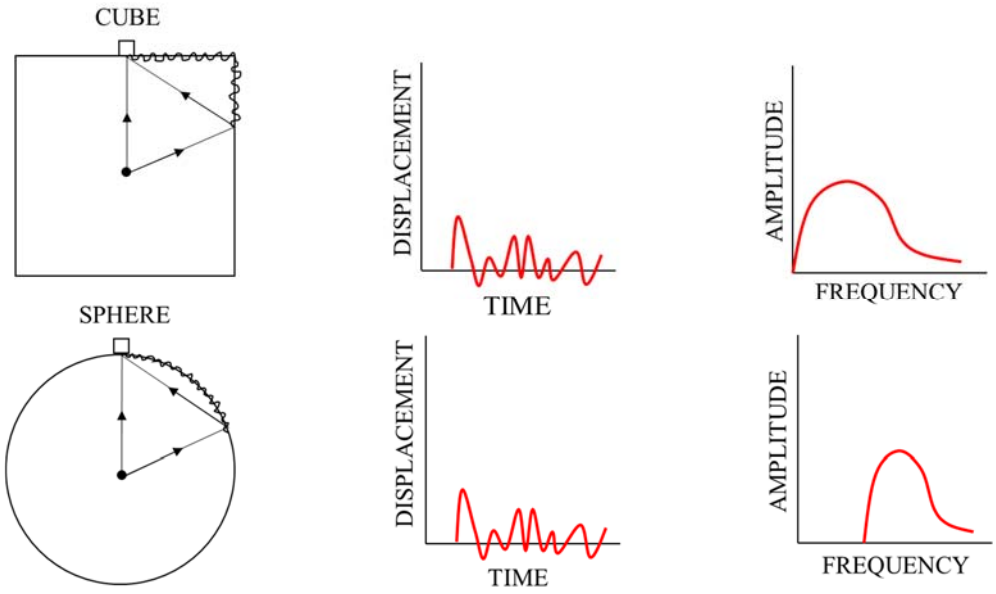

Figure 1.2.4. Modification of waveform and frequency characteristics of an acoustic signal due to specimen geometry [4].

In order obtain to reliable and meaningful diagnostics data from a successful acoustic emission test, the following three main tasks are required to be undertaken:

- Noise elimination of the polluted signals.
- Determination of source location of the acoustic emission signals.
- Source characterization of the signals of interest.

During an acoustic emission test, pollution of the recorded data by noise from various sources is inevitable. Noise sources may either be external or internal to the structure like crack breathing, friction, impact, ambient noise etc. [1]. Eliminating the noise recorded as an integral part the signal is an unavoidable appendage of acoustic emission testing.

One of the most widely used methods for noise elimination during acoustic emission testing is based on the use of band-pass filters. Applying this traditional signal cleaning technique to the acoustic emission data can, however, be counterproductive. Specimen geometry, material and non-homogeneities inside the structure may severely modify the frequency characteristics of the signal. Without taking necessary precautions, using band-pass filters on acoustic emission signals might result in filtering of the original signal along with the noise. Narrowing of the frequency pass band of the filter is more unlikely record the noise, but may also adversely affect the detection of the actual acoustic emission signals.

Although it is not very promising, the application of filters for noise elimination might be successful if proper preliminary investigation is undertaken to identify the frequency characteristics of the signals of interest.

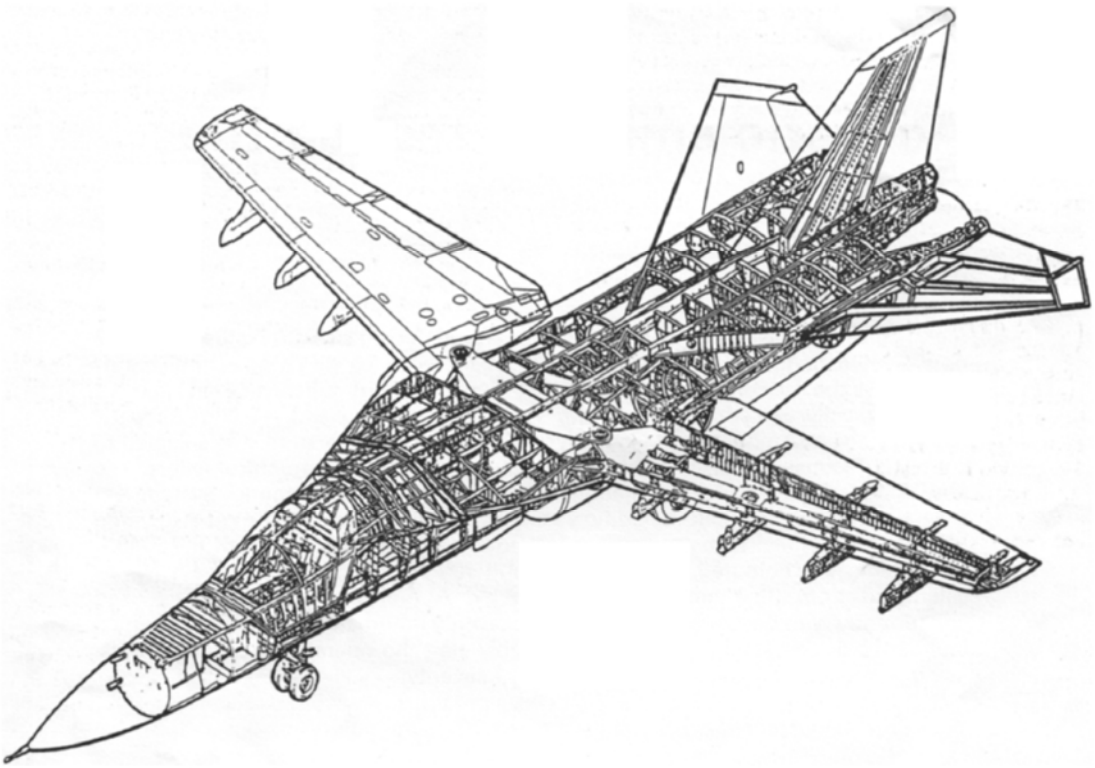

Figure 1.2.5. Structure of F-111 aircraft [5].

One of the most notable applications of filtering method for event detection and noise elimination in acoustic emission testing occurred during the production phase of the United States Air Force F-111 fighter bomber [5]. The general structural details of a F-111 aircraft are quite complicated, as can be seen in Figure 1.2.5. In this case, effective noise filtering was ensured by using the thresholding method, as evidenced by the results of the tests. It was discovered during the study that the acoustic emission signals caused by airframe damage had high energy and large amplitude in the 300 kHz frequency range. This information was used to build a filter for signal amplitude and energy with three different thresholds: moderate events, strong events and severe events. All of the data recorded by acoustic emission sensors were gathered and processed by an automatically

executed program. Thereafter, all the detected acoustic emission events were classified with the help of the threshold algorithm.

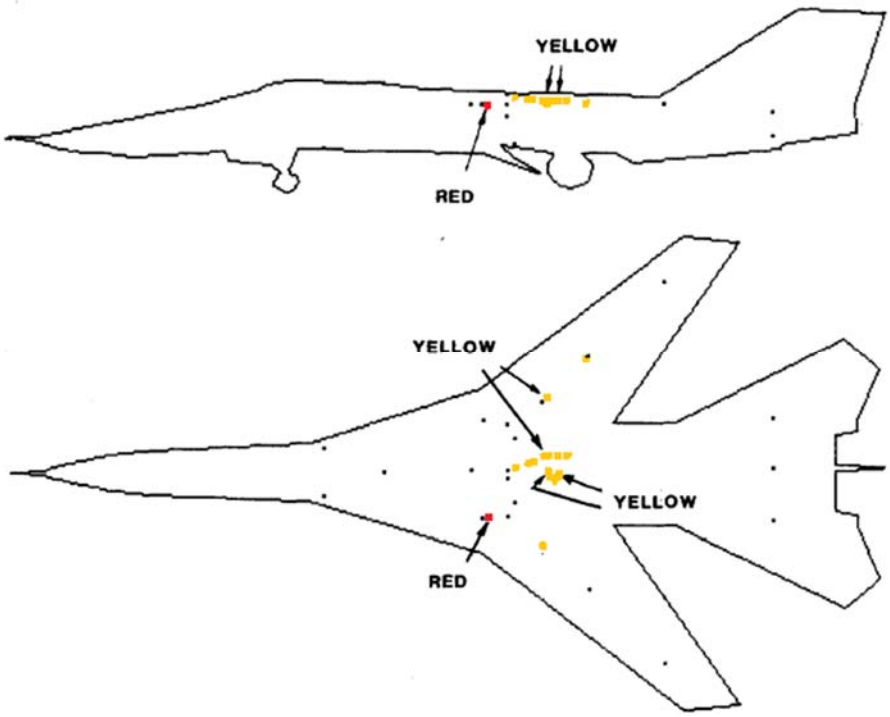

Figure 1.2.6. Diagrams of F-111 fighter jet with locations of acoustic emission events.

Recorded acoustic emission event locations can be seen on the outline diagrams of the aircraft shown in Figure 1.2.6. The events indicated as “yellow” were from a cracked tunnel truss and a disbanded wing joint, and the event indicated as “red” was from a broken wing carry-through box bolt.

In spite of this successful application of the thresholding technique, noise elimination and source classification of AE events by using this method is usually not always feasible due to the requirement of costly and time consuming preliminary investigations to determine the threshold values for signal processing. Additionally, this method is not applicable to bridge structures, since every bridge project is unique unlike

an aircraft structure. Therefore, the costly and time consuming preliminary investigations need to be repeated for each project which makes this method impractical for bridges.

One of the main goals of acoustic emission testing is usually the determination of the source of the signals. If the geometry and material of the specimen under test is simple and homogenous, determining the location of the source of the acoustic signals can be an easy task. Since the location of the sensors on the specimen are known and the velocity of the waves in a simple and homogenous specimen can be assumed to be constant, by using the arrival time differences of the acoustic emission waves on different sensors, the location of the source of damage can be predicted deterministically.

Number of unknowns in a deterministic source location problem is the time of occurrence of the event and the dimensional quantities that define the location of the source. For linear, planar and volumetric source location problems, the number of unknowns is two, three and four, respectively. Therefore, in an ideal case, the minimum number of sensors needed in a deterministic AE based damage identification scheme is two for linear (1D), three for planar (2D) and four for volumetric (3D) situations, since for each sensor there is a corresponding equation in the problem.

In the linear source location scheme, point of interest can be determined easily based on known linear distance between two sensors (l), wave velocity (v) and the arrival time difference (t) using Equation 1.2.1 below, in which x is the distance between the source location and the mid-point between the two sensors:

$$x = v \cdot t \tag{1.2.1}$$

Detection of AE sources on planar surfaces in 2D is more complex than linear source location. Pair of differences in arrival times determined for an array of three sensors

defines two hyperbolae and the source of the signal is located at the point of intersection of the two. Planar source location can be accomplished with the help of Equations 1.2.2 to 1.2.5, based on the geometry of the problem shown in Figure 1.2.7. By using the known positions of sensors, measured signal arrival time differences, and propagation velocity, the unknown "*r*" can be found. Planar acoustic emission source location on a spherical and a cylindrical surface can be determined easily by following a similar approach [6], [7].

$$\cos(\theta - \phi) = \frac{(A_2\delta_1 - A_1\delta_2)}{[(A_1x_2 - A_2x_1)^2 + ((A_1y_2 - A_2y_1)^2)]^{1/2}} \tag{1.2.2}$$

$$\tan\phi = \frac{(A_1y_2 - A_2y_1)}{(A_1x_2 - A_2x_1)} \tag{1.2.3}$$

Where:

$$A_1 = x_1^2 + y_1^2 - \delta_1^2 \tag{1.2.4}$$

$$A_2 = x_2^2 + y_2^2 - \delta_2^2 \tag{1.2.5}$$

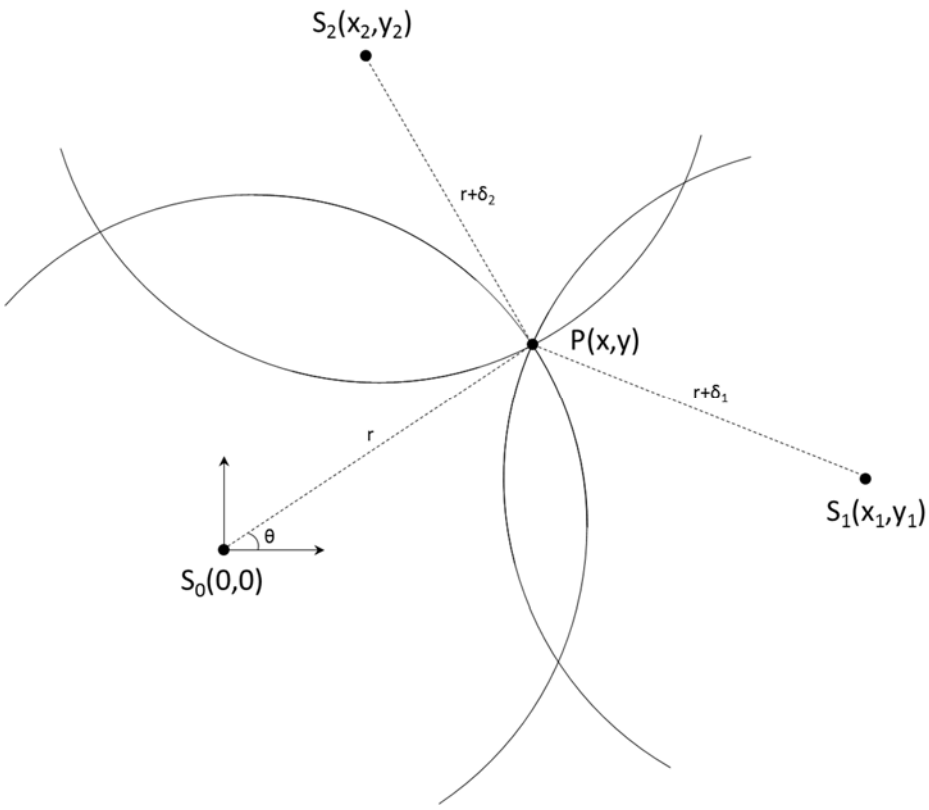

Figure 1.2.7. Geometric representation of the planar source location problem [8].

For structures and specimens with more complex geometry and non-homogenous material characteristics, deterministic source location methods described earlier may not be accurate enough, or may even lead to unsolvable equations. As the acoustic waves reflect back and forth on encountering non-homogeneity inside the specimen or on reaching the boundaries of the structure, the waves start to change modes and the path followed becomes unpredictable. Since the reflection of the waves and different types of behavior of different wave modes decrease the accuracy of source location methods described above, it is necessary to account for the geometry and material characteristics of a test specimen and also the operating frequency of the acoustic emission system, in selecting the proper source location method.

In one of the studies, damage source location detection on simple 7075-T6 type aluminum specimens were investigated [9]. Two types of methods were used to determine the source location of the events. The first method is a conventional constant velocity fixed threshold method and the other one is a frequency dependent velocity method. Frequency dependent velocities are determined by analyzing the first 100μs of the waveforms with wavelet transformation and generating a corresponding spectrogram. After the controlling frequency of the early arriving wave envelope is determined, the frequency dependent velocity of the waveform can be determined by using Equation 1.2.6 [10].

$$\frac{V_{ph}^2}{V_s^2} = \frac{2 \cdot \pi^2}{3 \cdot (1-\nu)} \cdot \left(\frac{h}{\lambda}\right)^2 \cdot \left[1 + \frac{2 \cdot \pi^2}{3 \cdot \kappa^2 \cdot (1-\nu)} \cdot \left(\frac{h}{\lambda}\right)^2\right]^{-1} \tag{1.2.6}$$

$$where, V_s = \sqrt{\frac{E}{2(1-\nu)\rho}} \; and \; \lambda = \frac{2\pi}{k_w}$$

In Equation 1.2.6, V_s is the shear wave velocity, ν is Poisson ratio, E is the modulus of elasticity, ρ is the mass density, h is the thickness of the plate, λ is the wavelength, k_w is the wave number and V_{ph} is the flexural wave phase velocity. Thereafter, linear source location of the signal is calculated by using Equation 1.2.7.

$$x = \frac{(t_1 - t_2) \cdot V_1 \cdot V_2 + V_1 \cdot L}{V_1 + V_2} \tag{1.2.7}$$

Here, V_1 and V_2 are the flexural wave velocities for the first wave frequency, t_1 and t_2 are arrival times for the first and second sensors, L is the distance between two sensors and x is the distance from the first sensor. Results of these methods demonstrated that although the conventional constant velocity method causes significant error, the frequency dependent velocity method reduces the location error significantly.

One of the main flaws of the frequency dependent velocity method stems from its assumption of AE waves having the same frequency characteristics during their travel from the source to the sensor. The wave velocity calculated using this method is based on the signal frequency at the sensor location. However, frequency characteristics of a AE wave gets significantly modified during its travel inside the structure on encountering boundaries, non-homogeneities, flaws, etc. Although this method worked well with simple aluminum specimens, it is not applicable to real structures which are more complex from geometry and materials point of view.

During practical applications, physical access to different parts of a structure of interest may be limited. Sometimes, in such cases, sources of acoustic emission events need to be determined by using only one acoustic emission sensor [11]. Another powerful method to determine the source location of an acoustic emission event is wavelet transformation. Acoustic emission waves travel through a structure in variety of modes with different attenuation and dispersion characteristics. By separating these modes during signal processing with wavelet transformation, the acoustic emission source can be located by using the differences in wave velocity between different wave modes. This method was used on a test specimen of thin steel plate, on which the acoustic emission events were simulated. Based on the results of the study, it was concluded that the method was successful in determining the source locations of acoustic emission events for specimens with simple geometry.

For structures with complex geometry like an aircraft, determining the location of an acoustic emission source is a difficult task [12]. Solving this type of extremely complex problems is deterministically impossible. The most feasible method for solving such

problems of highly non-linear nature is to use artificial neural networks (ANN). An intelligent locator based on general regression neural network has been tested on different types of specimens. Before the actual experiment, a set of tests were performed to train the intelligent locator. This was followed by actual tests on four different specimens with different acoustic emission sources. The specimens used were: bands, plates, rings and vessels. Following these tests, the source location results obtained from the neural network were compared with the results obtained by the conventional triangulation method. Based on the results of the study, it was concluded that the conventional source location method can be substituted by the intelligent locator. The same artificial neural network based intelligent locator was tested with multiple acoustic emission sources in another study and confirmed its success [13].

Several structural mechanisms and environmental sources including cracks, friction, impact, rain, airflow etc. may generate acoustic emission waves. Since another major interest of acoustic emission testing is the damage state of the structure, signals generated from sources other than damage mechanisms need to be effectively detected and eliminated.

In the successful development of a signal processing approach for the acoustic emission technique through advances in neural networks enabled automation of the process of crack detection and recognition. Early development of the approach relied primarily on laboratory testing [14], [15]. For this purpose, test objects were fabricated to simulate the aircraft pressure hull and tested under fatigue loading in the laboratory to destruction using several pressurization cycles. An artificial neural network was used to classify the recorded

signals generated by crack growth, rivet noise, rubbing and membrane noise with a success rate of 93%.

Automatic pattern recognition techniques and artificial neural network is also used during in-flight tests for separation of crack related acoustic emission signals from other sources [16]. Cessna T-303 Crusader aircraft was selected as a test-bed for the first phase of in-flight acoustic emission data collection. The special test object, which is a specimen made out of 7075-T6 aluminum alloy, was attached in the tail section of the aircraft as a passive element. The specimen was mounted behind the front spar of the vertical stabilizer. Due to the motion of the aircraft during the flight, the test object generated acoustic emission signals which were picked up by AE sensors.

During the second phase of testing, a more stringent in-flight test was conducted with a Piper PA-28 Cadet four-seat propeller driven aircraft [17]. Acoustic emission testing system was applied to the cowling of a Piper PA-28 Cadet aircraft and the structure was monitored with this system for crack detection during flight. The test-bed aircraft cowling and in-flight test setup can be seen in Figures 1.2.8 and 1.2.9, respectively.

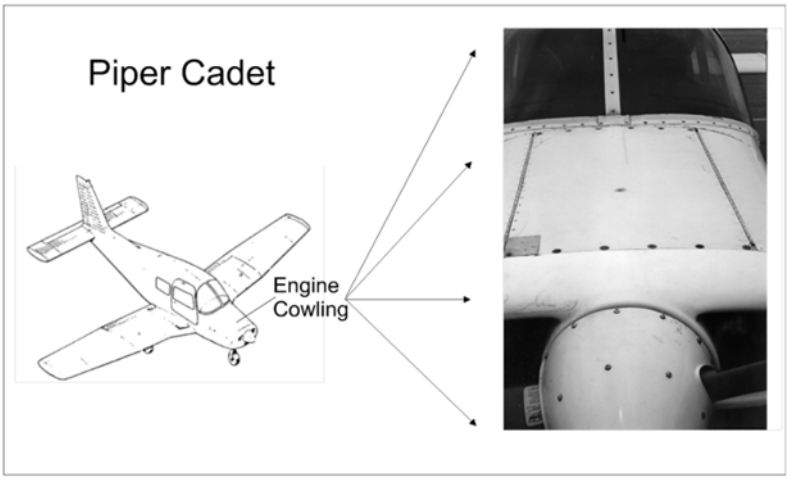

Figure 1.2.8. The test bed cowling of Piper PA-28 Cadet aircraft [17].

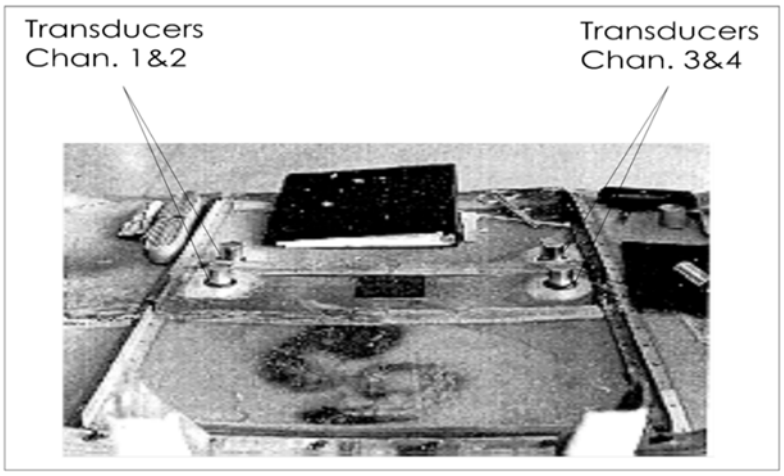

Figure 1.2.9. In-flight test setup [17].

After the in-flight tests, experiments were conducted under controlled laboratory conditions. The purpose of the laboratory work was to generate signature crack related acoustic emission data for neural network training by using specimens made out of the same alloy as used during in-flight tests. After the laboratory work, data gathered from laboratory tests was used to train a self-organizing neural network map. By using the trained neural network and the gathered in-flight data, crack related acoustic emission signals were successfully separated from other signals, which were generated by rubbing, extraneous noise or other clutter.

Although neural network approach is promising for source location and signal characterization of AE events for aircraft structures, some issues needed to be addressed before this method can be applied to bridges. All literature studies that adopted the neural network approach generated their training data sets in the laboratory by using simple specimens. Although those specimens and the structure of interest shared the same material, the geometrical characteristics were completely different. Therefore, the training

data sets generated by following this approach did not represent the real damage related signals of interest. This issue could be overcome if researchers generated their training data sets in the laboratory by testing real full-scale structural aircraft elements. This approach might work for aircrafts since aircraft components are relatively smaller than the bridge hardware elements making them better suited for full-scale laboratory investigations to generate training data set. On the other hand, conducting full-scale laboratory tests on structural bridge components is mostly very cumbersome.

Acoustic emission testing finds application in aircrafts, automobiles, pressure vessels, pipes and tanks. However, its application in bridge infrastructure is minimal. Since concrete is probably one of the most popular material system for modern bridges, a proper understanding of the acoustic emission characteristics of this material is extremely important. Researchers attempted to apply AE technique to both reinforced concrete and prestressed concrete with limited success [18], [19]. Additionally, none of the studies address the issues for the field application of the AE technique as a real-time SHM system, like the separation of the damage related AE events from the non-damage related ones, source location detection of signals of interest, etc.

1.2.3. FRP Patch Repair

After the nature and location of the damage is detected, necessary action must be taken to ensure continued safety of the bridge. As extreme measures like replacing and retrofitting a bridge is costly often exceeding the available resources, the life of a damaged bridge needs to be extended by adopting inexpensive, safe and reliable measures that can be implemented rapidly without creating traffic bottlenecks. For this purpose, one possible

approach is to repair the damage using bonded FRP (Fiber Reinforced Polymer) composite patches.

FRP's are typically plastic and polymer materials reinforced with glass, carbon, basalt, or aramid fibers. Main advantages of FRP composites over traditional repair materials like grout, cement, concrete and steel are high tensile strength to weight ratio, low maintenance costs and avoidance of traffic congestions and delays during the repair work. After the wide acceptance of FRP materials in the aerospace and automotive industries, construction industry can also benefit from this new type of material to ensure effective management of the national bridge inventory.

The most common types of deterioration observed in steel bridges are corrosion and fatigue cracking, and for concrete bridges it is delamination, spall and cracking. Damages caused by vehicle collision is another type of serious bridge deterioration which is quite common. Figures 1.2.10 through 1.2.12 show some examples of steel bridge deterioration. Primary factors that are responsible for decline of steel bridges are loss of material and stress cracking due to corrosion, inadequate fatigue life and design errors. For concrete bridges, deterioration is attributed to various factors like overstressing, design errors, impact damages, efflorescence, sulfate and acid attacks, carbonation, scaling, leaching, chloride-ion penetration, freezing and thawing, thermal cycles, poor quality construction materials and insufficient workmanship quality. Some examples of such deteriorations are presented in Figures 1.2.13 and 1.2.14.

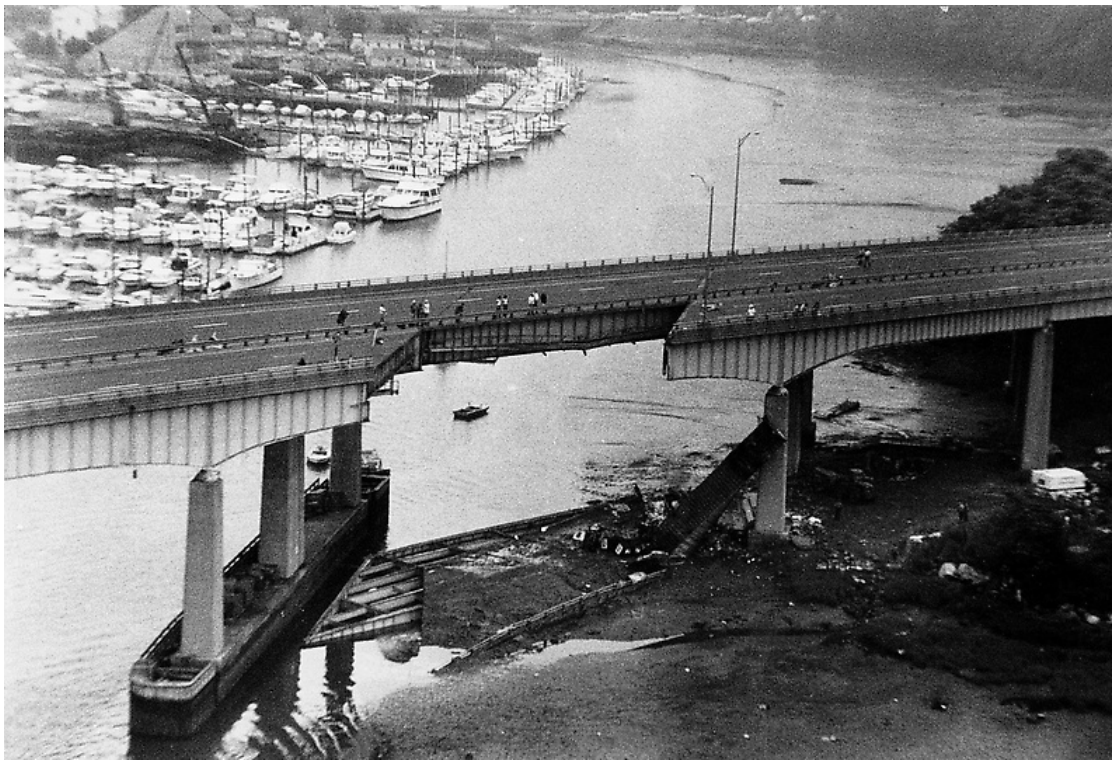

Figure 1.2.10. Collapse of Mianus Bridge, caused by rust formation within the bearing on a pin.

Figure 1.2.11. Corroded plates of Stillwater Bridge in Minnesota.

Figure 1.2.12. Bent steel girder due to impact damage.

(a) Flexural cracks (b) Longitudinal crack

Figure 1.2.13. Cracked concrete girders.

(a) Reinforcement corrosion and spall (b) Collision damage

Figure 1.2.14. Deterioration and damage of tee beams [20].

Although FRP materials are around for nearly 100 years, they have been started to be used for strengthening and repairing civil engineering structures in the late 20th century. The concept of repairing aerospace structures with metal patches and bonded composite laminates is around for a while and has been successful so far [21]. The proven usefulness of the method in other industries is a motivating factor for civil engineering community researchers for further exploration.

The early practical applications of repairing, retrofitting and post-strengthening of existing structures was with externally bonded steel plates. Due to many drawbacks of this methodology, researchers directed their interest to alternative materials. One of the most suitable candidate as a repair solution for damaged structures was found to be FRP by early researchers. Its low weight, high tensile strength, corrosion resistance and ease of application made FRP a viable option for extending the life of damaged bridge hardware.

One of the FRP repair schemes applicable to prestressed/post-tensioned/reinforced concrete beams is near-surface fiber reinforced polymer (NS-FRP) system. Behavior of post-tensioned concrete slab bridges strengthened with NS-FRP system has been investigated [22]. A half-scale model of a real post-tensioned slab bridge, which was

constructed in 1973 in Winnipeg, Manitoba, Canada, was fabricated. One of the test specimens was left un-strengthened and the other one was strengthened with embedded CFRP (Carbon Fiber Reinforced Plastic) bars. The strengthening process started by cutting grooves in the tension zone of the slab followed by the insertion of CFRP bars. Thereafter, the bars were covered by filling the grooves with epoxy resin. In Figure 1.2.15, the employment of the NS-FRP system on the slab specimen is shown. The slabs were tested under static loading by using a uniform line load on a width equivalent to the tire contact patch of an ASSHTO HSS-30 truck. The observed mode of failure for both the cantilevers was due to crushing of concrete. The strengthening scheme using NS-FRP increased the moment capacity of the slabs by 36%.

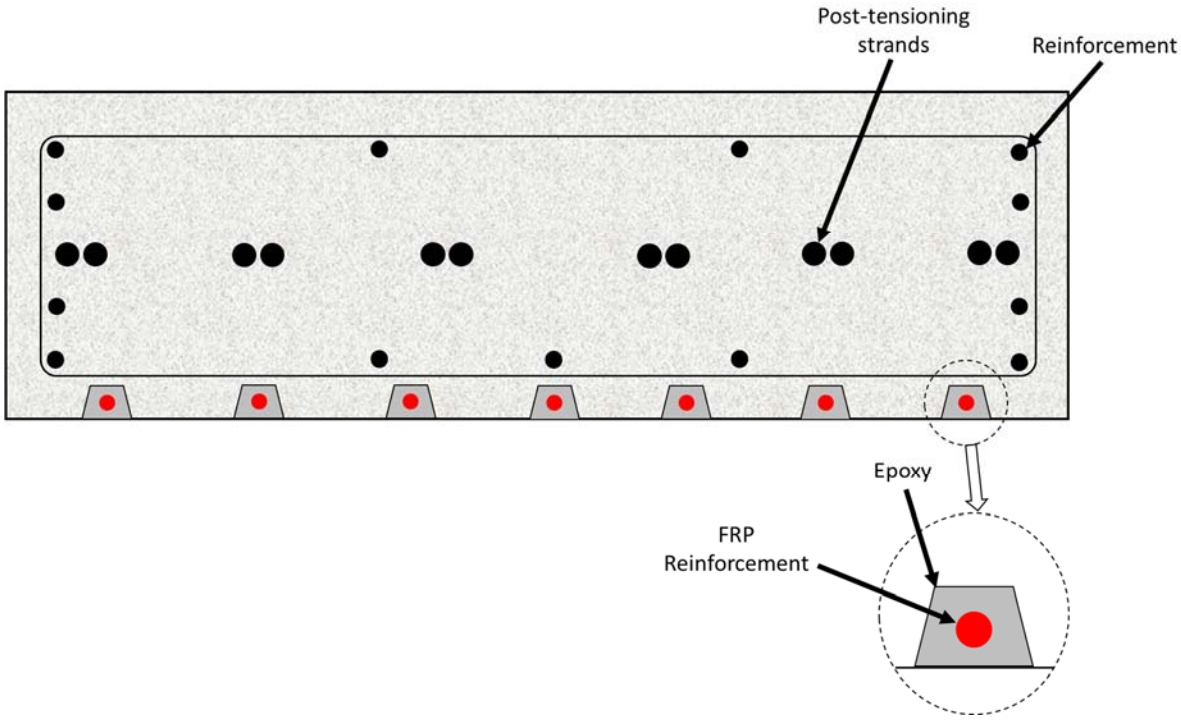

Figure 1.2.15. Post-tensioned concrete slab strengthened with NS-FRP.

Although NS-FRP system is an effective repair option for deteriorated concrete bridge beams. However, as this repair method require grooves to be sawed into the girder,

it poses the risk of causing further damage to the structure during the repair process by accidentally sawing the prestressing steel/post-tensioning strands/rebars along with the concrete.

Other two viable FRP composite repair methods, which are applicable to bridges, are prestressed FRP/CFRP (P-FRP/P-CFRP) and post-tensioned FRP/CFRP (PT-FRP/PT-CFRP) techniques [23], [24]. The efficiency of those two methods has been evaluated along with three other variants of CFRP-based repair systems for strengthening of impact damaged prestressed concrete girders [23]. The performance success of the procedure was offset by the difficulties of the procedures involved.

Another repair scheme, which is applicable to all types of girders, is externally bonded FRP patch repair [25], [26]. Four full-sized prestressed concrete girders were intentionally damaged to simulate impact damage, by removing concrete from the bottom flange of the beam and also splitting a number of prestressing strands in the laboratory [25]. Thereafter, the beams were repaired by patching the damaged area with CFRP sheets to restore the original flexural capacity. The test beams were strengthened with transverse CFRP jackets, in addition to the longitudinal flexural CFRP sheets, as shown in Figure 1.2.16. The method seemed to be effective when at least 85% of the strands are intact.

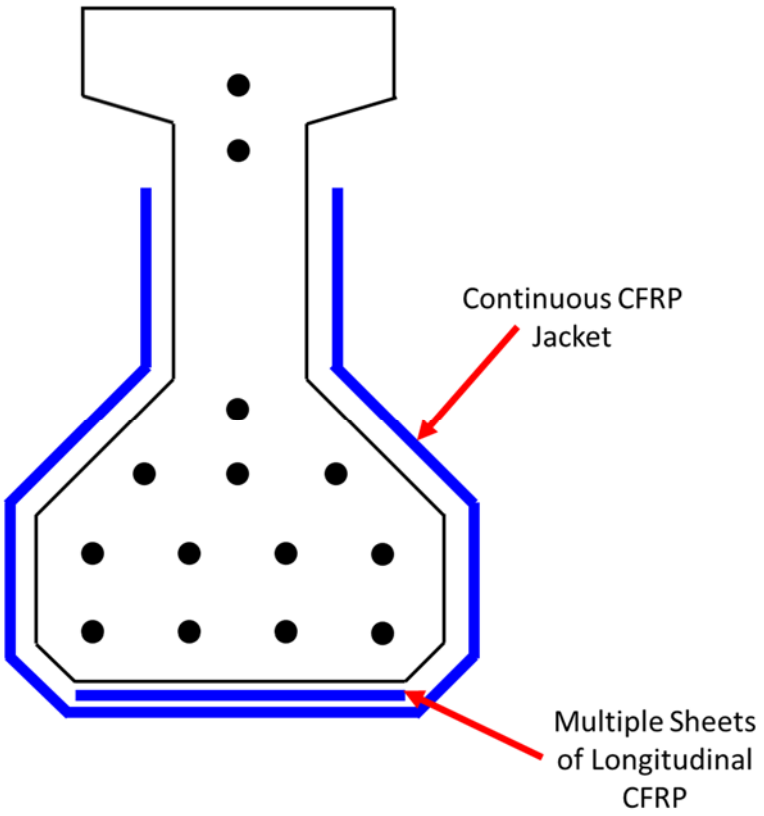

Figure 1.2.16. Bonded CFRP flexural patch configuration.

In addition to concrete beams, FRP repair scheme can provide a feasible repair solution for steel girders as well. In Figure 1.2.17, different retrofit schemes for steel girders are shown. Delaware Department of Transportation chose the I-704 Bridge to assess the effectiveness of CFRP based rehabilitation process on steel bridges. One of the steel girders of the bridge was strengthened by bonding one layer of CFRP to the outer face of the tension flange. Thereafter, six CFRP plates were installed over the full length of the girder using four overlapped sections. Two load tests were performed on the chosen girder, one prior to and the other after rehabilitation. The rehabilitation procedure improved the girder stiffness by 11.6% [27].

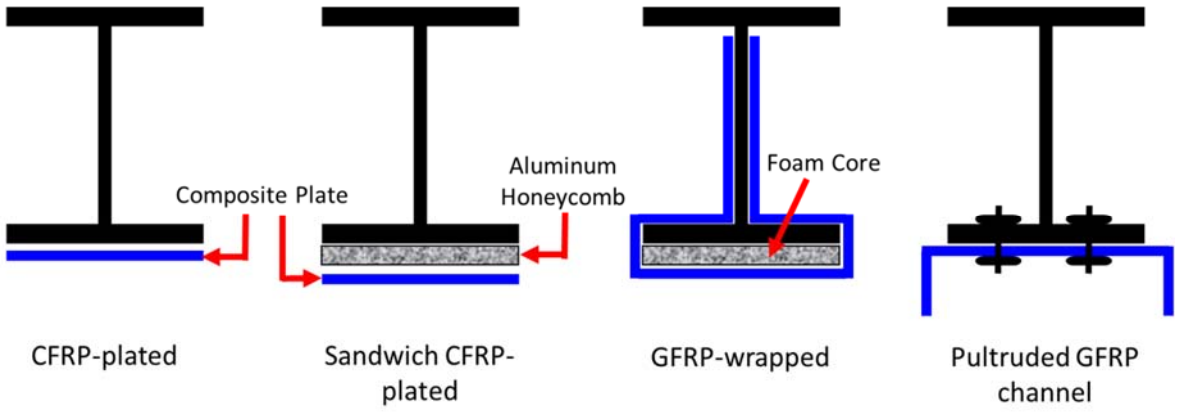

Figure 1.2.17. Different strengthening schemes for steel beams [28].

By using one or combination of the following approaches, feasibility and efficiency of retrofitting of mainly steel girders with bonded FRP patch is examined [28]. Repair of naturally deteriorated steel girders [29], repair of artificially notched girders to simulate fatigue cracks, section loss due to corrosion [30], [31], [32], strengthening of undamaged girders with inadequate capacity [33], [34], [35], and retrofitting of steel girders acting compositely with a concrete deck [36], [37]. It is clear that using bonded FRP sheets and plates can be effective in restoring the lost capacity of a damaged steel member and strengthening of steel structures to resist higher loads.

In literature and in design standards [38], [39], [40], it has been observed that for flexural repair, the usual practice is to bind the FRP patch along the full-length of the structural member, as shown in Figure 1.2.18. This practice is highly wasteful of repair material and expensive. This issue is addressed in this study

.

(a) Curved beam [41]

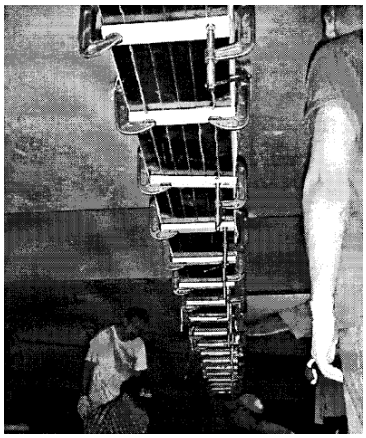

(b) Bridge girder [42]

Figure 1.2.18. Beams repaired against flexure with full-length FRP patches.

One of the most important properties of a FRP material, which is intended to be used for strengthening, is its modulus of elasticity. Especially when the substrate material is steel, choosing an appropriate FRP material for strengthening purposes is very critical. If a steel structural member is repaired with FRP with a low modulus of elasticity, most of the load will be carried by steel with very little redistribution of service load effects to the patch. As a result, the load capacity of the FRP patch cannot be utilized and the capacity of the degraded steel member will not experience the necessary relief.

Since the modulus of elasticity of steel is higher than most of the FRP materials in the market, new high modulus carbon fiber reinforced polymer (HM-CFRP) material may be a very suitable option for strengthening steel bridges. In a study, the performance of steel-concrete composite girders strengthened with HM-CFRP was investigated in the laboratory, both under overload and fatigue conditions [43] and found to be a very effective material for repairing and strengthening steel-concrete composite bridge girders.

Because of its high modulus of elasticity, other suitable candidates for repairing and strengthening of steel structures are ultra-high modulus carbon fiber reinforced

polymer (UHM-CFRP) and ultra-high modulus carbon/glass fiber reinforced polymer (UHM-CFRP/GFRP) materials. UHM-CFRP/GFRP is a composite system consisting of one laminate of glass fiber/epoxy composite fabricated on to both sides of two laminates of carbon fiber. The reason for using the GFRP laminate adjacent to the adhesive is to allow a more uniform load distribution.

Before the application of CFRP to a steel structure, an important physical phenomenon called galvanic corrosion needs to be taken into account. Galvanic corrosion is the build-up of corrosion at the contact surfaces of dissimilar materials which are carbon and steel in this case [44]. Since galvanic corrosion causes not only the accelerated corrosion of the steel but also the degradation of the CFRP, its prevention is essential for long-term durability of steel structures repaired with this material [45]. Prevention of galvanic corrosion can be accomplished by either using thicker epoxy layers or GRFP laminates between the steel and the CFRP [46], [47], [48], [49].

From the point of view of design, brittle natured debonding failures are one of the main concerns that need to be taken into account to ensure the effectiveness and safety of the repair system. Since premature debonding is a result of shear and normal stress concentrations at the ends of the bonded plates, procedures to predict the normal and shear stress concentrations at the ends of the bonded steel plates have been reported in [50]. After FRP material became more popular as a repair solution, work done on steel plates was extended to bonded FRP plates [51].

Analytical studies were undertaken on debonding problems in FRP bonded steel and concrete systems by a mechanistic based debond failure model [52]. Using a global fracture approach, debonding model is based on the assumption that the failure takes place

through the entire FRP reinforcement in a brittle fashion. The debonding failure criterion was arrived at by equating the total dissipated energy during the failure of the bond to the interfacial fracture energy required for debonding. The global debonding criterion can be seen in Equation 1.2.8. As the beam's curvature/deflection ratio increases under loading, the portion of the energy stored in the strengthened beam in excess of that stored in the un-strengthened beam reaches a critical value which causes debonding failure.

$$\Delta D = \frac{P_{2d}^2}{2K_2} - \frac{P_{1d}^2}{2K_1} = \left(G_{FII}\, I_f\, b_f + \Gamma_{FII}\, l_a\, b_a\right) + W_S^P \geq 0 \qquad (1.2.8)$$

Here, ΔD and δ_{Ld} are the energy dissipation and deflection at a point at which debonding takes place. P_{1d}, P_{2d}, K_1 and K_2, respectively, are un-strengthened beam load at the displacement δ_{Ld}, strengthened beam load at the displacement δ_{Ld}, Mode I and Mode II stress intensity factors. Furthermore, G_{FII}, Γ_{FII}, l_f, l_a, b_f and b_a are Mode II fracture energy of concrete, Mode II fracture energy of FRP-FRP interface, length of the FRP reinforcement, length dimension of anchorage area, FRP reinforcement width and width of the anchorage reinforcement. W_S^P is the plastic energy dissipation due to rebar yielding.

Failure of concrete and steel beams strengthened with FRP may be in several modes. The most common failure mode for FRP strengthened concrete beams are: concrete crushing, FRP rupture, cover delamination, FRP debonding and shear failure. In the case of steel beams failure may take place through: top flange buckling under compression, web buckling in shear, FRP debonding and FRP rupture. In Figures 1.2.19 and 1.2.20, most common failure modes of FRP strengthened concrete and steel beams are shown.

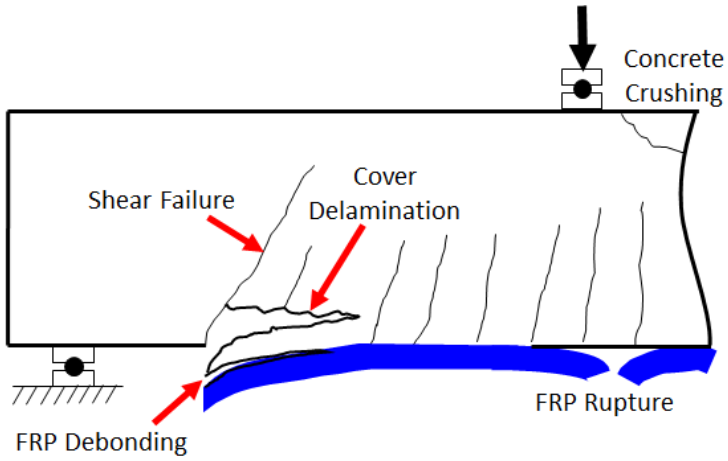

Figure 1.2.19. Most common failure modes for FRP strengthened concrete beams [53].

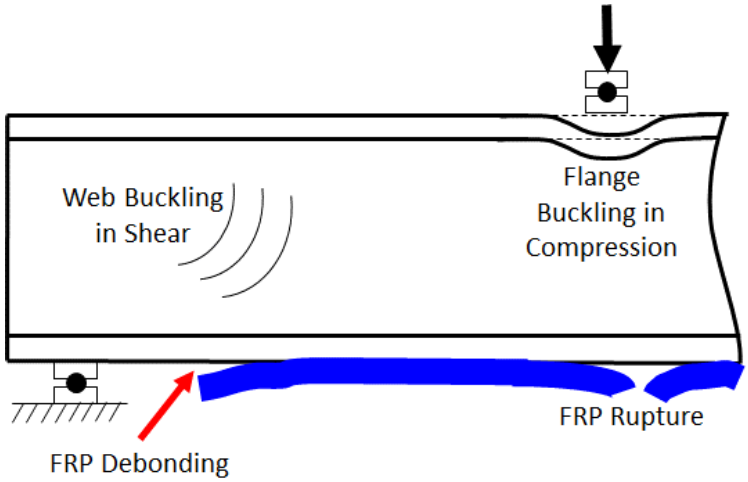

Figure 1.2.20. Most common failure modes for steel beams strengthened with FRP [53].

Early researchers put forth great effort to understand the nature of debonding. Although empirical formulas and mechanistic models were developed to analyze and design beams repaired with FRP against debonding, this failure mode is only one of the many ways that the structure may fail. Therefore, for design and analysis purposes,

analytical methods are needed which can capture the global behavior of beams repaired with FRP instead of just focusing on only one mode of failure.

1.3. Motivation

As stated in Section 1.2.1, for a bridge management system which can autonomously report damage to the engineers concerned, acoustic emission technique is chosen as the base of the monitoring module due to its advantages over other SHM methods. In a realistic situation, such a module needs a network of sensors and a data acquisition system to automatically gather data from the bridge, a telemetric data communication system to upload the recorded data to the cloud and, more importantly, a diagnostics system at the central station for sensor data interpretation and to help in decision making.

For the second part of this bridge management system, which is concerned with the repair of the bridge to extend its life, FRP composite repair method is chosen as the main approach. Among all the FRP repair methods, externally bonded FRP patch repair technique is selected due to its cost-efficiency, ease of application and effectiveness as previously stated in Chapter 1.2.1. In literature and in design standards, it has been observed that the universal practice is to bond the FRP patch mostly along the full-length of the structural member. In view of the fact that initial damage in a real bridge is highly localized and if the SHM can detect the same in real-time, one may get away with more cost effective localized bonded composite patch repair in much less time. Accordingly, the primary focus of this phase of the research will be this kind of repair using different types of available FRP materials. This will involve initial proportioning of patch material

followed by more rigorous evaluations of the local as well as global performance of such repair.

1.4. Objectives and Scope

The primary goal of this research is to develop an effective but simple scheme for real-time detection of damage (or cracks) in bridge superstructures by applying modern concepts in structural health monitoring and also to develop a scheme to repair a damaged bridge using bonded FRP. It is obvious that the desired objective can be realized by undertaking it in two distinct stages.

Objective - 1: Developing an effective AE based real-time bridge superstructure health monitoring system which can be applicable to conventional bridges, namely, those of steel, reinforced concrete, and prestressed concrete, using both experimental and analytical techniques followed by finite element simulations for generating data for both damage identification and validation. To achieve this objective, the following steps will be undertaken.

Task 1.1: After a thorough review of the existing hardware for AE based structural health monitoring, the most suitable hardware for the present study will be identified.

Task 1.2: Based on the specifications of existing test hardware and the hardware to be acquired, a set of representative test specimens will be proportioned and fabricated.

Task 1.3: Necessary hardware for undertaking cyclic loading test and data acquisition will be fabricated and, as needed, acquired.

Task 1.4: A scheme for processing AE signals will be developed.

Task 1.5: The specimen will be subjected to cyclic or quasi-static load testing, as needed, in the laboratory to cause damage and necessary sensor data will be acquired.

Task 1.6: The sensor data will be processed by denoising, damage source location identification and source classification.

Task 1.7: Finite element models of the test specimens will be created to simulate the test.

Task 1.8: All results will be discussed and necessary conclusions will be drawn.

Objective - 2: Developing a quick and inexpensive FRP patch repair system applicable to localized early stage damages in typical bridge superstructures, namely, those of steel, reinforced concrete and prestressed concrete. Apart from developing simple methods to detail the required repair work, analytical tools will be developed to study the local and global performance of the repair work and validate the same through experimental investigation.

Task 2.1: Available FRP patch material will be identified and the ones suited for the present study will be acquired.

Task 2.2: Simple procedures for proportioning local patch repair of the commonly used materials for bridge superstructures will be developed.

Task 2.3: Size of beam test specimen will be proportioned, fabricated, instrumented and readied for testing in the loading frame under quasi-static loads.

Task 2.4: Damage will be induced in the beams simulating real-life situations.

Task 2.5: Patch repair of the damaged beams will be undertaken and tested for assessing the resulting improvement in response under applied load.

Task 2.6: Tests will be undertaken in the laboratory to determine the mechanical properties of the bond material used to bind the patch material to the test beams.

Step 2.7: A mechanistic model will be developed to predict the performance of the patch repaired beam under load.

Task 2.8: Finite element models will be created to accurately predict the performance of the test beams under load before and after patch repair.

Task 2.9: All results will be evaluated and necessary conclusions will be drawn and appropriate recommendations will be made.

Outcomes of the aforementioned efforts are presented in subsequent chapters. For instance, the stated tasks undertaken for satisfying Objective 1 are presented in Chapter 2 and those under Objective 2 are covered in Chapter 3. In Chapter 4, conclusions and recommendation are presented. Appendices A to G contain various supplemental information like details of test specimens, test setups, material test data, etc.

CHAPTER 2

2. BRIDGE HEALTH MONITORING USING ACOUSTIC EMISSION TECHNIQUE

2.1. Introduction

The primary aim of developing a comprehensive bridge health management system is to design a self-sustaining, autonomous, wireless structural monitoring system based on stress, vibration and acoustic emission sensing, building the prototype, experimentally verifying it and lastly developing accurate finite element models for aiding the signal processing and decision making procedures. Figure 2.1.1 shows the general system architecture of such a system. However, only a part of the effort being undertaken in such a large interdisciplinary project is considered in the study presented herein. The three main components of the overall effort are as follows:

- A low-power Flash FPGA-based AE sensor platform, which will work as a data acquisition system.
- A vibration-based self-adaptive energy harvesting technology that works with a broad range of excitation frequencies.
- Quantitative structural health assessment analysis based on acoustic emission signals to de-noise the sensor data, characterize the signal source and identify the event location followed by component-level and system-level health assessment.

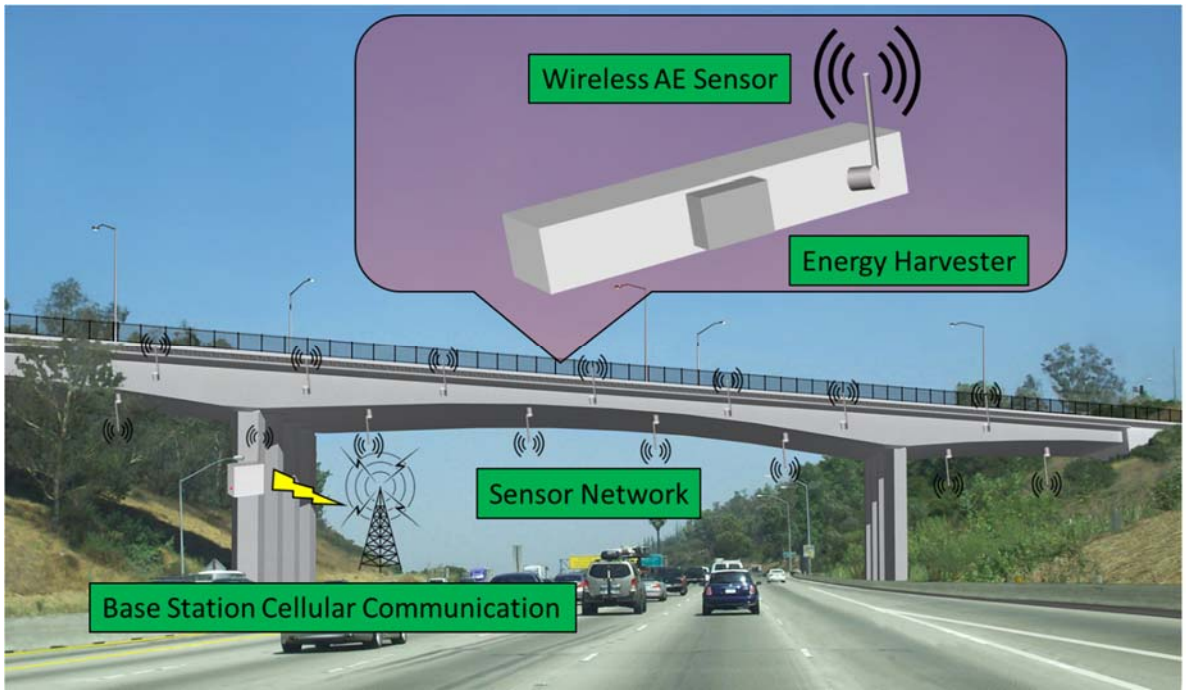

Figure 2.1.1. General architecture of the system.

The first two efforts were conducted though primary collaboration of researchers in Electrical Engineering and Mechanical Engineering Departments of Vanderbilt University. They developed wireless sensor data acquisition network platform and the energy harvester, respectively [54]. These major efforts are, however, not presented here. In this study, only the work done by the author related to the third effort is presented. The five main components of the author's effort were:

- Testing the whole SHM system on structural specimens representative of typical bridge components.
- Processing of sensor data for damage detection and noise elimination.
- Detection of the source of the acoustic signal of interest.
- Diagnosis of the nature of the signal for source characterization.

- Developing finite element models including the AE sensors and validate with experimental results.

2.2. Experimental Studies on Test Beams

As representative structural elements, steel, reinforced concrete and prestressed concrete beams were considered in this study. Design and fabrication details of the test specimens for this stage (stage-1) is given in Appendix-A. The first two stated beam types were tested by subjecting to cyclic loads and the third type could be subjected to quasi-static loading only, primarily, due to equipment limitations.

After the electrodynamic shaker and the support system were mounted on the strong floor and the sensors and the data acquisition system were setup and calibrated, the system was ready to perform the experiments on reinforced concrete and steel beams. Initial cracks were introduced to the steel beams to expedite the crack growth process. Five of the reinforced concrete beams were used in trial runs to fine tune the test procedure and the rest of the beams were subjected to final test runs. In each case, the signal data from four acoustic emission sensors were recorded using the data acquisition system, for further processing and evaluation. Also data from other transducers like strain gages (two at quarter points, one at top center and one at bottom center) and accelerometers were acquired for supplemental information on response.

The prestressed concrete beam could not be accommodated in the cyclic loading system setup for steel and reinforced concrete beams because of its larger dimension and heavy self-weight. In order for the retention of the prestressing force after unavoidable losses, prestressed beams of smaller dimensions was not feasible. Under the circumstances,

the only recourse was to subject the beam to four-point quasi-static loading till cracks appear creating strain waves which can be picked up by the AE sensors. All details of the supports, loading systems and testing equipment used during this stage are given in Appendix-B.

Since the method of pencil lead break testing is the most widely used method to calibrate and measure the performance of an acoustic emission system under laboratory conditions, several sets of pencil lead break test was performed on each type of test beam before actual cyclic loading. Pencil lead break testing is also known for generating acoustic signals which closely resemble the signals generated by cracks. Therefore, the data generated by pencil lead break tests can be used for training the neural network for locating the sources of signals from a real crack growth recorded during cyclic load testing.

2.2.1. Behavior of Reinforced Concrete Beam

Pencil-lead-break test stations and the general configuration of the reinforced concrete beam are shown in Figure 2.2.1. Pencil-lead-break test was undertaken successively by advancing from station-1 thru station-14, and then by retracing backwards from station-14 to station-1. This routine was repeated several times giving several sets of recorded data. In each set a total of 27 pencil-lead-break signals were generated.

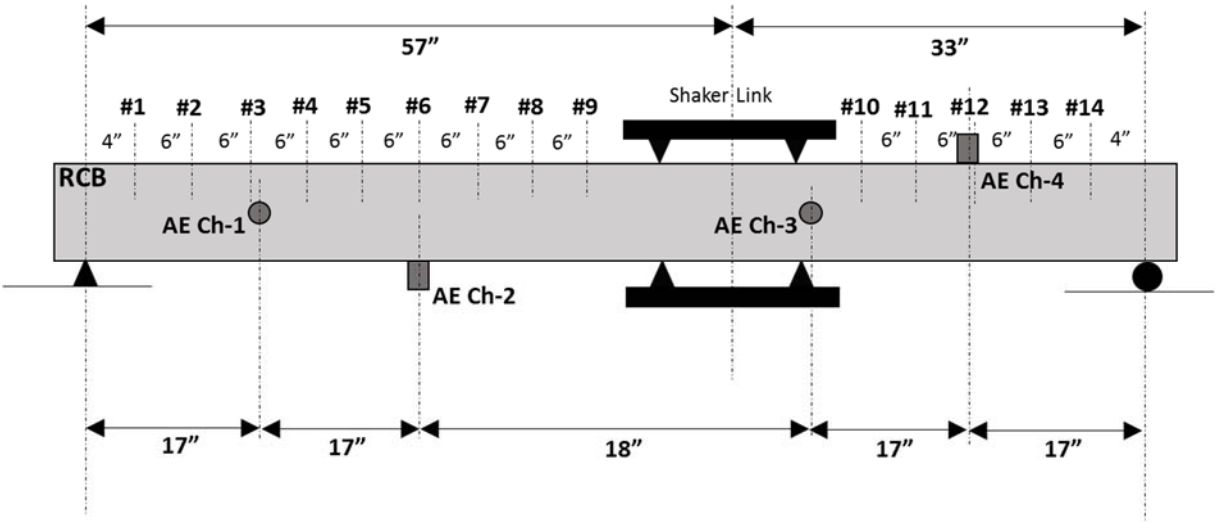

Figure 2.2.1. Location of pencil-lead-break stations for reinforced concrete beam.

After the conclusion of pencil-lead break-test, the beam was subjected to several sinusoidal dynamic loading cycles at 10Hz with different amplitude and durations. The load was applied through one pairs of closely spaced knife edges both at top and bottom causing downward and upward deflections in the beam during cyclic excitation. The applied amplitudes of cyclic sinusoidal displacement were 0.01”, 0.02”, 0.05”, 0.10” and 0.15”, respectively. The first two smallest amplitudes were specifically chosen to ensure recording of signals prior to any crack formation (or growth) from non-crack related sources like environmental noise, rubbing between the beam and supports, friction between the concrete and the reinforcement, etc. However, no such event could be identified during these two initial cycles.

During subsequent loading with amplitude of 0.05”, a crack appeared in the bottom of the beam at a distance of 7.5” from the center of shaker link. This crack eventually spread to the full depth of the beam when the excitation amplitude was increased to 0.10”. No additional major events were discernible when the amplitude was further increased to

0.15”. A general view of the test setup, showing the close-up view of the crack and locations of the accelerometer, gages and transducers can be seen in Figures 2.2.2 to 2.2.4.

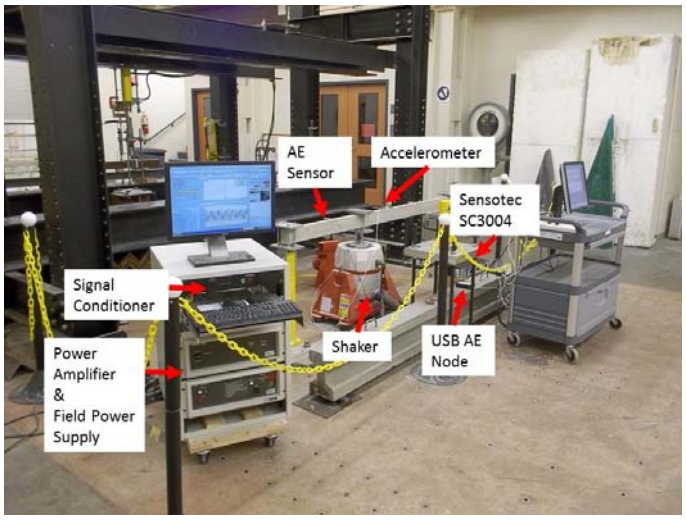

Figure 2.2.2. General view of test setup for reinforced concrete beam.

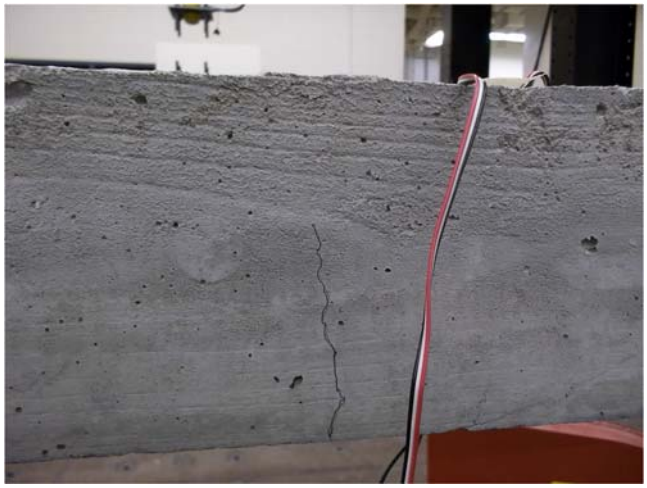

Figure 2.2.3. Cracking of reinforced concrete beam with excitation amplitude of 0.05”.

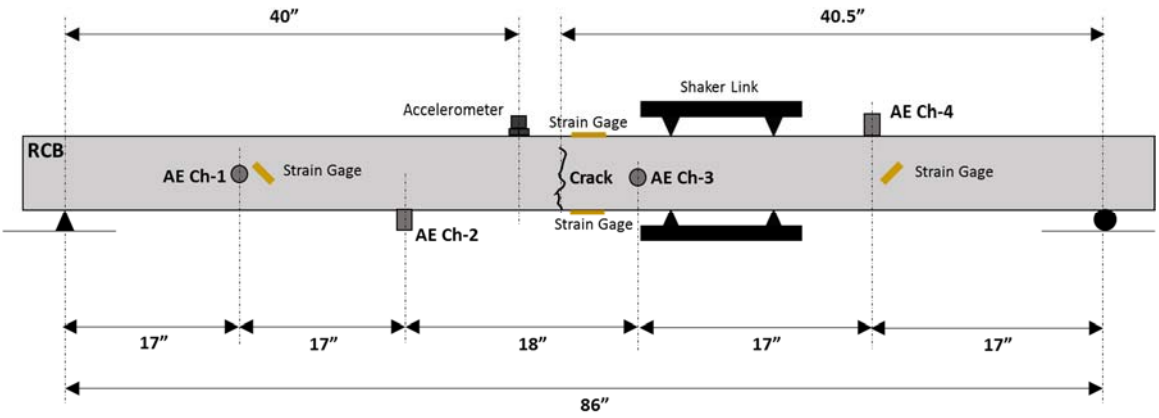

Figure 2.2.4 Locations of gages, AE sensors, accelerometer and crack of the reinforced concrete beam.

2.2.2. Behavior of Prestressed Concrete Beam

The results of quasi-static load tests on prestressed concrete beam PSCB3 only are considered. First, the test was undertaken on the original beam so that the maximum applied load caused crack-like damage to the beam. Secondly, the testing was repeated after the damaged beam was subjected to bonded FRP patch repair, following procedures discussed in Chapter-3. Acoustic emission activity of the beam was monitored during both the tests to allow for the determination of the modifying effect of the repair on the recorded signals. The top and side station-locations for pencil-lead-break tests are shown in Figure 2.2.5.

During the first loading stage, the beam was loaded up to a total load of 22 kips when two shear cracks appeared on each of the girder. During the first loading cycle, only two acoustic sensors were operational and one of these got detached as one of the shear cracks appeared right at the location of this sensor (see Figure 2.2.6). Close-up view of the cracks, a view of the general test setup and locations of gages and sensors are shown in Figures 2.2.6 to 2.2.8.

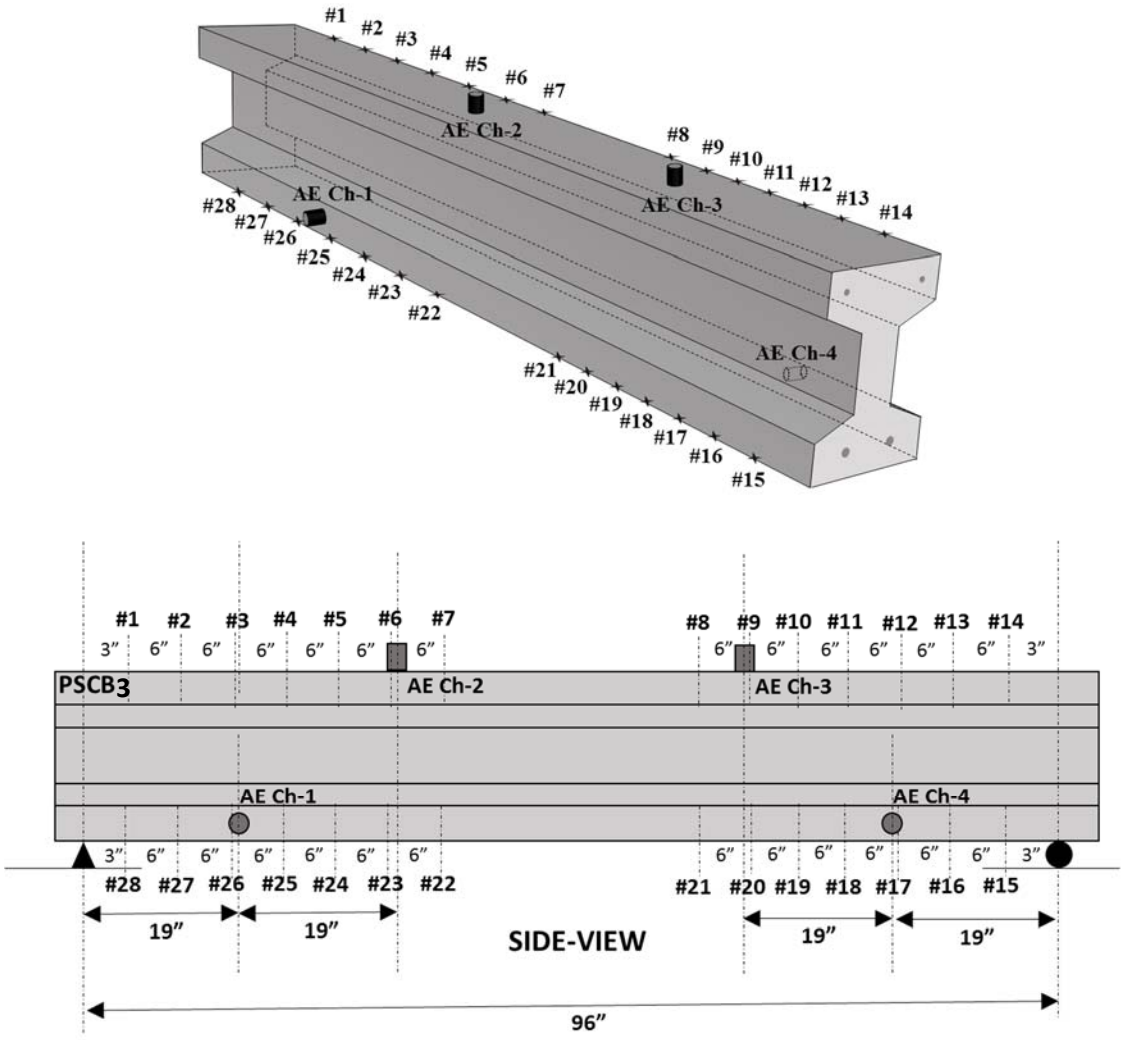

Figure 2.2.5. Pencil-lead-break stations of the prestressed concrete beam.

(a) Detached sensor (Channel-1) at first crack location

(b) Second shear crack (symmetrically placed)

Figure 2.2.6. Cracks of the prestressed concrete beam.

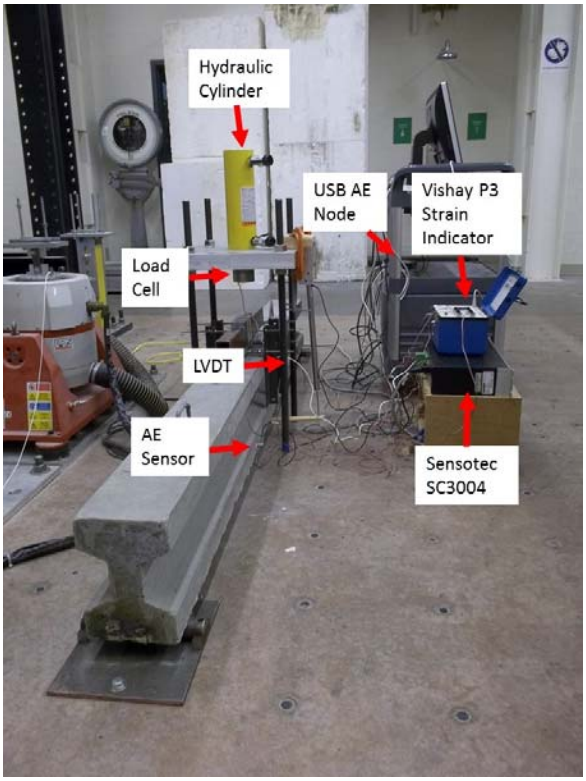

Figure 2.2.7. General testing setup for prestressed concrete beam.

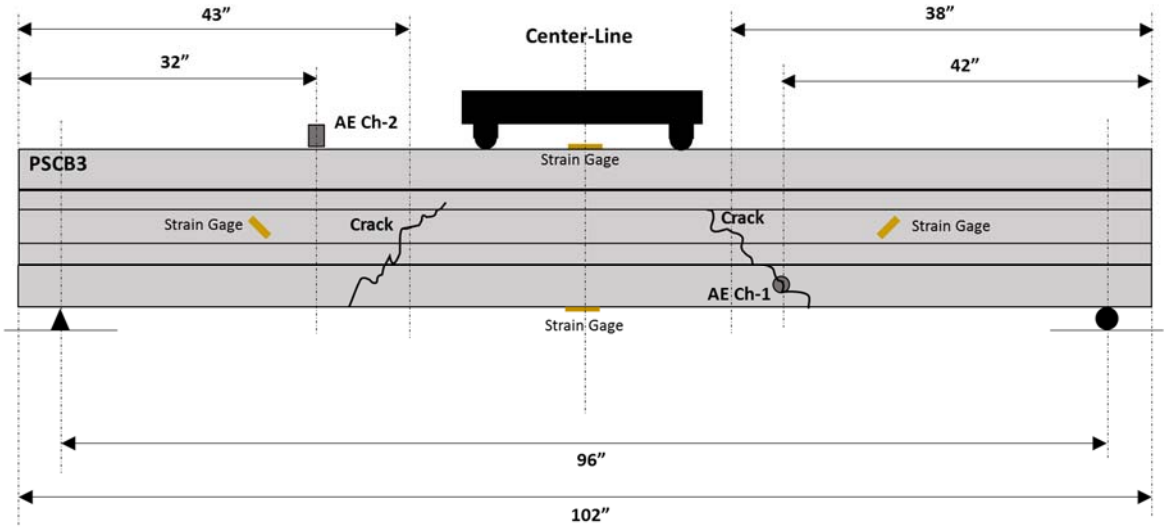

Figure 2.2.8. Locations of the gages, transducers and the cracks of the prestressed concrete beam before repair.

The repaired girder reached the limit state at a load of 17.3 kips showing shear compressive failure. One of the original cracks appeared during the first loading stage grew further by extending from the load application point to the support roller. During this loading stage, fortunately, all four AE sensors were active. Close-up views of the crack and locations of the gages and transducers are shown in Figures 2.2.9 and 2.2.10.

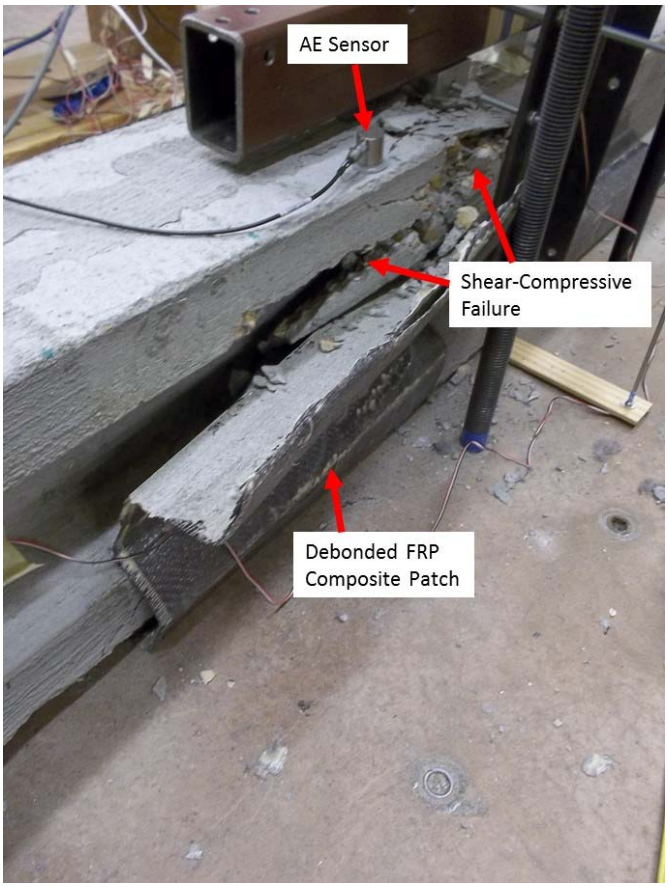

Figure 2.2.9. A view of the gages, transducers and the failure in the repaired girder.

2.2.3. Behavior of Steel Beams

Locations of the sensors, supports, loading configuration and pencil-lead-break test stations of all the three steel beams (SB-1, SB-2 and SB-3), are shown in Figures 2.2.11 to 2.2.13. For these beams, the pencil-lead-break tests were undertaken as before.

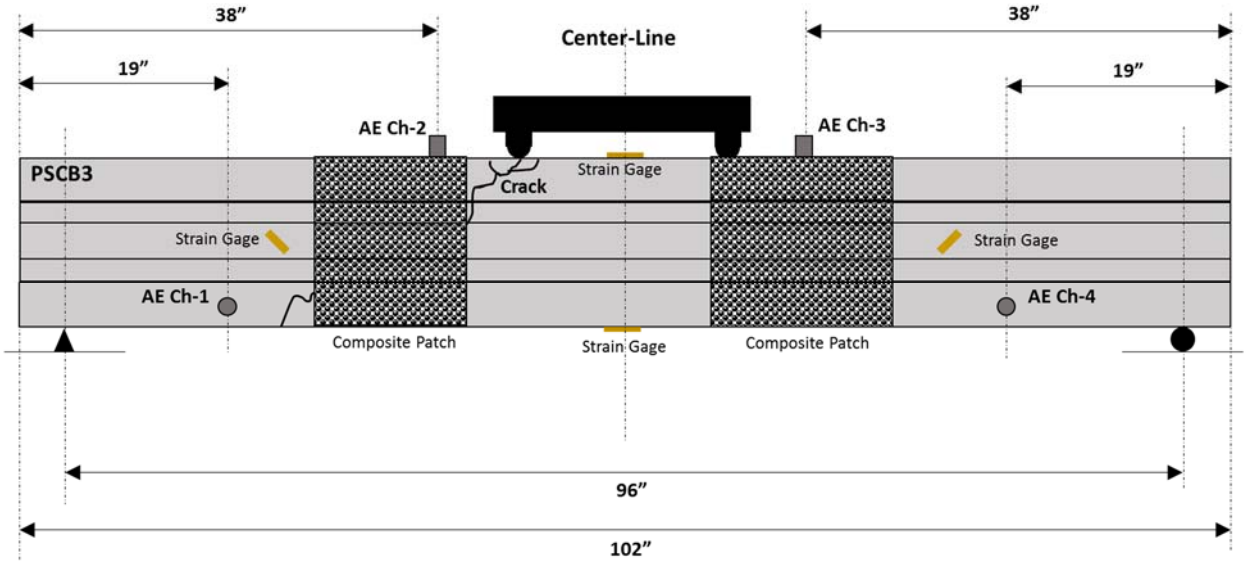

Figure 2.2.10. Locations of and cracks in the second loading stage.

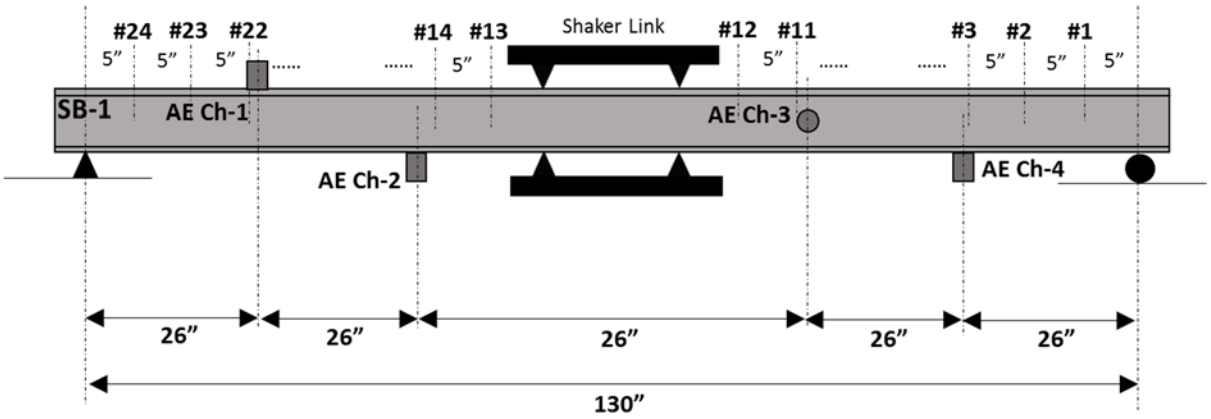

Figure 2.2.11. Pencil-lead-break test stations for steel beam SB-1.

Initially, a 10 Hz cyclic loading with displacement amplitude of 0.25" was applied to the undamaged steel beam SB-1 to determine if it generates any non-crack related signals. This led to the detection of several major acoustic emission events. The data generated here was later processed to identify the nature of the signals generated by non-crack related sources.

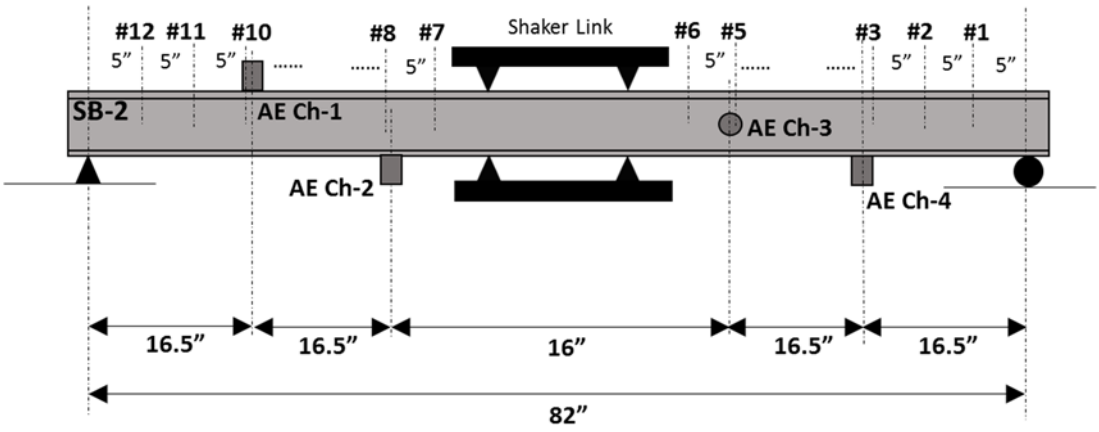

Figure 2.2.12. Pencil-lead-break stations for steel beam SB-2.

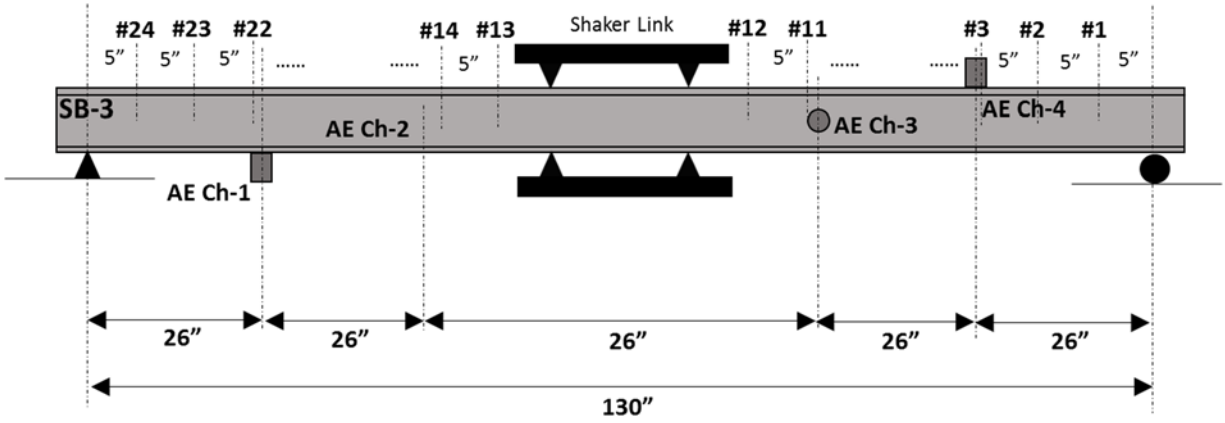

Figure 2.2.13. Pencil-lead-break stations for steel beam SB-3.

After the initial damages were introduced in the steel beams, as described earlier, the beams were excited with sinusoidal loads of 10 Hz with different cycles of increasing displacement amplitudes and different durations. For instance, SB-1 was loaded with three such cycles with amplitudes of 0.20", 0.25" and 0.50". SB-2 was loaded with four different cycles with displacement amplitudes of 0.085", 0.106", 0.212" and 0.150". SB-3 was loaded with three different cycles with the displacement amplitudes of 0.20", 0.25" and 0.30".

In the case of steel beams SB-1 and SB-2, the purposely induced initial cracks kept growing with increasing loading cycles, as detailed in Appendix-A. On the other hand, in the case of beam SB-3 with a pair of edge cracked holes in the bottom flange at midspan detailed in Appendix-A, needed cyclic loading for a much longer duration for crack growth to occur, unlike what happened with SB-1 and SB-2. Cyclic loading of SB-3 was stopped after a crack growth of very small size could be realized. During these test runs, the signals due to generated stress waves were recorded with the data acquisition system. The general view of test setup, a close-up of the crack in SB-1 and locations of the gages, accelerometer and transducers for all steel beams are shown in Figures 2.2.14 to 2.2.18.

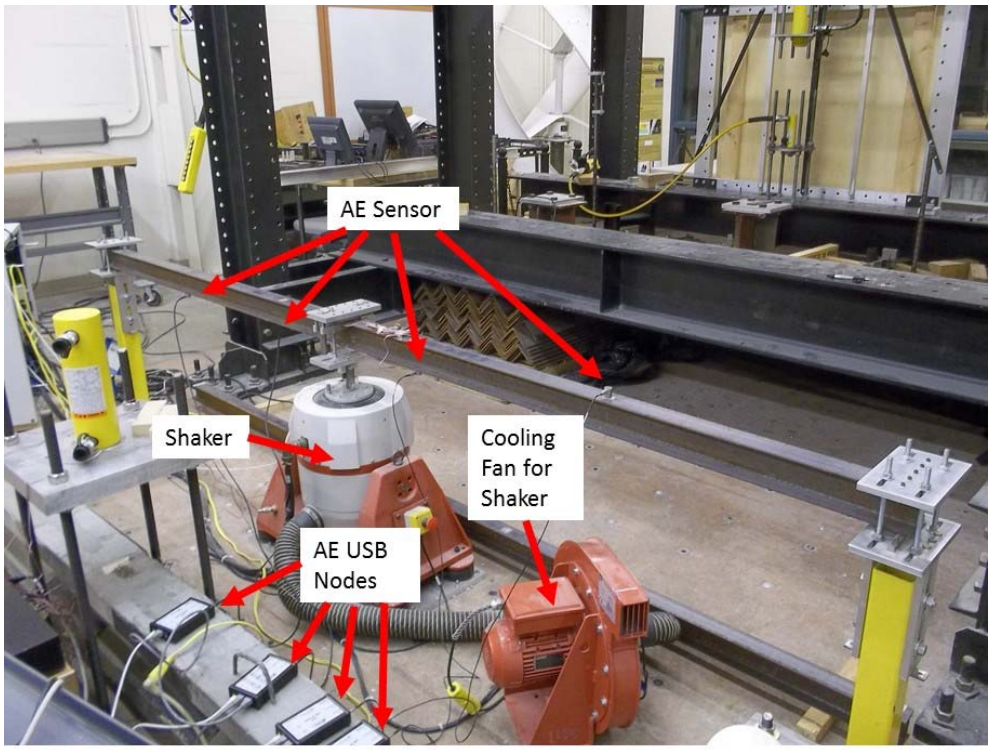

Figure 2.2.14. A view of test setup for steel beams.

Figure 2.2.15. Crack formation in steel beam SB-1 (highlighted).

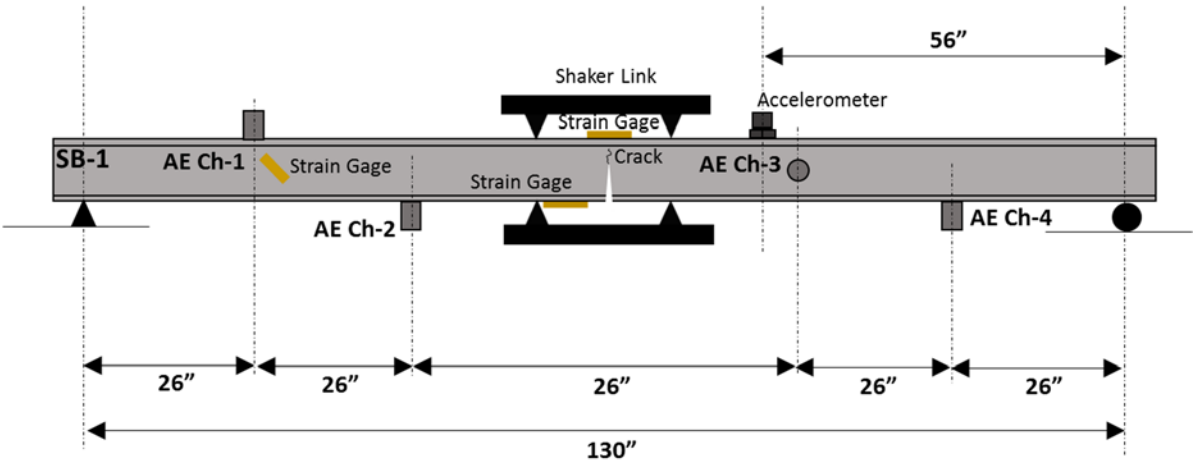

Figure 2.2.16. Locations of gages, transducers, accelerometer and crack in beam SB-1.

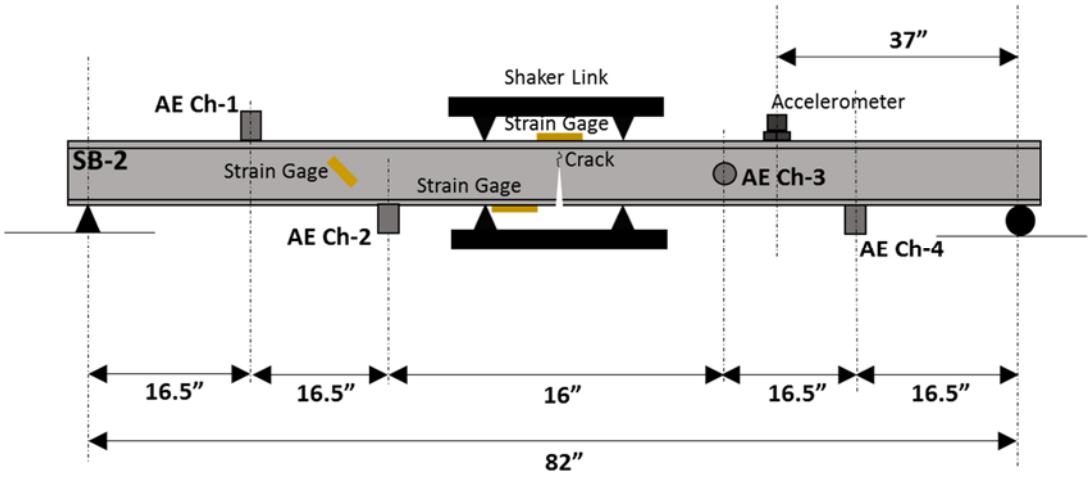

Figure 2.2.17. Locations of gages, transducers, accelerometer and crack in beam SB-2.

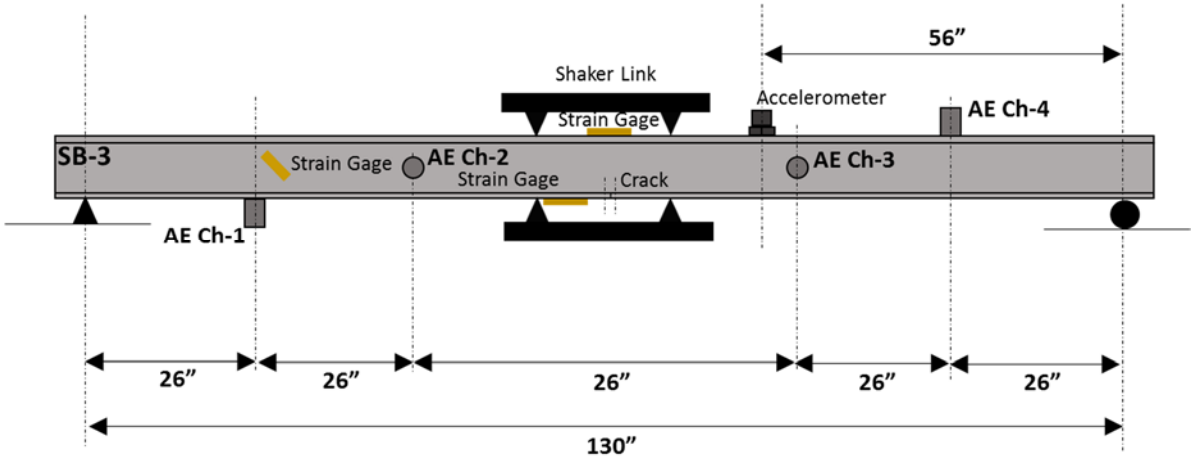

Figure 2.2.18. Locations of gages, transducers, accelerometer and crack in beam SB-3.

2.3. Signal Processing

The most challenging issues of AE sensor based health monitoring of structures is de-codifying the information carried by the recorded signals so that the location of the source of the signal and the nature of the processes causing it can be identified. This is a difficult proposition because the signal gets polluted by background noise from various sources and these noises need to be filtered out to enable the accurate location of the

damage. In order to identify the nature of the damage, it is necessary to have the classified information about various damage sources. Powerful tools like wavelet transformation, power spectrums, fast Fourier transforms and neural networks, are the most promising tools which could help achieving the desired objectives. In this study, these very tools were used for the elimination of the background noise, in the detection of the damage source and for classifying the de-noised signals based on their sources.

2.3.1. Noise Elimination

The noise sources of a recorded acoustic emission signal can be internal or external based on the equipment, structure under test and loading and environmental conditions. Some of the most common noise sources encountered during acoustic emission testing are crack breathing, friction, impact and ambient noise [1]. The traditional method among the researchers to eliminate the acoustic emission noise is simply to use band-pass filters. Although with necessary precautions and thorough preliminary investigations of the structure, environment and loading conditions, the method might work in some situations, but there is always a high probability of inhibiting the acoustic emission detection. This study attempts to use a more potent tool [55] like wavelet transformation to eliminate the background noise from the recorded AE signals.

Wavelet transformation is a natural extension of Fourier analysis. One of the alternative methods to separate tangled signals is windowed Fourier transformation with which one can accomplish this task only with limited success. On the other hand, all components of the signal with high and low frequencies and local details or discontinuities

can be detected easily with the help of wavelets. Consequently, wavelets are sometimes referred to as ‘mathematical microscope’ [56].

Wavelet transformation basically converts the signal into the information of numbers and coefficients. This information can then be used to represent the signal itself as a combination of multiple shifted and scaled wavelets. By knowing the mother wavelet and the information of numbers and coefficients, one can work on, transmit, store, analyse, or reconstruct the original signal. Wavelet transformation follows a similar path as the Fourier analysis to calculate the signal coefficients. The basic idea behind the method is to multiply together the signal and the function being analysed, and then to compute the integral of the resulting product. Comparison of wavelet and Fourier transformations is represented graphically in Figure 2.3.1. In a nutshell, wavelets can be considered as mathematical functions with limited duration and zero average value. In general, wavelet transformation is the breakdown of the original signal into scaled and shifted versions of the mother wavelet. Scaling the wavelet or changing of frequency can be achieved simply by squeezing or stretching the chosen wavelet or by changing the amplitude. Unlike other traditional signal analysis methods, wavelet transformation does not ignore the local details in the signal, which is the main advantage of the method. Therefore, signal de-noising can be accomplished with minimum degradation.

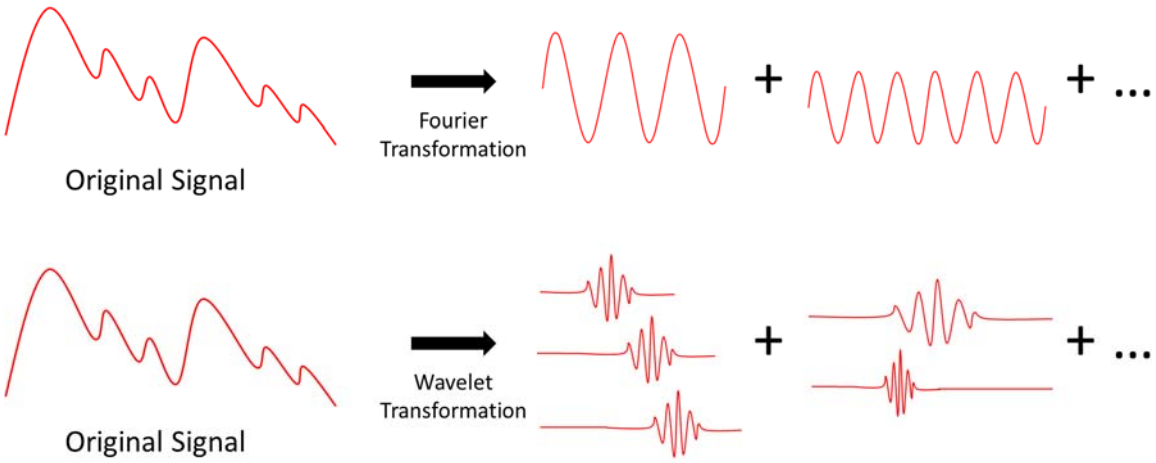

Figure 2.3.1. Graphical representation of Fourier and wavelet transformations.

A signal corrupted by noise can be represented mathematically by using Equation 2.3.1 where s_n, s_o, s, t and σ represent the noise, original signal, recorded signal, time and noise level, respectively.

$$s(t) = s_o(t) + \sigma . s_n(t) \qquad (2.3.1)$$

De-noising procedure used in this study is accomplished in three main stages, as explained below based on the sample noisy signal represented by Equation 2.3.1.

- After choosing a mother wavelet and a decomposition level, the noise function $s_n(t)$ is computed by using a "thresholding" method after the wavelet decomposition.
- A thresholding algorithm (hard or soft) is applied to the wavelet detail coefficients.
- The signal is reconstituted based on the unchanged (if any) and the modified detail coefficients by using wavelet reconstruction.

Decomposition of the signal is started by applying the mother wavelet at the smallest scale. This procedure is then repeated for each decomposition level by doubling the time scale, in other words by expanding the wavelet. This process is continued until the target decomposition level is reached. The decomposition level used during this study is 5.

The most popular wavelet thresholding algorithms are termed as hard and soft. Hard thresholding method can be described as a "keep or kill" procedure, in which wavelet coefficients which are below a selected threshold are eliminated. On the other hand, during the soft thresholding procedure, which is an extension of the hard version, the nonzero coefficients (above the threshold) get shrank towards zero in absolute value. In this study, since soft thresholding procedure give smoother signal outputs indicated by preliminary studies, the same is used here during the de-noising process. Hard and soft thresholding procedures are described mathematically and graphically in Equations 2.3.2 and 2.3.3 and Figures 2.3.2 and 2.3.3.

$$d_{jk}^{Hard} = \begin{cases} 0, & if\left|d_{jk}\right| \leq \lambda \\ d_{jk} - \lambda, & if\left|d_{jk}\right| > \lambda \end{cases} \tag{2.3.2}$$

$$d_{jk}^{Soft} = \begin{cases} 0, & if\left|d_{jk}\right| \leq \lambda \\ d_{jk} - \lambda, & if\left|d_{jk}\right| > \lambda \\ d_{jk} + \lambda, & if\left|d_{jk}\right| < -\lambda \end{cases} \tag{2.3.3}$$

Here, subscripts j and k represent decomposition/resolution level and index of the wavelet coefficients. Moreover, d_{jk}, δ and λ represent wavelet detail coefficients, thresholded wavelet coefficient and thereshold level, respectively.

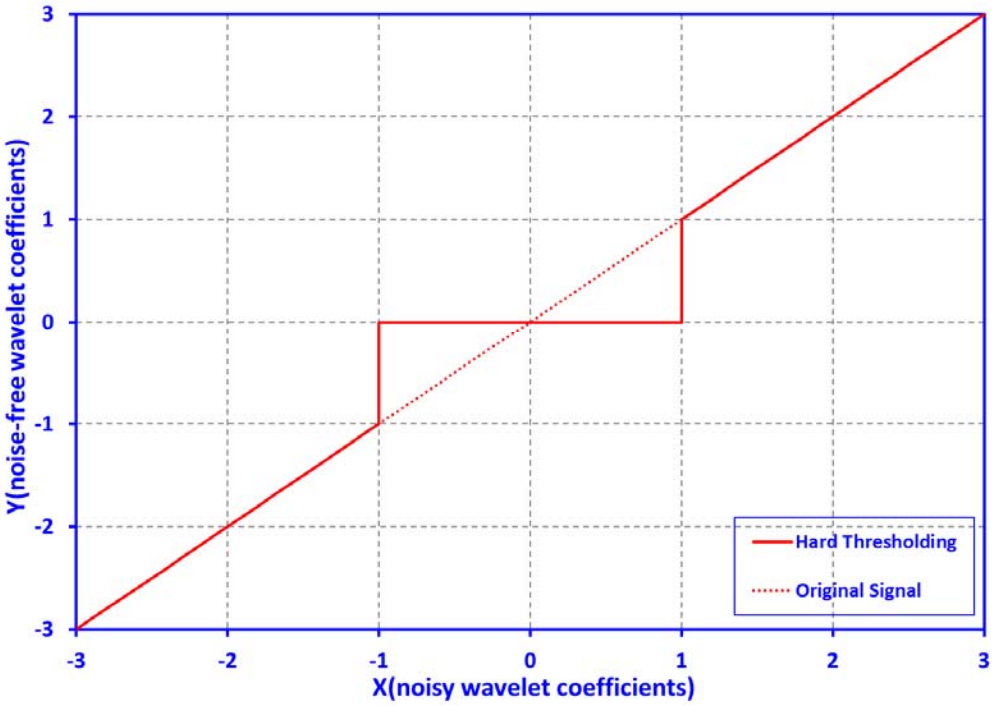

Figure 2.3.2. Hard thresholding and the original signal.

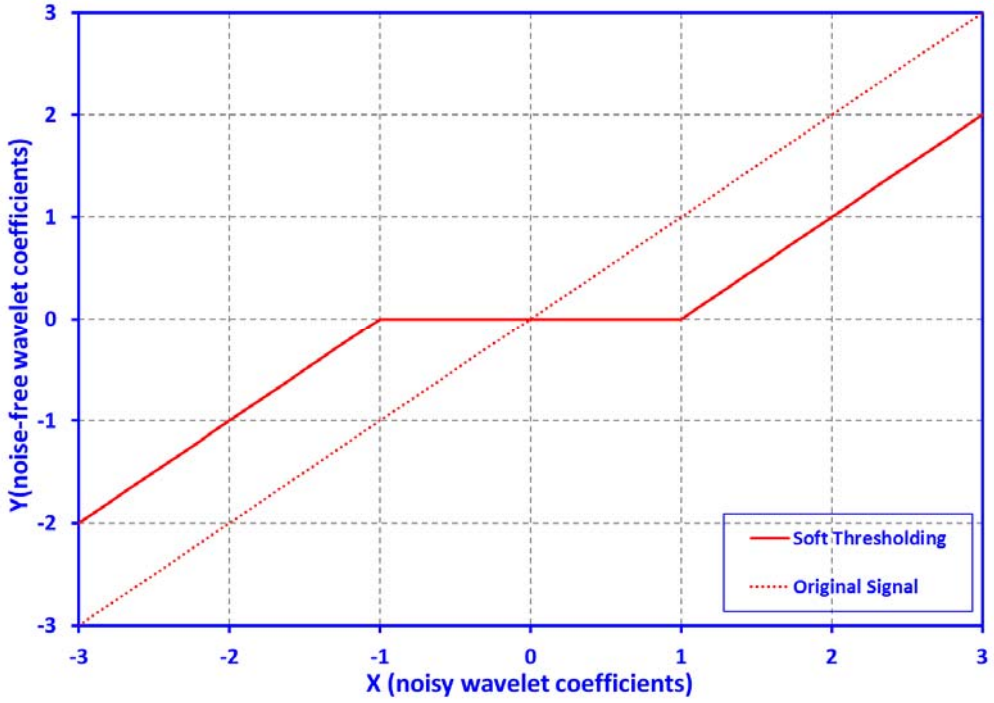

Figure 2.3.3. Soft thresholding and the original signal.

Choosing the threshold is a very delicate and important statistical problem. Threshold levels that are used during the de-noising procedure are determined by using the "Universal Threshold" method proposed by Donoho and Johnstone [57]. Theoretical considerations of the method yield the formula shown in Equation 2.3.9.

Let the wavelet coefficients of the noise be X_i for $i=1,\ldots,n$ where X_i is an i.i.d. $N(0,\sigma^2)$.

Defining: $Z = \left[\max_i X_i\right]$

By Jensen's inequality:

$$\left(\varphi(E[X])\right) \leq E[\varphi(X)] \tag{2.3.4}$$

Where φ is a convex function and E is the expected value.

$$exp\{tE(Z)\} \leq E\ exp\{tZ\} = E \max_i exp\{tX_i\} \leq \sum_{i=1}^{n} E[exp\{tX_i\}] \tag{2.3.5}$$

From the definition of Gaussian moment generating function which is the expected value of e^{tx} for a real random variable X.

$$E\ exp\{tZ\} \leq \sum_{i=1}^{n} E[exp\{tX_i\}] = n\left(e^{\mu t} e^{1/2 \sigma^2 t^2}\right) \tag{2.3.6}$$

Therefore:

$$tE\{Z\} = logn + \frac{t^2\sigma^2}{2} \tag{2.3.7}$$

Set t by using Equation 2.3.8 to get "Universal Threshold" relationship shown in Equation 2.3.9.

$$t = \frac{\sqrt{2logn}}{\sigma} \tag{2.3.8}$$

$$\lambda^U = \sqrt{2.\log n}\,.\sigma \tag{2.3.9}$$

Where λ, σ and n are threshold level, square root of variance of the noise and length of the input vector, respectively. During multi-resolution wavelet decomposition, empirical wavelet coefficients at the finest scale are essentially pure noise with a small fraction of exceptions [57]. The noise variance σ^2 is estimated as the median absolute deviation of the wavelet coefficients at the finest level divided by 0.6745.

The mother wavelet that will be used throughout this study is chosen as the symmetrical wavelet Symlets 8 (Sym8), shown in Figure 2.3.4. The family of Symlet wavelets is a modified version of Daubechies wavelets with increased symmetry. The main motivation for choosing this wavelet as the mother wavelet is mainly due to its past success in similar applications. For each test specimen, AE signals from crack initiation/growth, as raw records and those after de-noising, are shown in Figures 2.3.5 to 2.3.8. Due to the extremely small crack growth in the case of steel beam SB-3, no clearly measureable crack related acoustic emission data could be recorded and hence no processed data can be reported for this specimen.

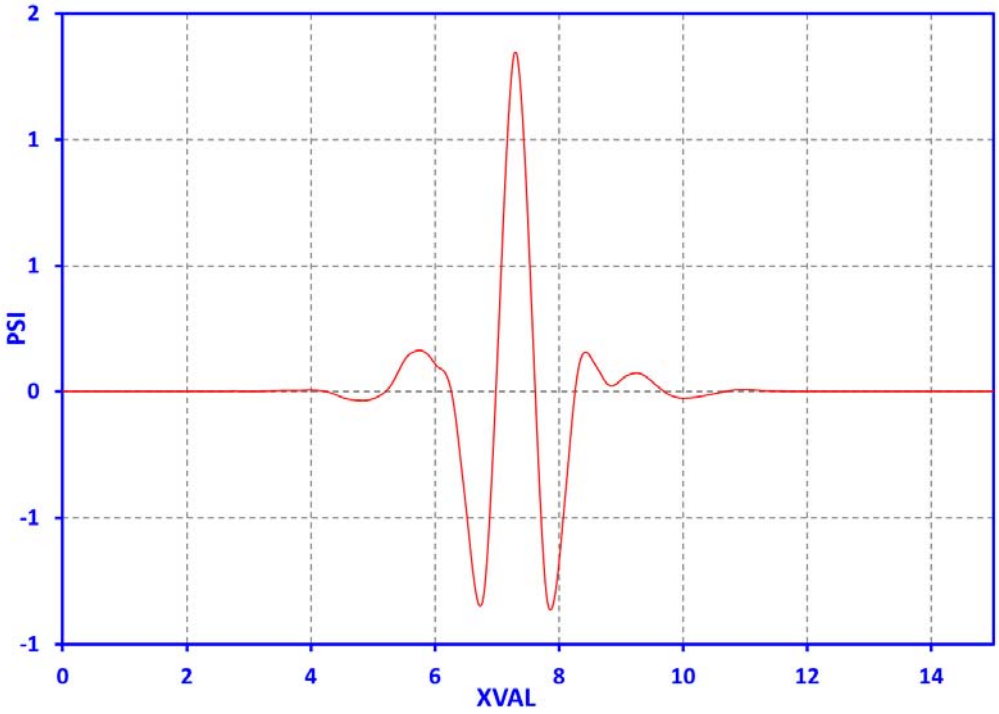

Figure 2.3.4. Mother wavelet Symlets 8 (Sym8).

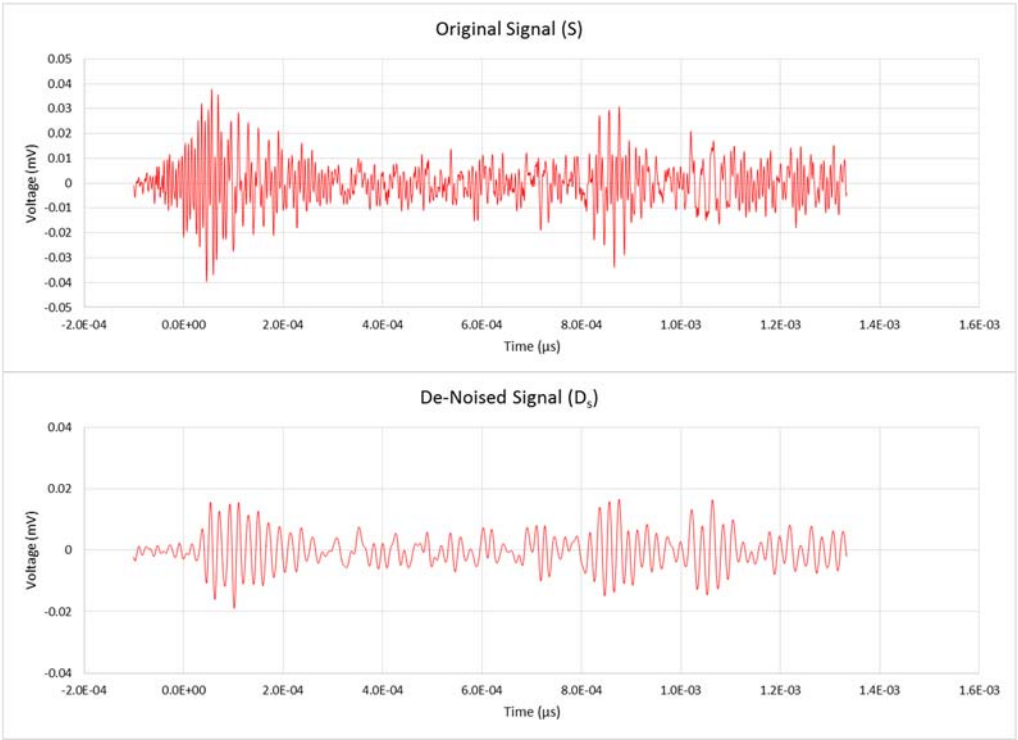

Figure 2.3.5. Original and de-noised crack signal from steel beam SB-1.

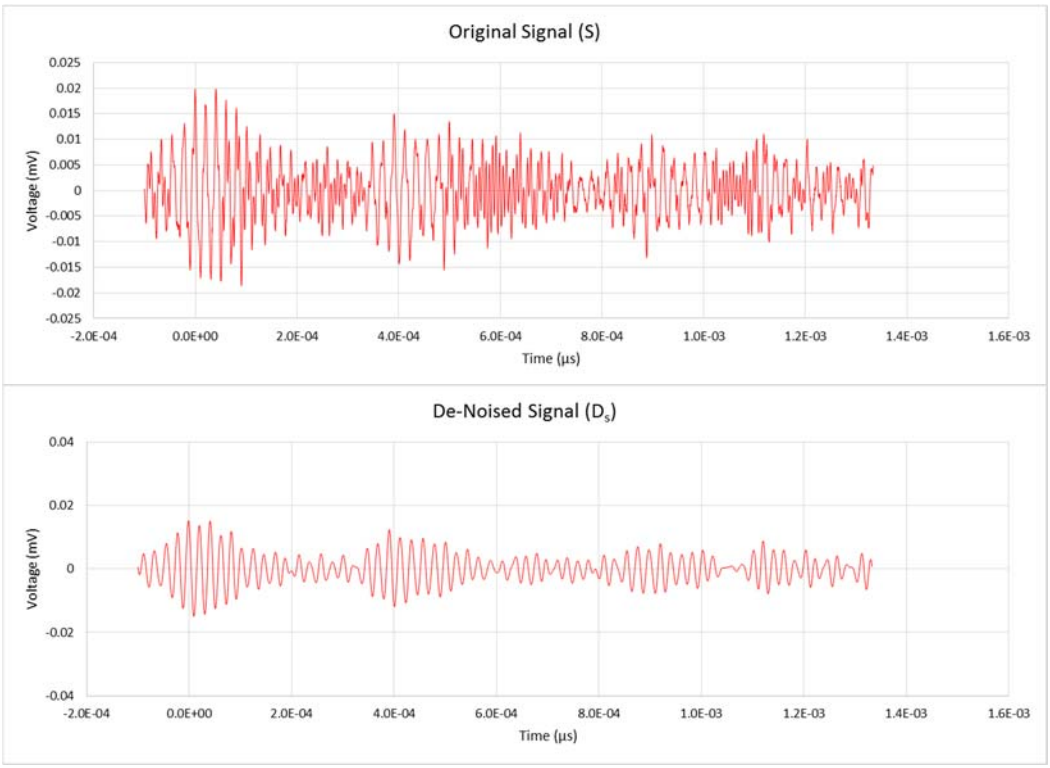

Figure 2.3.6. Original and de-noised crack signal from steel beam SB-2.

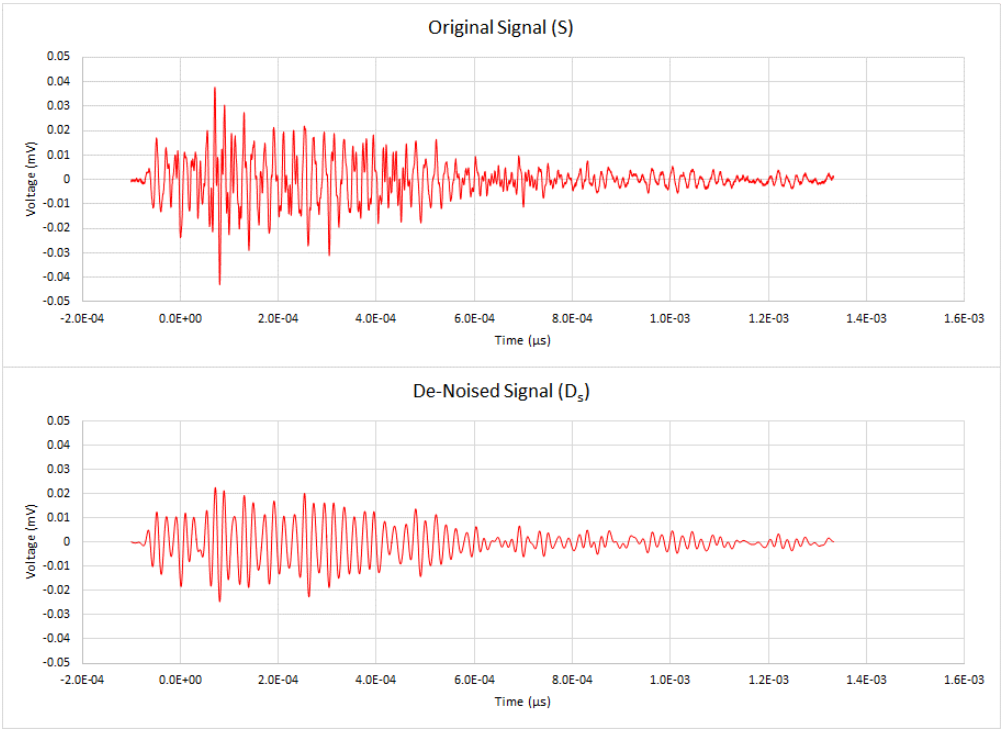

Figure 2.3.7. Original and de-noised crack signal from the reinforced concrete beam.

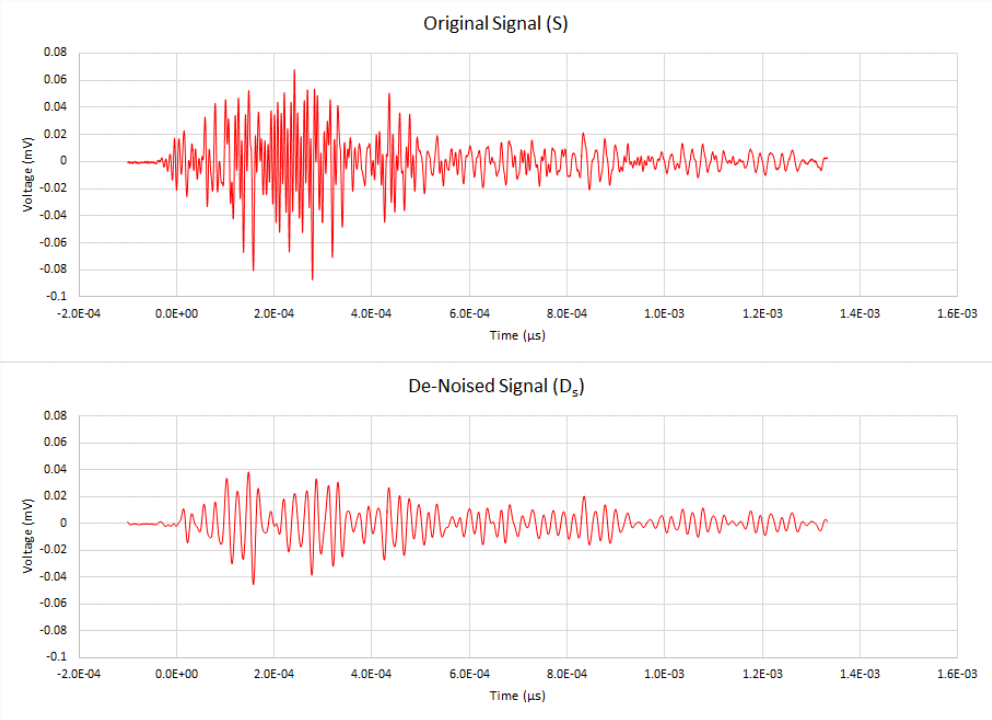

Figure 2.3.8. Original and de-noised crack signal from prestressed concrete beam.

After a close inspection of the signal records shown in Figures 2.3.5 and 2.3.6, it is evident that the de-noised signals of crack growth recorded for the steel beams SB-1 and SB-2 are quite similar with the theoretical signal shown in Figure 1.2.2. This similarity underscores the success of the applied de-noising procedure used in this study. However, similar agreement cannot be clearly emphasized in the case of reinforced and prestressed concrete specimen data shown in Figures 2.3.7 and 2.3.8. This may be attributed to the non-homogenous nature of concrete material as well as the presence of inclusions like steel rods and/or strands inside these beams. Consequently, it may be reasoned that the waves traveling inside the reinforced concrete and prestressed concrete specimens experienced significantly more modifications before reaching the acoustic emission sensors.

A theoretical acoustic emission signal based on Equation 1.1.1 is generated by selecting the values of the variables V_O, B and ω as 1, 95 and 3.03E+5, respectively.

Comparison between the theoretical signal and the real de-noised crack generated acoustic emission signal is presented in Figures 2.3.9 and 2.3.10 for steel beams SB-1 and SB-2. In both cases, the closeness between theory and experiment is striking.

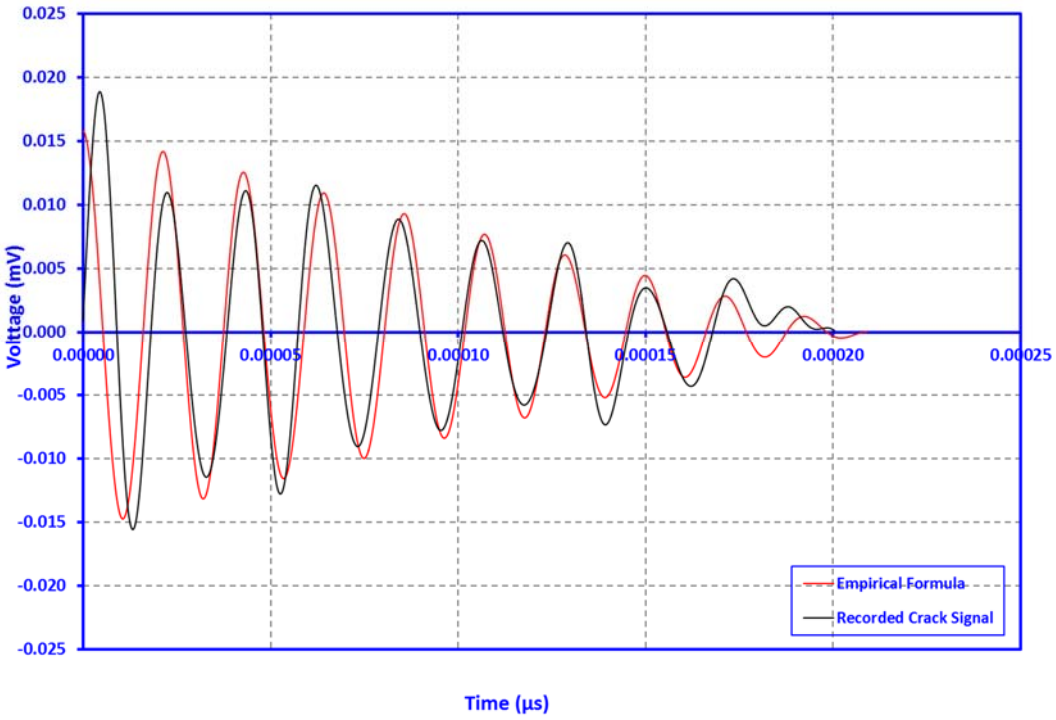

Figure 2.3.9. Comparison of empirical acoustic signal with experimental data for SB-1.

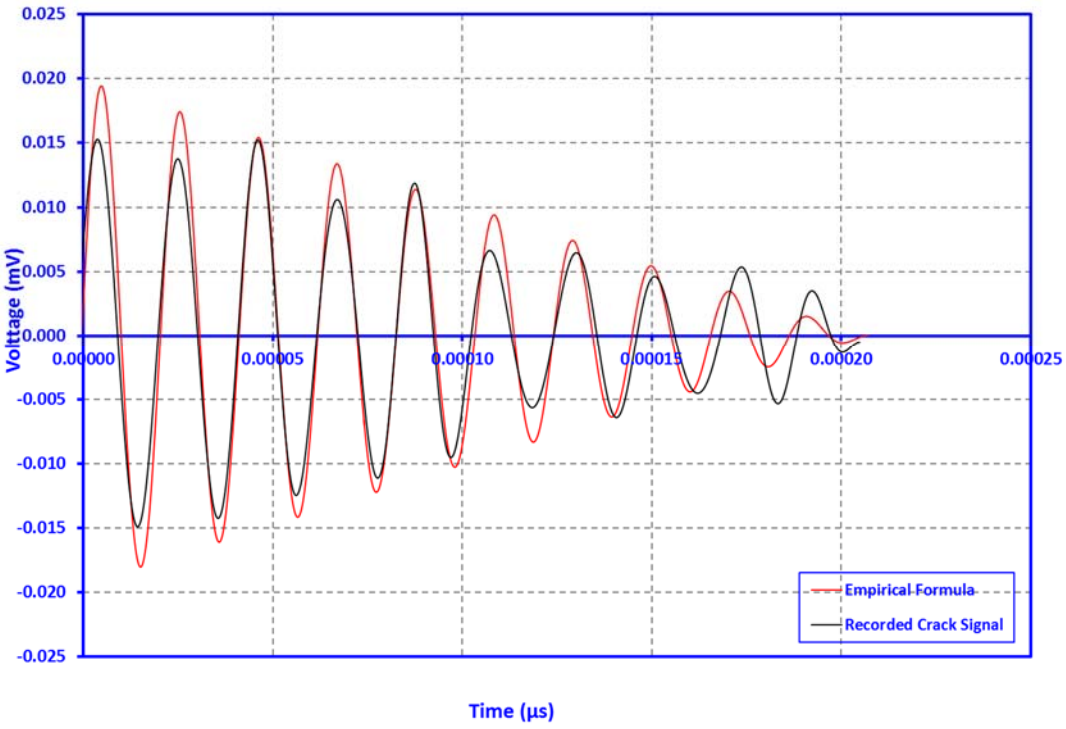

Figure 2.3.10. Comparison of empirical acoustic signal with experimental data for SB-2.

2.3.2. AE Event Source Location

During the travel of the stress wave inside the structure, spectral and modal characteristics of the wave changes significantly as it encounters complex shaped boundaries, non-homogeneities, damages or cracks, and the like. In addition, sensor and equipment limitations and the effect of sensor coupling agent, cause the stress wave to get severely modified before it gets converted into an electrical signal. Since the speed of the stress wave is highly dependent on the frequency and modal characteristic of the wave itself, determining the source of an acoustic emission signal becomes a highly nonlinear problem due to the factors described above, especially for reinforced concrete structures. This problem is represented in Equation 2.3.10 by Spall et al. for the output of a sensor located at distance *r*, corresponding to the instant of time *t* [58].

$$v(t) = \int_0^t \int_{structure} h(r, x, -\tau) \,.\, \beta(x, \tau).\, dx.\, d\tau \qquad (2.3.10)$$

Where, $v(t)$, x, β, h and τ are sensor output, source location, distribution of dilatation caused by acoustic emission event as a function of position and time, structural and sensor impulse response and time, respectively. Equation 2.3.10 looks like a simple relationship, but determining h and β appearing in the integrand can be extremely involved.

Classical deterministic time difference of arrival (TDoA) methods can only solve acoustic emission source location problems for relatively simple situations and structures like a simple plate or a solid cylindrical bar with homogenous material. In the presence of dispersion, significant background noise, and material non-homogeneity, the classical source location methods tend to fail because of excessive distortion of the AE signals during its propagation from the source to the sensor. Such signal modifications and distortions make the accurate detection of signal source highly uncertain. In this study, a new method based on Artificial Neural Networks (ANN) is proposed to be used to overcome this difficulty. The method is based on the use of the commonly used AE signal parameters such as frequency, rise time, maximum signal amplitude, signal energy, signal count and duration, in addition to signal arrival times to train the ANN which can then later be used for the determination of source location of the AE signals of interest. Before actual testing, several sets of data generated by using pencil lead break tests are used to train the ANN by combining the previously mentioned parameters covering the zone of interest.

The artificial neural network adopted in this study is a two layer (one layer being hidden) feed-forward network with sigmoid hidden neurons. Feed-forward networks are the most widely known and the most popular type of artificial neural networks. Such

networks have characteristically layered structures. A sample feed-forward neural network structure is shown in Figure 2.3.11. Each layer inside the network has multiple processing units called nodes. Each node in the network is connected to another node with a synapse (weight) which represents the importance of the connection. The connected nodes never belong to the same layer of the network. Functionality of the i^{th} neuron in a feed-forward network is defined by Equations 2.3.11 and 2.3.12.

$$\varphi_i = \sum_{j-0}^{k} w_{ij} \cdot y_j \tag{2.3.11}$$

$$y_i = f(\varphi) \tag{2.3.12}$$

Here w_{xy}, y_x, φ_x, $f(z)$ and k are the weight of the connection between the x^{th} and y^{th} neuron, output of the x^{th} neuron, potential of the x^{th} neuron, output function and the number of inputs feeding the current neuron, respectively.

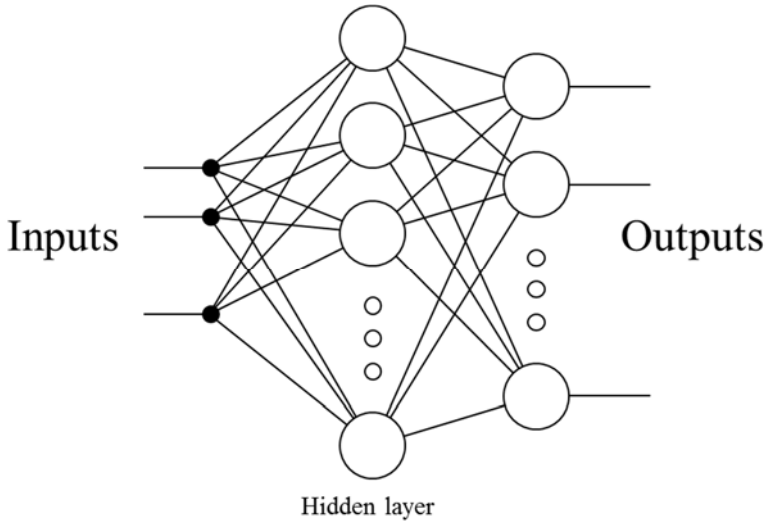

Figure 2.3.11. Sample structure of a one hidden layer feed-forward neural network.

There are two functions in an ANN that determine the way signals are processed by a neuron. The first one is the activation function which is defined by Equation 2.3.11

and the second one is the output function which appears as $f(z)$ in Equation 2.3.12. The combination of these two is called the transfer function. A transfer function basically takes the value from the activation function and turns it into a value between zero and one. This output then becomes an input for another neuron in a different layer. A non-linear sigmoid transfer function, which is used with the ANN of this study, is given by Equation 2.3.13 and shown in Figure 2.3.12.

$$f(\varphi) = \frac{1}{1 + e^{-\varphi}} \tag{2.3.13}$$

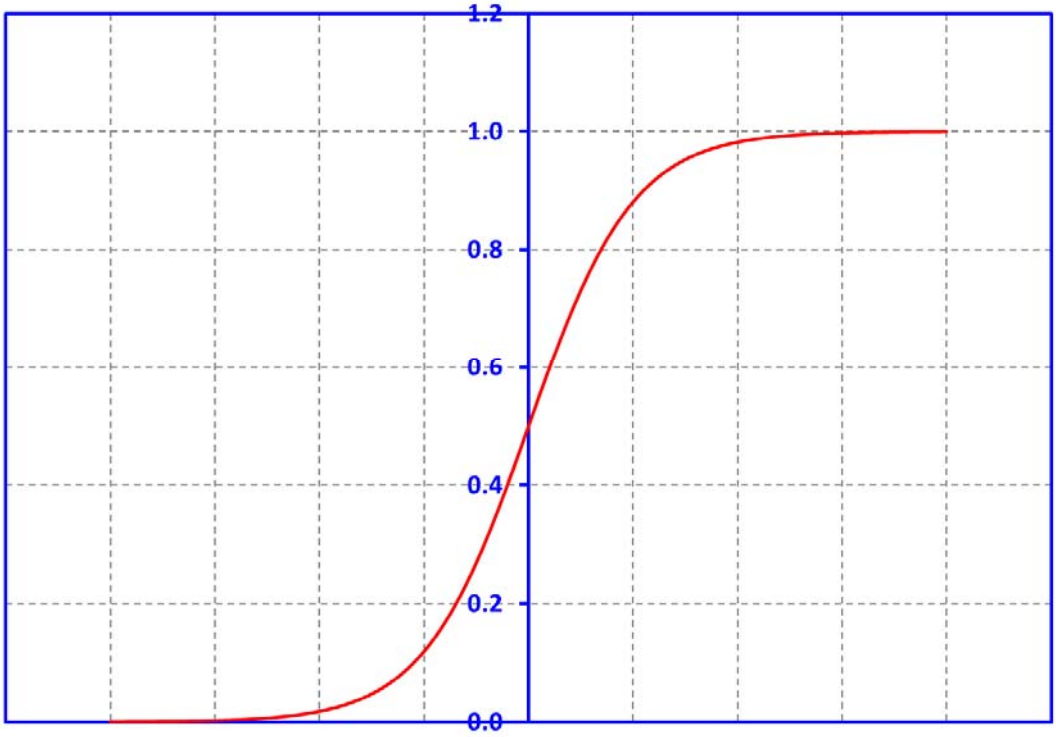

Figure 2.3.12. Sigmoid transfer function.

Leverberg-Marquardt back propagation algorithm [59] is used to train the ANN which is also known as the damped least squares method. Basically the goal of training is

to teach the ANN the associations between inputs and outputs. Steps followed during a Leverberg-Marquardt back propagation algorithm iteration is as follows [60]:

- Step-1: By using Equations 2.3.11 and 2.3.12, calculate the corresponding network outputs during the feed-forward phase.
- Step-2: Based on the network outputs, calculate the errors:

  $$e_i = t_i - y_i$$

  Then compute the sum of squares of errors over all inputs:

  $$V(\underline{x}) = \sum_{i=0}^{k} e_i^{\,2}(\underline{x})$$

- Step-3: It can now be shown that:

  $$\nabla V(\underline{x}) = J^T(\underline{x}) \cdot e(\underline{x})$$

  $$\nabla^2 V(\underline{x}) = J^T(\underline{x}) \cdot J(\underline{x}) + S(\underline{x})$$

  Where *J(x)* is the Jacobian matrix:

  $$J(\underline{x}) = \begin{bmatrix} \frac{\partial e_1(\underline{x})}{\partial x_1} & \frac{\partial e_1(\underline{x})}{\partial x_2} & \cdots & \frac{\partial e_1(\underline{x})}{\partial x_k} \\ \frac{\partial e_2(\underline{x})}{\partial x_1} & \frac{\partial e_2(\underline{x})}{\partial x_2} & & \frac{\partial e_2(\underline{x})}{\partial x_k} \\ \vdots & & \ddots & \\ \frac{\partial e_k(\underline{x})}{\partial x_1} & \frac{\partial e_k(\underline{x})}{\partial x_2} & & \frac{\partial e_k(\underline{x})}{\partial x_k} \end{bmatrix}$$

  and

  $$S(\underline{x}) = \sum_{i=0}^{k} e_i(\underline{x}) \nabla^2 e_i(\underline{x})$$

- Step-4: The following equation is solved to obtain Δx:

$$\Delta \underline{x} = \left[J^T(\underline{x}) \cdot J(\underline{x}) + \mu \cdot I \right]^{-1} \cdot J^T(\underline{x}) \cdot \underline{e}(\underline{x})$$

In which μ and I are the damping factor and the identity matrix, respectively. When $V(x)$ increases during a step, damping factor μ gets multiplied by factor β. When $V(x)$ decreases, μ is divided by β.

- Re-calculate $V(x)$ by using $x+\Delta x$. If $V(x)$ is smaller than the one computed in Step-2, reduce μ with β, let $x = x + \Delta x$, and go back to Step-2. If $V(x)$ is not reduced, then increase μ with β and go back to Step-4.
- The iterations stop when $\nabla V(x)$ defined in Step-3 is less than a predetermined tolerance or $V(x)$ defined in Step-2 has been reduced to some error goal.

There are total 28 input nodes for the ANN, namely, arrival time, frequency, maximum signal amplitude, rise time, signal count, duration and energy for each signal recorded by all four sensors. In the hidden layer there are 10 nodes. The only output node of the ANN is the location of the AE events. After the training phase of the ANN for each specimen is completed by using the data sets generated by pencil lead breaks, the source locations of real AE events are predicted by using these ANN's. Unlike the cases of reinforced concrete and steel specimens, the data recorded for the prestressed concrete specimen was not found to be suitable for determining the source locations of AE events. The main reason is the relatively large size of the prestressed concrete specimen as compared to the number of sensors used. Most of the acoustic signals were not picked up by more than three sensors due to attenuation which made it impossible to detect the signal source. Therefore four sensors are considered to be inadequate to determine the source location of the AE events for a girder of same or larger size and length as the prestressed concrete test beam. Comparison of the ANN source location predictions of some signals

with the real crack location for the steel and reinforced concrete test beams are presented in Tables 2.3-1 and 2.3-2, respectively. As can be seen from the results, source location of AE events can be predicted with high accuracy by using the proposed method, provided an adequate number of appropriately located sensors are used.

Table 2.3-1. Comparison of actual crack location in the steel beam SB-1 with neural network predictions (Distances are from left end).

Neural Network prediction	Actual crack location	Error
1618.42 mm	1651.00 mm	0.99%
1610.67 mm	1651.00 mm	1.22%
1469.52 mm	1651.00 mm	5.49%
1649.59 mm	1651.00 mm	0.04%
1720.52 mm	1651.00 mm	2.11%

Table 2.3-2. Comparison of actual crack location in the reinforced concrete with neural network predictions (Distances are from left end).

Neural Network prediction	Actual crack location	Error
993.91 mm	1028.70 mm	3.38%
1034.45 mm	1028.70 mm	0.56%
1005.77 mm	1028.70 mm	2.23%
1034.06 mm	1028.70 mm	0.52%
1016.51 mm	1028.70 mm	1.18%

2.3.3. AE Source Characterization

As was stated before, in the case of steel beam (SB-1) without initial crack, several major acoustic emission events were recorded. On the other hand, after the deliberate introduction of the initial crack, almost every major event recorded seemed to originate from crack growth. This may be attributed to the reduction of the stiffness of the beam because of the large initial damage, reducing the load capacity and hence the reactions experienced at the supports. A careful examination of the records before introduction of

the cracks indicated that the signals originated from outside the confines of the specimen. Realistically, the support systems seemed to be the source. The most probable cause of these events were rubbing and associated reversing friction forces between different components of the support system, like plates, bolts, nuts and washers.

It was expected that crack related acoustic emission signals will have quite different frequency components than signals generated by other types of sources [1]. Therefore, for an effective classification of such events, signals of interest need to be converted from time-domain into frequency-domain. The fastest and most effective way to accomplish this is to generate the power spectrums of the events by using fast Fourier transformation. On the other hand, it is feared that fast Fourier transformation may ignore local details of the signals. In addition, with this method, it is harder to visualize the information contained in different frequencies of the signal.

One alternative to using fast Fourier transforms to classify the acoustic emission events created by different types of sources, is to use continuous wavelet transformation (CWT). Graphical representation of the main idea behind the wavelet transformation is presented in Figure 2.3.1. The method basically works by representing the original signal by summing scaled and shifted versions of the mother wavelet. As a result of the continuous wavelet transformation, each scaled and shifted wavelet has a coefficient "*C"* and a scale "*a*". The coefficient "*C"* is a function of scale and position and it is used for storing the correlation information obtained from the continuous wavelet transformation. The higher the value of coefficient "*C*", the more closely correlated that wavelet is to a particular section of the original signal. On the other hand, scale "*a*" represents the stretching rate of

the wavelets. The higher the value of scale "*a*", the more stretched is the wavelet in the time axis.

An examination of the signals originating from the supports and those due to crack growth indicated that crack related signals have more high frequency information than non-crack related signals. To investigate it further, two crack-related and two rubbing/friction related, total four signals were converted from time domain to frequency domain. The crack related signals corresponded to what are shown in Figures 2.3.9 and 2.3.10. Chosen crack related and non-crack related time domain signals are shown in Figures 2.3.13 and 2.3.14, respectively. The conversion process from the time domain into the frequency domain is accomplished by both generating power spectrums with the help of fast Fourier transformation as well as by using continuous wavelet transformation. Power spectrums of the crack related and non-crack related signals are presented in Figures 2.3.15 to 2.3.18 and continuous wavelet transformations of the same signals are presented in Figures 2.3.19 and 2.3.20.

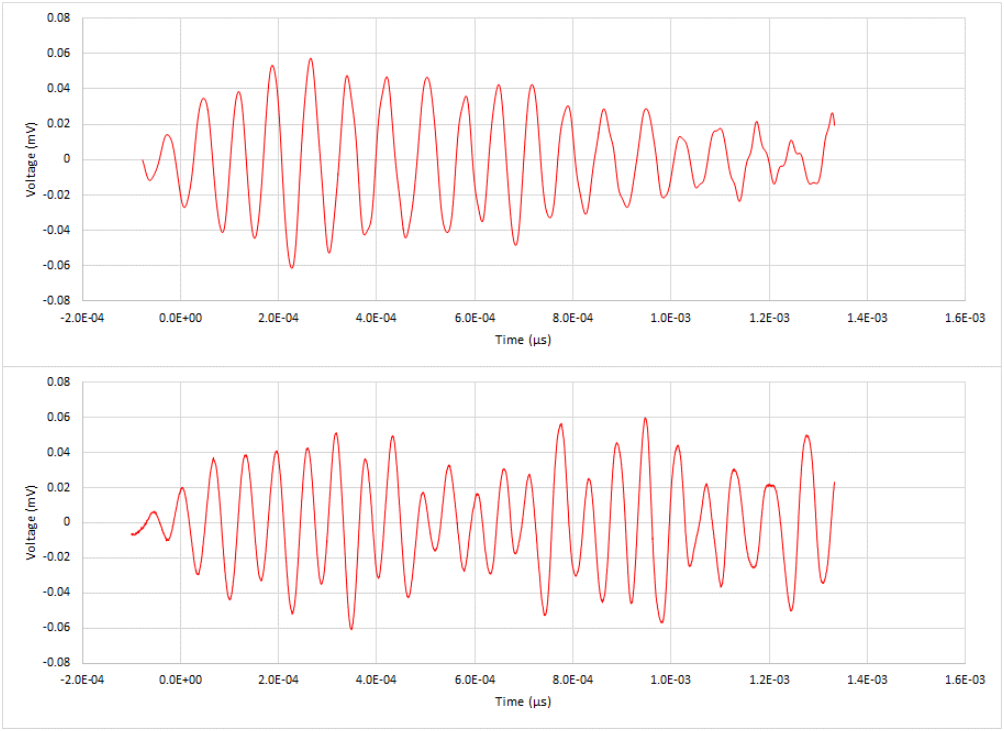

Figure 2.3.13. De-noised signals originating from rubbing/friction.

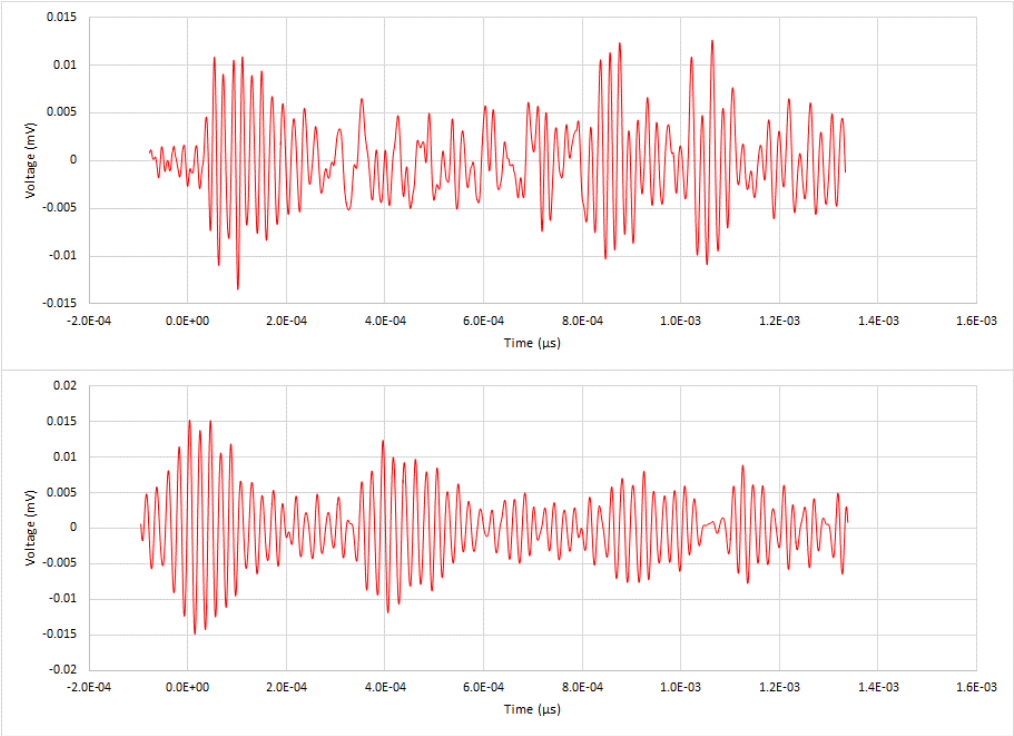

Figure 2.3.14. De-noised signals originating from crack growth.

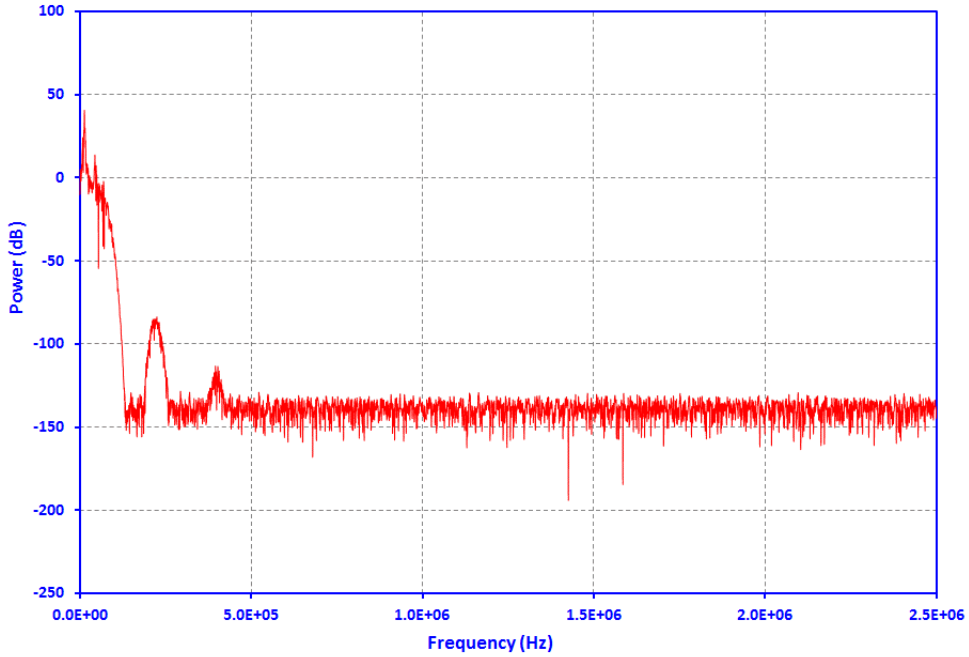

Figure 2.3.15. Power spectrum of the first signal generated by rubbing/friction.

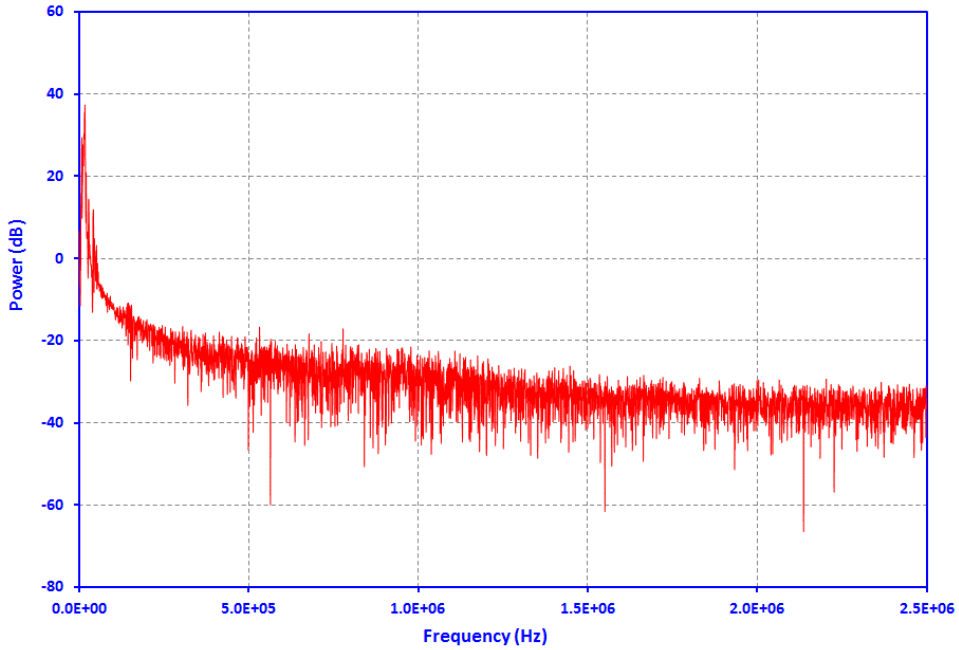

Figure 2.3.16. Power spectrum of the second signal generated by rubbing/friction.

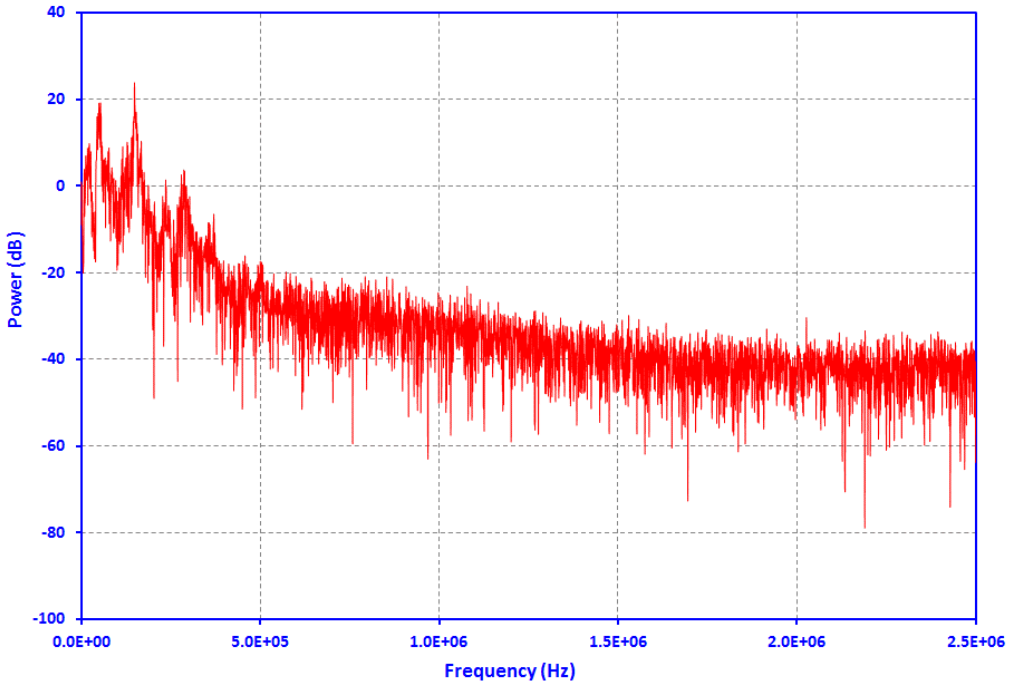

Figure 2.3.17. Power spectrum of the first signal generated by crack growth.

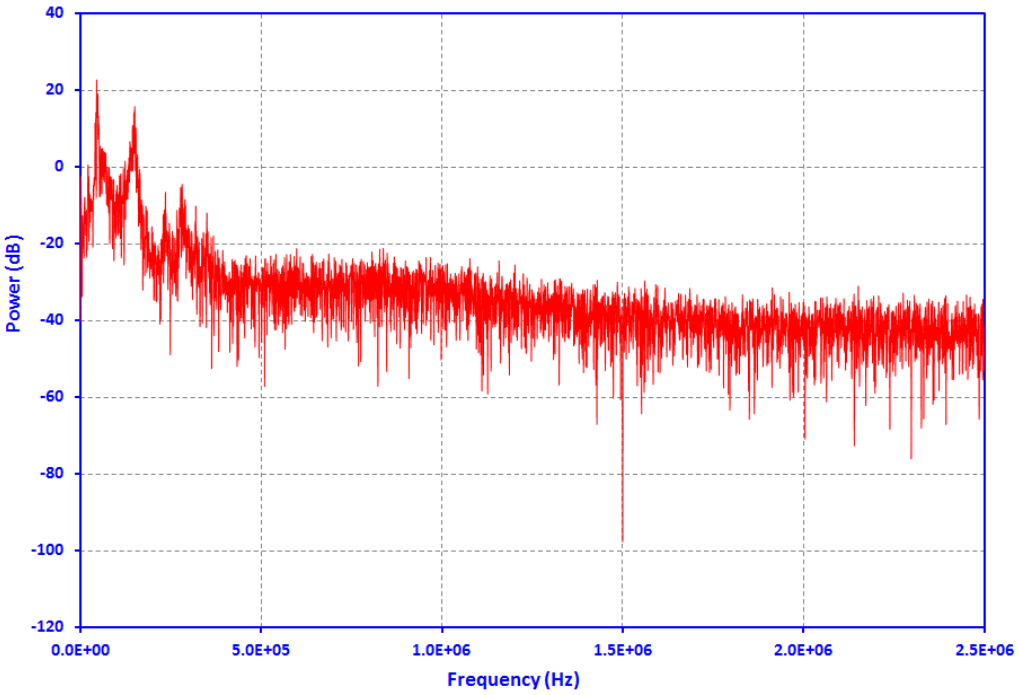

Figure 2.3.18. Power spectrum of the second signal generated by crack growth.

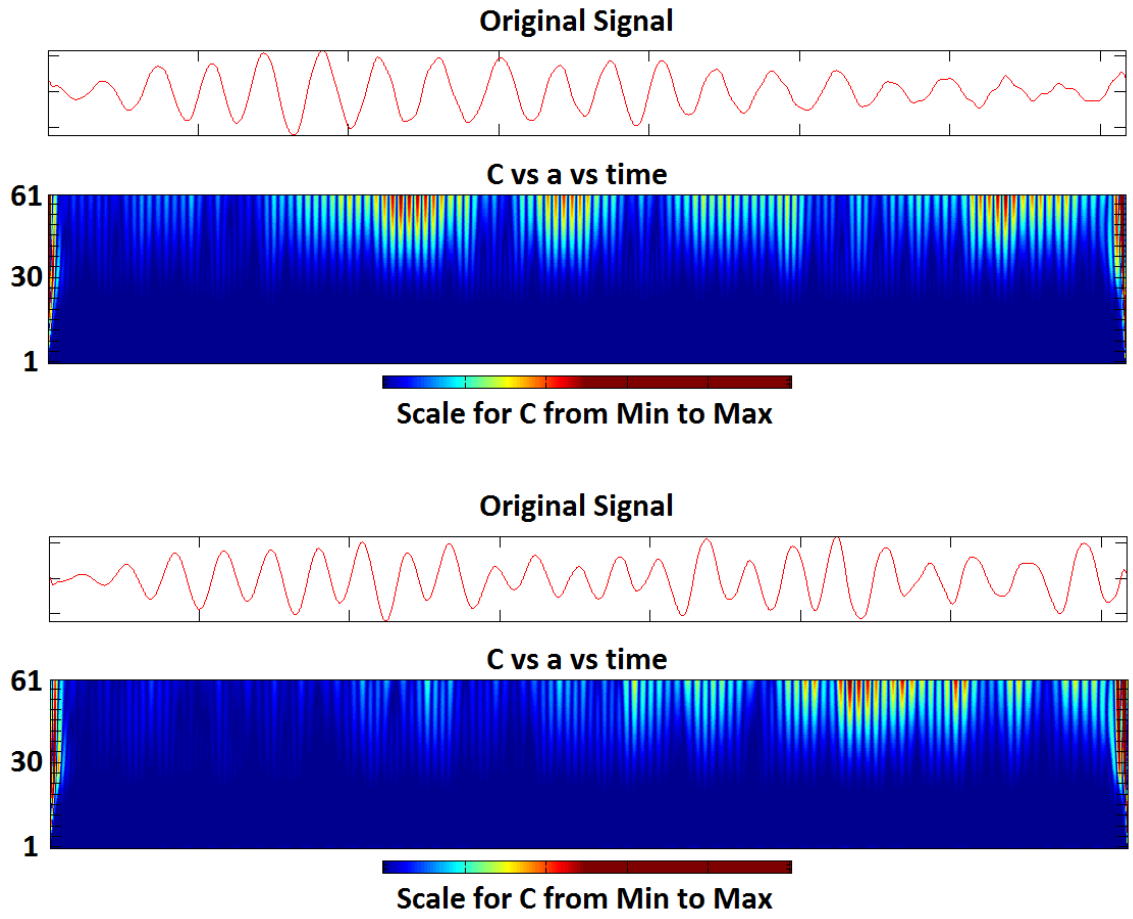

Figure 2.3.19. CWT of the signals generated by rubbing/friction.

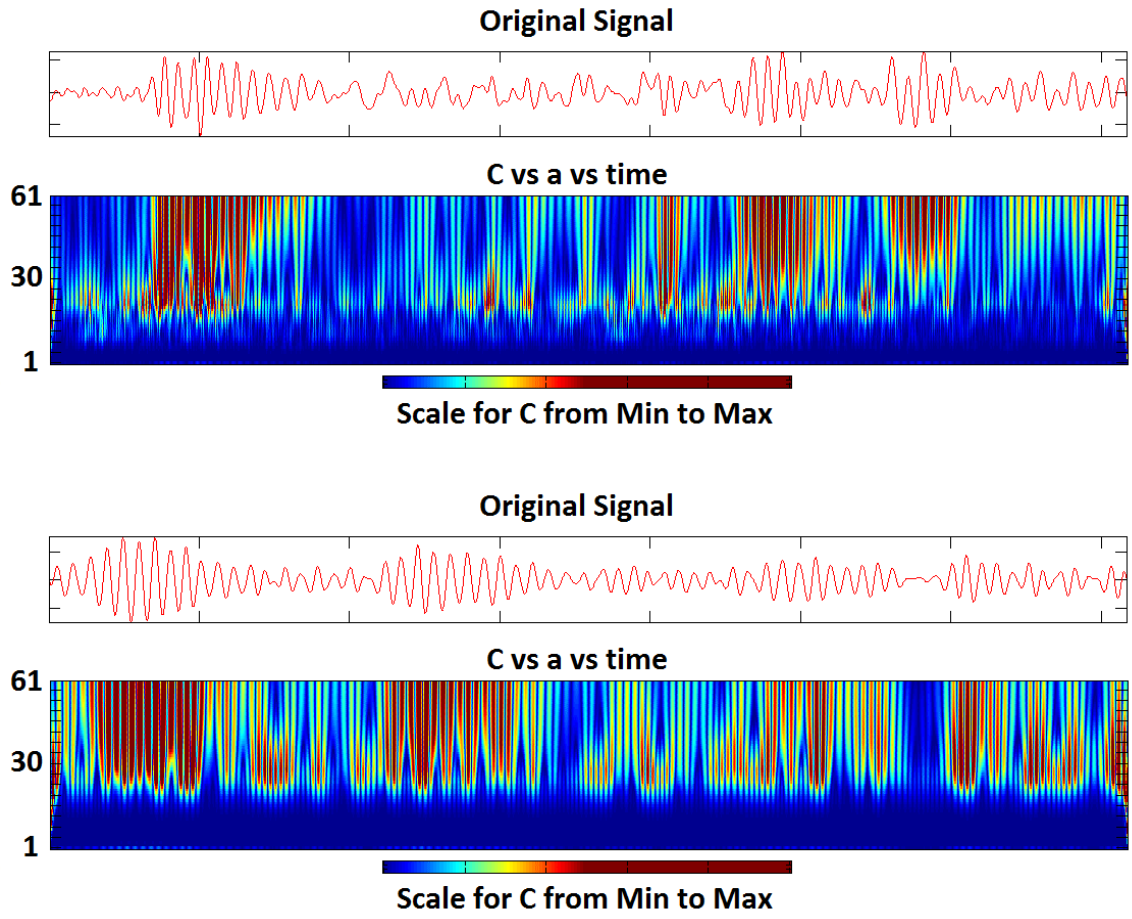

Figure 2.3.20. CWT of the signals generated by crack growth.

Even by a rough comparison of the power spectrums, one can notice that rubbing/friction related signals contain much more low frequency information than crack related signals. This conclusion can be verified with continuous wavelet transformation as well. Crack related signals are correlated with the mother wavelet on lower scales. On the other hand, signals generated by rubbing/friction are correlated with the mother wavelet for higher "*a*" values. This indicates that the wavelets are more stretched in the case of non-crack related signals. Since stretching a wavelet means lowering the frequency, CWT results agree with power spectrum data. As a result, non-crack related signals can easily be

separated from the signals generated by crack growth in steel beams by examining the nature of frequency difference between the two signal types.

2.4. Finite Element Modeling of the AE Phenomenon

As stated in Section 2.3, it is critical to have a proper training data set to determine the source locations of acoustic emission events of a structure by using the artificial neural network approach. Depending upon the situation, one possible way to generate such data sets is to do pencil-lead-break tests on the structure of interest. In the laboratory environment, generating those data sets by such tests for a structural component like beam may not be an issue. However, conducting such tests on a real bridge beam is unrealistic.

An attractive way to generate the training data sets for the artificial neural network is by using the finite element method. This is feasible only if crack signal generation and capture can be simulated in a finite element simulation of the structure and the corresponding voltage output values of the AE sensors can be obtained. The output signals from finite element simulation can then be processed further to clean the noise. Then the resulting clean signals can be used to train the artificial neural network which can subsequently be used for determining the locations of the acoustic emission events in the real structure.

For the generation of the training data sets accurately, actual mechanics of the acoustic emission phenomenon has to be faithfully accounted for during the simulation of the structure of interest mounted with acoustic emission sensors. As shown in Figure 2.4.1, the main components of the acoustic emission phenomenon required to be accounted for during the finite element modeling process are as follows:

- Accurate simulation of the incoming incident waves matching the characteristics of the real-life stress waves.
- Identifying the location of the components of the sensor in the time domain and calculating the force exerted by the mass of the sensor components on the piezoelectric material.
- Conversion of the strain exerted on the piezoelectric material to electric potential.

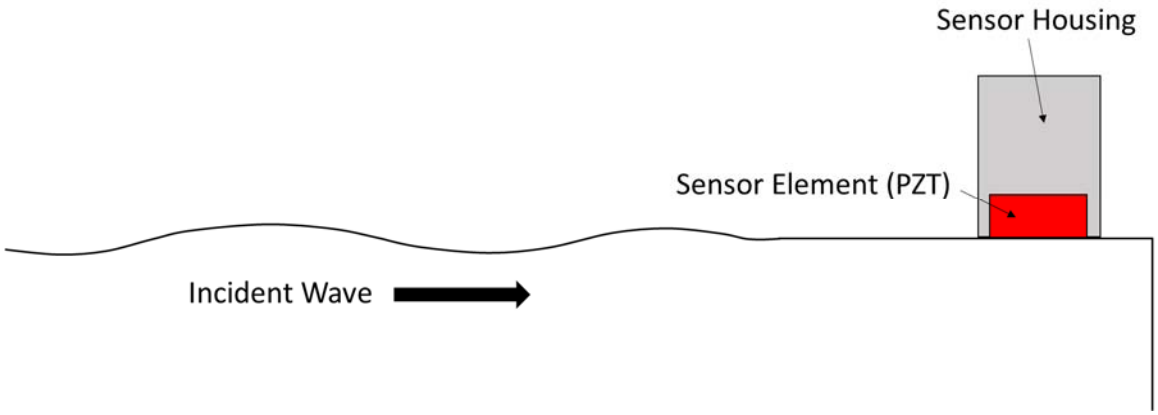

Figure 2.4.1. Acoustic emission phenomenon.

2.4.1. Material Properties and Geometric Details of Sensor Components

During the experimental work MISTRAS companies R15-α type sensor was used, and, accordingly, modeled in finite element simulation. As no data or drawings of the interior details of the sensors, except material properties of the components, could be obtained from the manufacturers, one of the sensors was actually disassembled for acquiring all the mechanical and electrical details of the sensor. After dismantling all the components of the sensor, dimensions and weight of each component were measured and the mechanics of the sensor was decoded. Details of the disassembly process are given in Appendix-C.

2.4.2. Finite Element Modeling of Piezoelectricity

A piezoelectric material undergoes strain when an electric potential gradient is applied to it. The process is reversible, that is it responds as electric potential gradient when subjected to change in stress. For defining basic electro-mechanical coupling, two parameters are used which are piezoelectric and dielectric properties. Piezoelectric property of a material represents how applied electric potential gradient is converted into strain or vice-versa. Dielectric property on the other hand, is the ratio of electric potential stored in a material after voltage is applied. Piezoelectric (e^{φ}) and dielectric (D^{φ}) properties of PZT-5H which is the crystal of the piezoelectric sensor are shown below:

$$e^{\varphi} = \begin{bmatrix} 0 & 0 & 0 & 741 & 0 & 0 \\ -274 & 593 & -274 & 0 & 0 & 0 \\ 0 & 0 & 0 & 0 & 0 & 741 \end{bmatrix} * 10^{-12}\, m/V$$

$$D^{\varphi} = \begin{bmatrix} 1.505 & 0 & 0 \\ 0 & 1.301 & 0 \\ 0 & 0 & 1.505 \end{bmatrix} * 10^{-8}\, F/m$$

In the piezoelectric property matrix $e^{\varphi}{}_{mij}$, the first index m (rows one to three) corresponds to the electric displacement (or electric flux). The second and third indices i (columns one to three) and j (columns four to six) on the other hand, refer to normal stresses and shear stresses, respectively. In the dielectric property matrix $D^{\varphi}{}_{ij}$, each diagonal value corresponds to the dielectric property of the material in each direction (x, y and z).

For finite element modeling of the piezoelectric AE sensor, Abaqus software was used. In this software, the electrical properties of piezoelectric materials are comprised of piezoelectric and dielectric effects, as shown in Equation 2.4.1.

$$q_i = e^{\varphi}_{ijk} * \varepsilon_{jk} + D^{\varphi}_{ij} * E_j \qquad (2.4.1)$$

Where q_i is the electric flux and e^{φ}_{ijk}, ε_{jk}, D^{φ}_{ij} and E_j are piezoelectric stress coupling, small-strain component, dielectric matrix and gradient of the electric potential, respectively.

The mechanical behavior on the other hand, can be defined by Equation 2.4.2 in terms of piezoelectric stress coefficient matrix.

$$\sigma_{ij} = D^{E}_{ijkl} * \varepsilon_{kl} - e^{\varphi}_{mij} * E_m \quad (2.4.2)$$

Here σ_{ij} is the mechanical stress tensor, D^{E}_{ijkl}, ε_{kl}, e^{φ}_{mij} and E_m are elastic stiffness matrix, strain tensor, piezoelectric stress coefficient matrix and electric potential gradient vector, respectively.

2.4.3. Selection of the Finite Element Solver and the Integration Scheme

Abaqus has two main solvers each of which work with a different integration scheme for solving dynamic problems. Implicit scheme is implemented by Abaqus/Standard and explicit scheme on the other hand is used by Abaqus/Explicit. Each integration scheme has its own advantages and drawbacks. The most efficient way of solving stress propagation problems involving degradation of the structure is to use the explicit finite element method. Therefore, the main solver chosen for finite element modeling of the acoustic emission testing stage of this study is Abaqus/Explicit.

In explicit finite element method, iteration and solution of systems of equations simultaneously are not required unlike the implicit integration scheme. Alternatively, the solution steps from one increment to the next by marching through time. In other words, Abaqus/Explicit treats the problem as a wave propagation problem. For obtaining a meaningful solution from the solver, each time increment of the solution must be smaller

than the minimum stable time increment. Otherwise, the solution obtained will be unstable, that is, oscillatory and unreliable. The minimum stable time increment can be represented by Equation 2.4.3.

$$\Delta t_{min} = \frac{2}{f} \cdot \left(\sqrt{1 + \xi^2} - \xi \right) \tag{2.4.3}$$

Here, f and ξ are cyclic frequency of the highest eigenvalue of the model and the fraction of critical damping for that eigenvalue. Alternatively, the minimum stable time increment can be defined as smallest transit time of a stress wave from one element to the next (Equation 2.4.4).

$$\Delta t_{min} = \frac{L^e}{c_d} \tag{2.4.4}$$

Where:

$$c_d = \sqrt{\frac{E}{\rho}} \tag{2.4.5}$$

In which, L^e, c_d, E and ρ are characteristic element length, wave speed, modulus of elasticity and material density, respectively.

Although Abaqus/Explicit is more effective than Abaqus/Standard for the solution of stress propagation problems, one of the main drawbacks of this solver is the limited number of element types it allows. In addition to regular stress/displacement elements to model the beam and secondary sensor components (i.e. sensor case, wear plate, etc.), piezoelectric elements are also required to model the piezoelectric crystal of the AE sensor. Piezoelectric elements are not available in the element library of Abaqus/Explicit. However Abaqus/Standard does have these. Therefore, the piezoelectric crystal inside the sensor is modeled with Abaqus/Standard and the rest of the model is simulated with

Abaqus/Explicit. During the analysis, these two solvers are made to inter-communicate with the help of the co-simulation engine of Abaqus, at the specified contact regions.

One other way of modeling this problem is to use Abaqus/Standard to solve the whole domain. But since the efficiency of the explicit solver is much higher than implicit solver for these types of problems, solving the whole model with the help of co-simulation engine by using two separate solvers is computationally much more efficient. Additionally, explicit integration scheme gives more accurate results for stress propagation problems than the implicit integration scheme which is another reason for preferring the co-simulation approach.

2.4.4. Element Selection for the Finite Element Model

A main limitation of Abaqus (both Abaqus/Explicit and Abaqus/Standard) is its restriction in the modelling of fatigue cracking as a dynamic event. The only direct way of modeling fatigue cracking with Abaqus is by using a quasi-static analysis procedure which assumes sub-critical cyclic loading conditions. Consequently, the energy released by crack formation needs to be modeled by different means.

During the modeling process, nodes across the crack are connected with a 1D truss type connector element, Figure 2.4.2. The nonlinearity of the connector element is defined in such a way that, after a certain amount of tension force is built-up linearly, the resistance of the connector drops immediately to zero. Therefore the crack snaps open which is very similar to what happens when an existing crack grows in real life.

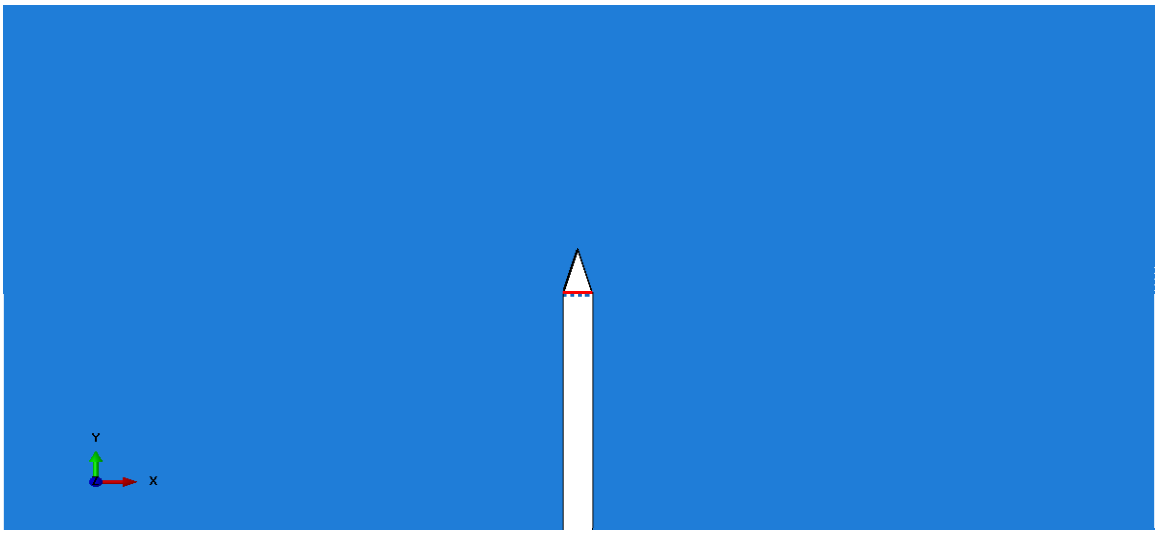

Figure 2.4.2. Truss element connecting the crack tip.

Since the thicknesses of the flanges and the web are small compared to the other dimensions of the beam, plane stress shell elements are used to model the steel beam specimen. In addition, the beam itself is the part of the model which requires the most elements to be discretized, therefore selection of the shell elements over the solids for that particular section of the model saves a lot of computational time. Piezoelectric crystal inside the sensor are modeled with solid piezoelectric elements. The other components of the sensor (i.e. sensor case, wear plate, etc.) are modeled with regular solid stress-displacement elements. Table 2.4-1 presents the details of the finite element mesh for the steel beam and the sensor models.

Table 2.4-1. Details of finite element mesh for the steel beam and the sensor.

Description of Item	Components of the Steel Beam and the Sensor Models			
	Beam		PZT	Sensor Case & Plate
Element Shape	Quadrilateral	Triangular	Tetrahedron	Tetrahedron
Element Family	2D Stress	2D Stress	Piezoelectric	3D Stress
Element Type	S4R: 4-node	S3: 3-node	C3D4E: 4-node	C3D4: 4-node
Geo. Order	Linear	Linear	Linear	Linear
No. of Elements	711,880	9,458	3,676	1,953

First-order linear elements are used to discretise both the beam and the sensor models. Lumped mass formulation of such elements gives an advantage over the consistent mass formulation of the second-order quadratic elements for stress wave propagation problems [61].

Another important concern that needs attention during element selection of stress wave propagation problems is the identification of acceptable size of the elements. The mesh element size needs to be selected in such a way that the mesh is able to represent the shapes of the stress waves with acceptable accuracy. This phenomenon is obvious from Figure 2.4.3. The displaced shape of the fine mesh shown in Figure 2.4.3(b) represents the mode and frequency characteristics of the stress wave much more accurately than the coarse mesh shown in Figure 2.4.3(a).

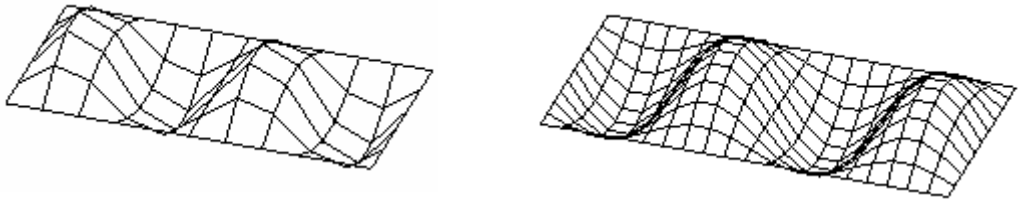

(a) Coarse mesh (b) Fine mesh

Figure 2.4.3. Effects of mesh fineness on wave characteristics [61].

As reported in the literature, length of each element has to be at least eight fold smaller than the wavelength of interest [62]. By using the Equation 2.4.6 given below, minimum required element dimension can be calculated.

$$L_{max} < \frac{C_{min}}{n_{min} \cdot \mathrm{f}} \tag{2.4.6}$$

In this equation, L_{min}, C_{min}, n_{min} and f are minimum element length, wave speed, required number of elements through the wavelength and the frequency of interest, respectively. By selecting C_{min}, n_{min} and f as 2.4e5 in/s, 8 and 350 kHz, the minimum required element size is calculated as 0.085 inch. Although most parts of the steel beam is meshed using this element size, regions around the crack and under the acoustic emission sensor are meshed with 0.010 inch elements, to get a better wave resolution around these regions.

2.4.5. Finite Element Analysis of the Test Specimen

Because of the non-homogenous nature of concrete, it is impossible to detect the randomly distributed impurities, regions with varying material properties or entrapped air pockets present inside the reinforced concrete and prestressed concrete beams. Since such defects have a considerable effect on the speed, mode and direction of the stress waves traveling throughout the structure, it is impossible and not advisable to analyse concrete beams numerically, at least, with respect to the problem in hand.

Finite element simulation was undertaken for the steel test specimen SB-1 only. The material and geometrical properties of the beam, as stated in Appendix-A, were used in the model. A very important component of the model is the piezoelectric AE sensor of which significant details was given earlier in this chapter. All bonds between the

components of the sensor and the adhesive between the beam and the sensor were modeled allowing for strain compatibility assumption. For saving computational effort, only the sensor designated as channel-1 shown in Figure 2.2.16 was modeled. The full acoustic emission sensor model attached to the steel beam is shown in Figure 2.4.4. Inside view of the sensor after the metal case is removed is shown in Figure 2.4.5.

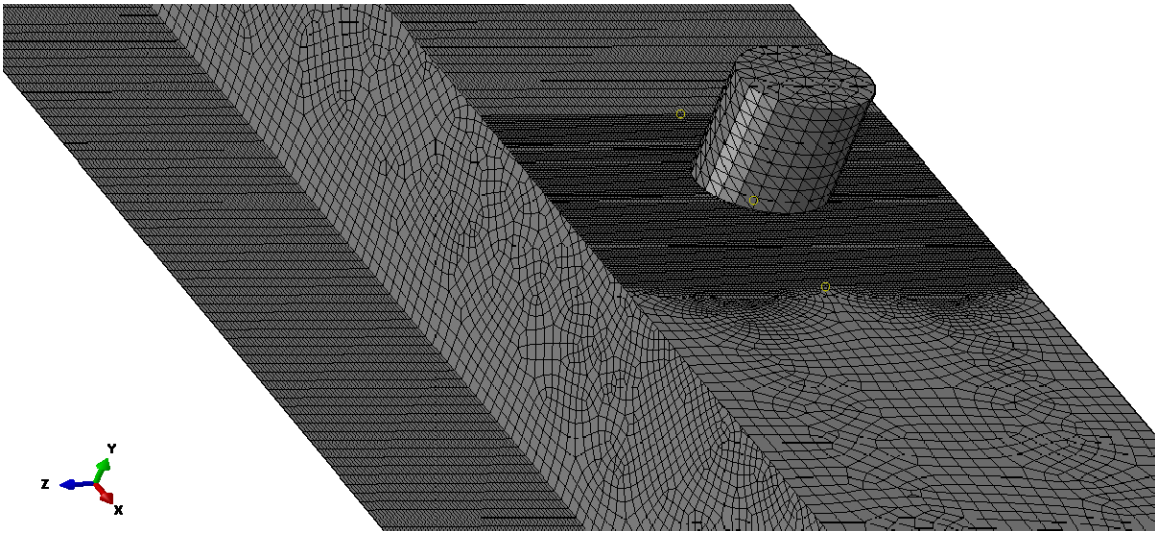

Figure 2.4.4. Full acoustic emission sensor model.

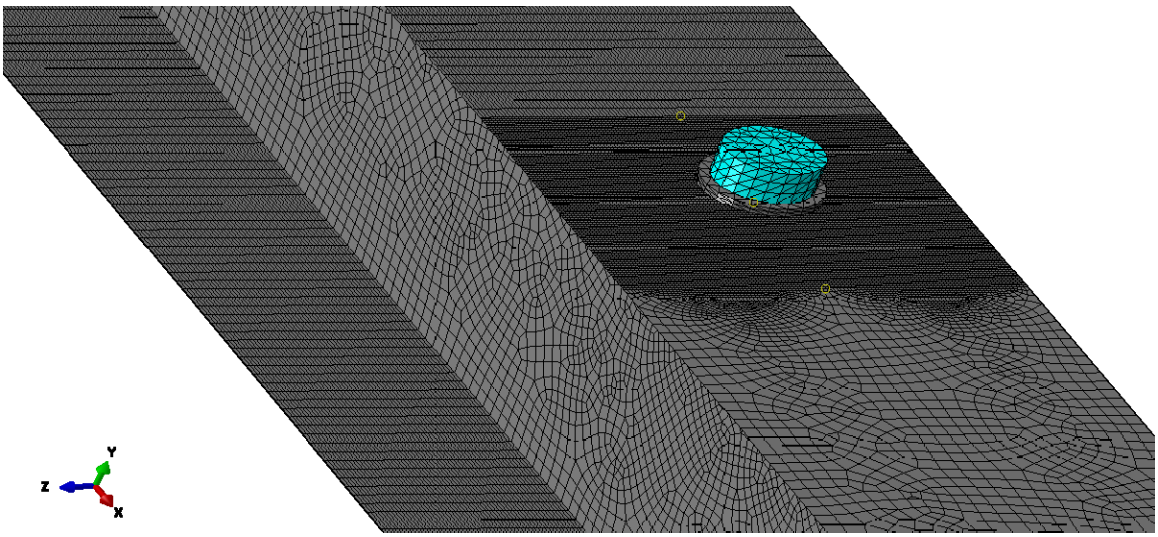

Figure 2.4.5. Sensor model after the steel case is removed.

The beam model was subjected to a sinusoidal displacement amplitude, virtually duplicating the way the test specimen SB-1 was loaded during regular cyclic load testing. After the growth of the existing crack, Figure 2.4.6 and Figure 2.4.7 show the stress waves leaving the crack tip at 400 and 800 μs after the crack growth event. Reflection of the stress waves into the web of the beam after encountering the boundaries of the flanges of the specimen are shown in Figure 2.4.8.

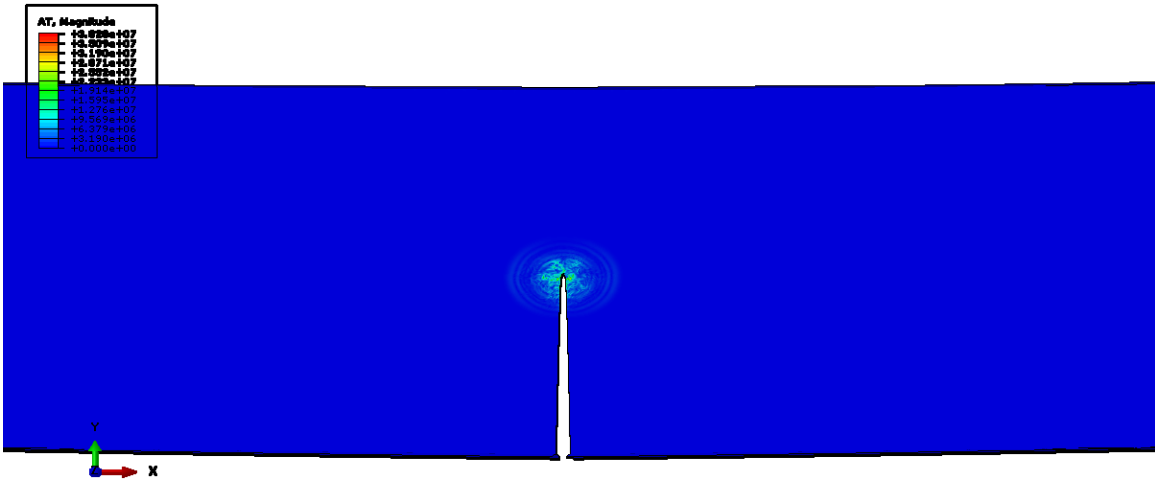

Figure 2.4.6. Stress waves leaving the crack tip 400 μs after crack growth.

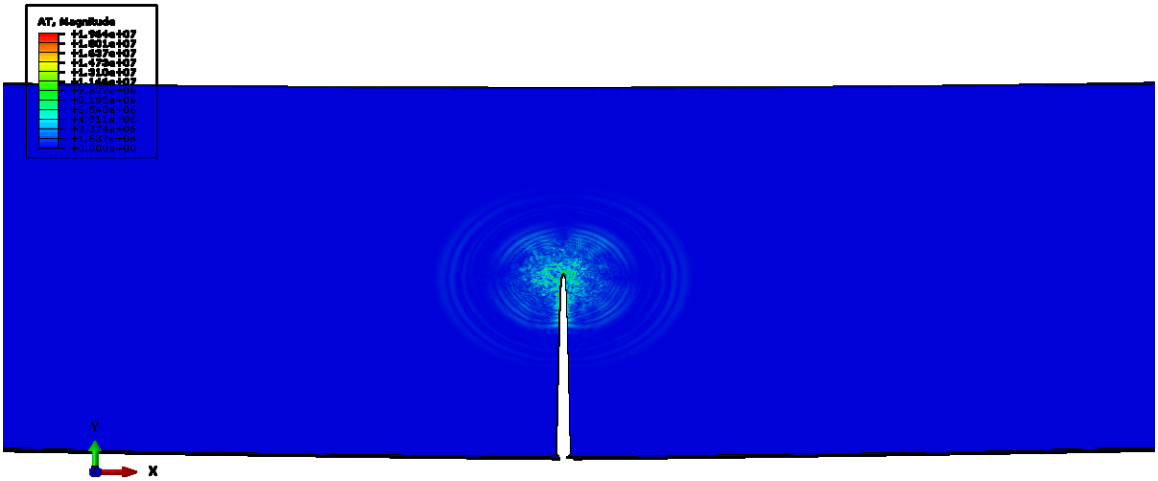

Figure 2.4.7. Stress waves leaving the crack tip 800 μs after crack growth.

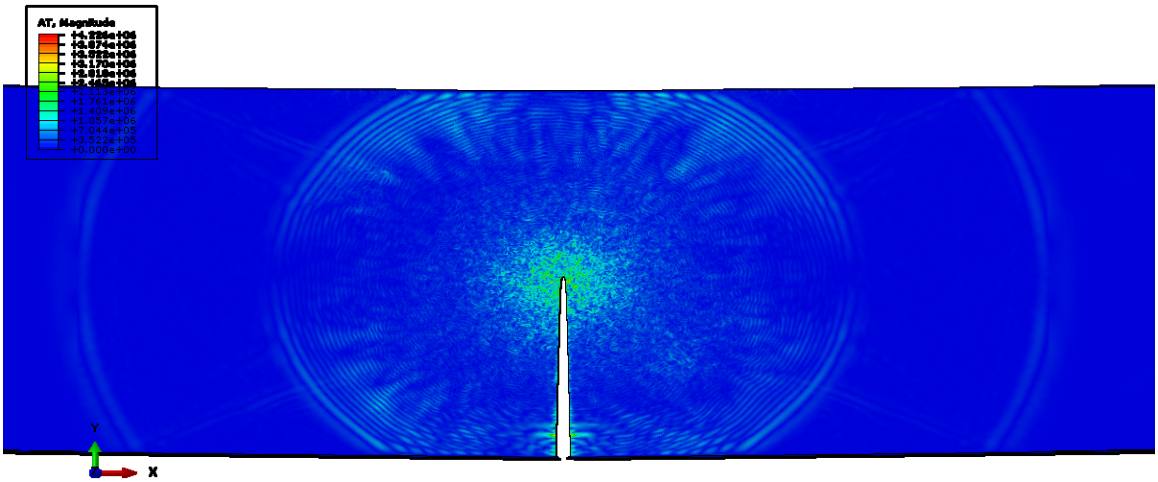

Figure 2.4.8. Stress waves reflecting back to the web from the boundaries of the flanges.

Thereafter, electric potential output history of the sensor is measured by calculating the voltage differences between the top and bottom faces of the sensor element. By selecting the frequency of interest as 350 kHz during the calculation of the minimum element dimension earlier in this chapter, high-frequency noise was automatically eliminated. The lower frequency noise was cleaned from the signal by using a procedure similar to what is described in Section 2.3. The acoustic signal data computed as output of the finite element model of the AE sensor is compared with experimental results and empirical data in Figure 2.4.9.

As can be seen from Figure 2.4.9, there is very good agreement between finite element data, empirical formula and experimental results. Especially in the frequency domain, the agreement of results based on experiment, empirical formula and simulation are excellent. Other signal parameters obtained from the finite element simulation like

arrival time, maximum signal amplitude, rise time, signal count, duration and signal energy also show good agreement too.

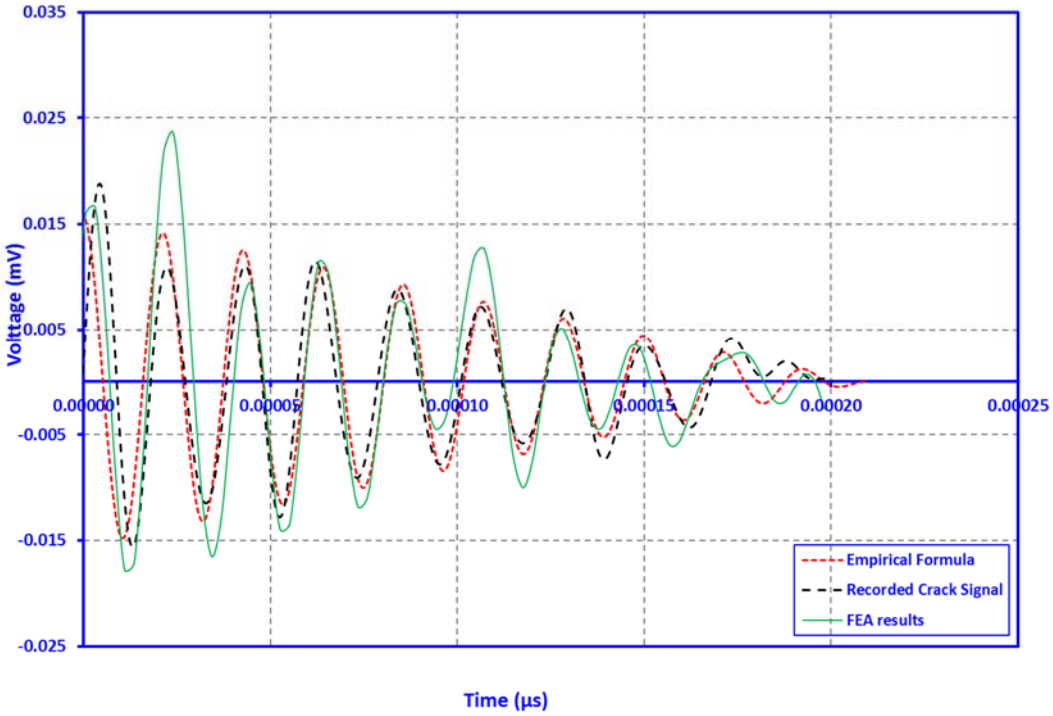

Figure 2.4.9. Comparison of finite element simulation results with experimental data and empirical acoustic signal for SB-1.

Form these results, it can easily be concluded that finite element simulation, if properly used, can be a very powerful tool to predict the behavior of the systems allowing for stress wave propagation and acoustic emission phenomenon. Additionally, these results show that finite element modeling is a very good candidate for generating training data sets for the artificial neural networks which later can be used for detecting the source locations of the acoustic emission events.

CHAPTER 3

3. REMEDIATION OF DAMAGED BRIDGE COMPONENTS USING BONDED FRP

3.1. Introduction

After the nature and location of the damage is thoroughly investigated and its presence is predicted by AE sensor based real-time health monitoring system, the follow up remedial action to ensure continued safety of the bridge has to be decided upon. There can be a range of possibilities like outright replacement, partial rehabilitation, or just local repair work. Since the damages can be detected in the early stages of formation with the help of autonomous real-time AE based health monitoring system presented in Chapter-2, the detected damages can be repaired while they are still local, without the need of replacement or retrofitting. Apart from conventional repair methods, a relatively new method is bonded FRP patch repair with obvious advantages. In this part of the study, the main objective is to develop analysis and design procedures for such repair, experimental investigation of the performance of the repair in the case of representative bridge components and developing nonlinear finite element analysis models for validating the experimental and mechanistic model results. The four main components of the research work that has been carried out in this context are as follows:

- Develop a simple but sufficiently accurate preliminary design procedure for FRP patch repair.

- Perform a series of experimental studies with representative specimens of damaged bridge girder.
- Develop a mechanics-based model to realistically capture the behavior of repaired structural components if full blown finite element analysis is not possible.
- Creating accurate nonlinear finite element models and validating the response quantities of interest with experimental data.

3.2. Details of Representative Test Beams and FRP Composites

As in structural health monitoring (SHM), here again the beam specimens used in this phase of the study were of the same three popular bridge construction materials namely, steel, reinforced concrete and prestressed concrete. The main difference between the experimental procedures of the two was the nature of loading and the associated objectives. For SHM, the test specimens were mostly subjected to dynamic excitation; whereas, for the present purpose, the test beams are exclusively subjected to 4-point quasi-static loading. The typical four-point loading scheme is shown in Figure 3.2.1. Fabrication details of the test beams and the quasi-static loading system used in this study are given in Appendices D and E, respectively and, also, in the associated TDOT research report [63].

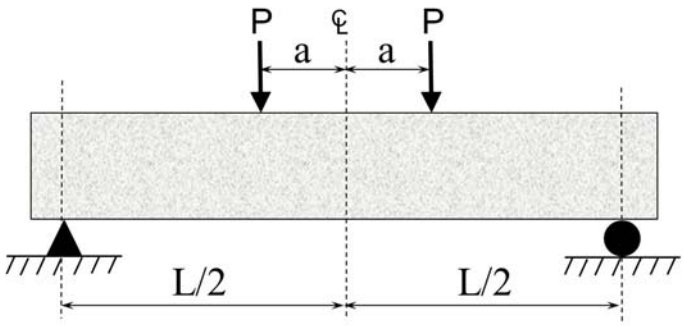

Figure 3.2.1. A typical 4-point loading scheme.

3.3. Development of Preliminary Design Procedure for FRP Patch

3.3.1. Description of the Design Procedure

Although there are some preliminary design procedures recommended by National Cooperative Highway Research Program (NCHRP), American Association of State Highway and Transportation Officials (AASHTO) and American Concrete Institute (ACI) [38], [39], [40], no matured and widely accepted design code for repairing bridge hardware with FRP composite patch materials existed at the time this study was undertaken. Therefore based on the principles of sound and basic mechanics, design of local bonded FRP patch repair is accomplished. The design procedure presented herein essentially follows the limit state approach used in current structural design practices. The main objective is to arrive at the type, size and configuration of the composite patch material so that the AASHTO specified capacity of the beam/girder can be restored or exceeded. The assumptions made during the design process are as follows:

- Due to uncertainties in the physical and mechanical properties of the composite systems, a resistance factor of 0.9 is used during the design procedure.

- Nominal strength is assumed to be 10% over the required strength.
- The required length of each patch can be calculated by allowing for required development lengths beyond the theoretical cut-off point at each end.
- Use of multiple layers and prestressing of the composite patches is not considered in this study, for the sake of simplicity.
- The details of the damaged structural member are known.
- In the case of concrete members, the damages are restricted to flexural and shear cracks caused by applied forces which cause the member's capacity in bending and/or shear to be exceeded.
- In the case of steel members, the loss of section due to damage extends for the full length of the member.
- Existence of perfect bond between the composite patch and the substrate material.
- Minimum patch width limit was taken as two inches, to prevent premature debonding.

Additionally, safety issues stated below need to be kept in view during the design process for a conservative and safe FRP patch repair practice:

- Structural members repaired with FRP should have enough residual strength to carry the service loads, so that in case FRP repair fails, the structure itself will not fail in tandem.
- Calculated development lengths should be extended to account for the effects of long-term creep and slippage. This cannot be explicitly implemented in the present study because long-term performance is outside the scope of this research work.

3.3.2. Strengthening in Flexure

In this study, nominal strength after the repair work is assumed to be 10% over the original strength of the repaired member. This requirement is embodied in Equation 3.3.1.

$$M_u \leq M_{n,repaired} = 1.1 \cdot M_{n,undamaged} \tag{3.3.1}$$

Where, M_u, $M_n|_{\text{repaired}}$ and $M_n|_{\text{undamaged}}$ are design flexural strength, nominal flexural strength after repair and nominal flexural strength before damage, respectively. Here, considered damage types are section loss at bottom or top flange and/or in the web due to corrosion. The same approach can be applied to cases where the section loss is in the bottom flange only, or both in the web and bottom flange due to crack formation. The needed repair patch can easily be proportioned by equating the capacity loss due to damage to the capacity gain due to repair. Since the thickness of the patch is known, the only unknown quantity that needs to be determined during the design process is the width of the composite patch material of given thickness. The flexural capacity contribution of the web of the beam and web patches can be ignored, assuming that the primary purpose of web patches is to resist shear. A more refined design procedure taking into account flexural resistance of the web patches, when there is section loss both at the bottom flange and web can be found in the corresponding TDOT research report [63].

The steel beam section shown in Figure 3.3.1 is considered, in which the section loss is only at the bottom flange caused by corrosion. In this case, the capacity loss due to damage and capacity gain from bonded composite patch repair can be represented by Equations 3.3.2 and 3.3.3, respectively. By solving these two equations along with Equation 3.3.1, the dimensions of the composite patch can be determined by using

Equation 3.3.4, where F_y and f_{pu} are yield strength of steel and tearing strength of composite patch material, respectively.

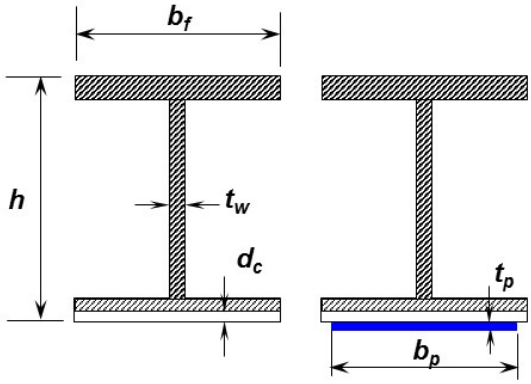

Figure 3.3.1. Steel beam section loss in the bottom flange and the repaired beam.

$$F_{loss} = b_f . d_c . F_y \tag{3.3.2}$$

$$F_{patch} = b_p . t_p . f_{pu} \tag{3.3.3}$$

$$b_p = \frac{1.1. b_f . d_c . F_y}{t_p . (0.9. f_{pu})} \tag{3.3.4}$$

If there is loss of strength due to corrosion in the top flange, which supports the concrete deck slab, the patch repair can be completed by bonding patch strips to the bottom exposed surface of the top flange on two sides of web, as shown in Figure 3.3.2. The bonded composite patch can again be designed by using Equation 3.3.4.

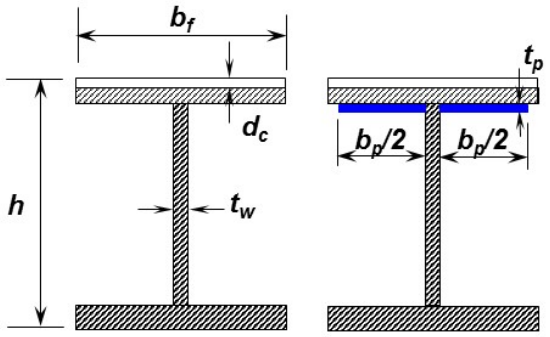

Figure 3.3.2. Steel beam section loss in the top flange and the repaired beam.

In the case where the section loss is in the bottom flange and also in the web due to a crack of the type shown in Figure 3.3.3, dimensioning of the patch can be done by using Equation 3.3.5 derived in a manner similar to the cases considered so far.

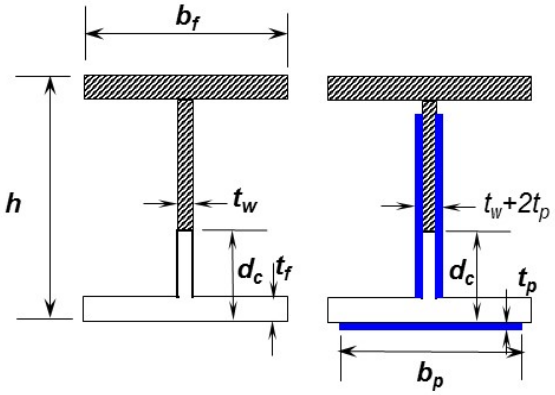

Figure 3.3.3. Steel beam section loss in the bottom flange and web and the repaired beam.

$$b_p = \frac{1.1.b_f.t_f.F_y}{t_p.(0.9.f_{pu})} \tag{3.3.5}$$

Since only flexural patch design of the steel beams is the focus of this study, details of the flexural patch design of reinforced concrete and prestressed concrete beams are given in another publication by the author [63].

3.3.3. Strengthening for Shear

As in flexural patch design, it was ensured that the nominal shear strength of the shear repaired beam exceeded the undamaged shear strength of the beam by at least 10%, as shown in Equation 3.3.6.

$$V_u \leq V_{n,repaired} = 1.1.V_{n,undamaged} \tag{3.3.6}$$

In which V_u, $V_n|_{\text{repaired}}$ and $V_n|_{\text{undamaged}}$ represent design shear strength, nominal shear strength after repair and nominal shear strength before damage, respectively. Since in this study, the focus will be only the shear strengthening of the prestressed concrete beams, details of shear strengthening of steel and reinforced concrete beams are reported in the corresponding TDOT research report [63].

The proposed shear strengthening design procedure is very similar to regular stirrup design. The U-jacket configuration shown in Figure 3.3.4 is considered in this study. The shear force that needs to be resisted by the patch (V_p) can easily be calculated by subtracting the contribution of the concrete (V_c) and stirrups (V_s) from the required shear strength ($V_n|_{\text{repaired}}$). This requirement is represented by Equation 3.3.7.

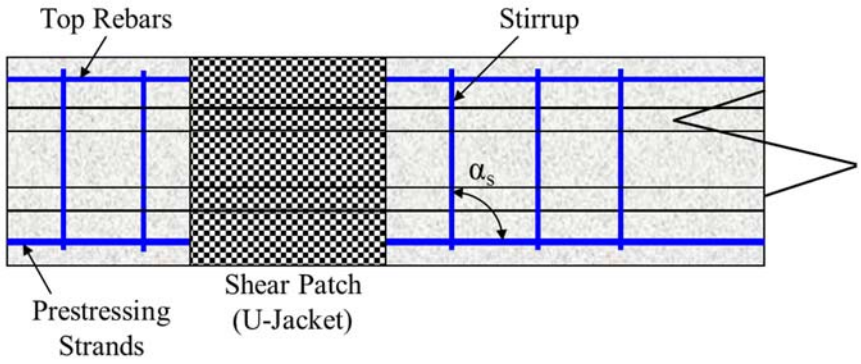

Figure 3.3.4. Typical shear strengthening scheme.

$$V_p = V_{n,required} (V_c + V_s) \quad (3.3.7)$$

Where:

$$V_c = \left(0.6\lambda\sqrt{f_c'} + 700\frac{V_u d_p}{M_u}\right) b_w d \quad (3.3.8)$$

$$V_s = A_v f_{yt} \frac{d}{s} \quad (3.3.9)$$

In which, λ, f_c', b_w, d, d_p, A_v, f_{yt}, s, V_u and M_u are modification factor, compressive strength of concrete, web width, distance between extreme compression fiber to neutral axis, distance between extreme compression fiber to prestressing steel, area of shear reinforcement, yield strength of shear reinforcement, spacing of stirrups, factored shear force at section and factored moment at section, respectively. The width of the patch (w_p) can now be determined by using Equation 3.3.10.

$$w_p = \frac{V_p}{t_p . (0.9. f_{pu})} \quad (3.3.10)$$

Where, t_p and f_{pu} are thicknesses of patch and fracture strength of composite, respectively. In addition to U-jacket configuration, the same design approach can be applied with minor modifications to two other shear repair bonding schemes, namely, wrapping and side plate configurations.

3.3.4. Determining the Length of the Composite Patch

As the damage is localized, the two ends of a patch need to be extended to a distance controlled by the profile of actual moment or shear force to be resisted. The moment profile to be resisted can be used to calculate the required length of a flexural patch to get the theoretical cut-off point. But the patch should be extended beyond such point to ensure a

smoother stress transition allowing an adequate development length avoiding the possibility of delamination near the ends of the patch. This is depicted in Figure 3.3.5.

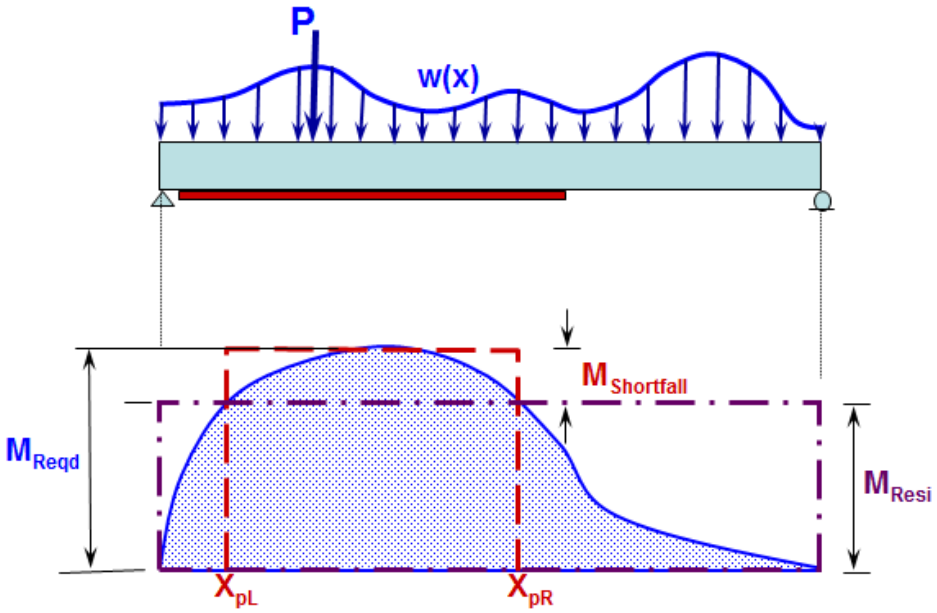

Figure 3.3.5. Required patch length.

Here, the shortfall in moment resistance capacity ($M_{\text{shortfall}}$) caused by damage, as shown in Figure 3.3.5, needs to be picked up by the composite patch. As show in Equation 3.3.11, theoretical patch cut-off point locations can be determined by using the residual capacity of the damaged beam, M_{Resi},

$$M(x) = M_{Resi} \tag{3.3.11}$$

Noting that $M(x)$ is a function of x^2, the two roots of this would be x_{pL} and x_{pR} respectively, which are the theoretical patch cut-off point locations. In addition to the distance between these two cut-off points, the length of the patch should be extended by the development length on both sides. Normally, the distribution of shear stress along that development length is a parabola which can be approximated by a triangle. The height and

base length of this triangle can be the maximum permissible shear stress (f_a) and development length (L_{pd}), respectively. The development length of the composite patch can then be determined by using Equation 3.3.12, in which t_p and f_{pu} are thickness of patch and its fracture strength.

$$L_{pd} = \frac{2.t_p.f_{pu}}{0.9.f_a} \tag{3.3.12}$$

3.4. Load Testing and Repair of Beam Specimens

3.4.1. Details of the Experimental Procedure

The primary objective of the experimental investigation is two-fold:

- To investigate the real-life behavior of bonded composite patch repair.
- To generate the test data needed for validating the results of modeling and simulation with different degrees of sophistication.

The first step of the experimental work is to simulate the damage in the test beams. The second step is undertaking the bonded composite patch repair. Lastly, the effectiveness of the repair are required to be assessed.

3.4.2. Baseline Performance by Preliminary Load Testing

The original concrete beams were first loaded individually using ASTM specified loading rates, to deliberately induce structural damage in the form of bending and/or shear cracks. In the case of steel beams, in which physical damages in the form of sectional area loss due to corrosion were deliberately induced by other means, no additional damage was induced during preliminary load testing.

Figure 3.4.1 shows the control steel test beam (undamaged) ready for four-point load application. The test results are shown in Figures 3.4.2 to 3.4.5. The load vs. central deflection plots of all four test beams are shown in Figure 3.4.2. Plots of total applied load vs. top surface compressive strain at center of the span are shown in Figure 3.4.3. In Figure 3.4.4, plots of tensile strain on the inside face of the bottom flange at center of the span are shown. In addition, the corresponding plots for diagonal tensile strain on the web at mid-depth near quarter-span are shown in Figure 3.4.5.

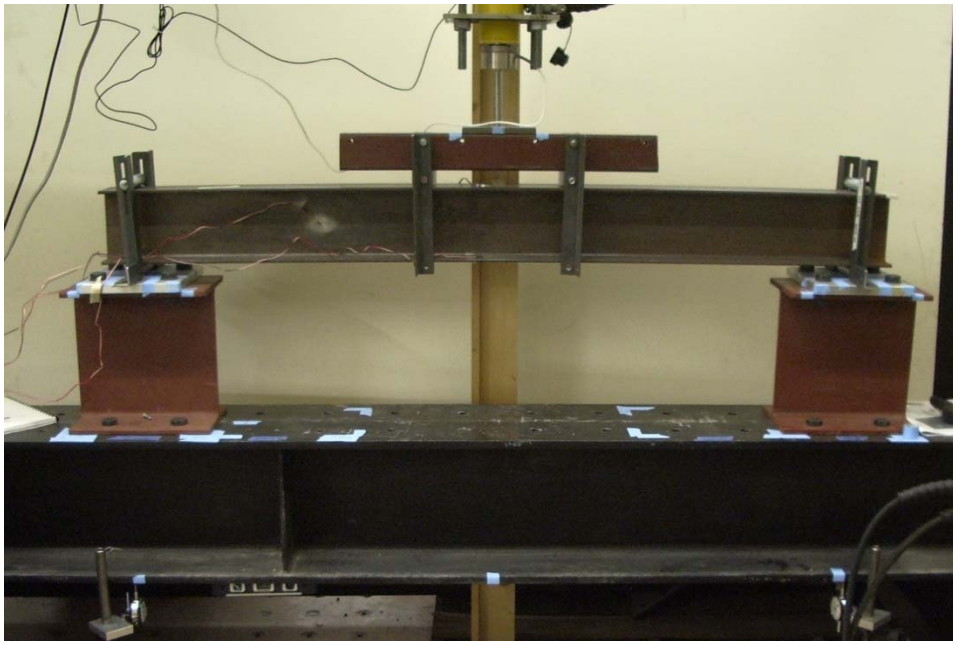

Figure 3.4.1. Preliminary load testing of control steel beam (SBC) [63].

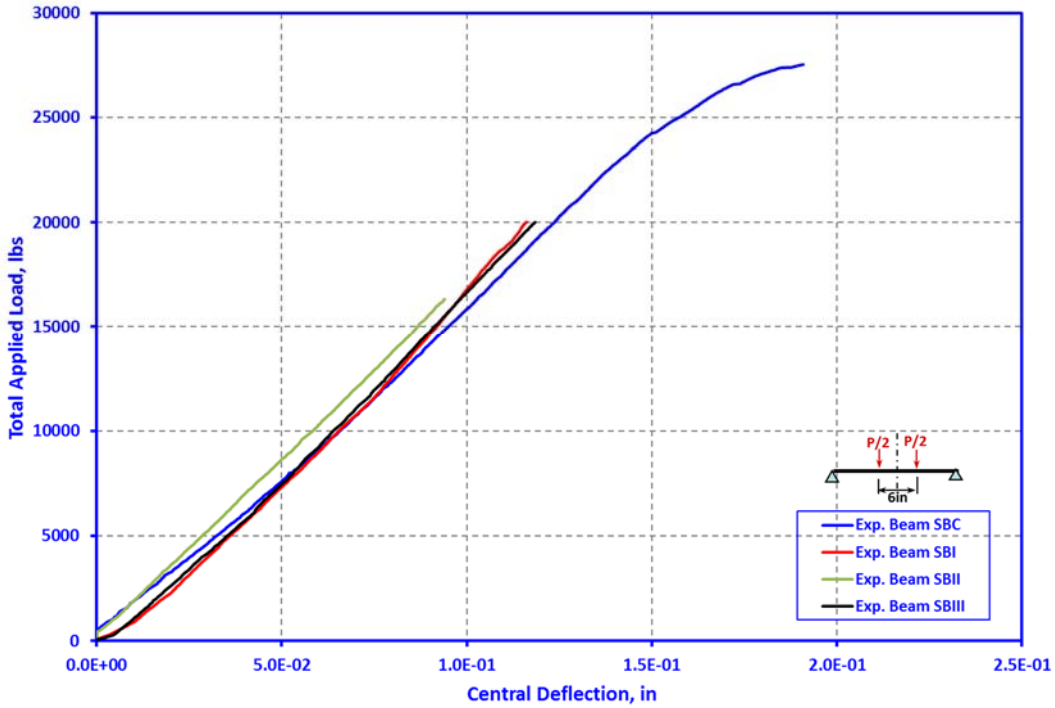

Figure 3.4.2. Load vs. central deflection plot for steel beams - preliminary loading.

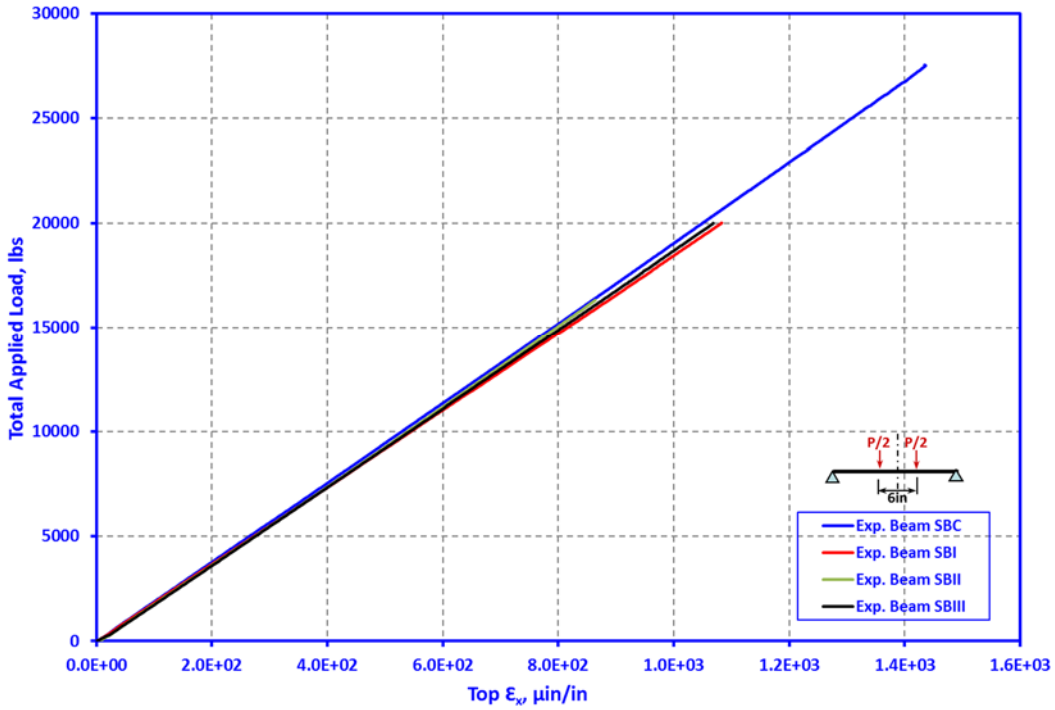

Figure 3.4.3. Plots of load vs. top flange strain plot for steel beams - preliminary loading.

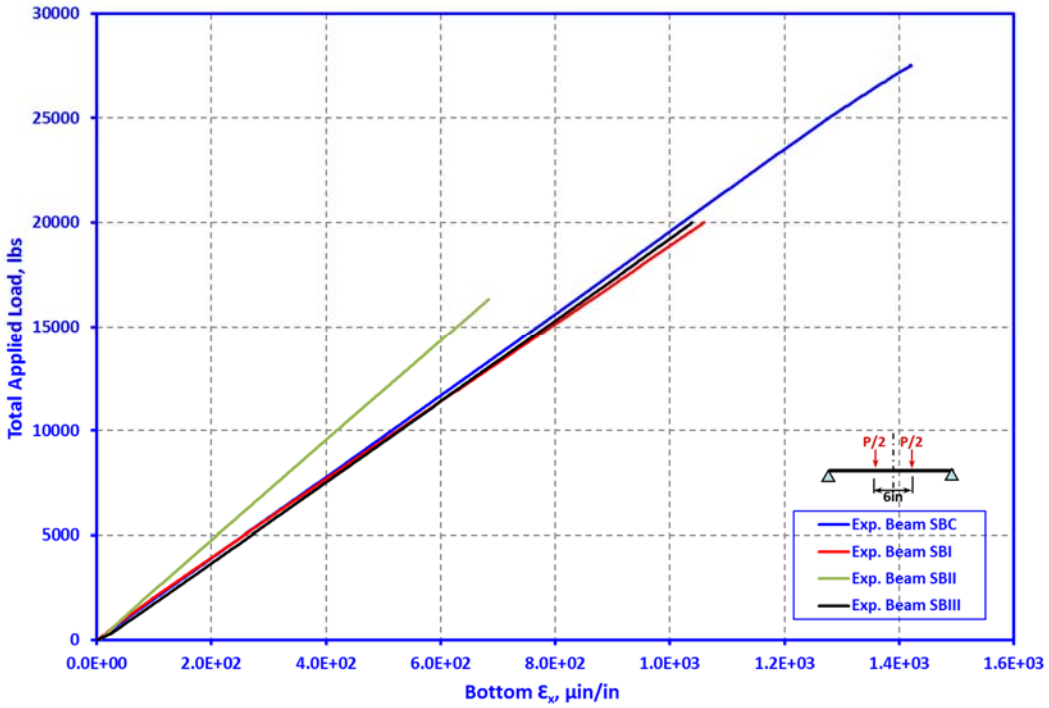

Figure 3.4.4. Plots of load vs. bottom flange strain for steel beams - preliminary loading.

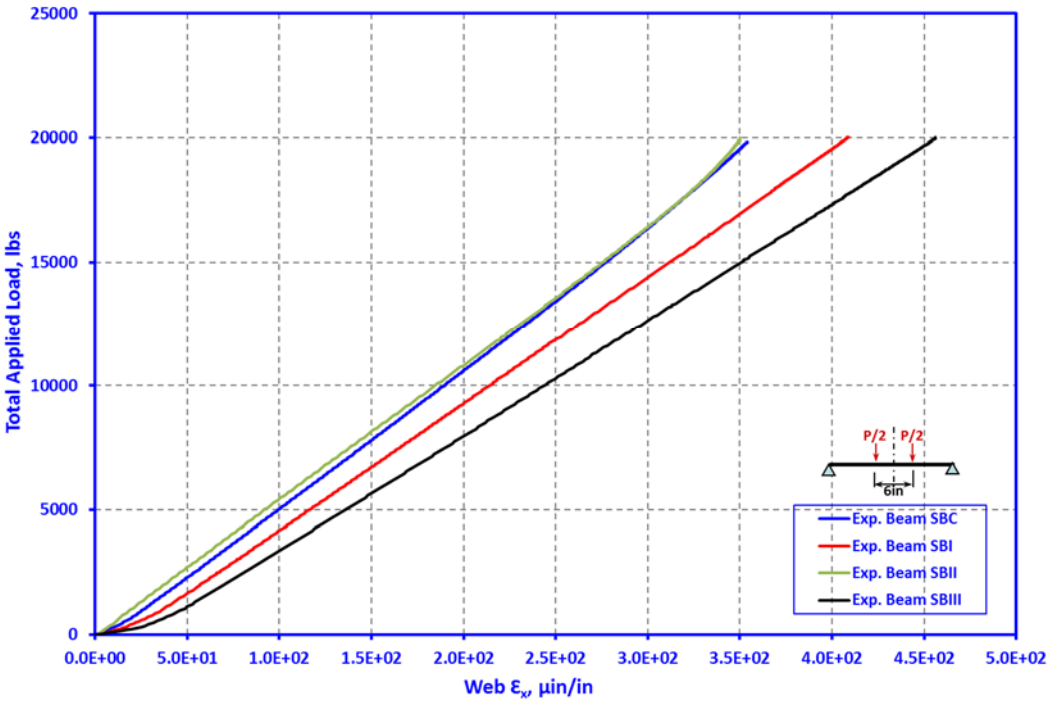

Figure 3.4.5. Plots of load vs. web tensile strain for steel beams - preliminary loading.

A typical concrete test beam positioned in the strong frame before the application of load is shown in Figure 3.4.6. Figure 3.4.7 shows the load vs. central deflection plots of ten “flexural” reinforced concrete test beams. Figure 3.4.8 shows the plot of measured top fiber compressive strain at the center of the same beams. Figure 3.4.9 shows the load vs. central deflection results for the “shear” beams. In Figure 3.4.10, the plots of applied load vs. top fiber strain at midspan for the five “shear” beams are shown.

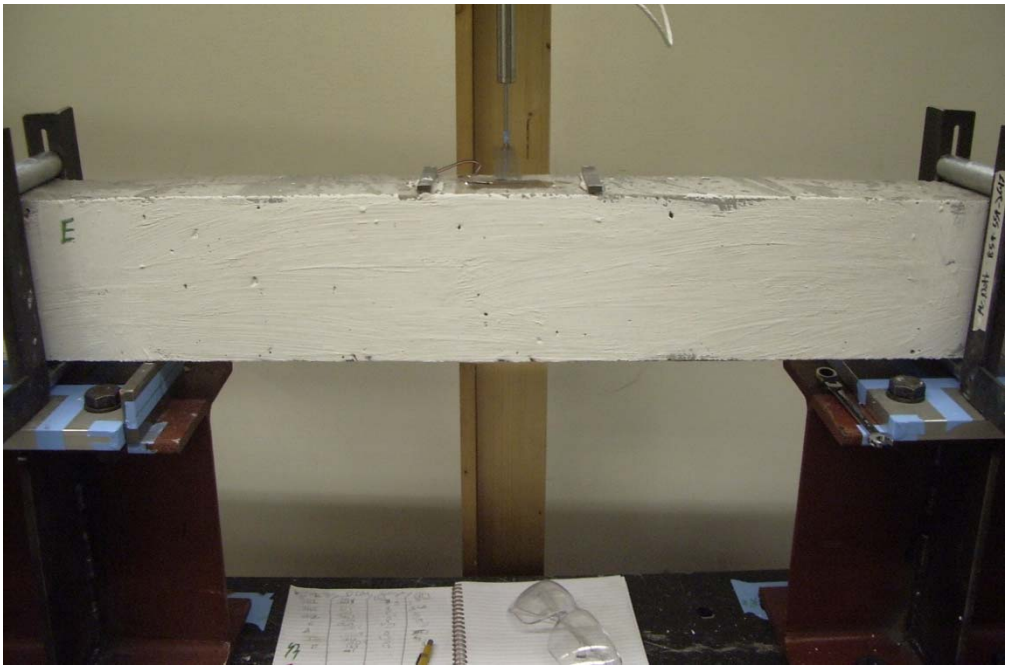

Figure 3.4.6. Preliminary load testing of a reinforced concrete beam [63].

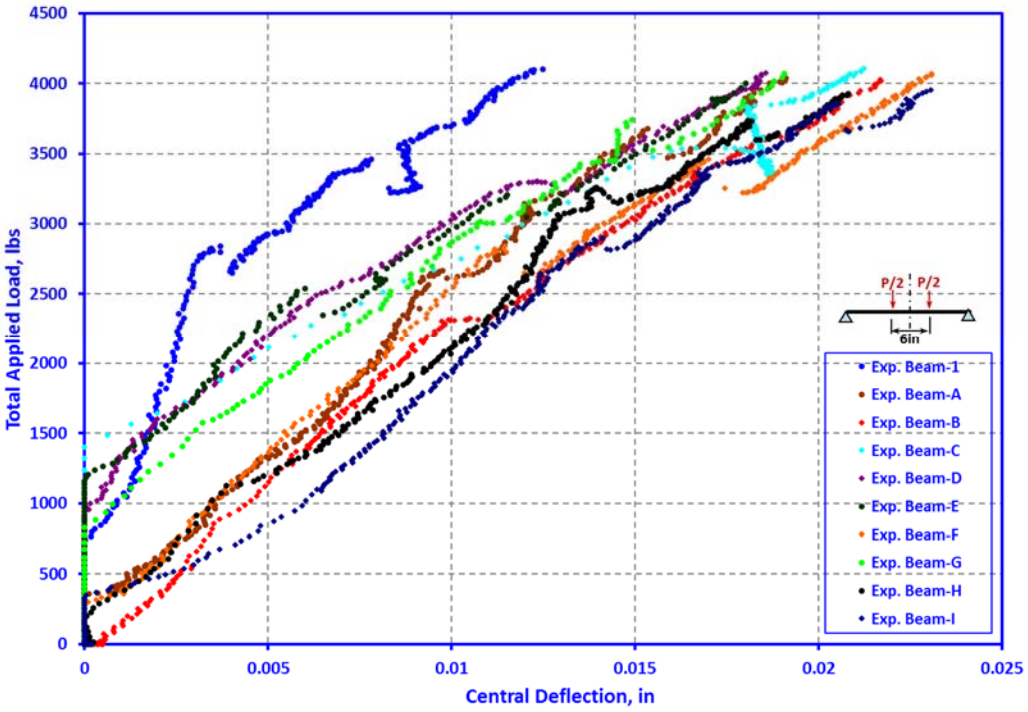

Figure 3.4.7. Plots of load vs. central deflection for "flexural" reinforced concrete beams - preliminary loading.

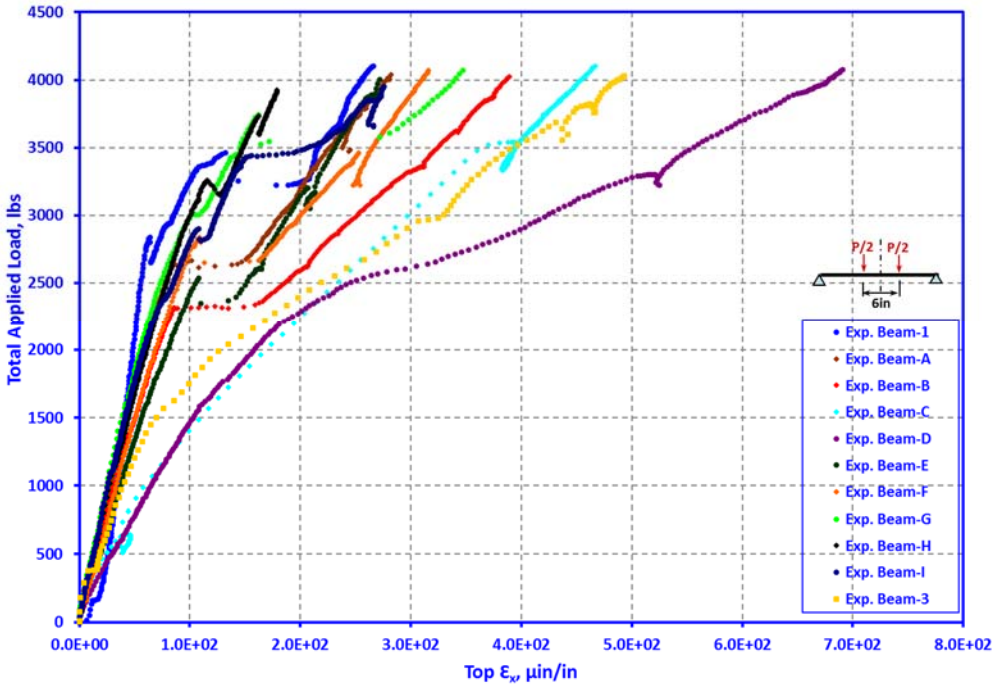

Figure 3.4.8. Plots of load vs. top fiber compressive strain for "flexural" reinforced concrete beams - preliminary loading.

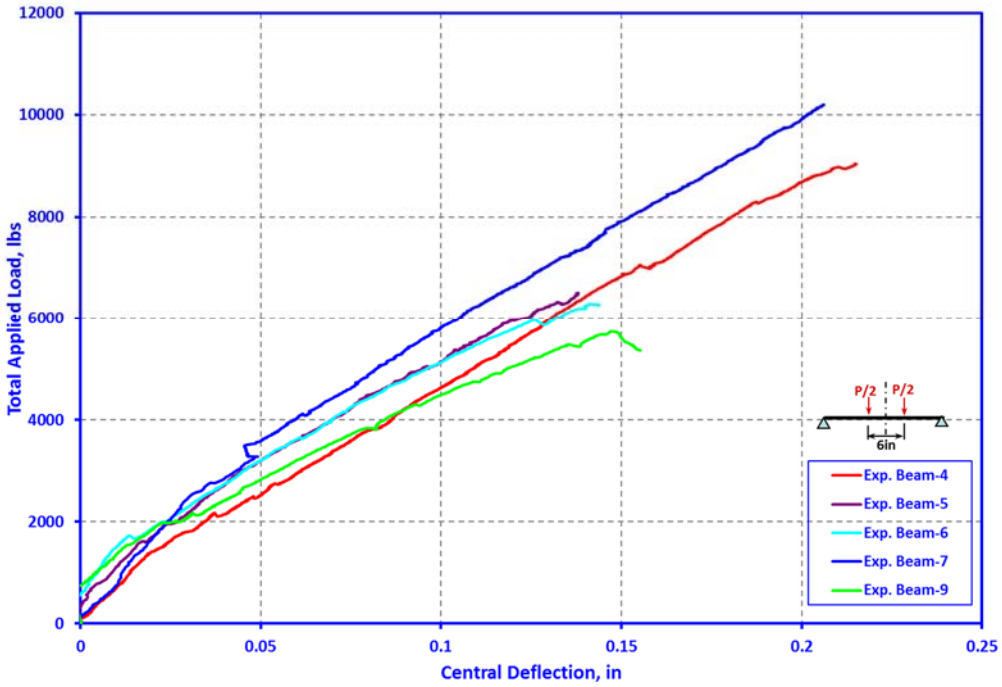

Figure 3.4.9. Plots of load vs. central deflection for "shear" reinforced concrete beams - preliminary loading.

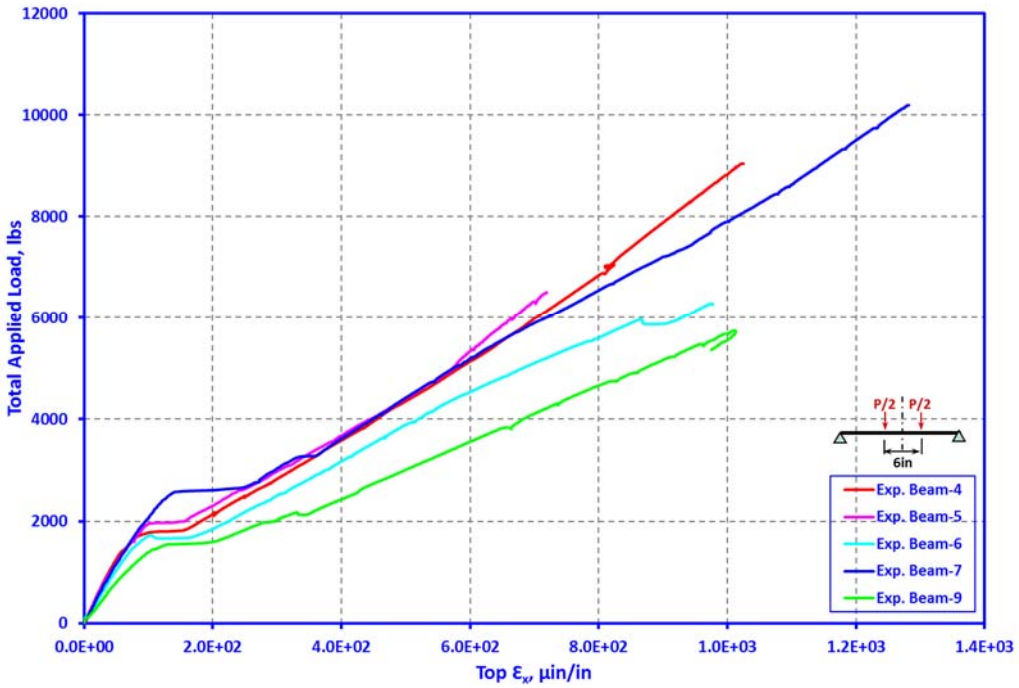

Figure 3.4.10. Plots of load vs. top fiber compressive strain for "shear" reinforced concrete beams - preliminary loading.

Although the prestressed concrete beams, PSCB1, PSCB2 and PSCB3, were manufactured for exactly the same details, during load testing, the type of the damages occurring in the beams were strikingly different. PSCB1 developed shear damage only on one side of the beam close to the support, suggesting construction flaws like the presence of local low strength due inadequate compaction of concrete during construction or, misplaced stirrups. On the other hand, the beam PSCB2 developed flexural cracks at the bottom of the beam near the center. During load testing of PSCB3, the beam developed two almost symmetrical shear cracks on either side of the beam. It is clear that even under controlled laboratory conditions, the variability of the load capacity of prestressed concrete beams cannot be avoided.

In the case of presetressed beams PSCB1 and PSCB2, the reliability of test results was in question due to faulty data acquisition process. In the case of PSCB1, the data was retrieved with the help of backup sensors. Fortunately, in the case of PSCB3, all data were recorded successfully. Figure 3.4.11 shows the load vs. central deflection plot of both PSCB1 and PSCB3. Figure 3.4.12 and Figure 3.4.13 show applied load vs. top fiber strain at midspan and web quarter-point strain for PSCB3.

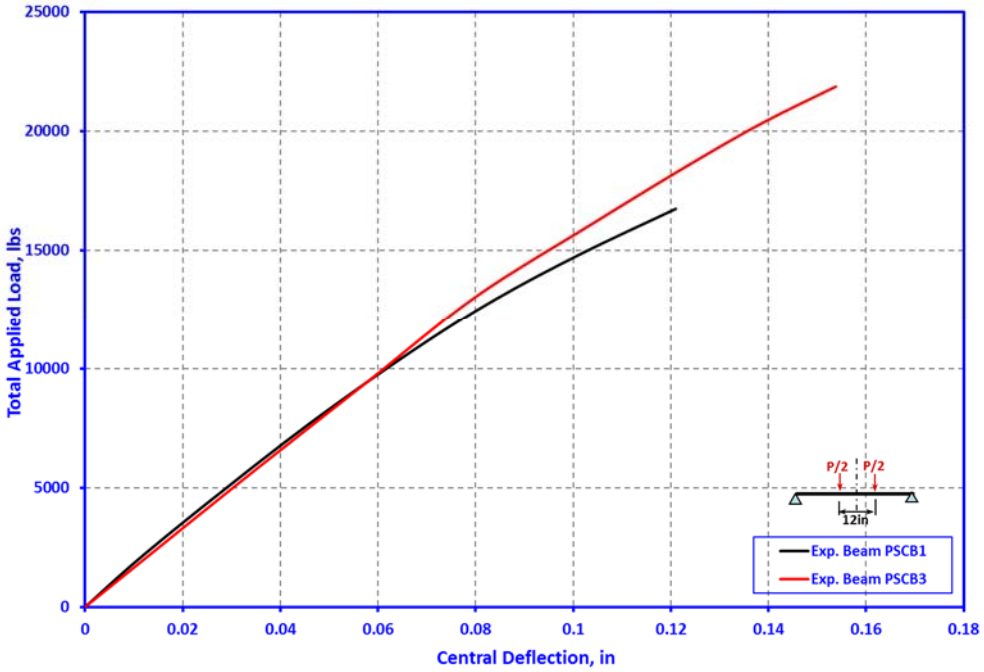

Figure 3.4.11. Load vs. central deflection plot for PSCB1 and PSCB3 - preliminary loading.

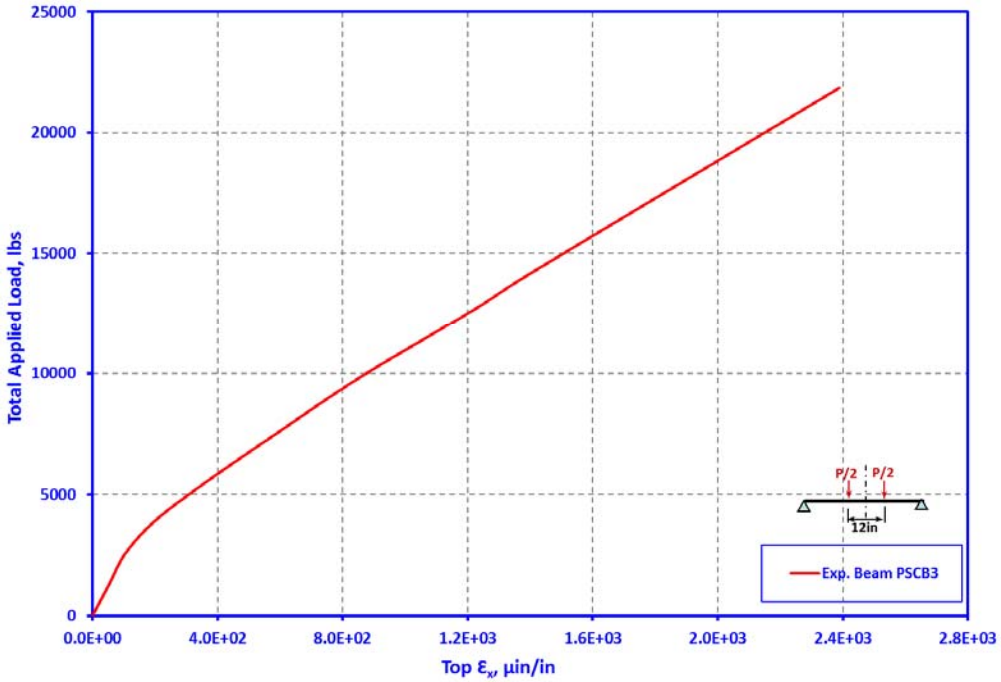

Figure 3.4.12. Load vs. top fiber compressive strain plot for PSCB3 - preliminary loading.

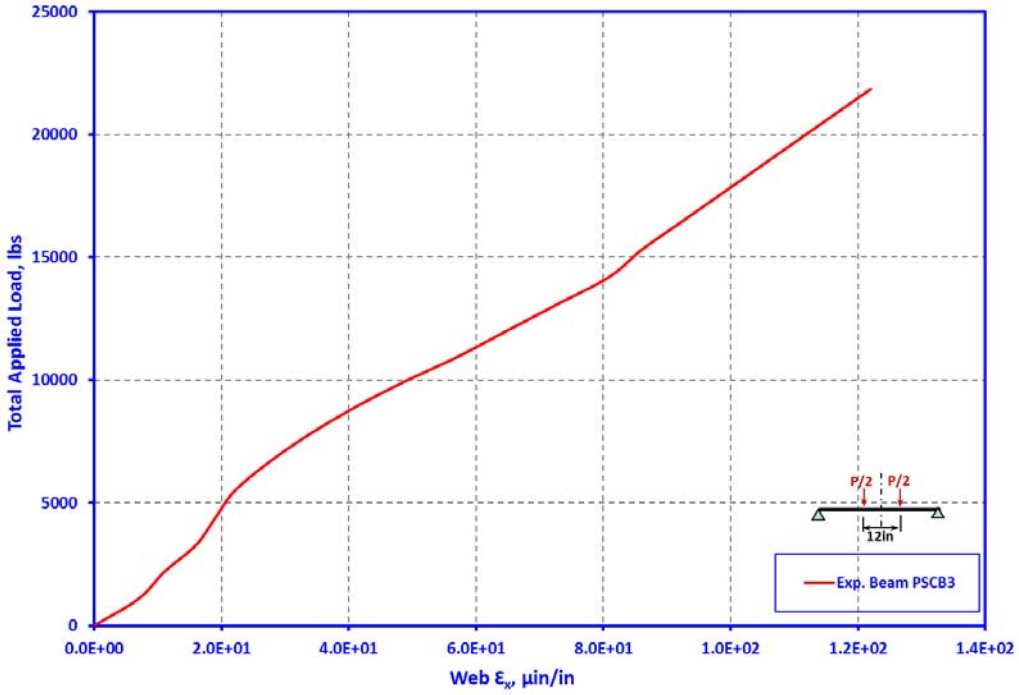

Figure 3.4.13. Load vs. web quarter-point tensile strain plot for PSCB3 - preliminary loading.

3.4.3. Load Testing After Composite Patch Repair

In this concluding step of the experimental work, after patch repair, all the beams were loaded up to failure. The performance of the repair processes were then evaluated by comparing the recorded data of the current step with the baseline performance of the original specimens. All details of the experimental effort related to the characterization of FRP materials and the adhesives are given in Appendix-F. More details of the FRP patch design and repair procedure of the test specimens are presented in Appendix-G.

All three patch-repaired steel beams SBI, SBII and SBIII were loaded up to the same maximum load level as was done before repair. The load vs. central deflection plots for the three patch-repaired steel beams are presented in Figure 3.4.14. Figures 3.4.15 to 3.4.17 show the same three repaired beams plots of total applied load vs. compressive strain

on the outside face of top flange, tensile strain on the inside face of the bottom flange, and diagonal tensile strain on the web, respectively. Loading was discontinued well before the strength limit state was reached, because the beams tended to undergo lateral torsional buckling (LTB). According to literature, composite patch strengthening cannot provide resistance to such behavior [64]. This aspect was further confirmed by this observation. FRP patch repair was found to be effective only when the critical limit state is yielding. As a result, the demonstration of significant gain in limit strength could not be experimentally demonstrated in the context of current effort. Such behavior is further confirmed by the fact that the elastic stiffness of composite being about 65% of that of steel and strength about 5 times that of steel, the capacity of the composite cannot be fully mobilized as a bonded patch material, in the elastic range. In order to fully utilize its high strength, the steel substrate has to undergo very large strains.

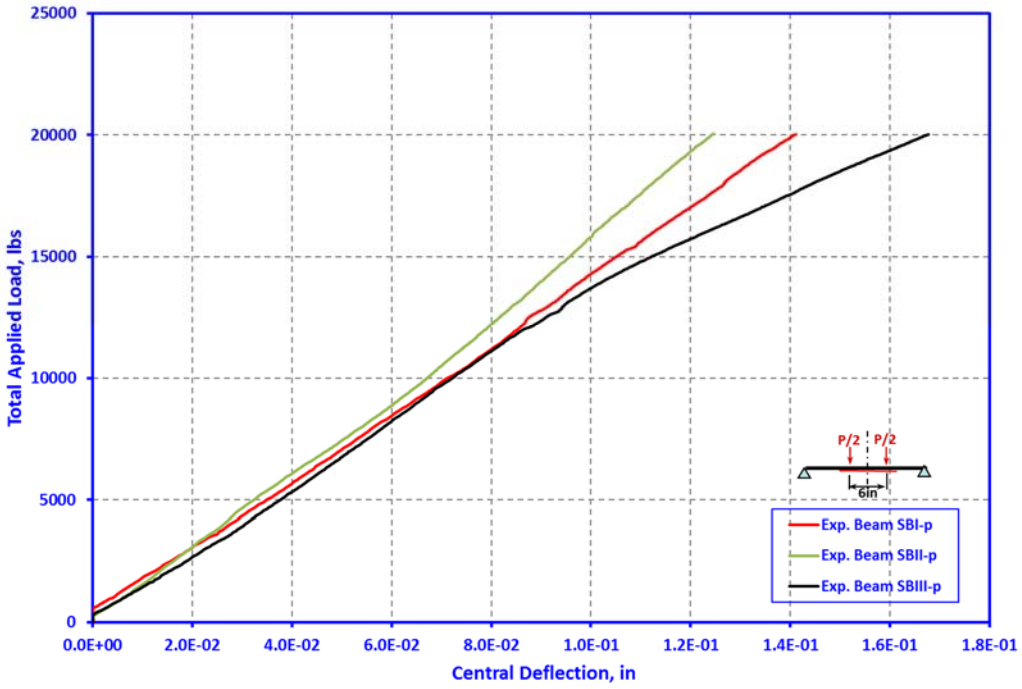

Figure 3.4.14. Load vs. central deflection plots for patch-repaired steel beams.

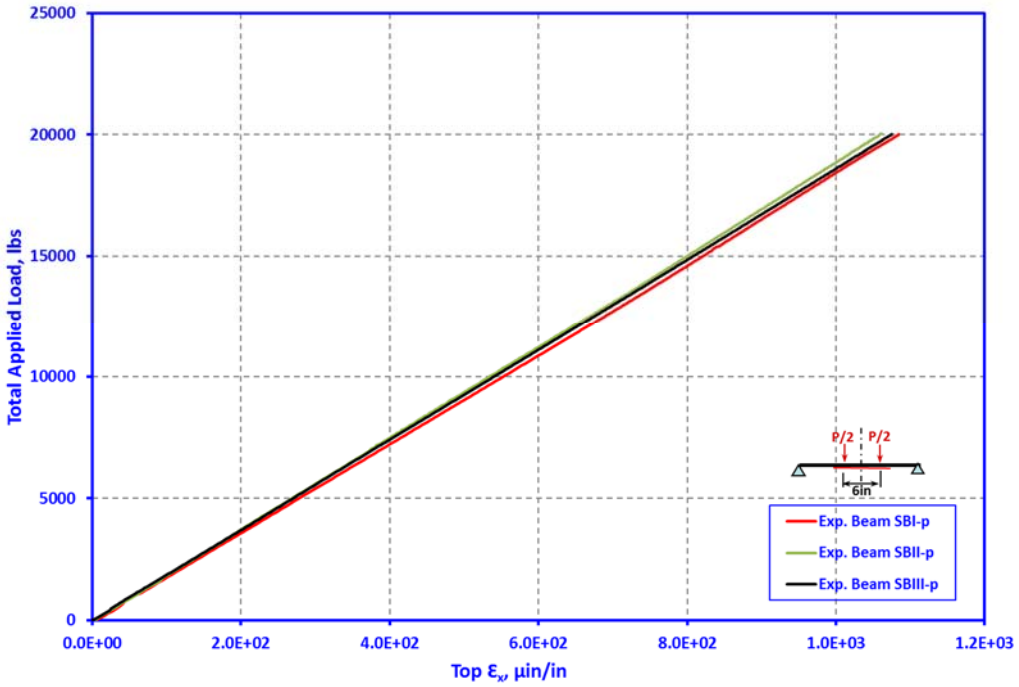

Figure 3.4.15. Load vs. top flange strain plots for patch-repaired steel beams.

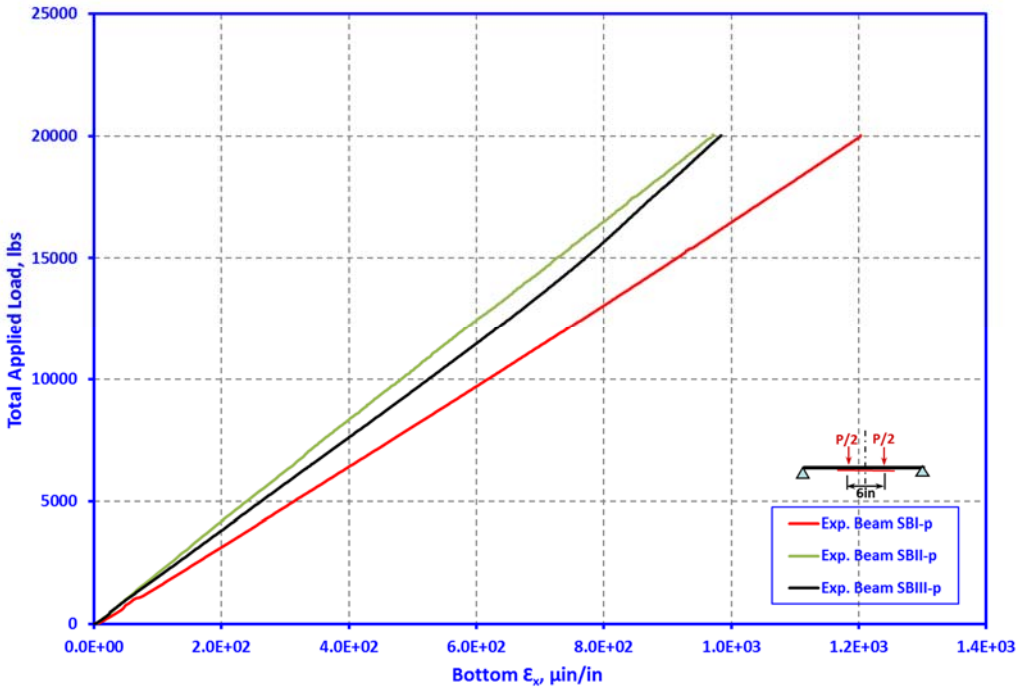

Figure 3.4.16. Load vs. bottom flange strain plots for patch-repaired steel beams.

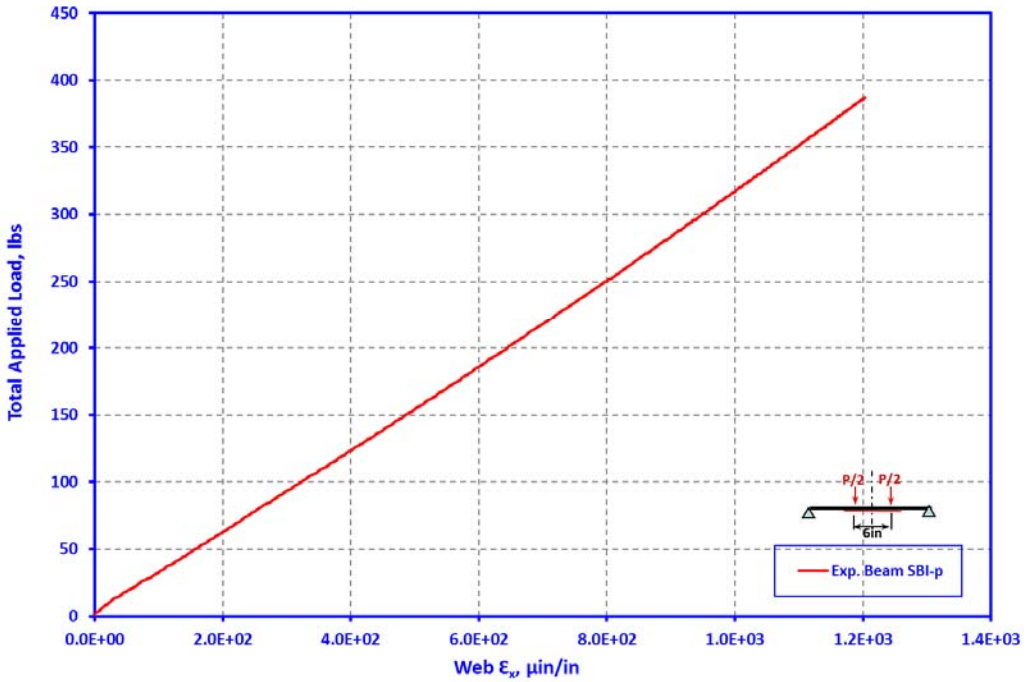

Figure 3.4.17. Load vs. web tensile strain plots for patch-repaired steel beams.

Unlike steel beams, composite patch repaired reinforced concrete beams could be loaded until failure. Appearance and growth of cracks during load testing of these patch-repaired beams were carefully traced and recorded, just as it was done during load testing of the original beams, before composite patch repair was undertaken.

The main failure mode of all of the "flexural" reinforced concrete beams was in shear. Experimental results of the patch-repaired "flexural" reinforced concrete beams are shown in Figures 3.4.18 and 3.4.19 as plots of applied load vs. central deflection and top flange strain. The applied load vs. patch strain values for composite materials are shown in Figures 3.4.20 and 3.4.21. Data recorded from the "shear" reinforced concrete beams being inconsistent are not presented here. The summary of the failure modes of all patch-repaired "shear" reinforced concrete beams with their maximum loads are given in Table 3.4-1.

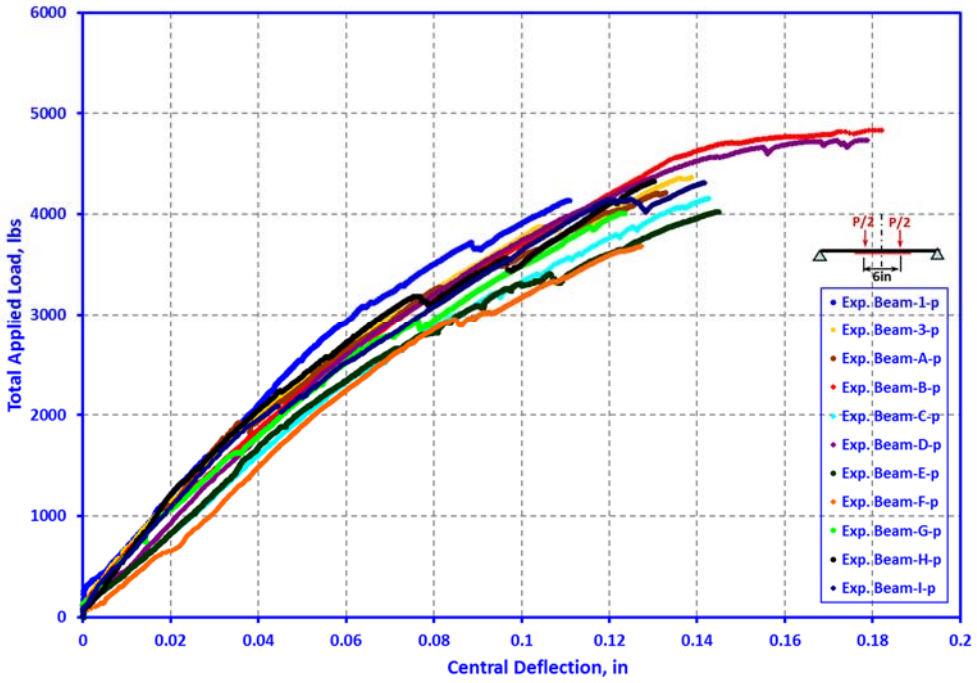

Figure 3.4.18. Load vs. central deflection plots for patch-repaired "flexural" reinforced concrete beams after repair.

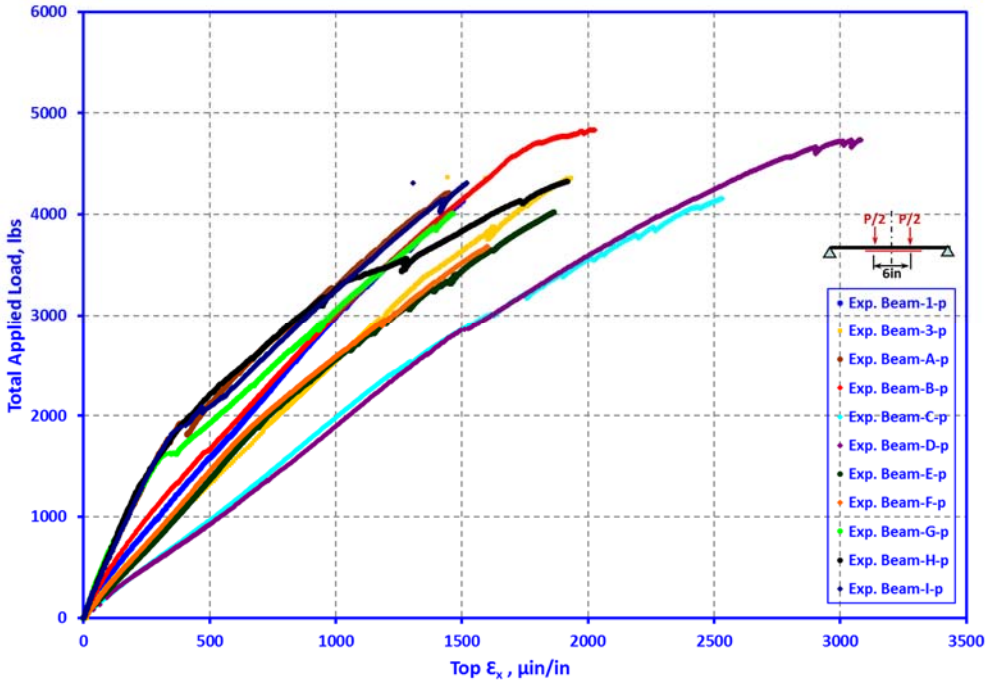

Figure 3.4.19. Load vs. compressive strain plot for "flexural" reinforced concrete beams after repair.

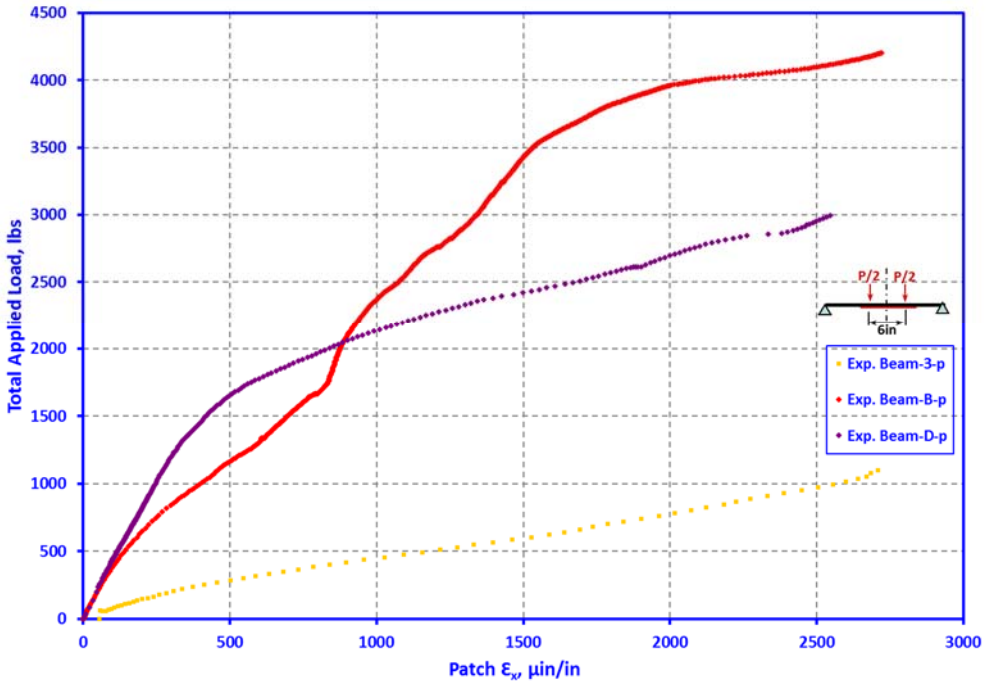

Figure 3.4.20. Load vs. patch strain plot for "flexural" reinforced concrete beams after repair.

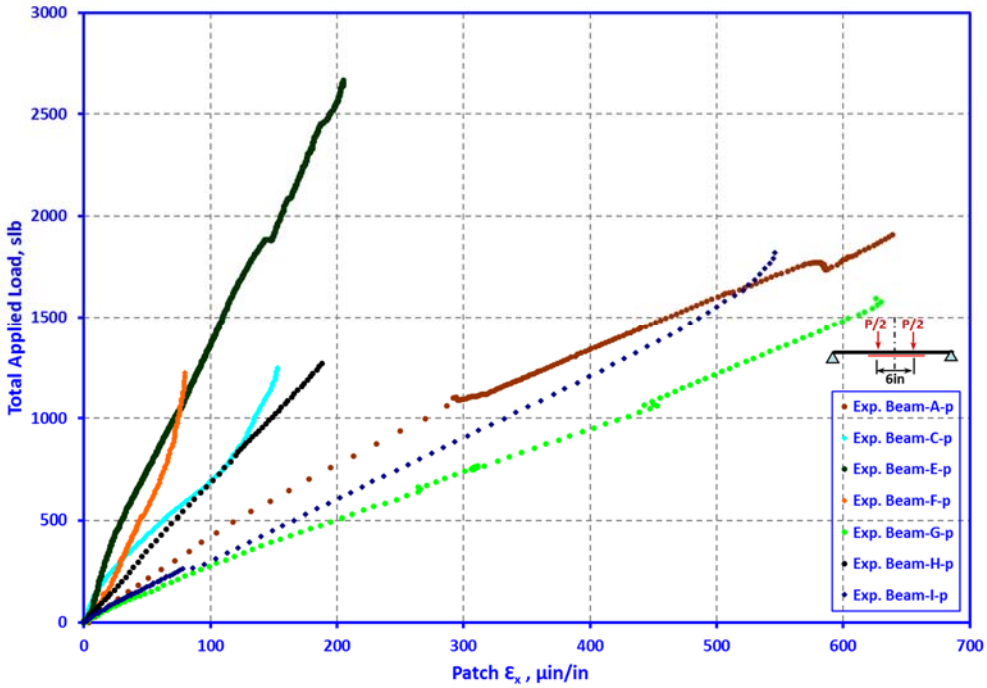

Figure 3.4.21. Load vs. patch strain plot for "flexural" reinforced concrete beams after repair (cont.).

Table 3.4-1. Failure mode and maximum load data of the "shear" reinforced concrete beams.

Beam ID	Repair Method	Maximum Load (lbs)	Failure Mode
4	U-Jacket	5775.0	Shear cracking with concrete cover separation
5	Inclined Side Plate	6400.5	Shear cracking
6	Inclined U-Jacket	3415.0	Composite patch debonding, primary steel debonding, concrete crushing, and shear cracking
7	U-Jacket	5230.0	Shear cracking with composite debonding
9	Inclined Side Plate	4442.5	Concrete crushing on top, concrete cover separation, and composite debonding

Values of displacement reduction, increase in moment capacity and original design value for "flexural" reinforced concrete beams are given in Table 3.4-2, for each type of FRP used. For "shear" reinforced concrete beams, minimum moment capacity increase was 35% over the original shear design capacity. More detailed performance information can be found in Tables 3.4-3 to 3.4-6 for both "flexural" and "shear" reinforced concrete beams.

Table 3.4-2. Performance improvement data for the "flexural" reinforced concrete beams after repair.

FRP Material	Displacement Reduction (%)	Moment capacity improvement (%)	
		Over required patch repaired design value	Over original design value
Carbodur	25%	31%	44%
Sikawrap	25%	20%	32%
LTC4300	25%	26%	39%

Table 3.4-3. Moment capacities of the "flexural" reinforced concrete beams repaired with LTC4300.

Beam ID	Moment Capacity (kip-in)		
	Before patch-repair	Required patch-repaired	Actual patch-repaired
A	46.87	51.56	72.50
G	47.07	51.78	71.36
H	47.05	51.76	65.46
I	46.96	51.66	60.35

Table 3.4-4. Moment capacities of the "flexural" reinforced concrete beams repaired with Sikawrap.

Beam ID	Moment Capacity (kip-in)		
	Before patch-repair	Required patch-repaired	Actual patch-repaired
3	46.88	51.57	62.05
B	46.49	51.14	55.19
D	43.39	47.73	62.36

Table 3.4-5. Moment capacities of the "flexural" reinforced concrete beams repaired with Carbodur.

Beam ID	Moment Capacity (kip-in)		
	Before patch-repair	Required patch-repaired	Actual patch-repaired
1	47.03	51.73	63.14
C	43.46	47.81	60.12
E	46.02	50.62	64.92
F	45.91	50.50	64.64

Table 3.4-6. Moment capacities of the "shear" reinforced concrete beams.

Beam ID	Moment Capacity (kip-in)		
	Before patch-repair	Required patch-repaired	% Increase
4	2832	5775	103.9
5	3064	6400.5	108.9
6	2794	3415	22.2
7	3010	5230	73.7
9	3028	4442.5	46.7

The repaired prestressed concrete specimen PSCB1 with original shear damage failed again in shear. The damage was initiated by elongation of existing cracks and creation of new cracks. This was followed by patch debonding with progressive cracking of the composite, see Figure 3.4.22. Although the failure load after repair hardly exceeded the design load, the beam PSCB1 continued to support the maximum failure load (16 kips) with increasing displacement showing significant ductile behavior.

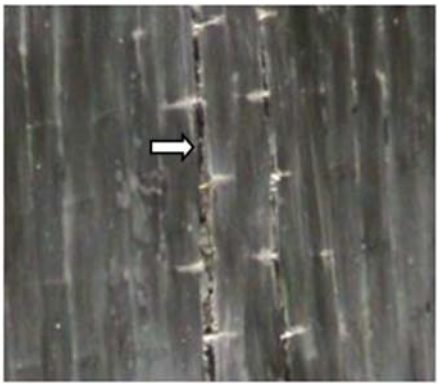

Figure 3.4.22. Cracking of the U-jacket composite patch of PSCB1 [65].

In the case of PSCB2 originally failing in flexure, ultimately failed in shear after repair, Figure 3.4.23. Here the failure was sudden and brittle unlike PSCB1. Signifying that FRP patch repair in shear tends to increase the ductility of the beam. The failure moment of PSCB2 (53.38 kip-ft) was much higher than its design moment (39.98 kip-ft) which proves the overall effectiveness of a properly designed repair scheme. This total 34% increase in moment capacity is significant.

Figure 3.4.23. Ultimate shear failure of the beam PSCB2 [65].

The repaired beam PSCB3, which originally developed two shear cracks on both sides of the beam, ultimately failed in shear accompanied by concrete crushing on top and debonding of repair material, Figure 3.4.24. Behavior of PSCB3 after repair was very similar with the ductile natured response of beam PSCB1. The failure load of PSCB3 (17.3 kips) was very close to its design value but it kept bearing this maximum load with increasing displacement. Plots of applied load vs. central deflection for beams PSCB2 and PSCB3 are shown in Figures 3.4.25 and 3.4.26, respectively. Web strain for the specimen PSCB3 at its quarter point is shown in Figure 3.4.27.

Figure 3.4.24. PSCB3 ultimately failed in shear in combination with concrete crushing on top and debonding.

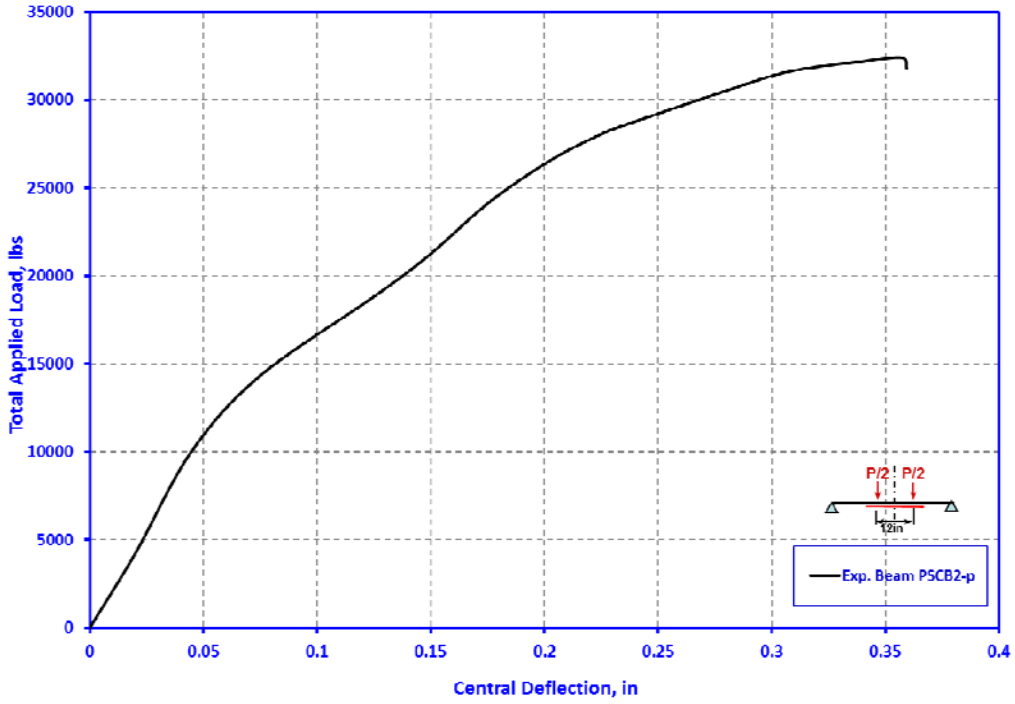

Figure 3.4.25. Load vs. central deflection plot for PSCB2 after repair.

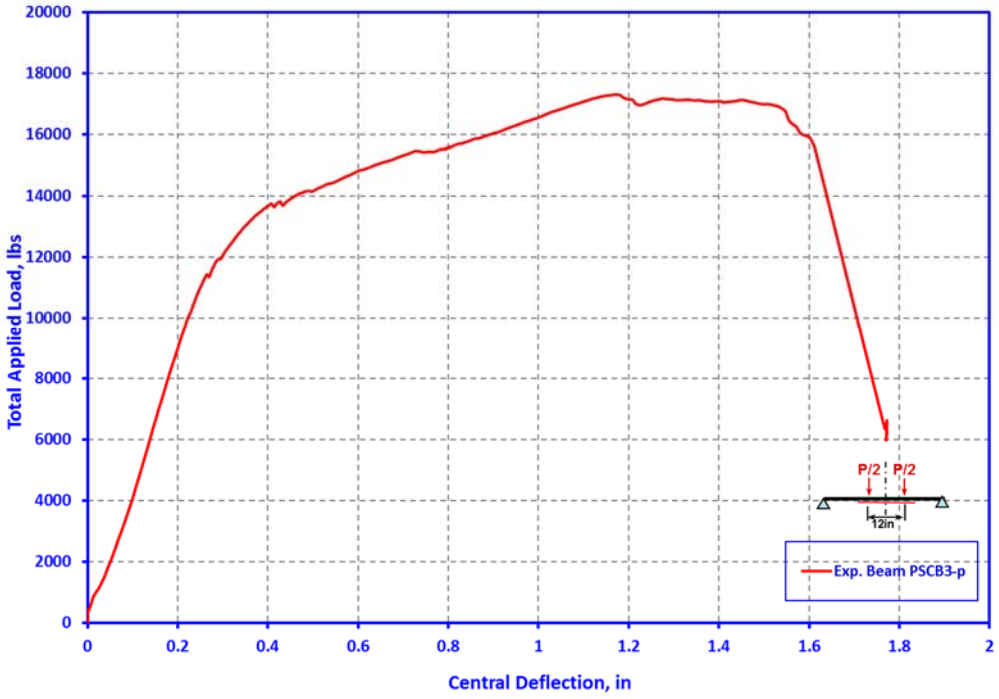

Figure 3.4.26. Load vs. central deflection plot for PSCB3 after repair.

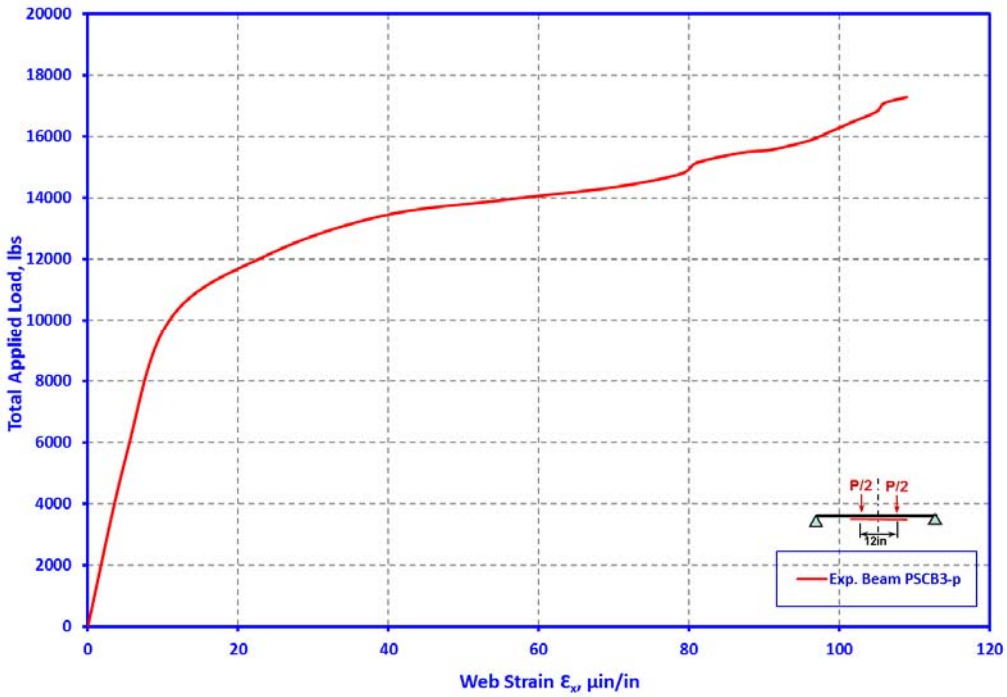

Figure 3.4.27. Load vs. web quarter point tensile strain plot for PSCB3 after repair.

3.5. Mechanistic Model for Patch Repaired Beams under Flexure

3.5.1. Description of the Model

Designing a patch repair for restoring bending or shear strength at a section was covered in Section 3.3. For proper detailing of the patch repair, it is necessary to have a clear understanding of the overall behavior of the repaired component by developing a simple mechanistic model which can be easily exercised in a design office environment obviating the need for full blown finite element analysis. For instance, an important failure mode in a patch repaired beam is debonding of patch layer causing separation from the substrate due to shear and/or tension failure, especially, near the ends of the flange patch. In order to more closely investigate this possibility, it is necessary to undertake more

realistic analysis than those considered in Section 3.3. This section is, therefore, concerned with developing a more realistic mechanistic model of the patch-repaired beam as a whole so that the interfacial stresses between the beam substrate and composite patch repair can be predicted with reasonable accuracy. In developing such a model, a number of simplifying assumptions are invoked, like:

- Euler-Bernoulli beam theory is valid.
- Only bending effect is considered.
- Patch repair is provided for restoring the moment capacity only.
- For the sake of simplicity, the beam is assumed to be simply supported and hence only bottom flange patch repair is considered.

It is desirable that the developed model is able to predict the behavior both under service load and overload conditions allowing, if necessary, accounting for nonlinear material behavior. The model developed in this chapter is applicable to steel, reinforced concrete, or prestressed concrete beams repaired to enhance the flexural strength. Due to simple mechanical properties of steel beams, application of this model to such beams is relatively straight-forward. On the other hand, because of the complex mechanical properties of concrete, the mechanistic model for reinforced concrete and prestressed concrete beams is expected to be more involved.

3.5.2. Elastic Model

An arbitrarily loaded simply supported patch repaired beam is shown in Figure 3.5.1. One of the main components of the proposed elastic model is to appropriately account for the role of adhesive in structural action. The main purpose of the adhesive is to

transfer the interaction forces between the composite layer and the substrate without undergoing slippage and separation. The resistance offered by the adhesive against sliding and separation forces can be represented by equivalent shear and axial spring elements as shown in Figures F.1 and F.2. For the sake of simplicity, these continuous springs can be assumed to follow Hooke's law. Values of equivalent spring constants were determined experimentally, as detailed in Appendix-F. As per Euler-Bernoulli principle, the plane sections in the beam and the patch are individually assumed to remain plane. In this model, the bond between composite patch and substrate is assumed to be uniform and continuous without any separation or delamination.

The spring forces in equivalent shear and tensile springs can be represented by Equations 3.5.1 and 3.5.2, where δ_v and δ_u are vertical and horizontal extensions of the springs and k_{sv} and k_{su} are corresponding spring constants.

$$F_v = k_{sv} . \delta_v \tag{3.5.1}$$

$$F_u = k_{su} . \delta_u \tag{3.5.2}$$

Based on change in length of vertical spring ($v_b - v_p$), force per unit length of adhesive:

$$F_v = k_{sv} (v_b - v_p) \tag{3.5.3}$$

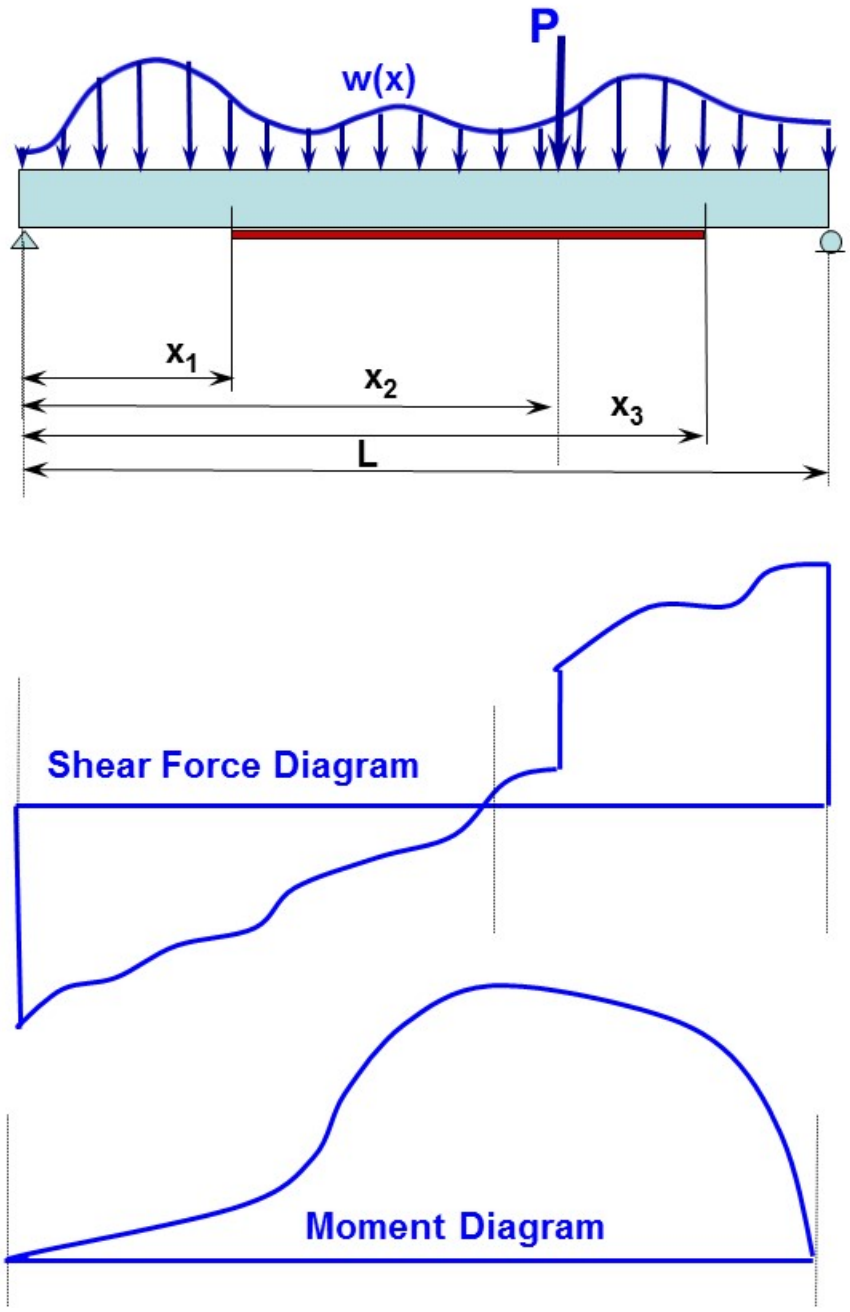

Figure 3.5.1. A simply supported patch repaired beam with shear and moment diagrams.

Likewise, the horizontal force carried per unit length adhesive can be expressed as:

$$F_u = k_{su}.(u_b - u_p) \tag{3.5.4}$$

Here v_b, v_p, u_b and u_p are the vertical and horizontal displacements of the beam and the patch, respectively. Horizontal and vertical displacements of an arbitrary point at the beam patch interface are show in Figure 3.5.2.

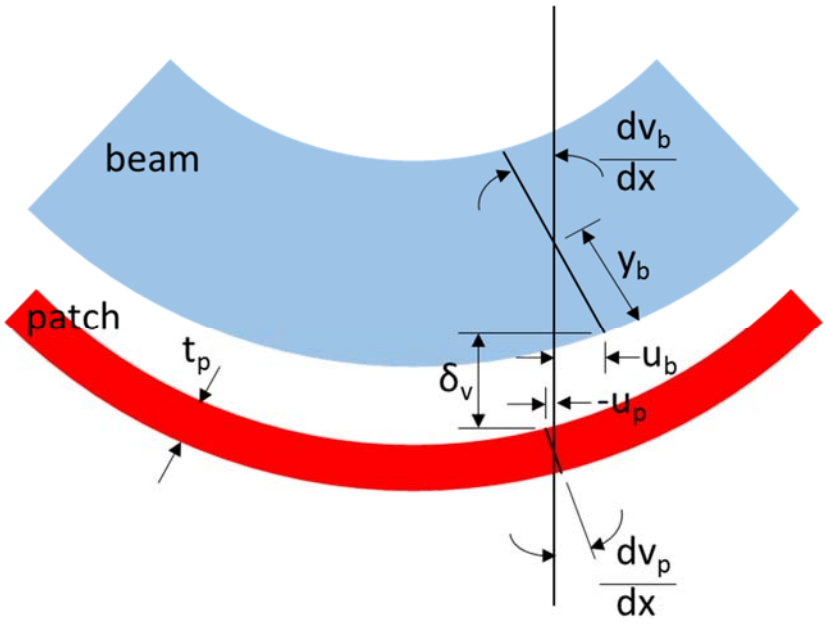

Figure 3.5.2. Displacements in vertical and horizontal directions for an arbitrary point at the beam patch interface.

For the interfacial point shown in Figure 3.5.2, horizontal displacements for the beam (u_b) and the patch (u_p) for small displacement condition can be represented by Equations 3.5.5 and 3.5.6, respectively.

$$u_b = y_b \cdot \frac{dv_b}{dx} = y_b \cdot v_b' \tag{3.5.5}$$

$$u_p = -0.5 \cdot t_p \cdot \frac{dv_p}{dx} = -0.5 \cdot t_p \cdot v_p' \tag{3.5.6}$$

If Equations 3.5.5 and 3.5.6 are substituted in Equation 3.5.3, the following relationship is obtained.

$$\delta_u = y_b \cdot v_b' - 0{,}5 \cdot t_p \cdot v_p' \tag{3.5.7}$$

Based on the start and end points of the patch, the beam length is divided into three typical segments, as shown in Figure 3.5.1. These are:

- Segment-1 from $x=0$ to $x=x_1$.
- Segment-2 from $x=x_1$ to $x=x_2$.
- Segment-3 from $x=x_3$ to $x=L$.

The energy contributions from these segments can be summed up, giving the total potential energy of the system, as shown in Equation 3.5.8.

$$\Pi = U_1 + U_2 + U_3 + W \tag{3.5.8}$$

In this equation, U_i is the strain energy of the *i-th* segment and W is the potential energy of the applied loads. The component W can be represented by Equation 3.5.9.

$$W = -\int_0^L w(x) \, . \, v_b \, . \, dx - P \, . \, v_b \, . \, x_2 \tag{3.5.9}$$

Strain energy contributions of Segments 1 and 3 to the potential energy, for the beam substrates, in terms of their flexural strain energies, are given by Equations 3.5.10 and 3.5.11.

$$U_1 = \frac{1}{2} \int_0^{x_1} EI \left(\frac{d^2 v_b}{dx^2} \right)^2 dx \tag{3.5.10}$$

$$U_3 = \frac{1}{2} \int_{x_2}^{L} EI \left(\frac{d^2 v_b}{dx^2} \right)^2 dx \tag{3.5.11}$$

In the case of Segment-2, the strain energy contribution will be from beam substrate, composite patch and adhesive. For this segment, the contribution will be due to bending as well as axial deformations which will be compressive in beam and tensile in the patch. Moreover, the strain energy of the adhesive will accrue from deformations in

equivalent vertical and horizontal springs. As can be seen in Figure 3.5.3, the net axial forces in the beam and the patch will be equal and opposite.

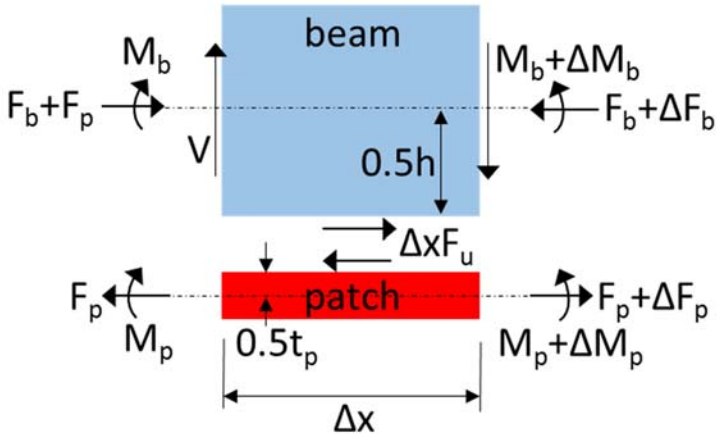

Figure 3.5.3. Internal force balance in beam Secgment-2.

Based on the internal force balance of the beam, composite patch and the adhesive shown in Figure 3.5.3, contribution of Segment-2 to the total potential energy of the system can be represented by Equations 3.5.12, 3.5.13, 3.5.14 and 3.5.15.

- Contribution of the beam:

$$U_2|_{Beam} = \frac{1}{2}\int_{x_1}^{x_3} (EI)_b \left(\frac{d^2 v_b}{dx^2}\right)^2 dx \tag{3.5.12}$$

- Contribution of the patch:

$$U_2|_{Patch} = \frac{1}{2}\int_{x_1}^{x_3} (EI)_p \left(\frac{d^2 v_p}{dx^2}\right)^2 dx + \frac{1}{2}\int_{x_1}^{x_3} (EA)_p y_p^2 \left(\frac{d^2 v_b}{dx^2}\right) dx \tag{3.5.13}$$

- Contribution of the adhesive:

$$U_2|_{Ad} = \frac{1}{2}\int_{x_1}^{x_3} [k_{sv}\delta_{sv}^2 + k_{su}\delta_{su}^2]\, dx \tag{3.5.14}$$

Therefore:

$$U_2 = U_2|_{Beam} + U_2|_{Patch} + U_2|_{Ad} \tag{3.5.15}$$

The two unknowns of the problem are the vertical deflection of the beam (v_b) and vertical deflection of the patch (v_p). Both of these can be approximated in terms of Fourier series expansions with unknown coefficients, given by Equations 3.5.16 and 3.5.17, respectively.

$$v_b = \sum_{i-1,\dots}^{n} C_i \sin\left(\frac{i\,\pi x}{L}\right) \tag{3.5.16}$$

$$v_p = \sum_{i-1,\dots}^{n} C_i \sin\left(\frac{i\,\pi x}{L}\right) + C_o\,\bar{x}\left(L_p - \bar{x}\right) \tag{3.5.17}$$

Where, $\bar{x} = x - x_1$

The zero displacement boundary condition at $x=0$ and $x=L$ is satisfied by both Equation 3.5.16 and the first term of Equation 3.5.17. The second term of Equation 3.5.17, represents the vertical displacement difference between the beam and the patch. Moreover, Equation 3.5.17 assumes zero relative deflection at the patch ends. By summing up the contributions of Equations 3.5.9, 3.5.10, 3.5.11 and 3.5.15, Equation 3.5.18 is obtained.

$$\Pi = \frac{1}{2}\int_0^{x_1} (EI)_b \left(\frac{d^2 v_b}{dx^2}\right) dx + \frac{1}{2}\int_{x_1}^{x_3} (EI)_b \left(\frac{d^2 v_b}{dx^2}\right) dx + \frac{1}{2}\int_{x_3}^{L} (EI)_b \left(\frac{d^2 v_p}{dx^2}\right) dx$$

$$+\frac{1}{2}\int_{x_1}^{x_3} (EI)_p \left(\frac{d^2 v_p}{dx^2}\right) dx + \frac{1}{2}\int_{x_1}^{x_3} (EA)_p y_p^2 \left(\frac{d^2 v_p}{dx^2}\right) dx$$

$$+\frac{1}{2}\int_{x_1}^{x_3} (k_{sv}\,\delta^2{}_{sv} + k_{su}\,\delta_{su}^2) dx - \int_0^{L} w(x).\,v_b\,(x).\,dx - P.\,v_b\,(x) \tag{3.5.18}$$

After substituting Equations 3.5.16 and 3.5.17 into Equation 3.5.18, there will be (n+1) unknown coefficients: C_i, i=0,1,...,n. By applying the stationary condition $\delta\Pi$=0 to Equation 3.5.18, those unknowns can be determined by using Equation 3.5.19.

$$\delta\Pi = \frac{\delta\Pi}{\delta C_o}\delta C_o + \sum_{i=1,\dots}^{n} \frac{\delta\Pi}{\delta C_i}\delta C_i = 0 \tag{3.5.19}$$

For arbitrary variation δC_i,

$$\frac{\delta\Pi}{\delta C_i} = 0, \quad i = 0,1,2,\dots,n \tag{3.5.20}$$

These (n+1) equations obtained from Equation 3.5.20 can now be solved for (n+1) C_i values. The deflections, strains and stresses can then be calculated at any point in the beam, patch or adhesive. Accuracy of the model depends on the number of terms (n) used in Equations 3.5.16 and 3.5.17. In this study, it was observed that 3 to 5 terms are enough to get accurate enough results from the model.

3.5.3. Specialization for Test Cases

The loading scheme used for testing throughout this study is shown in Figure 3.5.4. Consequently, Equation 3.5.18 becomes Equation 3.5.21 when the loading shown in Figure 3.5.4 is considered.

$$\Pi = \frac{1}{2}\int_0^{x_1} (EI)_b \left(\frac{d^2 v_b}{dx^2}\right)^2 dx + \frac{1}{2}\int_{x_1}^{x_4} (EI)_b \left(\frac{d^2 v_b}{dx^2}\right)^2 dx$$

$$+\frac{1}{2}\int_{x_4}^{L} (EI)_b \left(\frac{d^2 v_p}{dx^2}\right)^2 dx + \frac{1}{2}\int_{x_1}^{x_4} (EI)_p \left(\frac{d^2 v_p}{dx^2}\right)^2 dx$$

$$+\frac{1}{2}\int_{x_1}^{x_4}(EA)_p y_p^2\left(\frac{d^2 v_p}{dx^2}\right)^2 dx+\frac{1}{2}\int_{x_1}^{x_4}(k_{sv}\,\delta_{sv}^2+k_{su}\,\delta_{su}^2)\,dx$$

$$-\int_0^L q.v_b\,.dx-P.[v_b(x_2)+v_b(x_3)] \qquad (3.5.21)$$

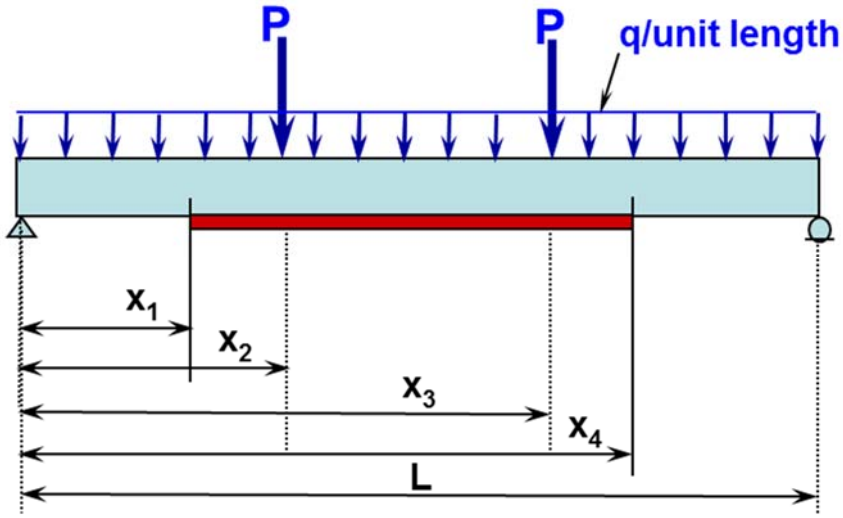

Figure 3.5.4. Loading scheme used for experimental work.

3.5.4. Application of Developed Model to Steel Beams

As pointed out earlier, application of the proposed mechanistic model to steel beams is less cumbersome compared to reinforced concrete and prestressed concrete beams due to the possibility of representing the mechanical properties of steel in terms of fewer parameters, namely, yield stress and elastic modulus when idealized as elastic-perfectly-plastic, as shown in Figure 3.5.5, σ_y and ε_y being yield strength and yield strain.

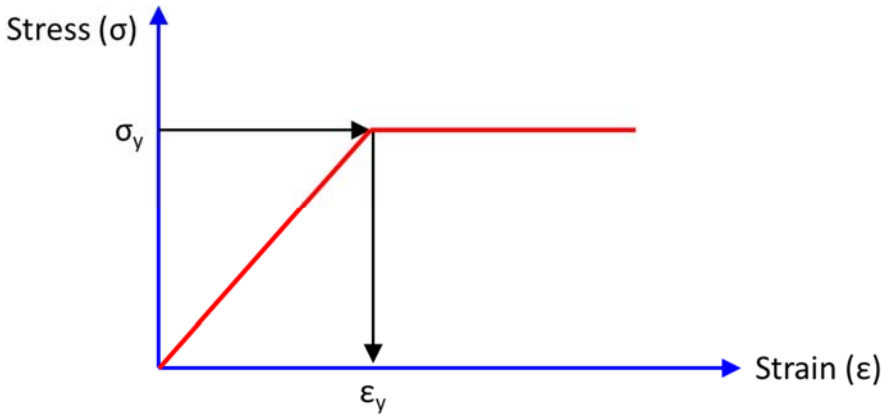

Figure 3.5.5. Elastic-perfectly plastic steel material behavior.

Based on the stated idealization, the internal forces of the beam can be calculated at any strain level. The internal forces in the steel beam for an arbitrary strain level when the section becomes partially plastic are shown in Figure 3.5.6. By enforcing the equilibrium of the internal forces, the moment-curvature relationship and the corresponding equivalent moment of inertia of the beam for any external load level can be calculated.

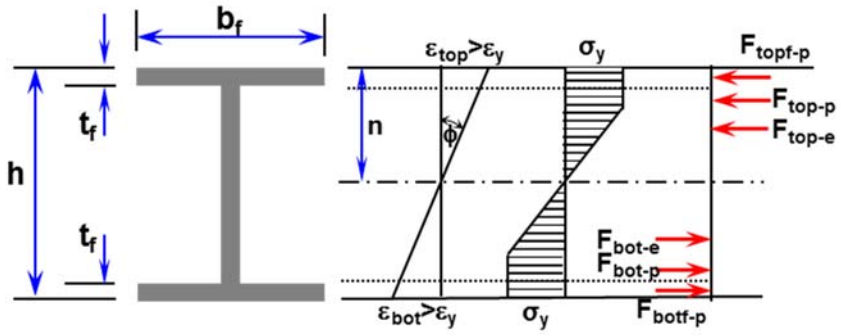

Figure 3.5.6. Internal loads of a typical steel section.

Additionally, unlike the reinforced concrete and prestressed concrete specimens, in this study, the composite patches were applied over the whole length of the steel beams. In that event, Equation 3.5.21 can be simplified into Equation 3.5.22 below:

$$\Pi = \frac{1}{2}\int_0^{L_1} (EI)_b \left(\frac{d^2 v_b}{dx^2}\right)^2 + \frac{1}{2}\int_0^{L} (EI)_p \left(\frac{d^2 v_p}{dx^2}\right)^2 dx$$

$$+\frac{1}{2}\int_0^{L} (EA)_p \, y_p^2 \left(\frac{d^2 v_p}{dx^2}\right)^2 dx + \frac{1}{2}\int_0^{L} (k_{sv}\,\delta_{sv}^2 + k_{su}\,\delta_{su}^2)\, dx$$

$$-\int_0^{L} q.v_b\,.dx - P.[v_b\,(x_2) + v_b\,(x_3)] \qquad (3.5.22)$$

It is instructive to note that the nonlinear behavior of the beam comes into play in Equation 3.5.22 through the parameter $(EI)_b$, the effective value of which drops as damage in the form of plastic accumulates in the substrate beam. This may be viewed as dropping value of effective I_b value, which may be termed as equivalent I_b. This representation will not be valid if the loading is not monotonic. As the only beam which was repaired against flexure alone was SBI, its experimental data is compared with the mechanistic model results, as shown in Figure 3.5.7. It is evident that the mechanistic model results show good agreement with test data. The comparison could be made in the elastic regime only, because the test had to be stopped prematurely, due to the tendency for lateral torsional buckling failure of the beam.

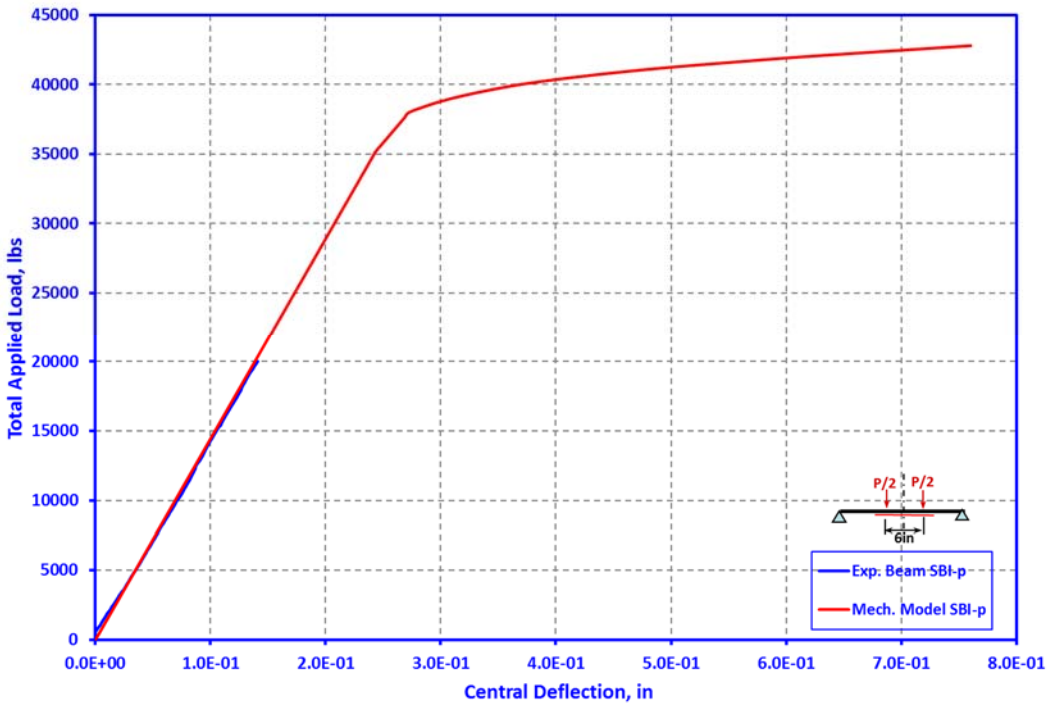

Figure 3.5.7. Comparison of mechanistic model results with test data for steel beam.

3.5.5. Application Mechanistic Model to Reinforced Concrete Beams

Because of cracking of concrete in tension, the value of equivalent moment of inertia will vary with the increasing load affecting the moment curvature relationship and hence the strain energy of the beam. The source of such nonlinear behavior is evident from Figure 3.5.8. In the conventional design procedures, the tensile strength of concrete is completely ignored after the appearance of the crack. In reality, the concrete around the tension rebar is found to carry some tensile load after such cracking. This phenomenon is called “tension stiffening” effect. Tension cracking of concrete and the tension stiffening effects are directly taken into account in Equations 3.5.10, 3.5.11 and 3.5.12.

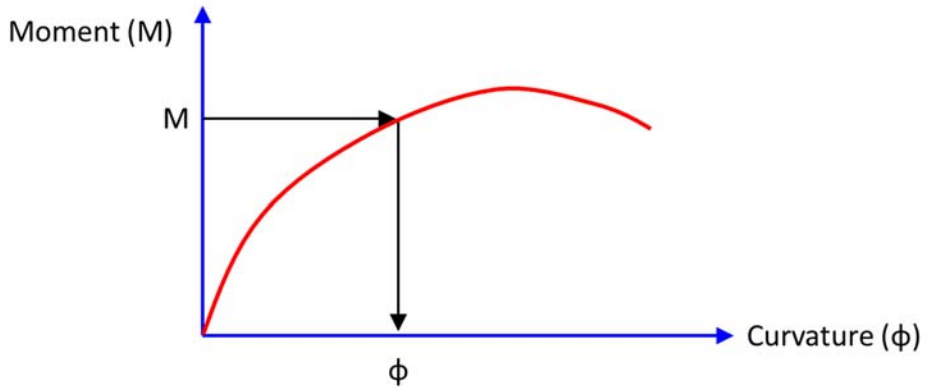

Figure 3.5.8. Moment-curvature relationship of a reinforced concrete beam.

Here the beam moment is represented by the usual simple beam formula as Equation 3.5.23. The concrete cracking strain is calculated by using ACI's rupture strain formula, which is shown in Equation 3.5.24 [66], in which f_c' and E_c are compressive strength and modulus of elasticity of concrete.

$$M = EI\phi = EI\frac{d^2v_b}{dx^2} \tag{3.5.23}$$

$$\varepsilon_{rup} = \frac{7.5\sqrt{f_c'}}{E_c} \tag{3.5.24}$$

By calculating the equilibrium of the internal forces in a beam section at different load levels, the moment-curvature relationship at that stage can be easily obtained. The internal forces of a beam section at an arbitrary load level are shown in Figure 3.5.9. The equivalent moment of inertia for that section can then be calculated based on this moment-curvature relationship.

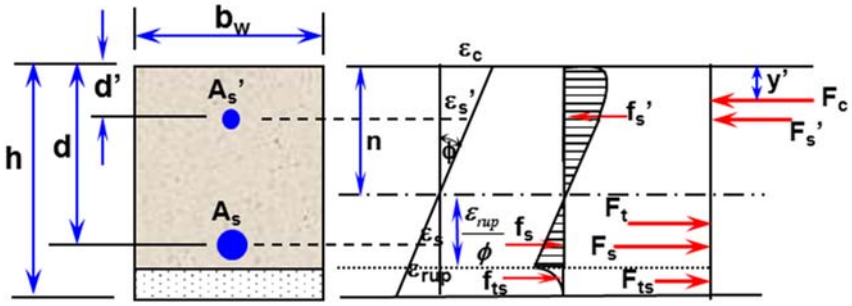

Figure 3.5.9. Internal loads of a typical reinforced concrete section.

Tension stiffening effect in concrete can be represented by Vecchio's model [67]. Figure 3.5.10 defines the relationship which is used for modeling the stiffening of concrete after tensile cracking, where f_t and ε_1 are modulus of rupture and strain over the depth of the beam. The compressive behavior of concrete is modeled by using the model proposed by Hognestad [68]. Details of Hognestad's concrete compressive behavior curve are presented in Figure 3.5.11. Detailed descriptions of these models, used for calculating the moment-curvature relationship of a beam section, is covered later in this chapter.

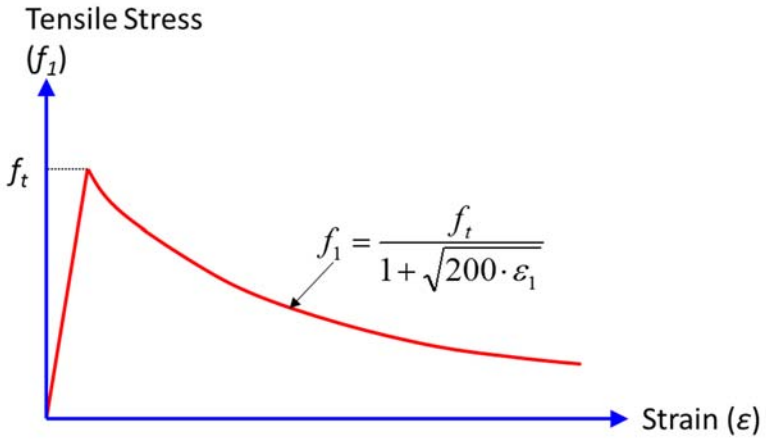

Figure 3.5.10. Tension stiffening model.

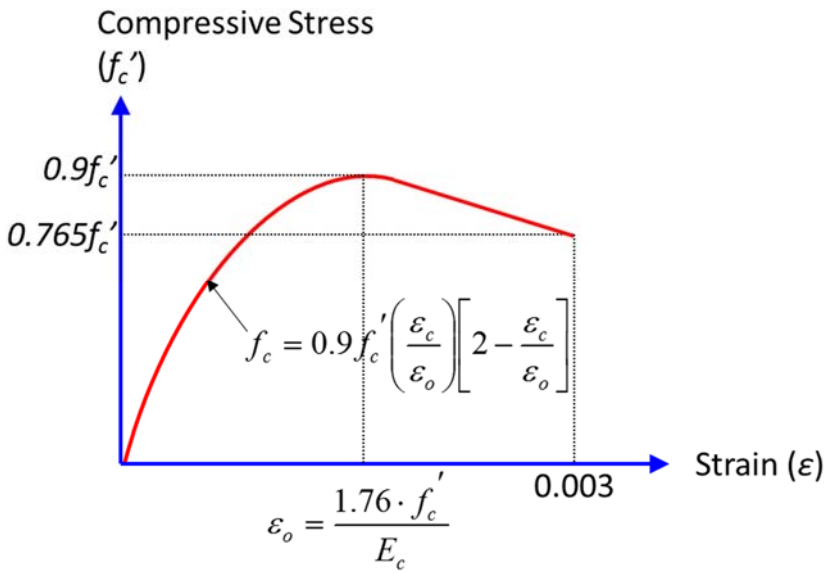

Figure 3.5.11. Compressive concrete behavior model.

For the calculation of the moment-curvature relationship of the section, the first critical point is assumed as the situation when the bottom flange of the concrete beam reaches the rupture strain ($\varepsilon_t=\varepsilon_{rup}$). In this state, the location of neutral axis can be calculated by using Equation 3.5.25.

$$n = \frac{A_c \frac{h}{2} + \frac{E_s}{E_c}(A_s\, d + A_s' d')}{A_c + \frac{E_s}{E_c}(A_s + A_s')} \tag{3.5.25}$$

Equations 3.5.26 to 3.5.28 present the strain values at top of beam section, top steel and bottom steel levels.

$$\varepsilon_c = \left(\frac{n}{h-n}\right).\varepsilon_{rup} \tag{3.5.26}$$

$$\varepsilon_s = \left(\frac{d-n}{h-n}\right).\varepsilon_{rup} \tag{3.5.27}$$

$$\varepsilon_s' = \left(\frac{n-d'}{h-n}\right).\varepsilon_{rup} \tag{3.5.28}$$

Steel forces and stresses for this condition can be expressed by Equations 3.5.29 to 3.5.32.

$$f_s = E_s \varepsilon_s \tag{3.5.29}$$

$$f_s' = E_s \varepsilon_s' \tag{3.5.30}$$

$$F_s = A_s f_s \tag{3.5.31}$$

$$F_s' = A_s f_s' \tag{3.5.32}$$

Based on the rupture stress, concrete tensile force can be calculated by using Equation 3.5.33, and by using the principle of equilibrium, the concrete compressive force can be calculated by using Equation 3.5.34.

$$F_t = \frac{1}{2} b_w (h-n) f_r \tag{3.5.33}$$

$$F_c = F_s + F_t - F_s' \tag{3.5.34}$$

The internal moment and curvature of the section can be calculated by using Equations 3.5.35 and 3.5.36, respectively.

$$M_r = F_c \left(\frac{\varepsilon_{rup}}{h-n}\right) + F_S'(h-d') - F_t \frac{(h-n)}{3} - F_s(h-d) \tag{3.5.35}$$

$$\phi_{rup} = \frac{\varepsilon_{rup}}{h-n} \tag{3.5.36}$$

After the concrete has cracked in tension, calculations become more complex. Total compressive force of concrete for the case when $\varepsilon_c < \varepsilon_o$ can be calculated by using Equation 3.5.37 which is basically based on the Hognestad representation, as shown in Figure 3.5.11.

$$F_c = 0.9 f_c' n^2 b_w \left(\frac{\phi}{\varepsilon_o}\right)\left(1 - \frac{n}{3} \cdot \frac{\phi}{\varepsilon_o}\right) \tag{3.5.37}$$

Now, the distance between the top fiber and the centroid of F_c can be calculated by using Equation 3.5.38.

$$y' = n - \bar{y} = \frac{n}{4}\left(\frac{4 - \frac{n\phi}{\varepsilon_o}}{3 - \frac{n\phi}{\varepsilon_o}}\right) \tag{3.5.38}$$

When $\varepsilon_c=\varepsilon_o$, total concrete compressive force and the distance between the top fiber and the centroid of F_c can be calculated with the help of Equations 3.5.39 and 3.5.40, respectively.

$$F_c = 0.6 f_c' n b_w \tag{3.5.39}$$

$$y' = \frac{3n}{8} \tag{3.5.40}$$

For the condition $0.003<\varepsilon_c<\varepsilon_o$, total concrete compressive force is given by Equation 3.5.41.

$$F_c = 0.6 f_c' \frac{\varepsilon_o}{\phi} b_w + b_w f_c' \left(\frac{n\phi - \phi_o}{\phi}\right)\left[0.9 - 0.0675 \frac{(n\phi - \varepsilon_o)}{\phi(0.003 - \varepsilon_o)}\right] \tag{3.5.41}$$

The total concrete compressive force F_c at the ultimate state of concrete can be calculated using Equation 3.5.42.

$$F_c = 0.6 f_c' \frac{\varepsilon_o}{\phi} b_w + 0.8325 f_c' b_w \frac{(0.003 - \varepsilon_o)}{\phi} \tag{3.5.42}$$

The case after the concrete is cracked in tension ($\varepsilon_t>\varepsilon_{rup}$) is described with the help of Equation 3.5.43. The only unknown in this equation is the neural axis depth *n* which can easily be calculated.

$$F_t + F_s + F_{ts} = F_c + F_s' \tag{3.5.43}$$

Here,

$$F_t = \frac{1}{2} . \frac{\varepsilon_{rup}}{\phi} b_w f_t \tag{3.5.44}$$

$$F_{ts} = \frac{f_t}{1 + \sqrt{200.\varepsilon}} \tag{3.5.45}$$

$$F_s = (d - n)A_s E_s \phi \tag{3.5.46}$$

$$F_s' = (n - d')A_s' E_s \phi \tag{3.5.47}$$

The total concrete compressive force F_c can now be determined by using Equations 3.5.37, 3.5.39, 3.5.41 or 3.5.42 based on the value of ε_c. After the neural axis depth n is calculated, the internal moment of the section can be computed using Equation 3.5.48.

$$M_r = F_c(h - y') + F_s'(h - d') - F_t\left[h - \frac{2}{3}\cdot\left(n + \frac{2.\varepsilon_{rup}}{\phi}\right)\right]$$

$$-F_s(h - d) - F_{ts}\left(h - y^{"}\right) \tag{3.5.48}$$

At this stage, it is also critical to check if the bottom and/or top reinforcing rod strains are in plastic region. In event of yielding of reinforcing rods, expressions for F_s and F_s' will require to be modified, as needed.

After the mechanistic model results were obtained for reinforced concrete beams repaired against flexure, the same were compared with the test results. In Figure 3.5.12, applied load vs. deflection relationships for the flexural reinforced concrete beam before and after composite patch repair are shown. Reasonably good agreement between the mechanistic model and experimental results is noted.

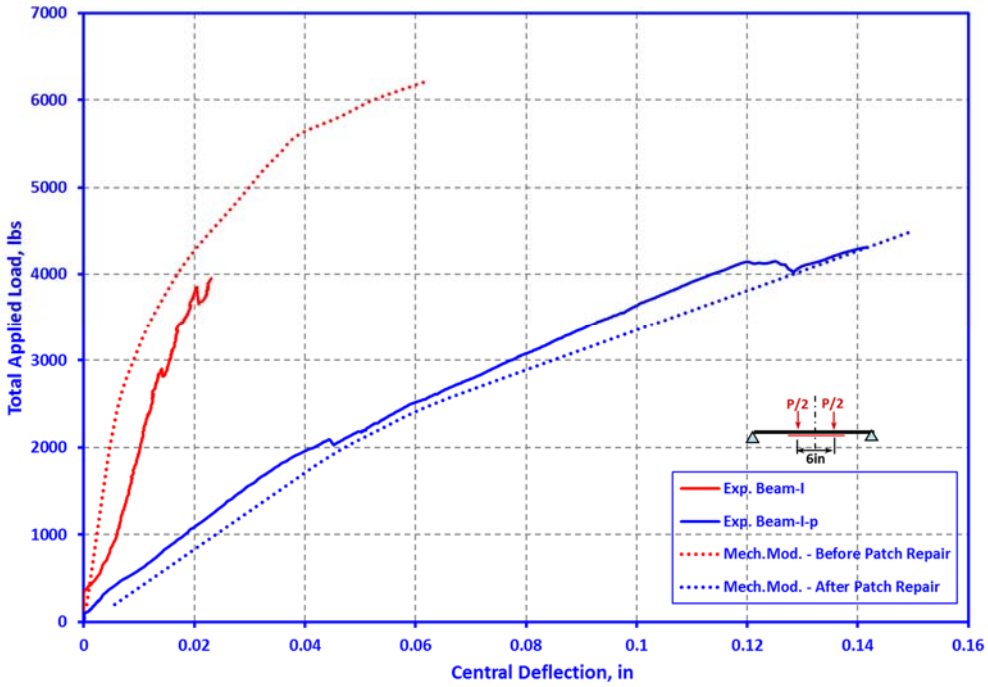

Figure 3.5.12. Comparison of mechanistic model results with test data for reinforced concrete beams.

3.5.6. Application of the Mechanistic Model to Prestressed Concrete Beams

Although in this case the procedure is very similar to that for reinforced concrete beam, but being of nonrectangular shape, the mechanistic model for prestressed concrete beam is more involved than the reinforced concrete beam model, as the neutral axis moved through different widths of the section when the applied load was increased towards the limit state. Allowing for this, the mechanistic model response was computed and then the results were compared with the experimental data obtained for the prestressed concrete beam PSCB2. Excellent agreement was noted between mechanistic model results and experimental data. In Figures 3.5.13 and 3.5.14, applied load vs. central deflection

relationship for the prestressed concrete beam, with and without flexural patch repair, obtained from the mechanistic model results and experimental data are presented.

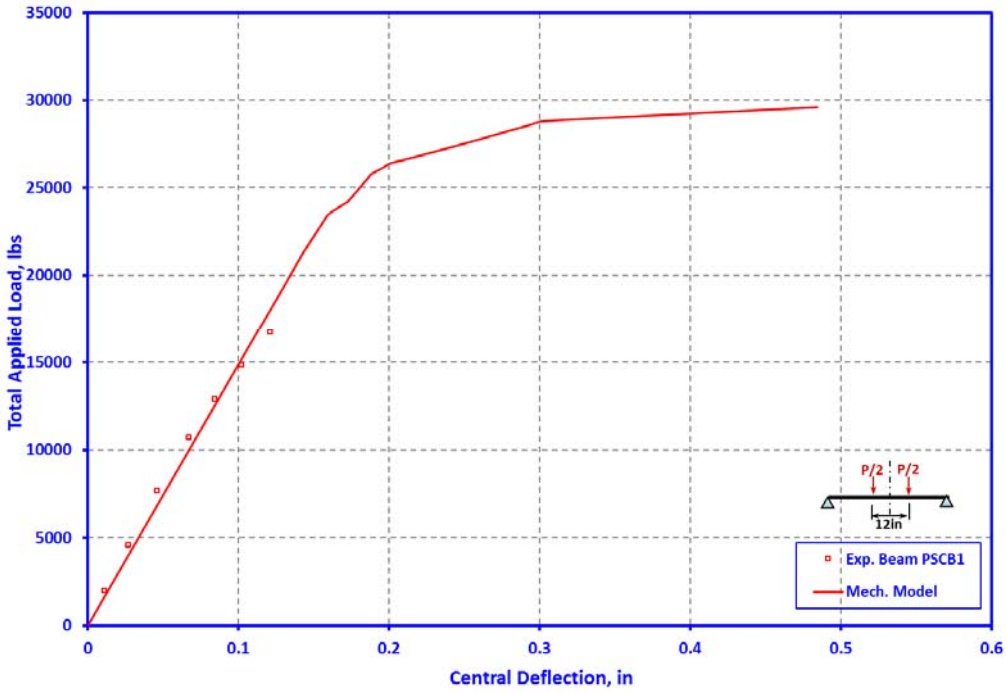

Figure 3.5.13. Comparison of mechanistic model results with test data for prestressed concrete beams before repair.

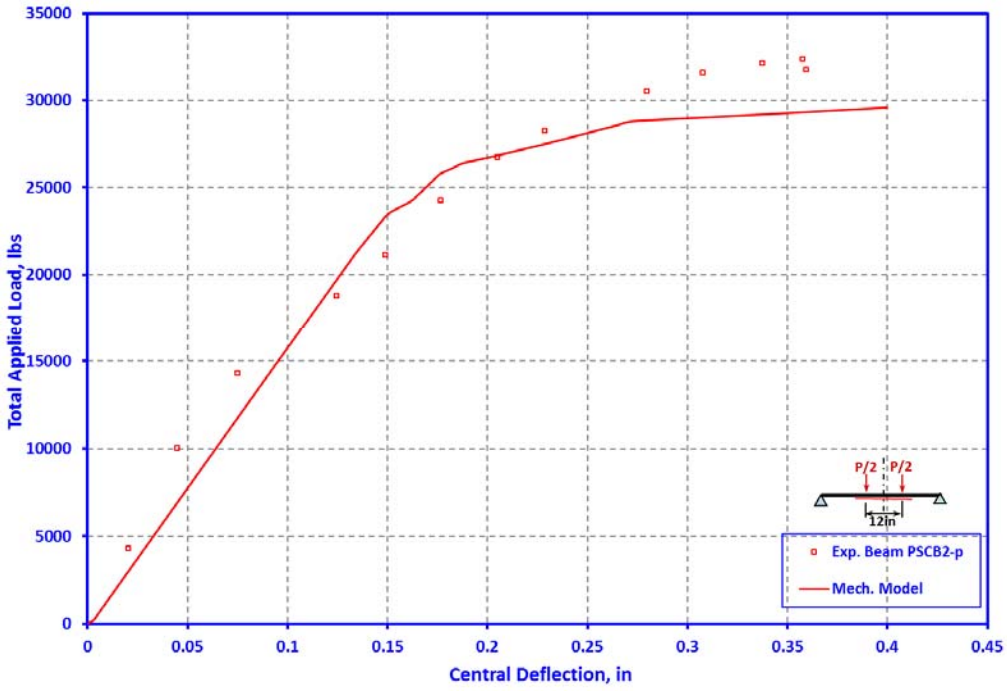

Figure 3.5.14. Comparison of mechanistic model results with test data for prestressed concrete beam after repair.

3.6. Finite Element Modeling of Concrete and Steel Beams

3.6.1. Description of the Modeling Scheme

The general purpose finite element analysis software Abaqus is used to model the steel, reinforced concrete and prestressed concrete beams before and after patch repair was undertaken and loaded for both conditions. Since all the beams are loaded quasi-statically, the static analysis module of Abaqus/Standard is used for the analysis. One of the main shortcomings of this module is its iteration algorithm. Abaqus/Standard uses the Newton method to solve nonlinear static problems. As the peak response is approached, the slope of the response curve tends to zero and the analysis is unable to proceed further and quits. To overcome this problem near the softening region of the response curve, the option of

switching to “modified Riks method” can be activated. This method uses the arc-length algorithm, mainly developed for overcoming the limit points in unstable problems (i.e. nonlinear post-buckling, collapse etc.) [69]. Being a variant of the Newton method, the “modified Riks method” moves along the current response curve by identifying the tangent direction at the current solution point. It then moves along this line and searches for equilibrium in the plane that passes through the point which is orthogonal to the tangent line [61].

Finite element models presented in this study accounts for actual mechanical characteristics of steel, reinforced concrete and prestressed concrete beams including the nonlinear material properties and interfacial bond between concrete, composite patch, adhesive, steel and strand. The slippage and friction between surfaces, Poisson radial expansion of the prestressing strands and the wedging effect, which will be explored in detail later in this section, are also taken into account accurately.

One important aspect of this study is that, this is the first successful realistic simulation of a pretensioned concrete beam. After a thorough literature survey, the author was surprised to find that not a single prior publication had done so correctly. The prestressed concrete beam models used in this study were created by faithfully following the construction sequence of the real pretensioned concrete beams including allowing for transfer of force from the released pretensioned strands by bond and mechanical action. The developed model also successfully simulated the plasticity and damage behavior of concrete, elastic-plastic material characteristics of steel (rebars and prestressing strands) and slip-bond failure behavior of strands.

3.6.2. Material Models and Bond Parameters

Plasticity-Damage (PD) model uses the concepts of isotropic damaged elasticity in combination with isotropic tensile and compressive plasticity to represent the inelastic behaviour of concrete. This material model is mainly a variation of the well-known Drucker-Prager failure criterion. Since the dominant mode of damage in metals is governed by the slip process, material models based on plasticity theories works well for such polycrystalline materials. In the case of concrete and quasi-brittle materials, the use of plasticity based failure surfaces accounting for the effects of pressure sensitivity; strain-hardening; etc. did not prove to be successful. Continuum damage theory based models with micro-cracking and strain-softening could not also adequately represent the mechanical behavior of concrete.

The main characteristic of concrete, which differentiates it from other materials, is the formation and propagation of micro-cracks with increasing stress. As these cracks propagate, they tend to cause loss of strength and degradation of physical properties. Figure 3.6.1 shows the situation when a concrete specimen gets unloaded from any point on the strain softening branch of the stress-strain curve. As the elastic stiffness of the material undergoes degradation, the unloading response is observed to get weakened. The degradation of the elastic stiffness is significantly different in tension and compression tests; in either case, the effect is more pronounced as the plastic strain increases. As can be clearly seen from Figure 3.6.1, both plastic behavior in the hardening region and damage through stiffness degradation in the softening region are included in the Plastic Damage (PD) material model.

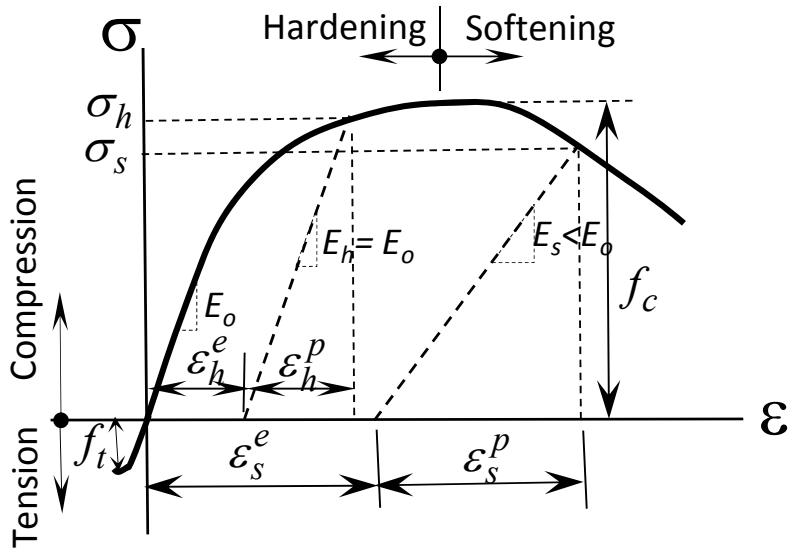

Figure 3.6.1. Compressive stress-strain relationship of PD model of concrete.

The combined effect of plastic behavior in the hardening region and damage through stiffness degradation in the softening region can conveniently be based on assumptions of isotropic hardening and isotropic damage. The combination of these effects is represented by Lee and Fenves with the effective-stress being defined in terms of the average micro-scale stresses acting on the undamaged material [70].

For successful concrete material modeling, in addition to accurately representing the response of concrete in both tension and in compression [71], taking into account of two damage and hardening variables for stiffness degradation is extremely important. The damage variable proposed by Kachanov [72] is introduced into the model to represent the stiffness degradation. This isotropic damage variable is based on specific area on the damage surface. The formation of two separate elastic-plastic yield surfaces for both compression and tension behavior of concrete is decoupled from the stiffness degradation

formulations. The proposed concrete material model is based on infinitesimal deformation, low confining pressure and strain-rate independence assumptions.

The total strain tensor (ε_{ij}) shown in Figure 3.6.1 has two components namely the elastic strain tensor (ε_{ij}^{e}) and the plastic strain tensor (ε_{ij}^{p}). By defining the scalar stiffness degradation parameter as d, with $0 \leq d \leq 1$, the constitutive 3D stress field relationship can be represented mathematically by using Equation 3.6.1, as shown below:

$$\sigma_{ij} = C_{ijkl}^{e} : \left(\varepsilon_{kl} - \varepsilon_{kl}^{p}\right) \tag{3.6.1}$$

Here, the degraded elastic stiffness tensor of rank four (C_{ijkl}^{e}) is shown in Equation 3.6.2 below.

$$C_{ijkl}^{e} = (1 - d).C_{ijkl}^{eo} \tag{3.6.2}$$

With σ_{ij} is the Cauchy stress tensor. The effective stress tensor, σ'_{ij} can now be represented by Equation 3.6.3.

$$\sigma'_{ij} = \frac{\sigma_{ij}}{1 - d} \tag{3.6.3}$$

Multi-softening as well as multi-hardening yield functions need to be used to take into account separate damage effects both in tension and compression. Because of the important differences in the ultimate strength in tension (f_t) and compression (f_c), the yield function in terms of effective stress can be defined by using Equation 3.6.4.

$$F\left(\sigma'_{ij}, f'_t, f'_c\right) \leq 0 \tag{3.6.4}$$

With effective tensile and compressive stress responses represented by using Equations 3.6.5 and 3.6.6, respectively.

$$f'_t = \frac{f_t}{1 - d} \tag{3.6.5}$$

$$f'_c = \frac{f_c}{1 - d} \tag{3.6.6}$$

In these equations, the parameter *d* can now be defined as:

$$d = 1 - (1 - d_c).(1 - d_t) \tag{3.6.7}$$

Where, d_c is the damage parameter for compression and d_t is for tension, while $0 \leq d_c$ and $0 \leq d_t$. So that the combined effect of tensile and compressive damages can be represented by using only one damage parameter, *d*. By using the hardening and softening variables ε_c'' and ε_t'' which are related to the dissipation of energy during the damage process, the individual damage parameters d_c and d_t can be represented. Such representation works fine in the case of monotonic loading. The yield surface can easily be represented by using Equation 3.6.8 below.

$$F'\left(I_1, J_2, J_3, \varepsilon_c^{"}, \varepsilon_t^{"}\right) \leq 0 \tag{3.6.8}$$

In which, F' is a function of first invariant of Cauchy stress tensor. In addition, it is also a function of the second and third invariants of deviatoric parts of the effective stress tensor which are given by Equations 3.6.9 to 3.6.11.

$$I_1 = \sigma'_{ij} . \delta_{ij} \tag{3.6.9}$$

$$J_2 = {}^1/_2 \, . S'_{ij} . S'_{ij} \tag{3.6.10}$$

$$J_3 = {}^1/_3 \, . S'_{ij} . S'_{jk} . S'_{kl} \tag{3.6.11}$$

Where:

$$S'_{ij} = \sigma'_{ij} - \delta_{ij} . \zeta \tag{3.6.12}$$

The term J_3 can be dropped for low confining pressures from the yield surface equation, which is represented by Equation 3.6.8. By using the Haigh-Westergaard coordinates in the principal effective stress space (ζ', ρ', θ'), the failure surface can also be defined. This representation is given by Equations 3.6.13 to 3.6.15 [73].

$$\zeta' = \frac{p'}{\sqrt{3}} = \frac{I_1'}{3} \tag{3.6.13}$$

$$p' = \sqrt{2J_2'} \tag{3.6.14}$$

$$\theta' = \frac{1}{3} cos^{-1}\left(\frac{3\sqrt{3}}{2} . \frac{J_3}{J_2^{3/2}}\right) \tag{3.6.15}$$

The plastic flow defined in terms of a plastic flow potential function, $g(\sigma_{ij}')$ is based on non-associative flow rule. This plastic flow is also a function of the effective stress tensor which is shown in Equation 3.6.16.

$$d\varepsilon^p = d\lambda \frac{\partial g(\sigma_{ij}')}{\partial \sigma_{ij}'} \tag{3.6.16}$$

In which $d\lambda$ and $d\varepsilon_p$ denote non-negative parameters which may vary throughout the loading history and the plastic strain increment, respectively. Here $\frac{\partial g}{\partial \sigma'_{ij}}$ represents plastic flow which may not necessarily be normal to the failure surface. For the preceding relationships, the conditions shown from Equations 3.6.17 to 3.6.19 hold.

$$F' \leq 0 \tag{3.6.17}$$

$$d\lambda \geq 0 \tag{3.6.18}$$

$$d\lambda F' = 0 \tag{3.6.19}$$

The expression of flow potential g is shown in Equation 3.6.20, when it is expressed in terms of Drucker-Prager hyperbolic function.

$$g = \sqrt{(mf_t . tan\psi)^2 + 3J_2'^2} - \frac{I_1'}{3} . tan\psi \tag{3.6.20}$$

In which, f_t, ψ and m are the uniaxial tensile strength of concrete, dilation angle, and the parameter m representing the eccentricity of the plastic potential surface, respectively. The method of Lee and Fenves is defined by Equation 3.6.21 [70].

$$d\varepsilon'^{p} = \begin{pmatrix} d\varepsilon_t^{"p} \\ d\varepsilon_c^{"p} \end{pmatrix} = \begin{bmatrix} r(\hat{\sigma}') & 0 & 0 \\ 0 & 0 & -\left(1 - r(\hat{\sigma}')\right) \end{bmatrix} . \begin{Bmatrix} d\hat{\varepsilon}_1 \\ d\hat{\varepsilon}_2 \\ d\hat{\varepsilon}_3 \end{Bmatrix} = \hat{h}(\hat{\sigma}, \hat{\varepsilon}^p) . d\hat{\varepsilon}^p \quad (3.6.21)$$

In which, the stress weight factor is represented by Equation 3.6.22.

$$r(\hat{\sigma}') = \frac{\frac{1}{2}\sum_{i=1}^{3}(|\hat{\sigma}_i'| + \hat{\sigma}_i')}{\sum_{i=1}^{3}|\hat{\sigma}_i'|} \quad (3.6.22)$$

Where $0 \leq r(\hat{\sigma}') \leq 1$. The corresponding yield condition can be expressed by Equation 3.6.23.

$$F' = \frac{1}{1-\alpha}\left(\sqrt{3J_2'} - \alpha I_1' + \beta\varepsilon^{"p}\,\hat{\sigma}'_{max} - \gamma\hat{\sigma}'_{min}\right) - \sigma_c'\,\hat{\varepsilon}_c'^{p} \leq 0 \quad (3.6.23)$$

Here α is represented by Equation 3.6.24 below.

$$\alpha = \frac{(f_{bo} - f_c)}{(2f_{bo} - f_c)} \quad (3.6.24)$$

In which, f_{bo} is the biaxial compressive strength with the ratio $\frac{f_{bo}}{f_c}$ which is often taken as 1.16, and β in Equation 3.6.24 is expressed by Equation 3.6.25.

$$\beta = \frac{\sigma_c'\left(\varepsilon_c^{"p}\right)}{\sigma_t'\left(\varepsilon_t^{"p}\right)}(1-\alpha) + (1+\alpha) \quad (3.6.25)$$

Where, σ_c' and σ_t' are effective compressive and tensile cohesive stresses, respectively. γ in Equation 3.6.23 is represented by Equation 3.6.26.

$$\gamma = \frac{3(f_{to} - f_{bo})}{(2f_{bo} - f_{to})} \quad (3.6.26)$$

In which, f_{to} is the triaxial compressive strength which is based on isotropic states of stress, like biaxial compressive strength. The values of α range over 0.08 to 0.12, and for γ the typical value is around 3 [61]. Equations 3.6.16, 3.6.20, 3.6.21, 3.6.23 were used

in modeling the behavior of concrete in this study. Schematics of a meridian of the yield surface and sectional view of octahedral plane are shown in Figure 3.6.2.

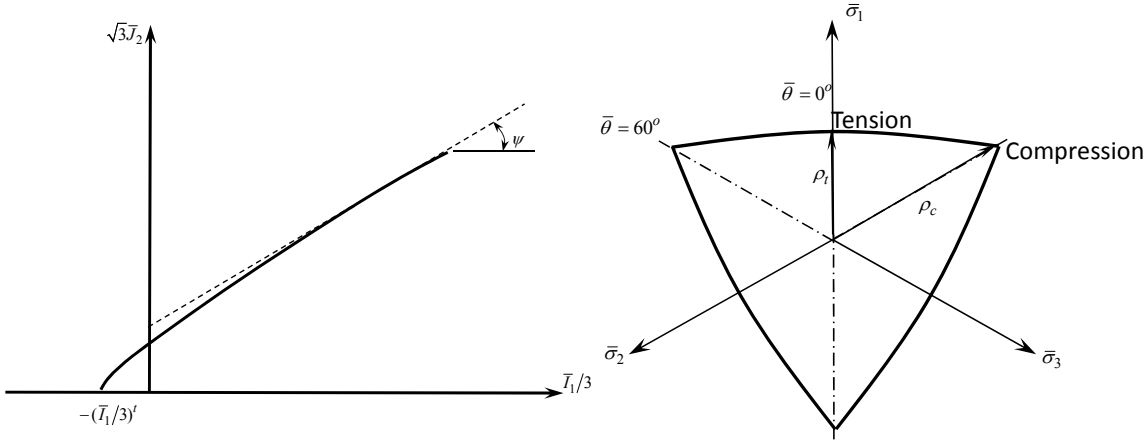

(a) Shape of failure surface meridian (b) Deviatoric section of the failure surface

Figure 3.6.2. Concrete failure surface.

The compressive behavior of concrete is represented by the stress-strain relationship of Hognestad which is shown in Figure 3.5.11 [68]. The ultimate compressive strength of concrete used during modeling was determined by using the concrete cylinder compression test data. The crushing strain of concrete was assumed as 0.003. Modulus of elasticity and tensile strength of concrete were calculated by using Equations 3.6.27 and 3.6.28, respectively based on the concrete compressive strength test data presented earlier in this chapter [66].

$$E_c = 4700\sqrt{f_c} \tag{3.6.27}$$

$$f_{ct} = 0.33\sqrt{f_c} \tag{3.6.28}$$

Tension stiffening effect in concrete is represented by using the built-in fracture energy cracking criterion module of Abaqus. Fracture energy of concrete is determined by conducting a regression analysis with the experimental data and the recommended values

in literature [61], [74], [75], [76]. Summary of the other plasticity parameters used for the plasticity-damage model of concrete is shown in Table 3.6-1.

Table 3.6-1. Plasticity parameters used for concrete material model.

Parameter	Value
Dilation Angle (ψ)	31°
Eccentricity ($_m$)	0.1
Ratio of initial equibiaxial compressive yield stress to initial uniaxial compressive yield stress (f_{bo}/f_c)	1.16
Ratio of the second stress invariant on the tensile meridian to the compressive meridian ($\rho_t/\rho_c = K_c$)	0.667
Viscosity Parameter (default – no effect)	0.001

The behavior of the reinforcing steel, prestressing strand and also the steel beams itself were defined as elastic-plastic using Mises yield surface to define isotropic yielding. The steel material models of the strands and rebars of the prestressed concrete and reinforced concrete models were based on PCI Design Handbook and experimental studies respectively [77], [78]. Material model of the steel beams are taken directly from the literature [79].

Since previous research showed no significant differences when using an isotropic or an orthotropic material model for the composite materials [80], the elastic-plastic isotropic material model is used for the composite patch like the rebar and the strand models. The material parameters used are gathered from the data available from the manufacturers and the data obtained from the experiments conducted for the purpose.

In both reinforced concrete and prestressed concrete beams, two phases are involved which are concrete and steel. Although there is only regular un-prestressed steel inside the reinforced concrete beams, there are two types of steel in prestressed concrete beams namely prestressing strands and secondary steel reinforcing rods. Properties of steel

can be assumed to be the same both in tension and in compression, unlike concrete. The approximations of bilinear or elastic-plastic variations are not uncommon for the stress-strain curve of the prestressing steel which does not have a well-defined yield point. The mechanism of mutual transfer of forces through the concrete-steel interface needs to be defined appropriately for defining the composite action between the two material surfaces accurately, for both reinforced concrete and prestressed concrete beams.

The main force transfer mechanisms between concrete and steel are adhesion, friction, and mechanical interlock action. Adhesion is generated by the chemical bonding of concrete to steel which also includes the effect of the stresses created during the hardening process. For steel with no indentations like ribs or surface roughness, adhesion and friction effects become important. Otherwise, mechanical locking action also comes into picture. In prestressed concrete beams, another force transfer mechanism also plays an important role during force transfer called the wedging effect. Wedging effect also called as "Hoyer effect" is caused by the tendency of the strand to return to its original size from the reduced diameter resulting from the initial pretensioning force (Figure 3.6.3).

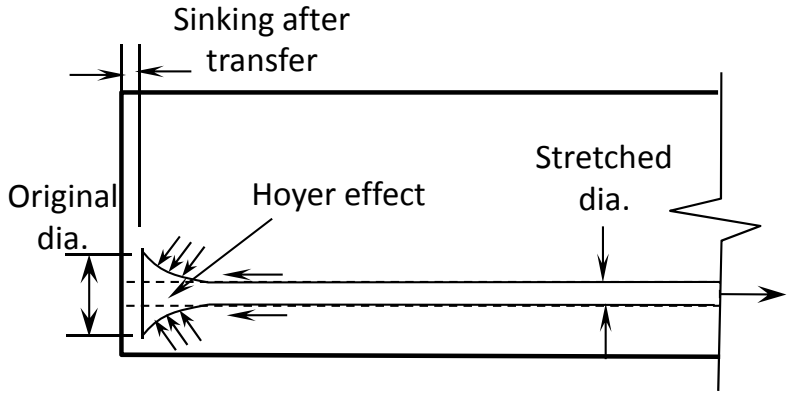

Figure 3.6.3. Wedging or "Hoyer" effect.

In this study, the combined effect of adhesion and mechanical interlock is taken into account by way of an idealized bond-slip behavior created by using interfacial spring elements of zero dimensions to transfer normal and tangential forces at concrete-steel interface. Linear behavior followed by stiffness degrading slippage, and complete separation can be assigned to these interfacial springs on the basis of pull-out test data undertaken for this purpose. Since the bond data in the literature is not suitable for direct use, bond parameters of the concrete-steel interface for the models were correlated on the basis of concrete strength and total interfacial contact area for both reinforced concrete and prestressed concrete beams [81]. The effect of friction was accounted for by using the corresponding friction-interaction module in Abaqus.

The linear part of the combined effect of adhesion and mechanical interlock bond effect between concrete and steel is modeled by using a cohesive behavior model. By taking cohesive behavior into account, effect of relative deformation between the concrete and the reinforcing rods or strands can be properly represented over the whole length of the beam. Stiffness degradation, slippage and complete separation between the two surfaces are modeled with the help of a damage behavior model. Damage behavior represents the degradation of the cohesive stiffness values of the interfacial springs after a critical bond stress or slippage displacement value is reached. Increased bond force between the reinforcing rods or strands and the concrete due to friction at the interface is represented by using a friction-governed tangential behavior. The pressure exerted on the strands or reinforcing rods by the concrete is variable over the length of the beam. The pressure values at the concrete-steel interface are higher at the parts of the beam which are close to end supports and at load points. Consequently, the friction values at the concrete-

steel interface are variable along the beam. This effect is taken into account accurately with the help of the friction-governed tangential behavior. By using a hard contact-normal behavior, penetration of concrete and steel surfaces into each other is prevented and also the necessary pressure field data for friction calculations is generated. Also, the "Hoyer" effect and Poisson radial expansion of the strand are automatically account for in the chosen model.

In several publications, researchers have incorrectly assumed perfect bond at concrete-steel interface. In this study, by using the combined effect of different types of Abaqus interaction sub-modules which were mentioned earlier, the true interfacial bond behavior between concrete and reinforcing rods or strands is fully accurately accounted for. A summary of the bond parameters used for the bond models of the rebars and strands in the prestressed concrete beam model is given in Tables 3.6-2 and 3.6-3, respectively.

Table 3.6-2. Bond parameters of rebar for prestressed concrete beam model.

Parameter	Value
Stiffness of interfacial spring elements (K)	108857lb/in
Coefficient of friction (k)	0.4
Normal behavior	Hard contact
Maximum separation for damage initiation	0.016537in
Total/Plastic displacement	1.00in
Damage evolution exponential parameter	4.3

Table 3.6-3. Bond parameters of strand for prestressed concrete beam model.

Parameter	Value
Stiffness of interfacial spring elements (K)	273427lb/in
Coefficient of friction (k)	0.4
Normal behavior	Hard contact
Maximum separation for damage initiation	0.016537in
Total/Plastic displacement	1.00in
Damage evolution exponential parameter	4.3

Behavior of the epoxy resin used for bonding the composite patch to the beam is modeled by following a similar but a simpler approach like the bond model between concrete and steel. Bond model for the epoxy is created based on the tensile and shear strength tests performed on the adhesives, presented in Appendix-F. The constitutive behavior of the epoxy layer was defined in terms of traction versus separation. Typically exponential traction-separation behaviour is shown in Figure 3.6.4, with t_n^0, δ_n^0 and δ_n^t representing traction, damage initiation separation and separation with complete bond failure in the normal and shear directions.

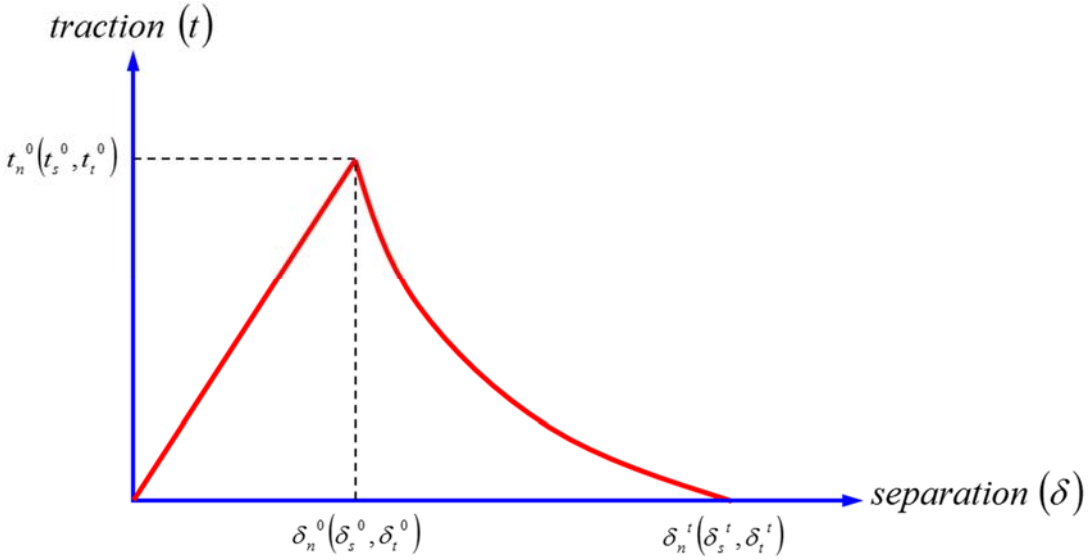

Figure 3.6.4. Exponential traction separation response [61].

The epoxy bond model assumes initially linear elastic behaviour following by the initiation and evolution of damage which was assumed to behave exponentially. Like the concrete-steel interface bond model, linear part of the bond model for the epoxy is represented by invoking the cohesive behavior. The degradation of the bond after damage initiation is represented by using damage behavior. A summary of the bond parameter

values for the epoxy SikaDur 30, which was used to bond Carbodur composite patches to reinforced concrete and prestressed concrete beams, is shown in Table 3.6-4.

Table 3.6-4. Bond parameters of the epoxy SikaDur 30.

Parameter	Value
Stiffness of interfacial spring elements (*K*)	345793lb/in
Maximum separation for damage initiation in normal direction	0.005401in
Total/Plastic displacement	0.005762in
Damage evolution exponential parameter	Linear

All beam models were created by using solid, linear 3D stress-displacement elements. Parent beam and composite patch model meshes were created using tetrahedron and hexahedron shaped elements. All beams were modeled as simply supported undergoing 4-point bending, simulating the experiments. The supports of the beams were modeled as strips of small areas but finite width instead of knife-edge contact line to avoid unrealistic concentration of stresses at such locations. The applied load transfer points were also treated likewise.

According to preliminary studies, effects of stirrups to the overall response of the reinforced concrete and prestressed concrete beams were found to be negligible in the elastic regime. However after the beams started undergoing plastic deformations, influence of stirrups became apparent. In addition, as all the stirrups used in test reinforced concrete and prestressed concrete beams did not form closed loops, little confining effect was expected. Consequently, stirrups were not included in reinforced concrete and prestressed concrete beam models.

3.6.3. Finite Element Modeling of Steel Beams

Based on the material and geometrical properties presented earlier in this chapter and by following the modeling procedures described, nonlinear finite element models of the steel beams were created. Although modeling steel beams was relatively straight-forward compared to reinforced concrete and prestressed concrete beams, all of the true mechanics of each structural component was allowed for during modeling. Details of the finite element mesh for all the steel beam models are given in Tables 3.6-5 to 3.6-8.

Table 3.6-5. Details of finite element mesh for the steel beam SBC.

Description of Item	Components of the Steel Beam and the Patch	
	Beam	Patch
Element Shape	Tetrahedron	-
Element Family	3D Stress	-
Element Type	C3D4: 4-node	-
Geo. Order	Linear	-
No. of Elements	39,416	-

Table 3.6-6. Details of finite element mesh for the steel beam SBI-p.

Description of Item	Components of the Steel Beam and the Patch	
	Beam	Patch
Element Shape	Tetrahedron	Hexahedron
Element Family	3D Stress	3D Stress
Element Type	C3D4: 4-node	C3D8R: 8-node
Geo. Order	Linear	Linear
No. of Elements	26,328	9,980

Table 3.6-7. Details of finite element mesh for the steel beam SBII-p.

Description of Item	Components of the Steel Beam and the Patch	
	Beam	Patch
Element Shape	Tetrahedron	Hexahedron
Element Family	3D Stress	3D Stress
Element Type	C3D4: 4-node	C3D8R: 8-node
Geo. Order	Linear	Linear
No. of Elements	29,412	29,700

Table 3.6-8. Details of finite element mesh for the steel beam SBIII-p.

Description of Item	Components of the Steel Beam and the Patch	
	Beam	Patch
Element Shape	Tetrahedron	Hexahedron
Element Family	3D Stress	3D Stress
Element Type	C3D4: 4-node	C3D8R: 8-node
Geo. Order	Linear	Linear
No. of Elements	9,453	78,833

The finite element model for the control steel beam (SBC) is shown in Figure 3.6.5. In Figure 3.6.6 the stress fringes (or, contours) of von Mises effective stress (S-Mises) and those for normal stress (S33) parallel to the axis of the beam are presented. Maximum stresses are concentrated around the mid-region of the beam as expected.

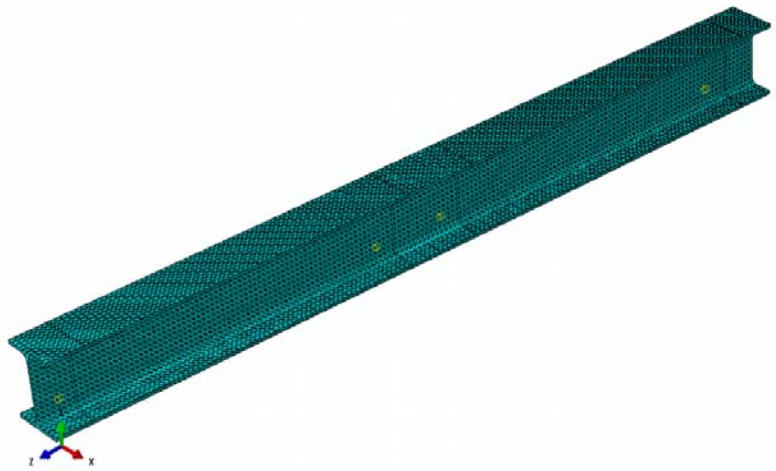

Figure 3.6.5. Finite element model for the steel control beam (SBC).

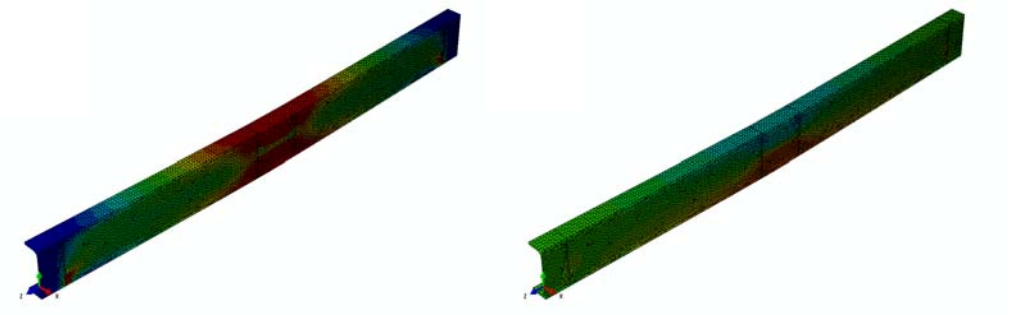

(a) Effective stress (b) Normal stress

Figure 3.6.6. Effective and normal stress fringes for the steel beam SBC at its ultimate limit state (Longitudinal sectional view).

Figure 3.6.7 shows the two views of the finite element model for steel beam SBI after patch repair (SBI-p) in which the bottom flange thickness was reduced to simulate corrosion. Von Mises effective stress fringes (or, contours) of the beam and the normal stress fringes parallel to the axis of the beam are shown in Figure 3.6.8. As can clearly be seen from these figures, stress concentrations at the mid-region of the beam is effectively reduced with the help of the proposed patch repair scheme.

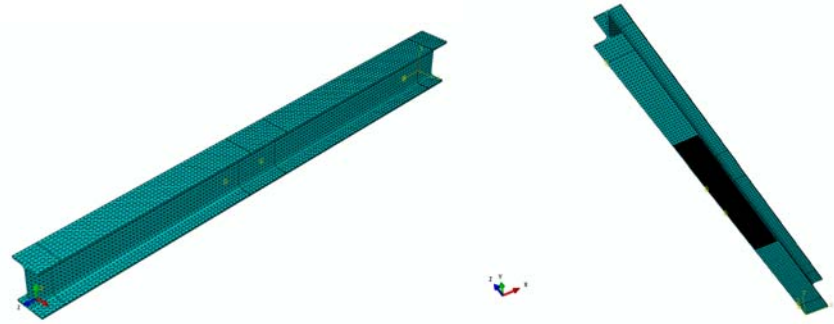

(a) General view (b) View showing bottom patch

Figure 3.6.7. Two views of finite element model for the steel beam SBI-p.

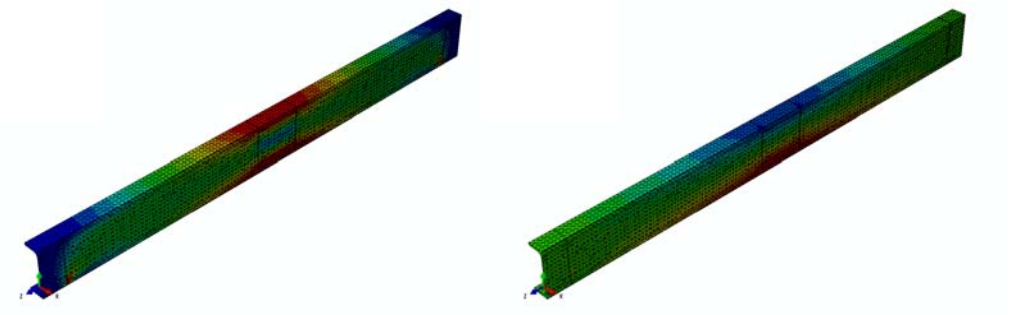

(a) Effective stress (b) Normal stress

Figure 3.6.8. Effective and normal stress fringes for the steel beam SBI-p at its ultimate limit state (Longitudinal sectional view).

Two views of the finite element model for steel beam SBII after patch repair (SBII-p), in which the web thickness was reduced to simulate corrosion, is shown in Figure 3.6.9. In Figure 3.6.10, von Mises effective stress fringes and normal stress fringes are presented. Like the specimen SBI-p, effective stresses at the mid-region of the beam SBII-p is also reduced thanks to the proposed FRP patch repair procedure.

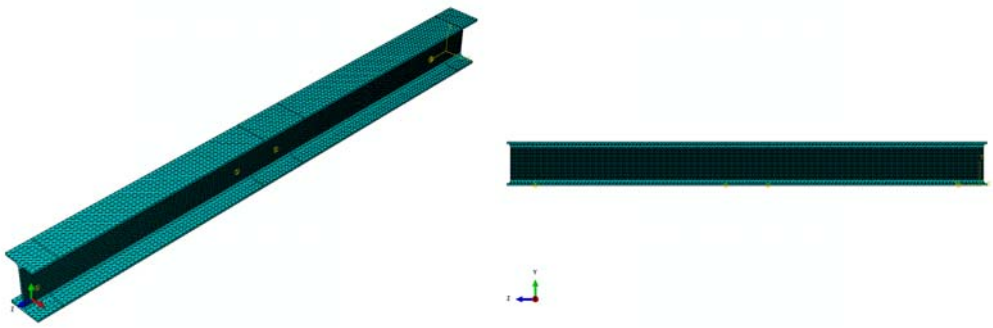

Figure 3.6.9. Two views of finite element model for steel beam SBII-p.

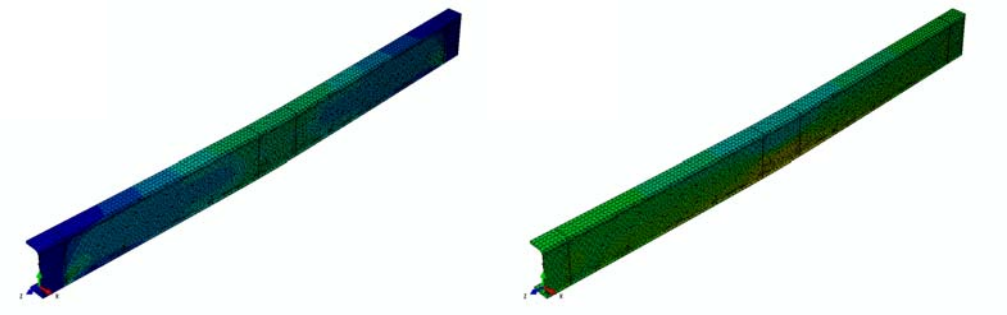

Figure 3.6.10. Effective stress and normal stress fringes for the steel beam SBII-p at its ultimate limit state (Longitudinal sectional view).

Two views of finite element model for steel beam SBIII after patch repair (SBIII-p), with web and bottom flange thickness loss, are presented in Figure 3.6.11. Figure 3.6.12 presents the stress fringes (or, contours) of von Mises effective stress and normal stress fringes parallel to the axis of the beam. With the help of the proposed patch repair scheme, stress concentrations around the mid-region of the beam SBIII-p is effectively reduced similar to the other repaired steel specimens SBI-p and SBII-p.

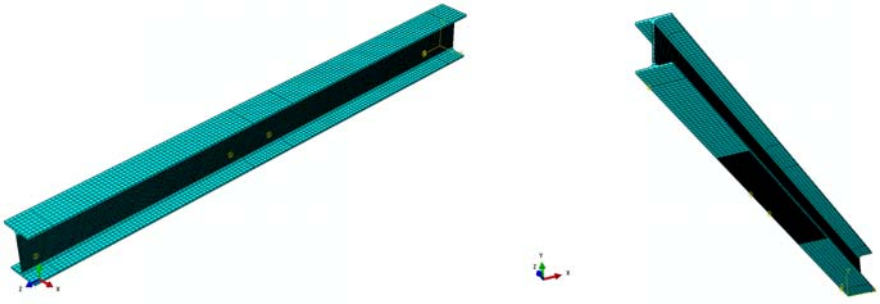

Figure 3.6.11. Finite element model for the steel beam SBIII-p.

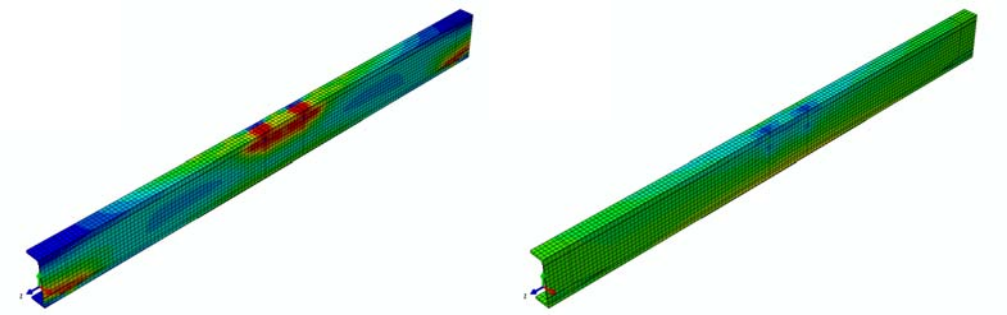

Figure 3.6.12. Effective normal stress fringes of the steel beam SBIII-p at limit state.

Applied load vs. central deflection response of all steel beams are plotted along with the mechanistic model results and corresponding experimental data in Figure 3.6.13. The close agreement between finite element analysis data, mechanistic model results and experimental observations is evident.

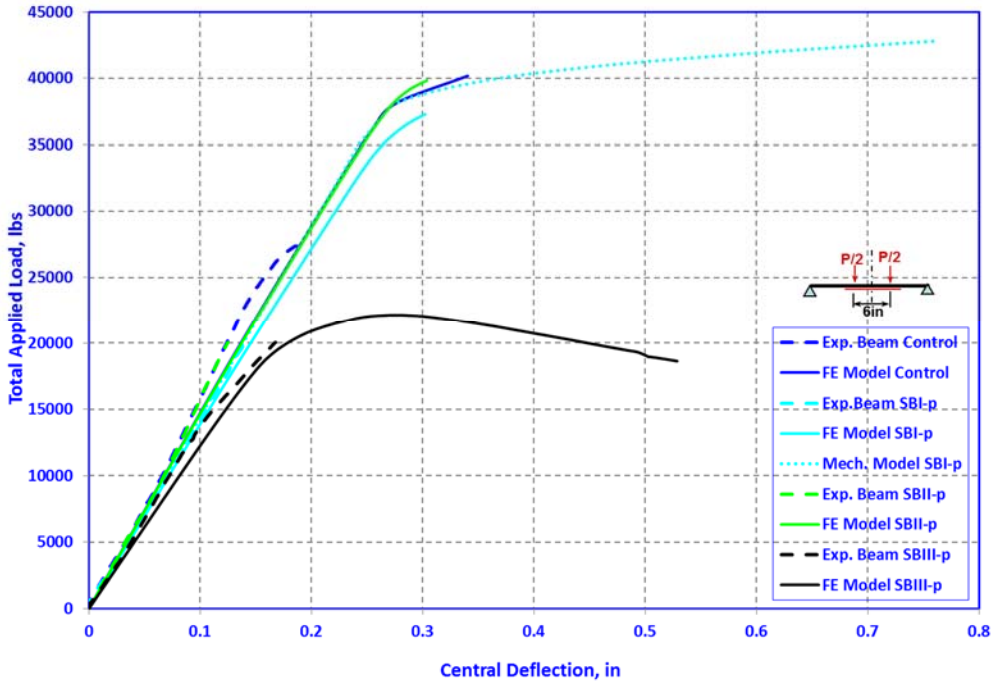

Figure 3.6.13. Load vs. central deflection plot for steel beams after repair.

Performance of Patch Repaired Steel Beam with Crack: In this case, the performance of the repaired beam corresponding to two limit states need to be assessed – (a) sectional moment and shear capacities, and (b) stress intensity factor which controls the fatigue life against brittle fracture. The focus of this part of investigation is, however, the determination of improvement of the stress intensity factor (say, K_I) after repair. In Linear Elastic Fracture Mechanics (LEFM) computations, the crack-tip plasticity is assumed to be confined to a small zone and brittle fracture assumption is valid. This is often governed by crack size as compared to other dimensions and material properties like yield strength, fracture toughness etc.

In 1968, Leibowitz and Sih [82] showed that the stress field near the crack tip at a body which is shown in Figure 3.6.14 can be expressed by Equation 3.6.29.

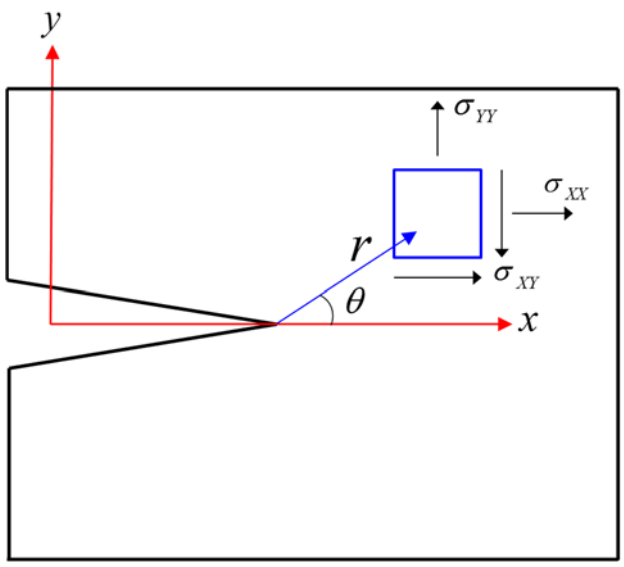

Figure 3.6.14. Crack in random body.

$$\sigma_{ij} = \frac{K_I}{\sqrt{2\pi r}} \cdot f_{ij}(\theta) \tag{3.6.29}$$

In which, σ_{ij} is the stress field at a distance r from crack tip at an angle θ. K_I and $f_{ij}(\theta)$ are the stress intensity factor for mode-I and the known functions of θ respectively. For $\theta = 0$, Equation 3.6.29 becomes Equation 3.6.30 below:

$$\sigma_{yy} = \frac{K_I}{\sqrt{2\pi r}} \tag{3.6.30}$$

LEFM predicts infinite stress at the crack tip which is not possible in real materials. There is a finite plastic zone at the crack tip that reaches the yield strength. As this plastic zone becomes larger, the elastic analysis becomes more inaccurate. Some corrections need to be made for moderate crack tip yielding for more accurate stress intensity factor predictions. By replacing the σ_{yy} in Equation 3.6.30 with the yield strength (σ_{YS}), size of that plastic zone around the crack tip can be estimated with Equation 3.6.31 for plane-stress conditions.

$$r_y = \frac{1}{2\pi}\left(\frac{K_I}{\sigma_{YS}}\right)^2 \tag{3.6.31}$$

Irwin proposed a crack size correction method to take into account the effects of moderate crack tip yielding during stress intensity factor predictions [83]. The effective crack length can be calculated by adding the size of the plastic zone to the size of the actual crack (Equation 3.6.32).

$$a_{eff} = a + r_y \tag{3.6.32}$$

The effective stress intensity factor can then be calculated by inserting the effective crack length in Equation 3.6.33.

$$K_{eff} = Y(a_{eff})\sigma\sqrt{\pi a_{eff}} \tag{3.6.33}$$

Since the geometry correction factor Y is dependent on the effective crack length a_{eff}, the following iterative procedure can be used to calculate effective stress intensity factor K_{eff} .

1- Stress intensity factor is determined in the absence of a plasticity correction.

2- The first order estimate of aeff is calculated with the help of Equation 3.6.32.

3- Effective stress intensity factor is calculated by inserting aeff into Equation 3.6.33.

4- New effective crack length is estimated with the Keff calculated in Step-3.

5- Iterations are repeated until effective stress intensity factor estimates converge.

For investigating the effect of patch repair on the stress intensity factor of a beam with a sharp crack, the cracked beam SB-1 considered during SHM is selected. Based on the methods presented in Section 3.3, the required size of bottom flange patch of two types is arrived at leading to the following three cases requiring modeling and simulation.

- SB-1 without patch repair.
- SB-1 repaired with Carbodur FRP patch.
- SB-1 repaired with Fibreglast FRP patch.

Two views of the finite element mesh around the cracked region, with and without web patch, for the steel beam SB-1 repaired with Fibreglast are presented in Figures 3.6.15 and 3.6.16, respectively. These finite element models are analyzed to determine the ultimate moment capacities, stress intensity factors (K) and J-integral values. Details of the finite element mesh for the steel beam model repaired with Carbodur, Fibreglast and unrepaired half-cracked steel beam are given in Tables 3.6-9, 3.6-10 and 3.6-11, respectively.

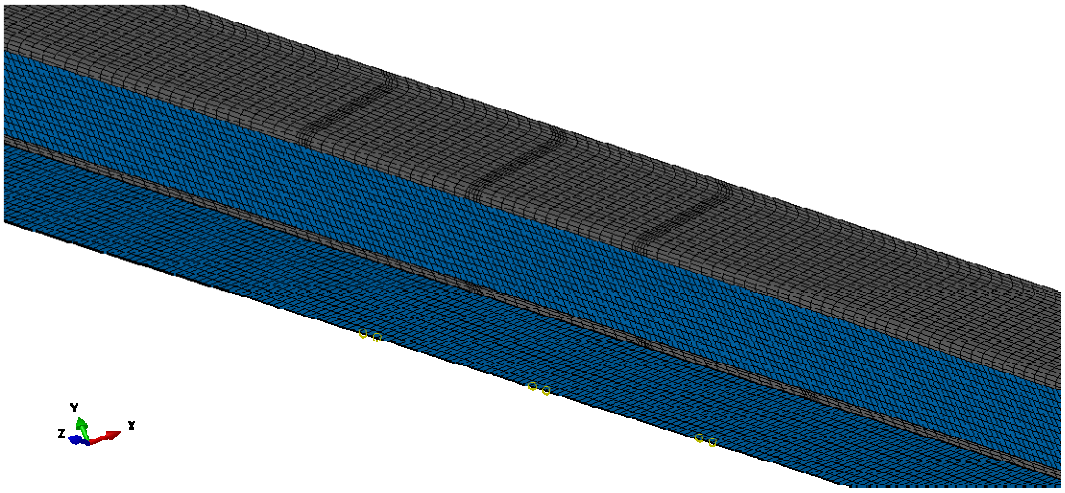

Figure 3.6.15. Finite element mesh for steel beam SB-1 around the crack with web patch (half-model, x-symmetry).

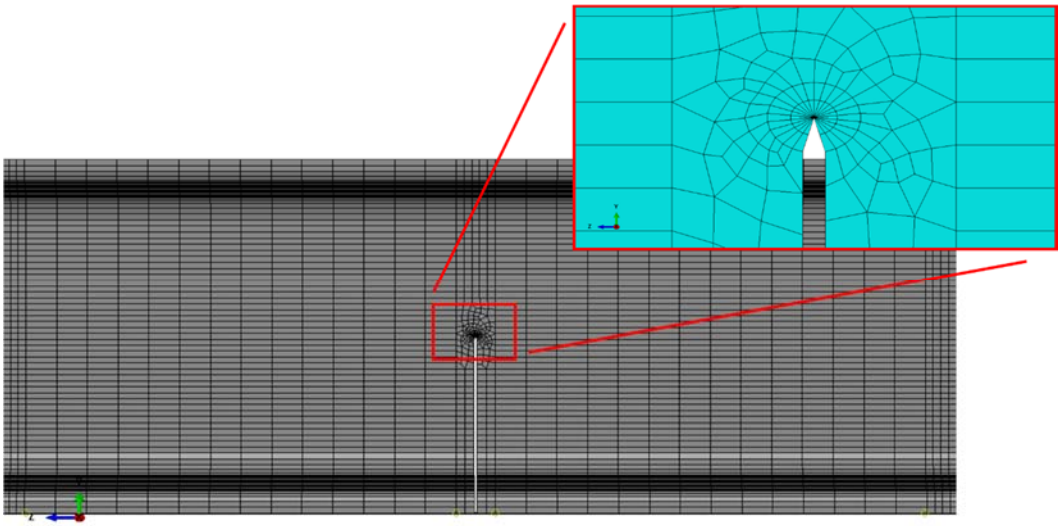

Figure 3.6.16. Finite element mesh for steel beam SB-1 around the crack without web patch.

Table 3.6-9. Details of finite element mesh for the steel beam SB-1 repaired with Carbodur.

Description of Item	Components of the Steel Beam and the Patch	
	Beam	Patch
Element Shape	Hexahedron	Hexahedron
Element Family	3D Stress	3D Stress
Element Type	C3D8R: 8-node	C3D8R: 8-node
Geo. Order	Linear	Linear
No. of Elements	264,864	7,360

Table 3.6-10. Details of finite element mesh for the steel beam SB-1 repaired with Fibreglast.

Description of Item	Components of the Steel Beam and the Patch	
	Beam	Patch
Element Shape	Hexahedron	Hexahedron
Element Family	3D Stress	3D Stress
Element Type	C3D8R: 8-node	C3D8R: 8-node
Geo. Order	Linear	Linear
No. of Elements	264,864	10,240

Table 3.6-11. Details of finite element mesh for the unrepaired half-cracked steel beam SB-1.

Description of Item	Components of the Steel Beam and the Patch	
	Beam	Patch
Element Shape	Hexahedron	-
Element Family	3D Stress	-
Element Type	C3D8R: 8-node	-
Geo. Order	Linear	-
No. of Elements	264,864	-

In this study, sizes of the plastic zones were directly measured from the finite element results. Calculated J-integral and stress intensity factor values for all the studied cases are summarized in Table 3.6-12. The plot of applied load vs. central deflection for cracked and repaired steel beam SB-1 is presented in Figure 3.6.17. Comparison of calculated stress intensity factor values with the fracture toughness curve of ASTM-A36

steel is shown in Figure 3.6.18 [84]. For all three cases, the effective (von Mises) stress fringes near the crack tip at their limit loads are shown in Figures 3.6.19 to 3.6.21.

Table 3.6-12. Calculated J-integral and stress intensity factor values for SB-1.

Condition	J-integral (psi.√inch)	Stress Intensity Factor (psi.inch)
Cracked (before repair)	53.6	41330
Repaired with Carbodur	3.6	10711
Repaired with Fibreglast	12.3	19798

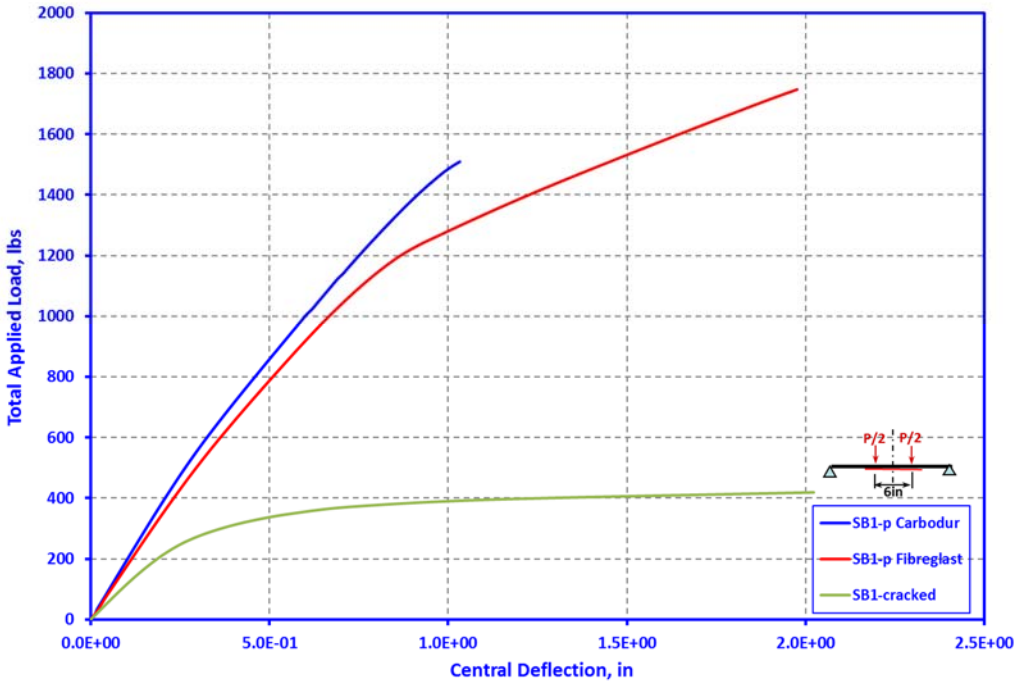

Figure 3.6.17. Applied load vs. central deflection plot of steel beam SB-1 before and after patch repair.

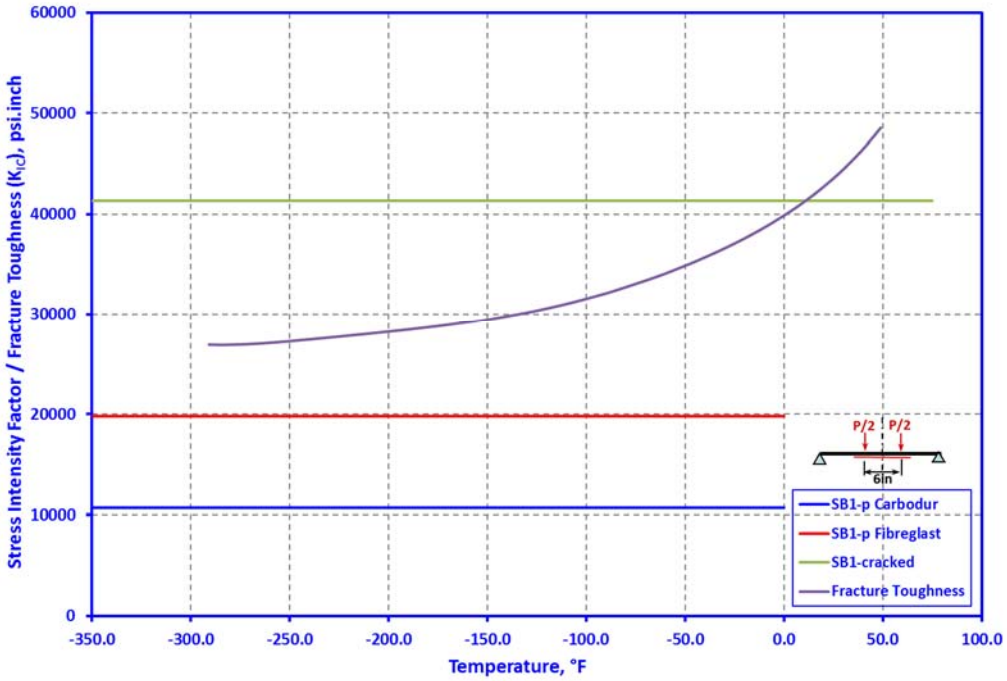

Figure 3.6.18. Comparison of fracture toughness curve of ASTM-A36 steel with calculated K values of steel beam SB-1 before and after patch repair.

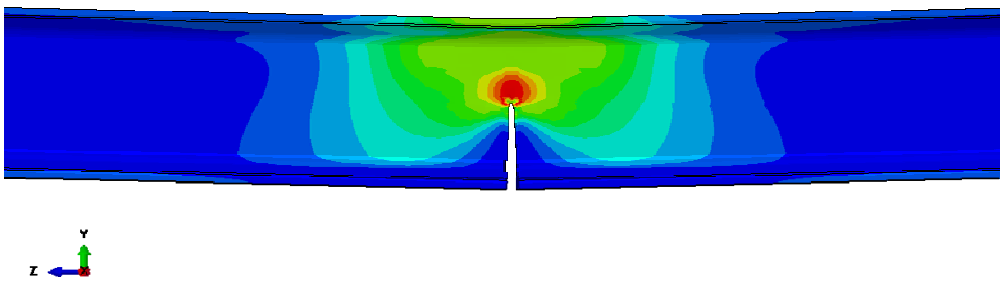

Figure 3.6.19. Effective (von Mises) stress fringes near the crack for the cracked steel beam at the limit load.

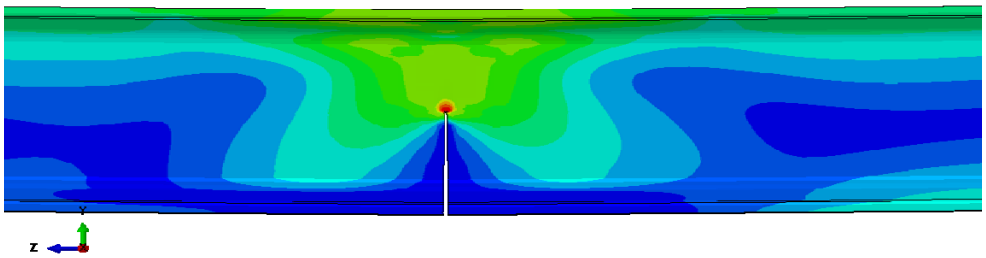

Figure 3.6.20. Effective (von Mises) stress fringes near the crack for the steel beam repaired with Carbodur at the limit load (patches are removed).

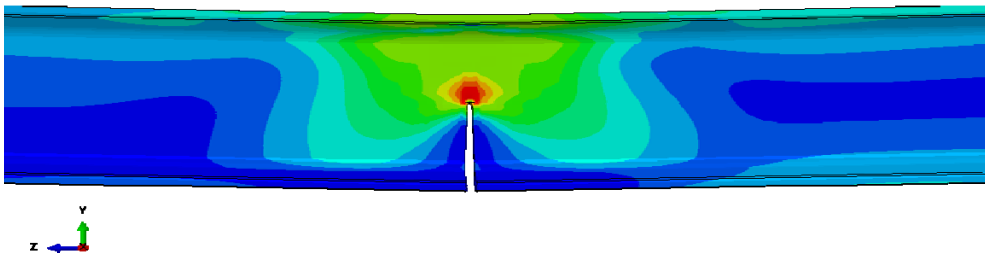

Figure 3.6.21. Effective (von Mises) stress fringes near the crack for the steel beam repaired with Fibreglast at the limit load (patches are removed).

As can be seen in Figure 3.6.17 the cracked steel beam has significantly lower limit strength but shows significant ductility. In the case of Carbodur patch repair, there is an increase in strength with respect to cracked case (360%) but there is significant loss of ductility. In the case of Fibreglast patch repair, there is significant gain in strength as compared to cracked beam (417%) and also the ductile behavior improves significantly compared to the beam repaired with Carbodur. Both of the repaired beams ultimately failed

due to the debonding of the composite patch. As can be seen in Figure 3.6.18, the proposed patch repair scheme also dropped the stress intensity factor values of the steel beam significantly, well below the fracture toughness value of the A36 steel. The unrepaired cracked steel beam on the other hand is highly susceptible to brittle fracture.

3.6.4. Finite Element Modeling of Reinforced Concrete Beams

As was seen in Section 3.6.2, finite element modeling of reinforced concrete beams is more involved than steel beams, due to the heterogeneous and anisotropic material characteristics and the need to account for complex concrete-steel interfacial properties. Details of the finite element mesh used is given in Table 3.6-13.

Table 3.6-13. Details of finite element mesh for the reinforced concrete beam I-p.

Description of Item	Components of the Reinforced Concrete Beam and the Patch			
	Beam	Bottom Rebar	Top Rebar	Patch
Element Shape	Tetrahedron	Tetrahedron	Tetrahedron	Hexahedron
Element Family	3D Stress	3D Stress	3D Stress	3D Stress
Element Type	C3D4	C3D4	C3D4	C3D8R
Geo. Order	Linear	Linear	Linear	Linear
No. of Elements	238,073	14,508	7,583	2,000

Two general views of the “flexural” reinforced concrete beam model after patch repair are shown in Figure 3.6.22. In Figure 3.6.23, plots of von Mises effective stress and longitudinal normal stress fringes are shown. A close-up view of limit state normal stress fringes near the patch repair region is shown in Figure 3.6.24. Widening of the crack due to patch deformation is noticeable.

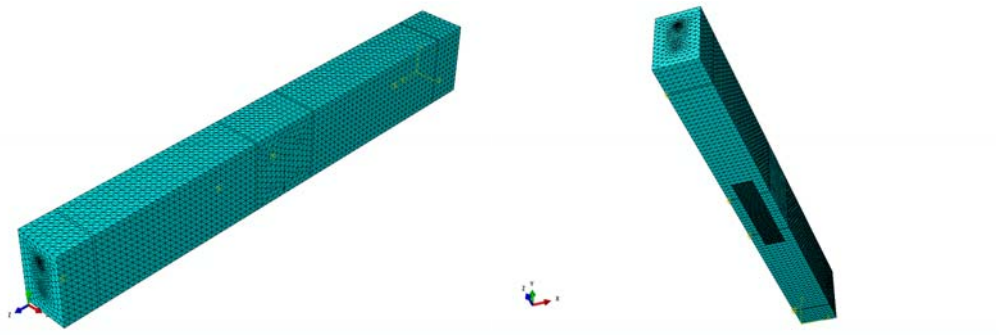

(a) General view (b) View showing patch

Figure 3.6.22. FE mesh for “flexural” reinforced concrete beam with patch-repair.

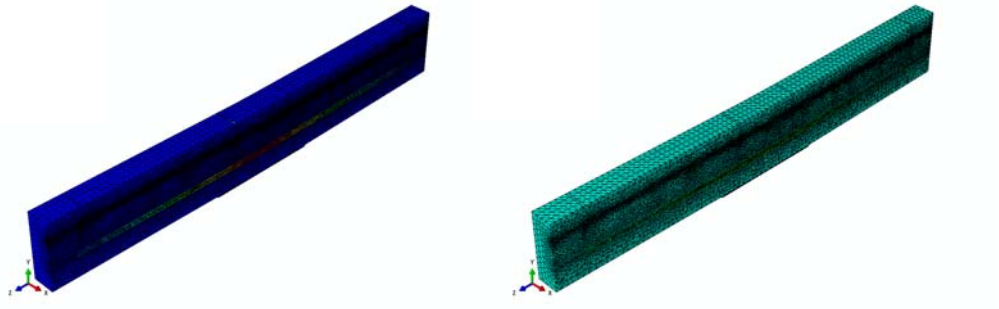

Figure 3.6.23. Limit state von Mises effective and longitudinal stress fringes of “flexural” reinforced concrete beam (Longitudinal sectional view).

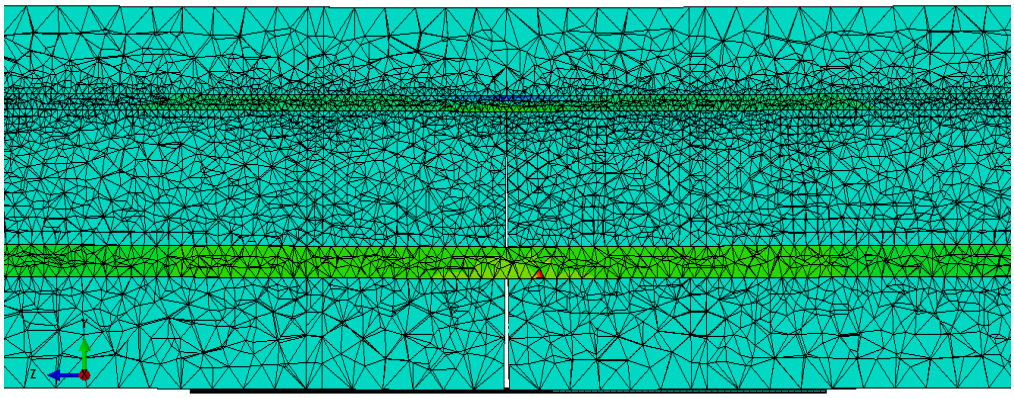

Figure 3.6.24. Close-up view of longitudinal normal stress fringes of the "flexural" reinforced concrete beam with widening crack in the patched region (Longitudinal sectional view)

In the case of "flexural" beam before patch repair, the predicted peak load capacity was 8,000lbs. The maximum central deflection, at the limit state, was 0.32". The corresponding top fiber concrete strain was 0.0079 and bottom steel strain was 0.0092, both at center of span. After patch repair to bottom flange at the crack location, the predicted peak load capacity was 5,750lbs. The maximum central deflection at the limit state was again 0.32". The corresponding top fiber concrete strain was 0.0095 and bottom steel strain was 0.024. It is evident that as per finite element predictions, the patch repair could not restore the full original predicted capacity and at the same time the beam appeared to be more ductile.

In Figure 3.6.25, the plot of applied load vs. central deflection curves based on finite element predictions for the "flexural" beam before and after repair is verified with experimental data. The experimental curves tend to follow the predictions pretty well

except at higher loads for which experimental data could not be shown because the test was discontinued after the formation of the first cracks in the case of original beam. In the case of patch repaired beam, the test was not continued up to complete collapse to avoid damage to LVDT and other sensors. The finite element simulations were, of course, continued up to the point of imminent collapse. The flatter slope of curves for crack-repaired beam shows loss of flexural stiffness caused by cracking of concrete but hardly any loss of ductility.

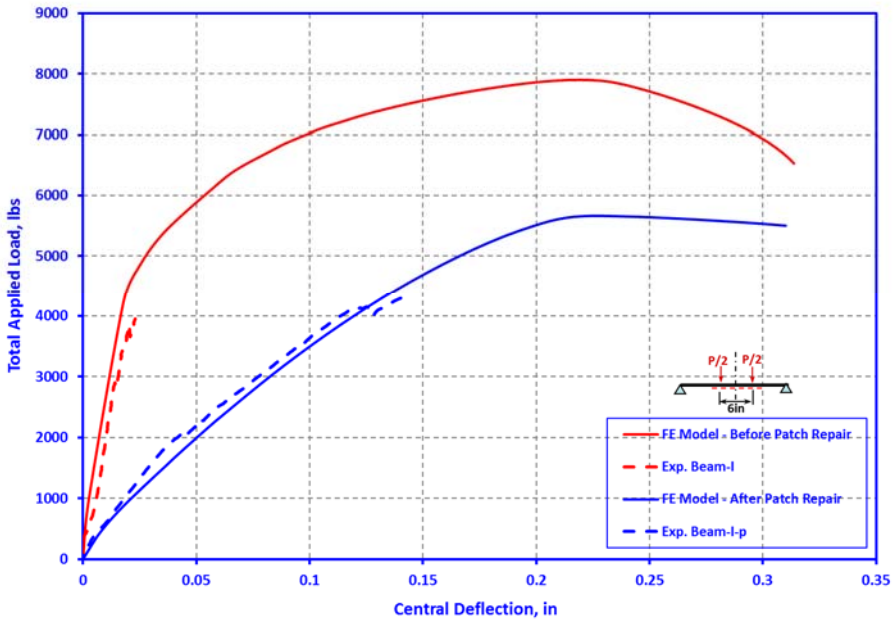

Figure 3.6.25. Validation of predictions with test data for “flexural” beam.

3.6.5. Finite Element Modeling of Prestressed Concrete Beams

The most complex modeling effort among the three types of test beams was with the prestressed concrete beam. The simulation involved multi-step analysis simulating the actual construction sequence of a real pretensioned concrete beam so that the real-life behavior of such beams could be faithfully reproduced. Details of the finite element mesh

for the prestressed concrete beam models before and after patch repair is given in Tables 3.6-14 and 3.6-15, respectively.

Table 3.6-14. Details of finite element mesh for the prestressed concrete beam PSCB3.

Description of Item	Components of the Prestressed Concrete Beam and the Patch			
	Beam	Bottom Strands	Top Rebars	Patch
Element Shape	Tetrahedron	Tetrahedron	Tetrahedron	-
Element Family	3D Stress	3D Stress	3D Stress	-
Element Type	C3D4	C3D4	C3D4	-
Geo. Order	Linear	Linear	Linear	-
No. of Elements	57,042	2,786	2,808	-

Table 3.6-15. Details of finite element mesh for the prestressed concrete beam PSCB2-p.

Description of Item	Components of the Prestressed Concrete Beam and the Patch			
	Beam	Bottom Strands	Top Rebars	Patch
Element Shape	Tetrahedron	Tetrahedron	Tetrahedron	Hexahedron
Element Family	3D Stress	3D Stress	3D Stress	3D Stress
Element Type	C3D4	C3D4	C3D4	C3D8R
Geo. Order	Linear	Linear	Linear	Linear
No. of Elements	57,042	2,786	2,808	420

To save computational effort, advantage was taken of symmetry, so that only one-half of a prestressed concrete beam needed modeling. The strands and reinforcing rods inside the beam were modeled as equivalent rectangular cross sections without affecting the mechanics of the system, so that the mesh shapes at the concrete-steel interface could be optimized, obviating the associated meshing problems. To faithfully follow the construction sequence, the analysis of the test prestressed concrete beam was undertaken in three steps.

Step 1: This step corresponds to the stage of initial prestressing of strands before pouring and hardening of concrete. The prestressing force is applied to the strands by

inducing an extension of 0.34” as boundary condition, without allowing for bonding of steel to concrete. The extension of 0.34” corresponds to a stress of 193.3 ksi. Also, a hard contact normal behavior only was defined at the concrete-steel interface, to prevent inter-penetration of concrete and steel meshes. No prestress have yet been induced to the concrete as shown in Figure 3.6.26 (a).

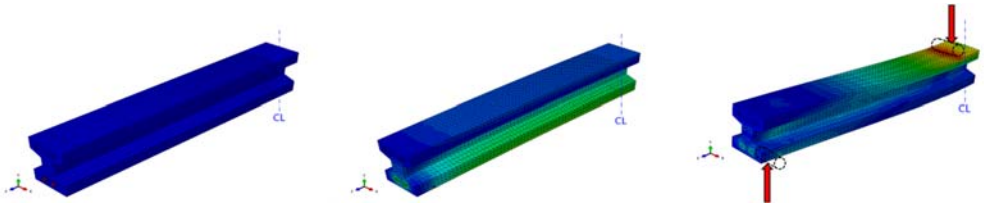

(a) No interfacial bond (b) Bond mobilized (c) External 4-point load

Figure 3.6.26. Stress fringes in simulation steps 1, 2 and 3.

Step 2: This step simulates the transfer of prestressing force after the concrete has gained strength. In this step the full bonded condition comprising of a hard contact normal behavior, a friction-governed tangential behavior, a cohesive behavior, and a damage behavior, is mobilized at the strand-concrete interface. This is followed by the removal of externally applied strand force used to cause extension. The prestress induced in the beam is evident from the stress fringes shown in Figure 3.6.26 (b).

Step 3: This step corresponds to the final working condition. In this step, external or operational loads are applied to the beam and the global response of the specimen is determined. Figure 3.6.26 (c) shows the stress fringes caused by 4-point bending load. Figure 3.6.27 (a) and (b) show the stress fringes of von Mises effective stress (S-Mises) at the end of the 2nd and 3rd steps before repair, respectively.

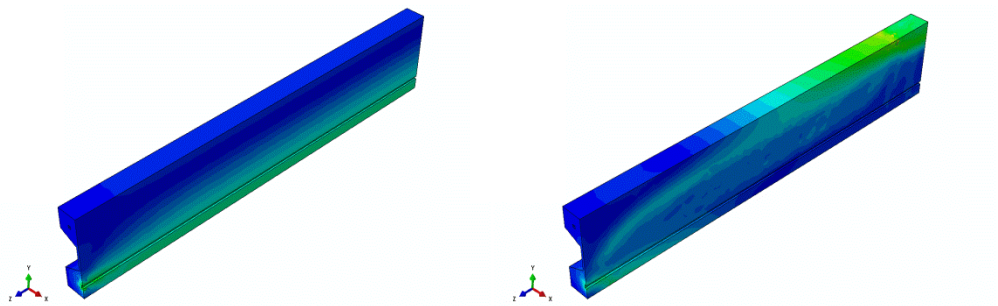

(a) End of 2nd Step (b) At limit state in 3rd step

Figure 3.6.27. Longitudinal sectional views with von Mises equivalent stress fringes.

The nature and magnitude of stress fringes for the original pretensioned beam shown in Figure 3.6.27 are consistent with analytical and experimental results. During the design process of a regular prestressed concrete beam, distribution of the effective bond stress is assumed to be linear. However, the actual variation of the effective bond stress between the concrete and the strand is hyperbolic [85]. Due to the slippage of the strand, the effective stress at the end-zone of the beam is very small which is evident from Figure 3.6.27(a). With increasing distance from the end of the beam, the effective stress around the strand keeps increasing until the full development length is realized. Variation of effective stress around strand between the end of the beam and the point where the strand stress gets fully developed appears to resemble a hyperbolic curve as reported in the published literature. After the beam is loaded externally in Step 3, the highest stresses are localized around the supports and load points as expected, which is evident from Figure 3.6.27(b). However, the stress-field around the strands caused by the prestressing force transferred to the concrete by the strands tended to remain unchanged.

During experimental studies, the most reliable data before patch repair was obtained from the prestressed concrete beam PSCB3. So, finite element modeling results for the prestressed concrete beam model before repair is compared with experimental data

from PSCB3. After composite patch repair, data from the beam PSCB1 could not be properly recorded due to data acquisition system problems. Also the specimen PSCB3 was accidentally loaded into the plastic range making it unsuitable for validating the finite element modeling results. Consequently, only finite element model of beam PSCB2 was generated and compared with experimental results after patch repair. Figure 3.6.28 shows the plots of applied load vs. central deflection for finite element modeling data, mechanistic model results and experimental observations for prestressed concrete beam PSCB3 before patch-repair. Likewise, similar plots for the same beam after patch repair are shown in Figure 3.6.29. In both cases, the numerically and mechanistically predicted response curves show excellent agreement with the experimental ones. Moreover, patch repair tended to increase the load capacity.

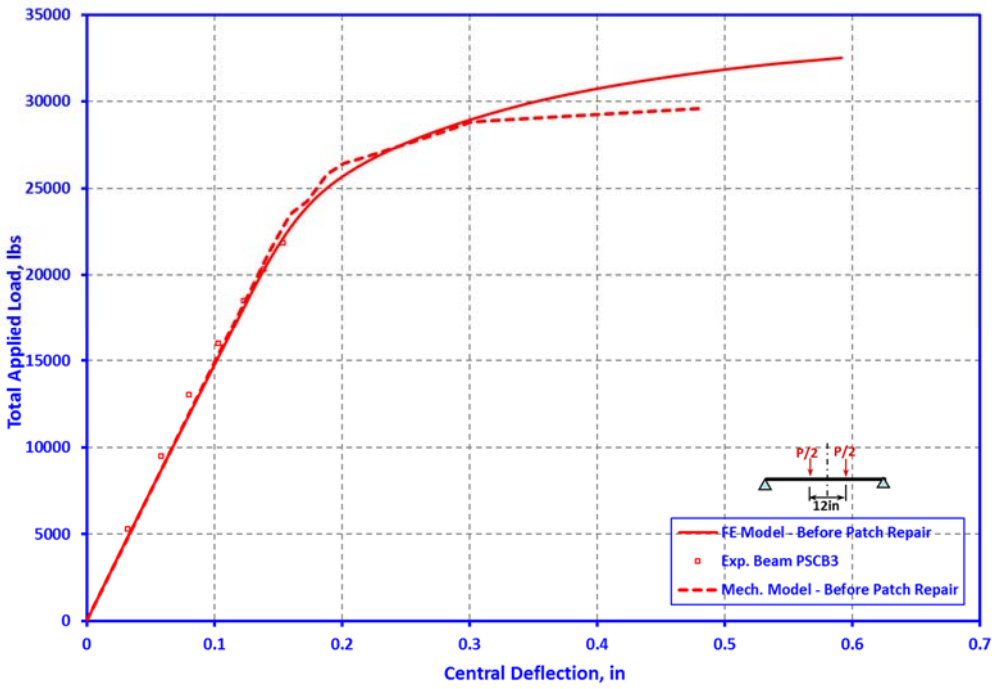

Figure 3.6.28. Load vs. central deflection plots for prestressed concrete beam PSCB3 before repair.

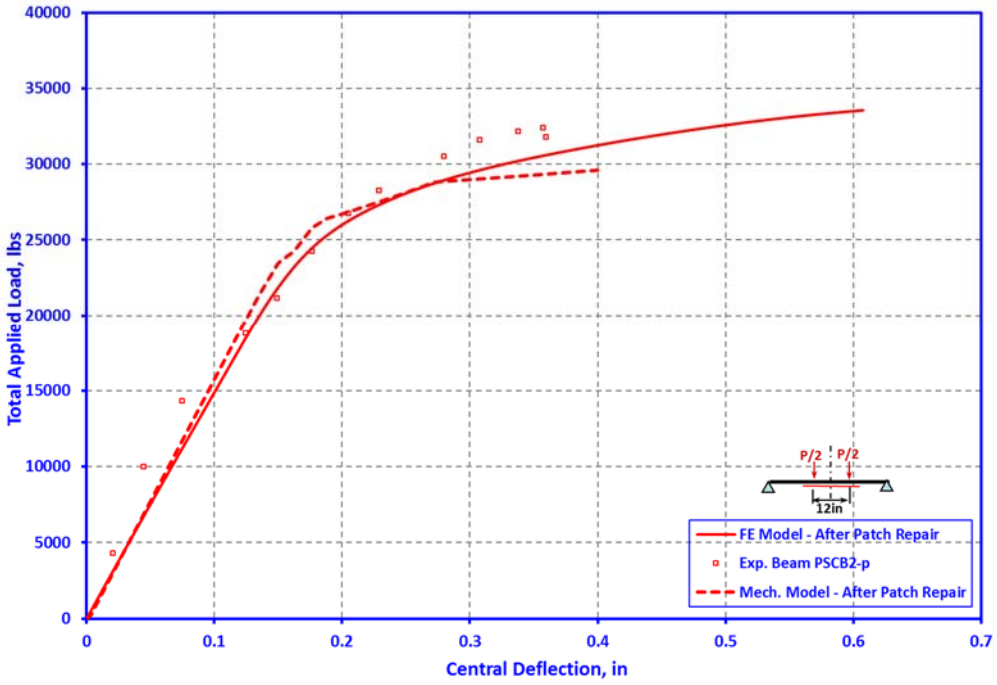

Figure 3.6.29. Load vs. central deflection plots for prestressed concrete beams PSCB2-p after repair.

In the proposed modeling scheme, all of the mechanisms that transfer the prestressing force from the strand to the concrete were faithfully reproduced. The first three of these mechanisms, which are adhesion, friction and mechanical interlock was taken into account by taking advantage of the bond behavior sub-modules of Abaqus. However, the last mechanism which is the wedging (or Hoyer) effect was automatically accounted for in the model without the need for any special treatment.

The variation of the diameter of the strand along the length of the beam at the end of the 2nd step is shown in Figure 3.6.30. From this figure, it is clear that the wedging effect is accounted for accurately in the proposed modeling scheme. This conclusion was further verified by examining the enlarged view of the predicted deformed shape of the strand near the end zone.

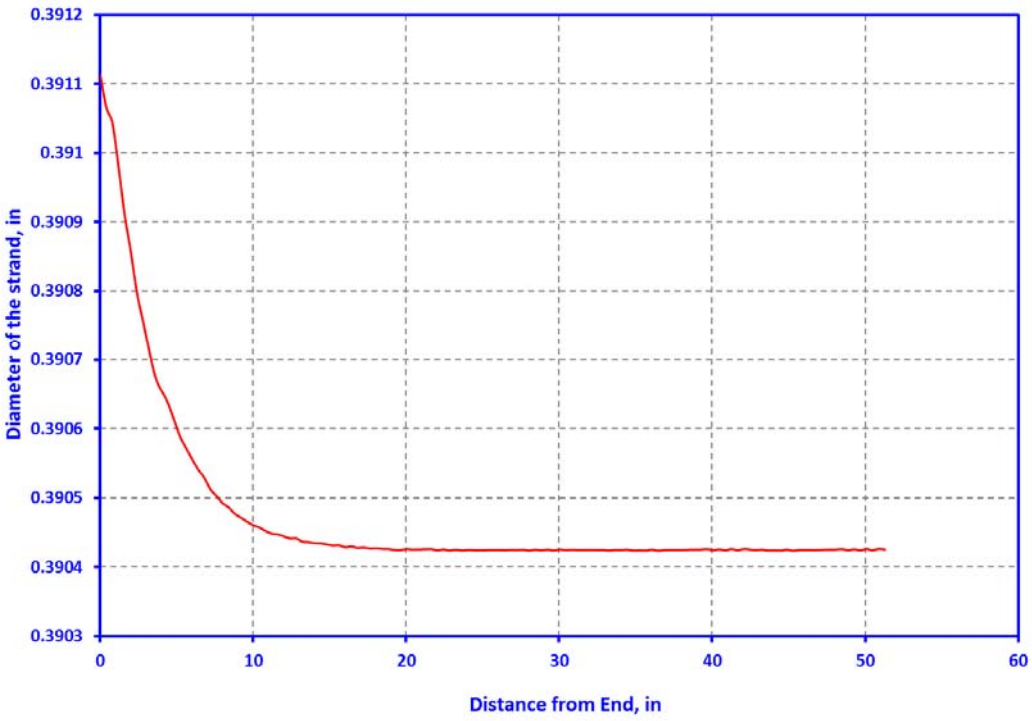

Figure 3.6.30. Variation of strand diameter along beam length in Step 2.

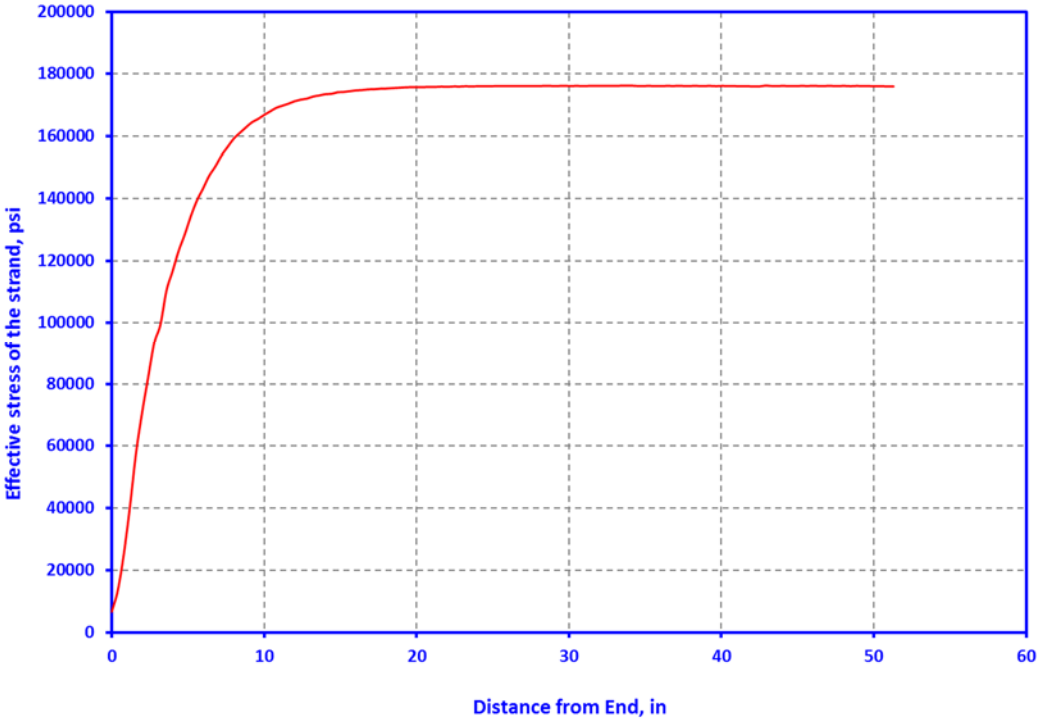

Figure 3.6.31. Variation of strand stress along beam length in Step 2.

One of the most important parameters, that characterizes the unique behavior of prestressed concrete beams, is the transfer length. This length can be defined as the distance from the end of the beam at which the effective stress of the strand is fully developed. The variation of effective strand stress along the length of the beam is shown in Figure 3.6.31. It is clear from this plot that the nature of stress transfer between strand and concrete is indeed hyperbolic. The corresponding variation of bond stress along beam length shown in Figure 3.6.32 also confirms this fact.

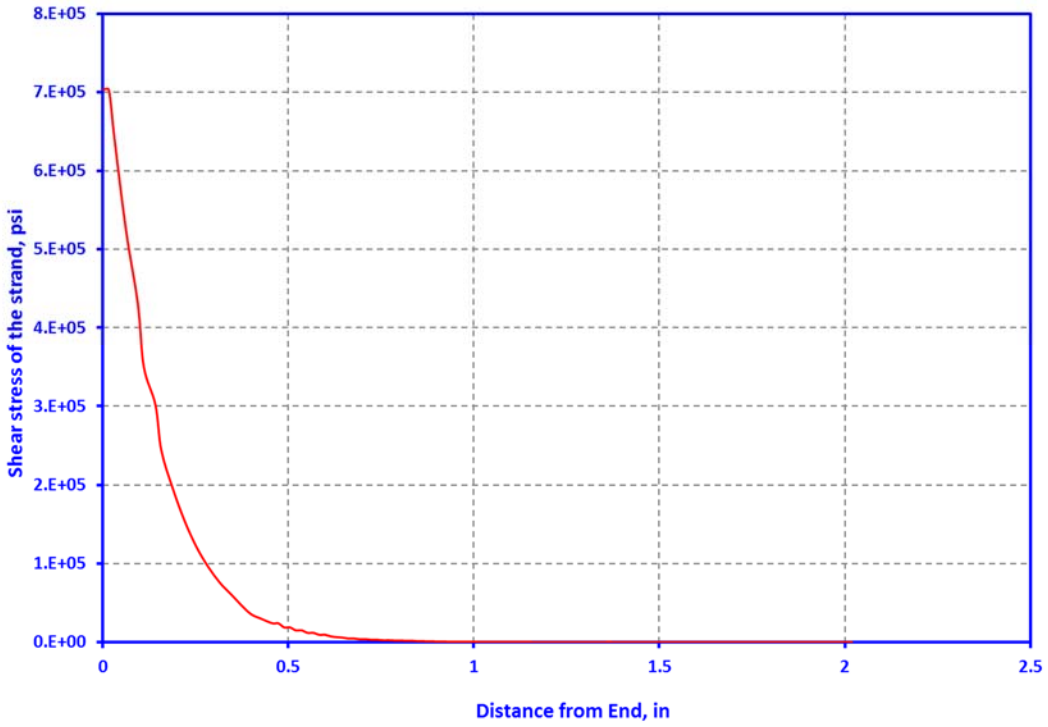

Figure 3.6.32. Bond shear stress variation along beam length at the end of Step 2.

The formation of cracks in a concrete beam can be monitored by observing the growth of plastic tensile strain [61]. Figure 3.6.35 shows the principal plastic tensile strains and their directions before and after patch repair of prestressed concrete beam PSCB2. In Figures 3.6.33 (a) and (b), cracks forming before and after patch repair during the load

testing of the beam are shown. In Figure 3.6.34, yellow lines depict the cracks that were formed before composite patch repair and the red lines indicate the ones forming after patch repair.

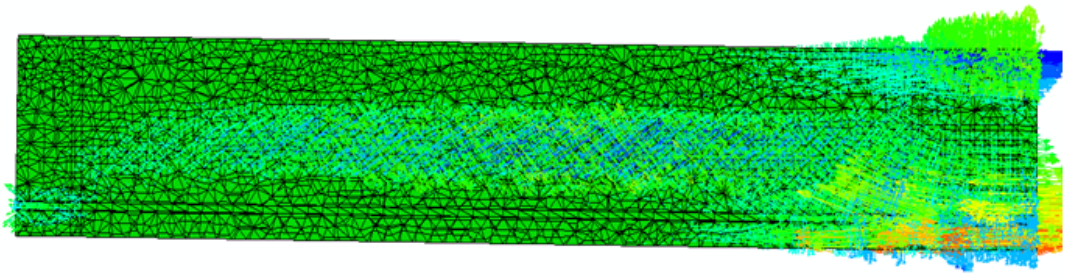

(a) Original beam – before patch repair

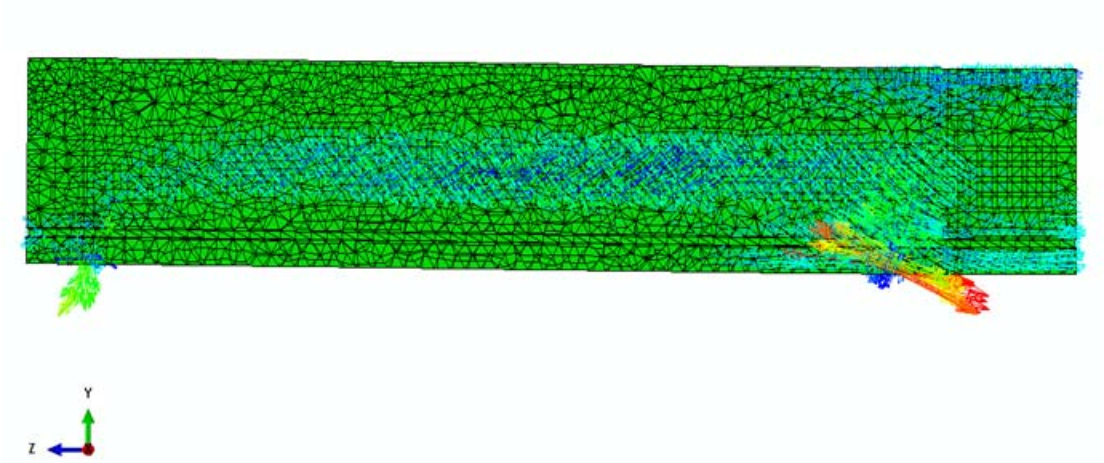

(b) Patch repaired beam

Figure 3.6.33. Principal plastic tensile strain directions at limit state.

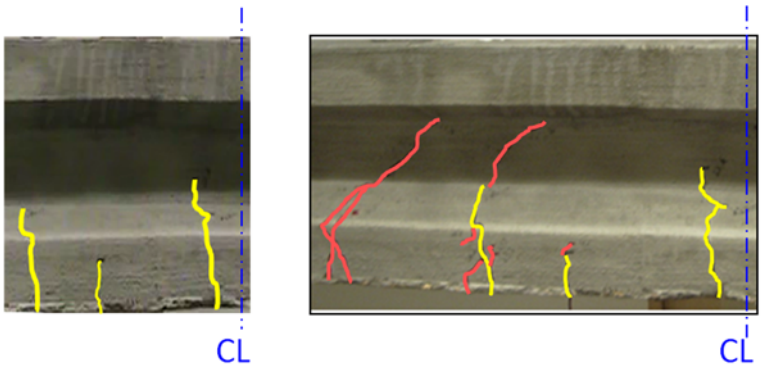

(a) Cracks formed before repair (b) Cracks formed after repair

Figure 3.6.34. Crack formation in PSCB2 before and after composite patch repair.

Beam PSCB2 cracked in flexure at the middle before repair and developed additional flexural cracks near the same location when loaded again after composite patch repair but at the limit state failed in shear near one of the supports. This can easily be explained by comparing the principal tensile strain trajectory plots shown in parts (a) and (b) of Figure 3.6.33. In Part (a), three flexural cracks at the middle of the beam can be identified and in Part (b), a small flexural crack at the middle repaired region of the beam and a major shear crack at the support can be identified. This can be verified by the experimental findings shown in Figure 3.6.34. The agreement between the experimental results and data obtained from finite element models are striking. This establishes the capability of the proposed modeling scheme to capture the actual behavior of a real prestressed concrete beam up to the limit state. Crack identification can also be simply based on just the magnitude of principal plastic tensile strains [71]. In Figure 3.6.35 principal plastic tensile strain contours for the beam PSCB2 is shown which agrees with the experimental results shown in Figure 3.6.34 confirming again what was stated earlier.

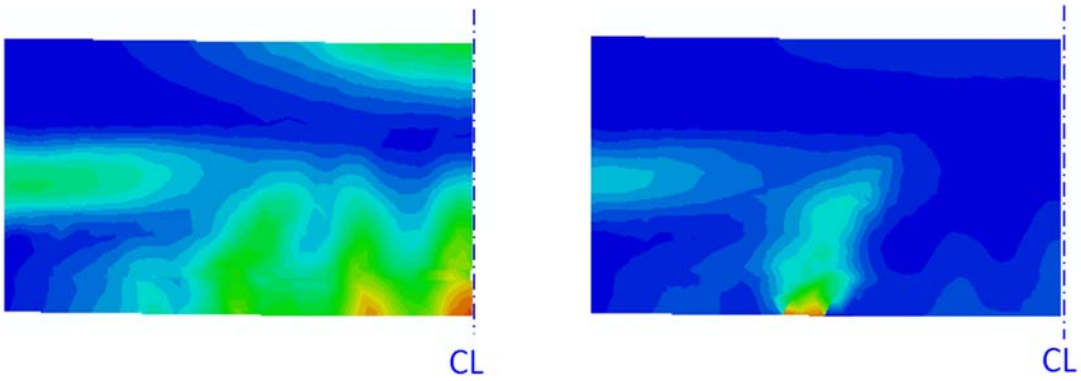

(a) Principal plastic strain plot before repair (b) Principal plastic strain plot after repair

Figure 3.6.35. Principal plastic strain plots before and after patch repair at limit state.

3.6.6. Evaluation of Recently Published Modeling Attempts for PSC Beams

The problems presented in references Ayoub et al. [86], Arab et al. [87], and Okumus, et al. [88] were simulated by the author again using the proposed finite element modeling scheme. By a comparison of the performance of the present model and the models presented in the cited references, it is not difficult to conclude that the finite element models used in references 86, 87 and 88 were relatively crude and yielded inaccurate results. The proposed method shows excellent agreement with the relevant experimental data for these three problems proving that the presented modeling technique can faithfully capture the real behavior of a wide variety of prestressed concrete structures. Problems considered in these studies are modeled and simulated by using the proposed finite element modeling scheme. The results obtained with the current model were compared with the numerical results presented in the referred studies and experimental data used therein, to show the superiority of the proposed modeling scheme over the existing attempts.

Problem of Reference 86: This reference presents attempts of Ayoub and Filippou to model a prestressed concrete beam by using a mixed formulation based model with the help of the general purpose Finite Element Analysis Program (FEAP) [89]. The model presented in this study is mainly composed of three main components:

- Fiber beam-column element which represents the behavior of concrete and embedded reinforcement.
- 1D truss element for representing the prestressing tendon.
- Bond elements placed at the nodal locations for transferring the interfacial forces between concrete and prestressing strand.

The presented model has questionable validity due to some of the assumptions made in the study. First, 1D representation of the prestressing strands is far from representing the real behavior of a pretensioning tendon. With this assumption, one of the most important force transfer mechanisms of the prestressed concrete beams at the steel-concrete interface is ignored which is the wedging effect (Figure 3.6.3). Wedging effect or Hoyer effect is 3D in nature and with a 1D strand representation, it is impossible to capture that phenomenon. Additionally, the model presented in this study ignores the effects of cracking and tension stiffening.

After defining all the material and bond properties appropriately, a finite element model of the problem presented in reference 86 was created by using the proposed modeling technique. The results of the present model are then compared with the experimental work of Mitchell [90]. All the material and geometric properties of the prestressed concrete beam problem were taken from the associated publications [86], [90]. The general mesh configuration and effective stress fringes of the present finite element

model of the problem are shown in Figures 3.6.36 and 3.6.37, respectively. As can be seen in Figure 3.6.36, all components of the present problem are characterized in the 3D domain. The model of reference 86 however, represented the tendons for the same problem in 1D, which can at best be a gross approximation of real life behavior. Additionally, the effects of cracking and tension stiffening in concrete were not properly represented.

The present finite element model of the problem of reference 86 reached its limit state at the maximum moment of 34.3 ft-kip. As can be seen in Figure 3.6.38, the present finite element model shows excellent agreement with the experimental data. On the other hand, the accuracy of the numerical results presented in reference 86 is less at locations closer to the middle of the beam. Especially near the middle of the beam, the finite element modeling results of reference 86 is almost 50% of the experimental data. Additionally, important data like crack locations of the beam cannot be extracted by the model of reference 86. Locations of the cracks are estimated by comparing the calculated strain values in the concrete with the assumed cracking strain of model of reference 86. On the other hand, the present finite element model also gives accurate prediction of crack locations in the beam. Hyperbolic variation of strand stress near the beam end after the release of strands is characterized by the pattern of stress fringes shown in Figure 3.6.37, proving that the true mechanics of the stress transfer is accounted for in the present model.

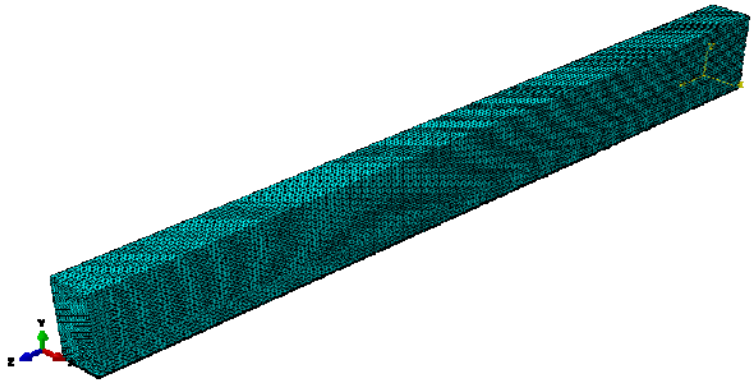

Figure 3.6.36. FE mesh for (1/4th) of the beam of problem presented in reference 86.

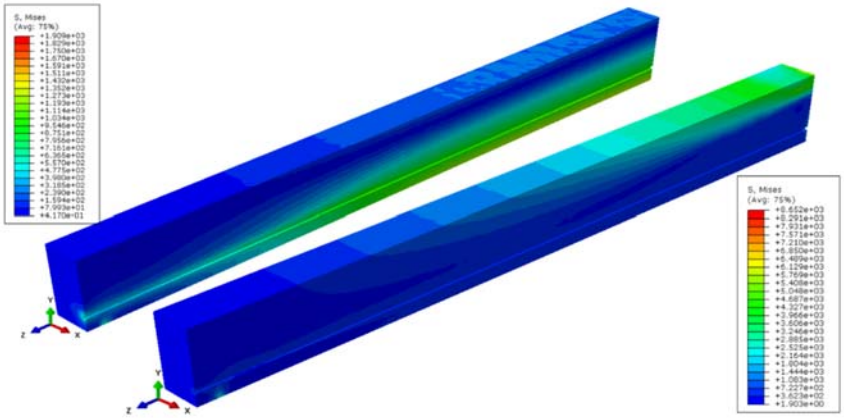

Figure 3.6.37. Equivalent stress fringes at transfer (Left) and limit state (Right), problem presented in reference 86.

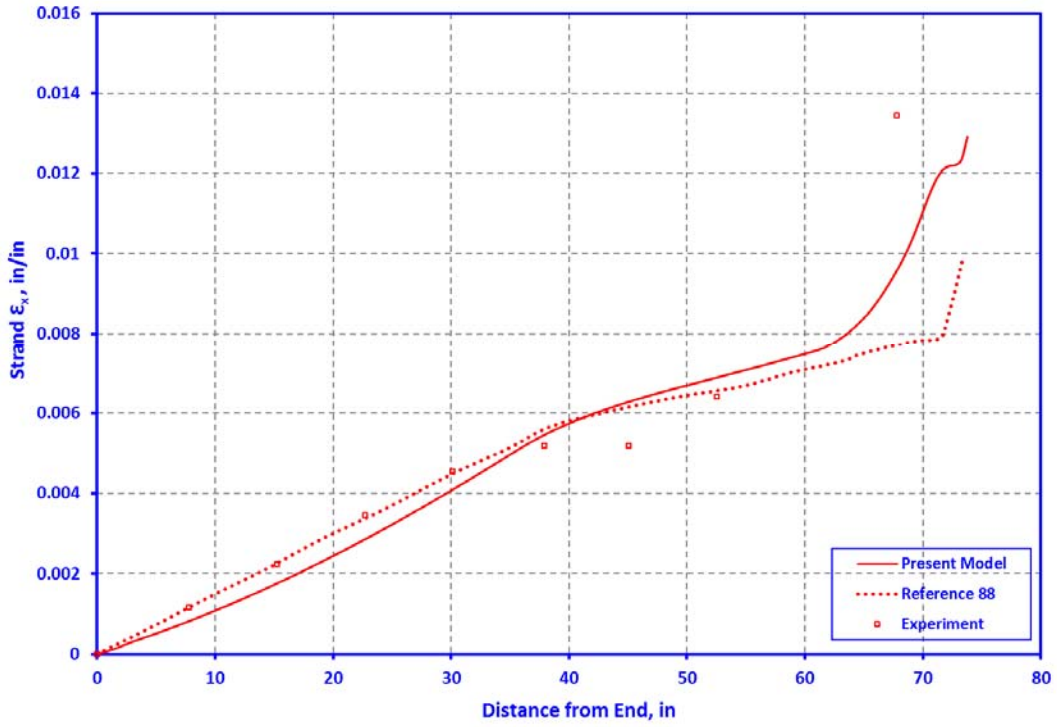

Figure 3.6.38. Plot of effective strand strain variation along the beam length for the problem of reference 86.

***Problem of Reference 87*:** Here, Arab et al. used the commercial finite element software package Abaqus to model a prestressed concrete beam. The concrete material was represented by using the Concrete Damaged Plasticity (CDP) model available in Abaqus. The interaction at the steel-concrete interface was represented by trying two idealization methods based on – (a) extrusion approach and (b) embedment approach. After appropriately defining the material and bond properties, the proposed modeling technique was applied to the test problem and the results are compared with the experimental data of Akhnoukh [91]. In reference 87 and Akhnoukh's [91] studies, results are presented for different stirrup configurations. As negligible difference in the preliminary results of the present simulation was noted for cases with and without stirrup, the stirrups were taken out

of the subsequent simulations. The finite element model used (on right) and the equivalent stress fringes (on left) are shown in Figure 3.6.39.

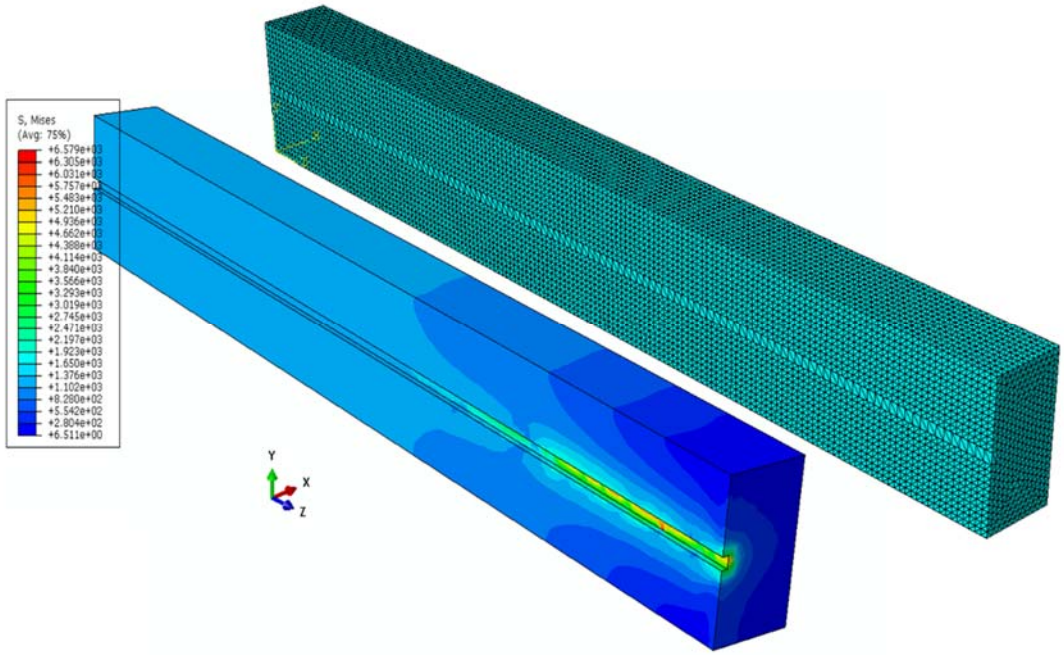

Figure 3.6.39. Equivalent stress fringes (Left) and general mesh configuration (Right), of the finite element model ($1/4^{th}$) of the problem of reference 87.

As stated before, reference 87 results are qualitative and hence could not be compared with. On the other hand, the experimental data used in reference 87 was found to be almost two orders of magnitude larger than what was obtained by the present model and also verified by simple hand calculations. Plots of variation of side strain of the beam with respect to the beam length along with the hand calculated value are presented in Figure 3.6.40. Consequently, the results from these references could not be relied upon.

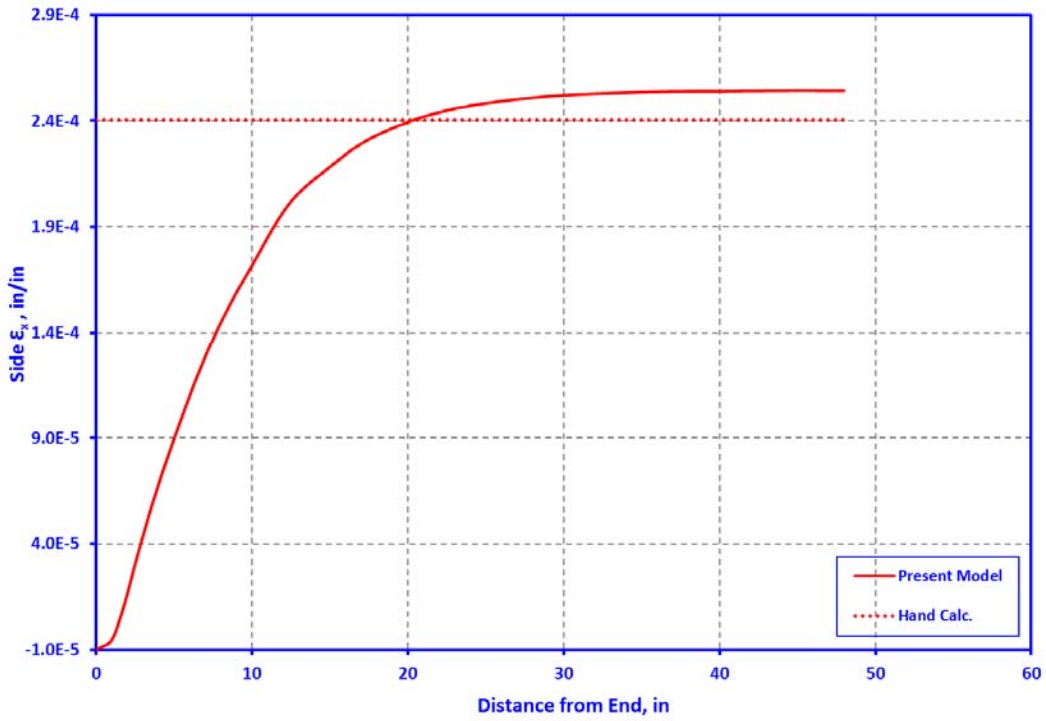

Figure 3.6.40. Variation of side strain vs distance from end of the beam for the finite element model of the problem of reference 87.

Problem of Reference 88: The assumptions made in this reference is mostly unreasonable and overly simplistic which cause the finite element model of reference 88 to fail to capture the real behavior of the corresponding prestressed concrete beam problem. After a similar treatment of the problem of this reference as in the other two cases, the prestressed concrete finite element model of this problem based on the proposed scheme was created and simulated. Thereafter, the results were compared with the experimental work of O'Callaghan [92]. As mentioned before, since modeling of stirrups did not make any difference in the results, the stirrups have been disregarded during the present modeling process. All the associated material and geometric information for the prestressed concrete beam problem were taken from [88] and [92]. The general view of the finite element model

can be seen in Figure 3.6.41. As there was no bond property information or test data available corresponding to the strand-concrete bond in the study of O'Callaghan [88], the model of this problem was created with bond properties calculated indirectly on the basis of concrete strength. The comparison of strain values of one of the strands obtained by the present finite element model and the experimental work of O'Callaghan is shown in Figure 3.6.42.

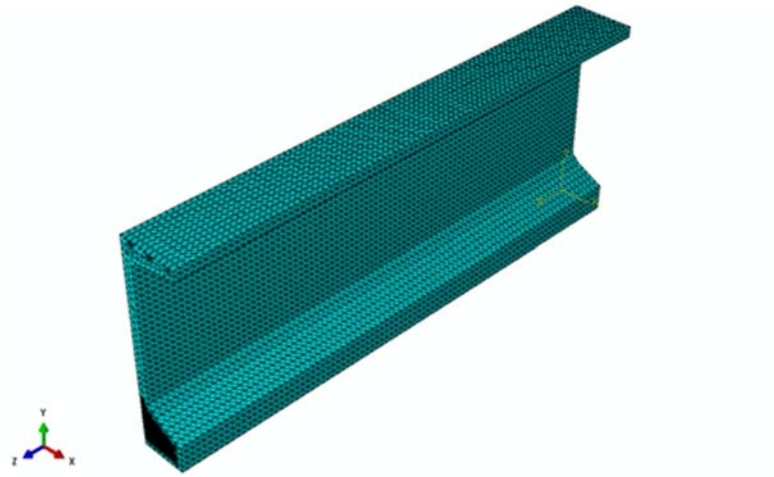

Figure 3.6.41. FE mesh of 1/4th beam of the problem of reference 88.

Since prestressing strands are not physically present in the model of reference 88, the data shown in Figure 3.6.42 could not be obtained by Okumus's model. As a result, the strand stress values obtained from the present finite element model have only been compared with O'Callaghan's experimental data. Curiously, in reference 88, the only data that has been compared with O'Callaghan's experimental work is the stresses in the stirrups.

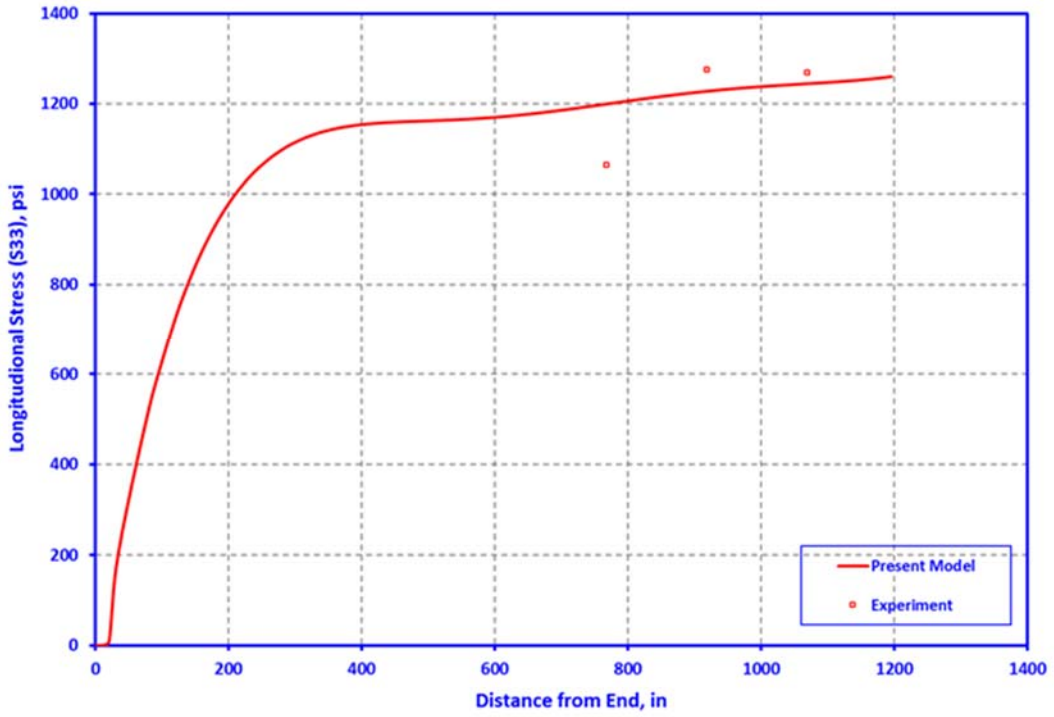

Figure 3.6.42. Plot of longitudinal stress (S33) of the strand "R8C7" vs distance for the problem of reference 88.

Figure 3.6.43 shows von Mises equivalent stress fringes of the problem of reference 88 based on the present model after the release of the strands. Plot shown in Figure 3.6.43 confirms the appropriate representation of the nature of force transfer between the strands and the concrete, which varies hyperbolically along the strand length. Figure 3.6.44 compares the experimentally observed cracks with the plots of maximum principal plastic strain fringes and the principal plastic tensile strain directions based on the proposed model after the release of the strands. It is obvious from this figure that good agreement exists between the actual behavior of the beam and predictions of the present finite element model. In contrast, only the principal strain directions of the total strain are plotted in reference 88. As far as crack formation in concrete is concerned, the consideration of total

strain does not mean much. The principal plastic tensile strain directions, as presented in Figure 3.6.44, make much more sense.

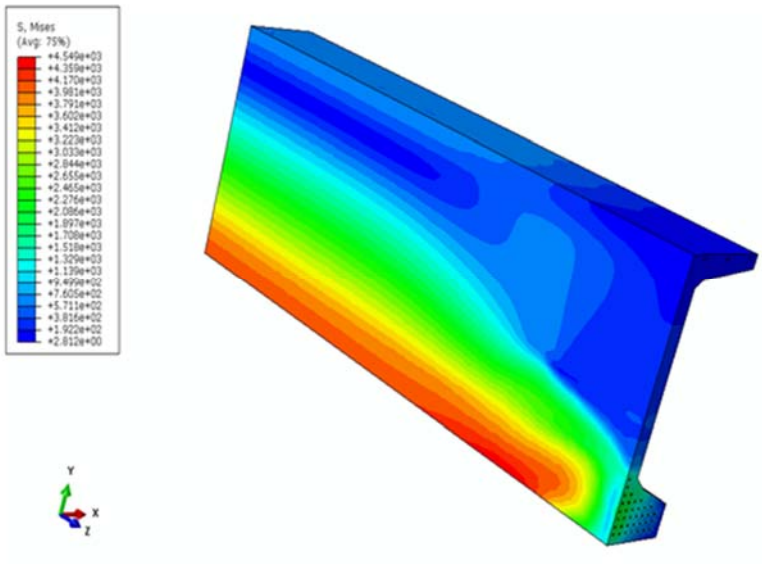

Figure 3.6.43. Equivalent stress fringes of problem of reference 88 after transfer.

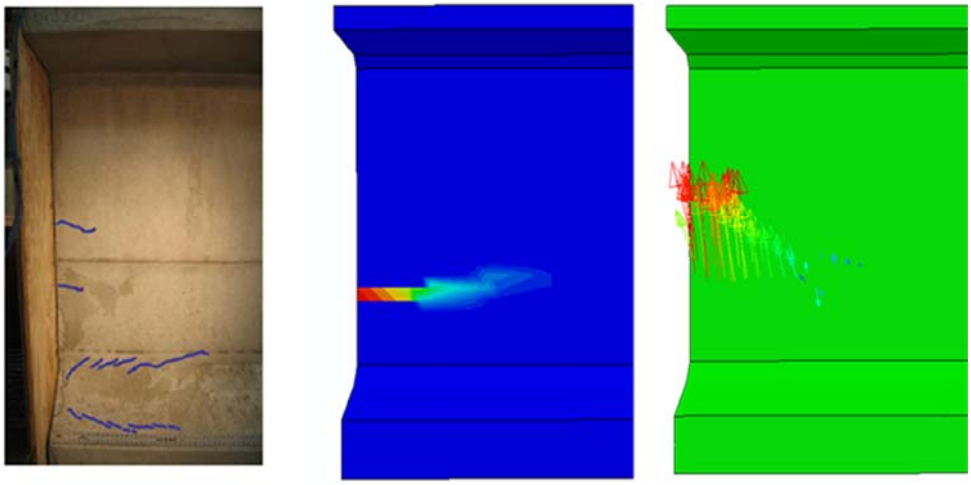

Figure 3.6.44. Experimental cracks at stress transfer; principle plastic strain; principal plastic tensile strain directions (for problem of reference 88).

CHAPTER 4

4. CONCLUSIONS AND RECOMMENDATIONS

4.1. Summary

In order to achieve the first objective, real-time structural health monitoring, the following tasks were undertaken:

1- Thoroughly reviewed the state-of-the art of SHM based on AE technique and the following shortcomings and research needs were noted:

- Most of the researchers did not pay enough attention for sensor attachment and calibration.
- The collected data is used for explaining the material damage qualitatively.
- In some research work, proper distinction was not been made between the noise and AE signals of interest.
- Some research studies did not separate damage related AE signals from other irrelevant AE sources.
- Modifications of modal and frequency characteristics of AE signals due to sensor limitations, diffusion, reflection, refraction and acoustical transfer characteristics of the coupling agent were not properly taken into account.
- Very few studies have been conducted that are concerned with application of the AE technique on concrete bridges. Issues related with field application of this method have not been properly addressed.

2- Based on the existing facilities, decision was made about acquiring cyclic loading facility and controls, AE sensors and associated data acquisition system:

- Cyclic loading system and controls (Appendix-B).
- AE sensors and data acquisition system (Appendix-B).
- Accelerometers and strain gages (Appendix-B).

3- A number of jigs and fixtures were designed and fabricated for cyclic as well quasi-static load application as detailed below:

- Load application jig details for cyclic load (Appendix-B).
- Support details for cyclic loading system (Appendix-B).
- Quasi-static loading system of stage-1 (Appendix-B).

4- Proportioned and fabricated the test beams of steel, reinforced concrete, and prestressed concrete based on the capacity of the loading system. Due to practical limitations on minimum allowable size of prestressed concrete beam, cyclic loading could only be applied to steel and reinforced concrete beams. Design and fabrication details of the test specimens are given in Appendix-A.

5- The deficiencies of existing schemes for processing the AE sensor signals were thoroughly evaluated and the following deficiencies were noted:

- Using the band-pass filter method for noise elimination, which is the most popular noise cleaning method among researchers, may cause inhibition of detection of the real AE events, if needed time consuming and costly preliminary studies were not conducted.
- In some research studies, empirical source location methods (i.e. time difference of arrival, frequency dependent source location, etc.) have been used

even for structures with complex geometry. Although these methods work well for simple specimens, their accuracy drop significantly as the geometry becomes more complex or non-homogeneities abound in the material.

- Some researchers used ANN approach for source location and signal characterization of AE events. The training data sets for those ANN's are generated by conducting basic tests (i.e. uniaxial tension) on simple specimens. Although those specimens and the structure of interest have the same material properties, their geometrical characteristics are completely different. Therefore, the material failure related signal sets recorded from such simple specimens, cannot be expected to share the same signal characteristics with the damage related signals recorded from the structure of interest. As a result, those ANN's were not capable of detecting real damage related signals.

6- The test beams were instrumented with AE sensors, strain gages and, as needed, accelerometers and subjected to cyclic or quasi-static loading till damage is noticed. In the case of concrete beams damage initiation was allowed to occur during the test but in the case of steel beams, to expedite the test, initial damage was deliberately introduced before the test and thus AE sensors could pick up the effect of damage growth only.

7- A new scheme was developed to process and interpret the test data based on noise elimination by using wavelet transformation, and event source location by using neural networks and source characterization by using fast Fourier and continuous wavelet transformations. The scheme included training of the neural network

through a series of experiments undertaken before the cyclic test and also by results obtained by finite element simulation.

8- A new finite element modeling scheme based on the use of the commercial software Abaqus was developed to simulate the cyclic load tests and also to generate the training data for ANN.

9- Test results and analytical predictions were mutually verified and validated.

In order to achieve the second objective, involving localized FRP patch repair to extend bridge life, the following tasks were undertaken. It should, however, be noted that, although desirable, this phase could not be worked upon as a continuation of Objective 1 because the research funding for Objective 2 preceded that for Objective 1 and that too from a different sponsoring agency.

1- In this stage, the first step was to review the state-of-the-art of repair of bridge superstructures and the state of FRP use for the same purpose. It was found that FRP use was limited to strengthening the whole length of a deficient bridge, and strengthening the round pier columns against earthquake by wrapping with the same material. These were done mostly by the wet method in which the fabric is impregnated into the matrix during application, as opposed to the dry method so common in other industries. In the dry method, for proper adherence of the composite to the structure, both heat and pressure needs to be applied on the surface of the prepreg, which is a ready-made resin impregnated system. A survey of commercially available FRP materials of both types as well as other variations was undertaken and four material types were chosen for the present study.

2- The size of test beams as representative structural elements were again decided upon based on the available test equipment in the laboratory and ensuring that different failure modes could be mobilized. Here too, the same three material types as for Objective 1 were chosen and the test specimens were fabricated accordingly, following standard procedures. Detailed design procedures for all stage-2 test specimens can be found in a TDOT research report [63]. Fabrication details of all stage-2 test beams are provided in Appendix-D.

3- The jigs and fixtures for 4-point load testing of the concrete beams were designed and fabricated in-house. Design and fabrication details of the stage-2 jigs and fixtures can be found in another publication by the author [63]. Each reinforced and prestressed concrete test beam was loaded till first local damage (in flexure or shear) could be induced. In the case of steel beams, however, the damage was assumed to be caused by section loss due to corrosion, as required by the sponsoring agency. Such damage was simulated by shaving off material from the flange and/or web of steel test beams.

4- Before undertaking local bonded patch repair of the test beams, it was necessary to decide upon the type of patch repair and proportioning of the same. Simple formulas were developed first to determine the repair needs of the weakened section. Thereafter, extension of the patch along the length of the beam beyond the theoretical cut-off was considered to prevent any overstressing. The required patch sizes for each damaged test beam were decided upon.

5- As the patch proportioning method used in the last step was based on simple mechanics, it was necessary to develop more rigorous methods to study the global

behavior of patch repair without resorting to full-fledged finite element analysis, which is normally outside the scope of routine structural design procedures followed in the civil engineering discipline. In this context, it may also be stated that dynamic analysis for predicting, say, fatigue life of a cracked bridge may also fall in the same category. Normal procedure is to treat a cracked beam at failure by the ultimate strength approach [66] which assumes linear strain across the depth. In the improved analysis procedure, to be called as the mechanistic model, the whole length of the beam was considered, instead of just a section. The strengthening was in flexure with the FRP patch applied to a certain length of the beam. The most important feature of the treatment was that the shear and tension properties of the adhesive used to bond the patch to the substrate was allowed for explicitly based on actual shear and tensile tests undertaken for the purpose. These properties were used as tensile and shear spring constants allowing for separation as well as slippage of the patch material with respect to the substrate. The whole treatment is based on the assumption that the beam substrate and the bonded patch individually satisfy the simple beam bending theory. Allowing for inelastic behavior in the case of steel beam was not an issue. In the case of concrete beams, however, the procedure got very complicated due to the use of actual stress vs. strain curve for concrete and allowing for the tension stiffening effect.

6- All three types of test beams were subjected to nonlinear finite element analysis in two stages (a) before any patch repair beginning with as fabricated, undamaged, beams, and (b) after patch repair of the damaged beams. The commercial finite element analysis software Abaqus [61] was used for this purpose after thoroughly

reviewing the Concrete Damage Plasticity model for concrete beams and suggesting some modifications for the problems in hand.

7- The repaired steel and concrete beams were again loaded on the original test bed and loaded to failure. The history of strain and deflection based on strain gages and LVDT readings were recorded.

8- The strain and deflection results from tests, mechanistic method, and finite element simulations were compared for verification and validation.

Based on the above steps, suitable conclusions are drawn in the following section regarding the efficacy of the proposed localized FRP bonded patch repair scheme and the analysis tools of different sophistication developed for the purpose.

4.2. Conclusions

The main conclusions of this study are stated below.

AE Based Structural Health Monitoring:

- The success of AE sensors in acquiring real-time data of damage events in monitoring the health of common bridge superstructures was a resounding success. The method could be successfully applied to bridges of all three typical material types, namely, steel, reinforced concrete and prestressed concrete.
- The most challenging part of real-time SHM effort was the interpretation of recorded signals. Due to a number of pollution sources, the recorded signals were very noisy. Unlike common experience in current practice, the author's efforts to denoise the signals using wavelet transformations was highly successful. The

cleaned up signals showed good agreement with the theoretical ones, proving the veracity of the developed approach.

- The sources of recorded signals, an extremely complex nonlinear problem, were successfully identified by devising a method based on the artificial neural network approach. Before using the artificial neural networks, they are required to be trained by incorporating data sets generated by pencil lead break testing which generates acoustic emission signals very similar to the ones generated by structural cracks. Damage locations predicted by the artificial neural networks showed remarkable agreement with actual visual observations.
- As last step in signal processing, the characterization of the actual source of the recorded signals was successfully undertaken with the aid of power spectrums generated by fast Fourier transformation and continuous wavelet transformation plots. Unlike past reservations about the applicability of Fourier transformation to a range of problems, it was found from this study that both of the methods could be equally applied successfully, at least, for the type of problem in hand.
- Highly realistic finite element models of the steel test specimens along with those of attached acoustic emission sensors could be successfully created reflecting real-life geometric and material details. The multiphysics character of the problem, involving stress wave propagation and piezoelectricity, could be successfully simulated using two different Abaqus solvers (Abaqus/Explicit and Abaqus/Standard) in a coupled manner by using the co-simulation engine (CSE) of Abaqus. The resulting finite element simulation predictions showed excellent agreement with experimental data and theory.

- In real-life application of the proposed SHM technique to bridge structures, it is difficult to generate training data for artificial neural networks by following the pencil-lead-break test method used in the laboratory. The successful finite element modeling of the problem paves the way to generate such data by this simulation scheme for training ANN in real-life SHM of bridge structures.

Strength Remediation Using Bonded Composite Patch:

- Experimental studies were conducted with fabricated representative beam specimens of steel, reinforced concrete and prestressed concrete to create crack-like damages and to check the performance after bonded composite patch repair intended to restore and thus extend bridge life. The results of the study indicated that in most cases the proposed localized patch repair method reasonably improved the performance of the damaged beams.
- The developed mechanistic model of the damaged bridge girders patch repaired for flexure could accurately predict the structural performance in the post-repair stage. The model accurately accounts for the nonlinear nature of construction materials including the elastic-plastic behavior of steel, complex stress behavior of concrete under compression and tension stiffening effect between tension rebar and concrete. The adhesive attaching the composite patch to the parent beam is represented by a combination of zero-dimensional shear and tension interfacial springs. Results of the mechanistic model for all types of beams showed very good agreement with experimental data. The proposed model can be used by engineers

as a useful design aid without the need for using any large-scale commercial simulation software.

- The developed scheme for accurate nonlinear finite element modeling of representative structural members of steel, reinforced concrete and prestressed concrete is based on accurate material and bond models including an elastic-plastic material model for the rebar and the strand, the Plasticity-Damage material model for concrete, bond-slip interfacial behavior model for the interface between concrete and rebar or strand and a cohesive-failure bond model for representing the adhesive at the beam-composite interface. Predictions by finite element simulation exhibited excellent agreement with experimental data.
- Bonded patch repair is highly successful in reducing the stress intensity factor in steel beams with through cracks in the bottom flange. The extent of such reduction depends upon the type of composite patch used.
- In this first ever fully successful nonlinear finite element model of a pretensioned prestressed concrete beam represented the true mechanics of the problem under all stages, from construction to service. Shortcomings of the most recent finite element models reported in the literature were clearly evident from the critical evaluations undertaken by the author.

4.3. Research Outcomes Advancing the State of the Art

1- The use of AE sensors in real-time health monitoring of bridge structures is established.

2- The applicability of this method in the case of metallic systems was done by others in the past. However, the applicability of this method of SHM in the case of concrete bridge super-structures is firmly established through the present effort.

3- This work makes significant contribution in making sense out of the recorded AE signals. The developed acoustic emission based SHM system can effectively clean the background noise, detect the source locations of the signals accurately, characterize the acoustic emission events based on their sources and most importantly can easily be automated. In the process, this study will help remove the long-standing stigma against the use of this tool in real-time SHM. With the developed system, damage related signals can be communicated to engineer's desk autonomously along with the supplemental data for decision making, without the need for human interference.

4- This work has also removed the long-standing perception that for accurate SHM in a 3D system like a bridge girder, installing utmost four AE sensors is adequate. It was found that for effective SHM, sensors should be provided at all the exposed faces in adequate numbers, say, at every 6 to 7 feet.

5- In contrary to the common knowledge, it has been found that all damage types (i.e. shear cracks, flexural cracks, etc.) have a very similar AE signal signature. Therefore it is not possible to assess the type of damage by just looking at the AE waveforms. However since the locations of the cracks can be determined accurately by using the proposed source location methodology, this information can be used to make a preliminary damage assessment (i.e. shear cracks usually appear close to the supports, flexural cracks are usually observed at the middle).

6- Numerous attempts have been made over the last 50 years to accurately predict the state of stress in a pretensioned prestressed concrete beam, but not a single case of success could be located, even in publications published as late as 2012. It is for the first time, this research effort has shown how it can be done successfully by nonlinear analysis in which all the nonlinearities in material behavior are accounted for faithfully. In addition, all the loading stages of the beam from construction to operational condition are considered accurately.

7- It is again for the first time that finite element models of a realistic piezoelectric acoustic emission sensor attached to the substrate was created accurately by using the general purpose finite element software Abaqus. Signal output obtained from the finite element model of the acoustic emission sensor showed good agreement with the output data recorded during experiments from the real acoustic emission sensors. For the first time, a finite element model is created, which can successfully generate a crack originated stress wave through the model of a steel beam and can convert that wave into an electrical signal through an acoustic emission sensor model. This finding will allow effective training of the ANN during processing of AE signals in SHM.

8- A new mechanistic model is developed for predicting the behavior of a full locally patch repaired beam. The model accurately takes into account the mechanical behavior of adhesive in tension and shear, elastic-plastic behavior of steel, compressive behavior and the tension stiffening effect of concrete. Results obtained from the mechanistic model showed excellent agreement with experimental data.

9- Created an easy to install, repeatable and cost-effective local bonded FRP patch repair method which significantly improved the performance of bridge beams repaired against shear and flexural cracking and section loss due to corrosion. Followed by this successful study, the method is also being implemented by TDOT for field applications.

4.4. Recommendations

Given that some of the important elements have been addressed in this study for an effective and efficient bridge management system, several recommendations are in order:

- In this study, only four acoustic emission sensors could be used to monitor the beam specimens during testing due to budget limitations. Although the developed system effectively de-noised the output signals, accurately detected the source locations of the acoustic emission events and successfully separated the crack related signals from the signals generated by other types of sources for steel and reinforced concrete beams, the same success could not be achieved with the prestressed concrete beam specimen which is relatively larger than the other beams. During field applications, although a small network of sensors (four or less) is enough for small scale bridge members like angles, eyebars, cables, etc., a larger number of sensors is needed for larger scale bridge members like a prestressed concrete girder.
- During testing, it has been observed that acoustic signals were getting severely modified during their travel inside the concrete material unlike steel. This problem can be attributed to the non-homogenous nature of concrete. Therefore, a network

of larger number of sensors is needed for concrete structures compared to the steel ones for increasing data reliability and processing.

- During field applications, extra safe-guards may be needed to eliminate the additional sources of acoustic signals (traffic, rain. etc.) originating from the deck. ANN approach implemented in this study is a good candidate to accomplish that.
- During the repair of steel beams, instead of using regular FRP materials, composites with relatively higher modulus of elasticity should be used to effectively mobilize the effectiveness of patch material in the elastic range. High modulus carbon fiber reinforced polymer (HM-CFRP), ultra-high modulus carbon fiber reinforced polymer (UHM-CFRP) or ultra-high modulus carbon/glass fiber reinforced polymer (UHM-CFRP/GFRP) are good candidates for the repair of steel beams.
- In this study, for convenience, the bonded FRP composites were applied in single layer. In the case of laminated carbon fibers, the effect of applying patch in multiple layers needs further investigation.
- Only short term performance of bonded FRP patch repair is investigated in this study. Performance of this repair system under fatigue loading and also long-term effects of environmental conditions like moisture, temperature, etc. needs to be investigated further.
- Further studies related to controlling the fatigue life of a bridge member with crack will be useful.

APPENDICES

APPENDIX A. DESIGN AND FABRICATION DETAILS OF TEST SPECIMENS FOR SHM

Sizing of the test specimens were based on the following considerations: rated capacity of the test facilities and available loading equipment, convenience in handling, feasibility of in-house fabrication and type of tests planned to be undertaken. The type and number of test specimens considered were:

- Six rectangular reinforced concrete beams
- One precast prestressed concrete I-section beam; and
- Three steel beams of S-shape.

Reinforced Concrete Beam: The cross-sectional dimensions of the 7'-6" long beams were 2.5" wide x 4" deep. The main reinforcement in each beam was a #2 steel rod (A_s = 0.049 inch^2, f_y=60ksi), as shown in Figure A.1.

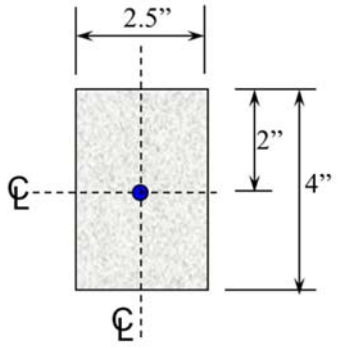

Figure A.1. Cross-section of the reinforced concrete beam.

The weight of reinforced concrete test beam was around 78 lbs. Another limiting factor in the selection process of the test specimen was the rated capacity of the electrodynamic shaker and the area of the strong floor available for mounting the supporting system for the test beams. Mix design of concrete was based on approved methodology described in the literature [93]. The 28-day compressive strength of concrete was targeted to be 3 ksi (f_c'). The aggregates comprised of fine sand and course aggregate of maximum size equal to ⅜".

The cyclic loading system essentially comprised of two end supports and shaker excitation was transferred through two closely spaced knife edges, placed both above and below the beam creating essentially a three-point loading condition. During preliminary calculations, for the three-point loading situation, as shown in Figure A.2, the limiting load value was chosen as 225 lbs which corresponded roughly to a displacement of 0.06" at the load point.

The reinforced concrete beams were designed as per ACI-318 [66]. For the loading case shown in Figure A.2, the capacity of the beam against shear failure, P_{shesar}, was found to be 264 lbs, and that for flexure, $P_{flexure}$, it was 220lbs, ensuring flexural failure under cyclic loading.

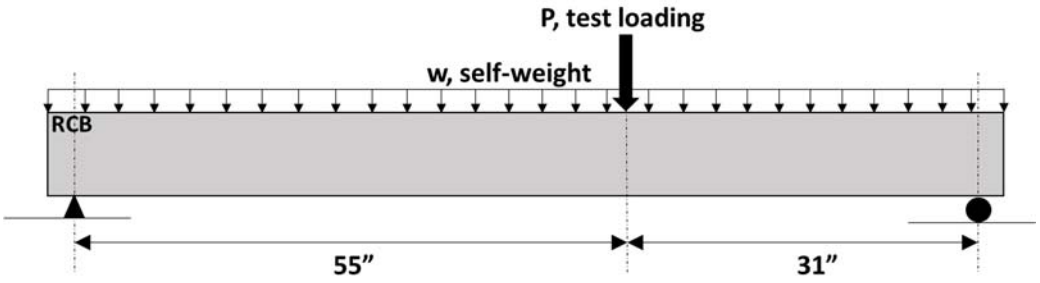

Figure A.2. Reinforced concrete specimen design loads.

The reinforced concrete test beams and accompanying 4” dia. x 8” long test cylinders were cast and cured following standard procedures. Figures A.3 (a) and (b) show the formwork after they have been assembled with reinforcing rods in place. Also, eleven cylinders were made, four of which had #2 embedded rods for pullout test.

(a) Beam formwork with rebar

(b) Test cylinder with burlap cover

Figure A.3. Beam formwork and test cylinders.

The cylinders were tested for 28-day compressive as per ASTM C39 standards [94], with the results of the test given in Table A-1.

Table A-1. Concrete Cylinder Strength Values (f_c’).

Cylinder #	Batch #	Failure load (lbs)	Comp. Str. (psi)
1	1	47070	3746
2	1	60580	4821
3	2	69910	5563
4	2	79190	6302

Three of the concrete cylinder specimens were tested for tensile strength by split-cylider test as per ASTM C496 standard [95]. The corresponding split cylinder strength values are shown in Table A-2.

Table A-2. Concrete Split Cylinder Strength Values (f_{ct}).

Cylinder #	Batch #	Failure load (lbs)	Split Ten. Str. (psi)
1	2	27190	541
2	2	23310	464
3	1	18950	377

Four concrete cylinders with embedded rebars were subjected to pull-out test to determine the bond strength. Results of this test are shown in Table A-3. These results were later used for determining the bond characteristics between concrete and steel.

Table A-3. Concrete Bond Strength Values.

Cylinder #	Batch #	Failure load (lbs)	Bond Str. (psi)
1	1	4170	664
2	2	4770	759
3	2	4550	724
4	1	4180	665

Prestressed Concrete Beam: Details of the prestressed concrete beam is shown in Figure A.4. The design of I-shaped cross-section of the beam was based on AASHTO Specifications [96]. The relevant details of the design beam are shown in Table A-4. The beam has two ½" diameter prestressing strands at the bottom and two top #3 hanger bars, one on each side. The size of the stirrups is #2. Yield strength of the top hanger bars and stirrups are 60 ksi and the yield strength of the prestressing strands is 270 ksi. The overall length of the beam is 8'-6".

Table A-4. Relevant design parameters of prestressed concrete test beam.

Parameter	Value
f_c' (psi)	5000
f_{ci} (psi)	4000
f_u (ksi)	270
Sectional area (in^2)	52
Self-weight (lb/ft)	54.17
I_x (n^4)	557.83
M_n (kip-ft)	38.98

The prestressed concrete beam was constructed using the standard casting bed at a local precast concrete plant (Construction Products, Inc. near Memphis, TN). The concrete mix design was done to achieve the target minimum compressive strength of 5000 psi. Results of concrete test cylinder compressive strength tests are given in Table A-5.

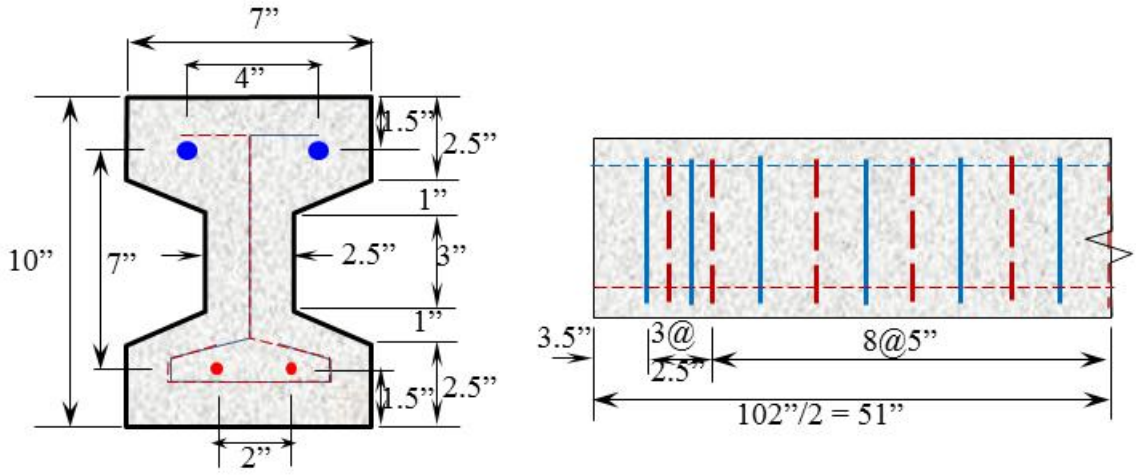

(a) Details of cross-section (b) Stirrups

Figure A.4. Prestressed concrete test beam.

Table A-5. Concrete compressive strength testing results for prestressed concrete beam.

Cylinder #	Failure load (lbs)	f_c' (psi)
1	88500	7043
2	81500	6486
3	83000	6605
4	80000	6366

Steel Beams: For the steel beam specimens, an ASTM S3x5.7 section (ASTM A36) was selected because of similarities of overall size compared with the reinforced concrete beam, so that the same fabricated support and loading systems can be used for both types of beams. AISC section properties of the section are shown in Table A-6 [97]. Total length of the first and third steel beams, SB-1 and SB-3, are 11' and the length of the second beam SB-2 is 7'-2".

Table A-6. S3x5.7 properties from 2010 AISC Steel Manual.

A =	1.66	in^2	k =	0.53	in
d =	3.00	in	T =	1.75	in
t_w =	0.17	in	I_x =	2.50	in^4
b_f =	2.33	in	I_y =	0.447	in^4
t_f =	0.26	in			

In the case of specimens SB-1 and SB-2, to expedite the cracking process during the cyclic load tests, artificially introduced initial cracks were created at the center of the beams through the bottom flange and extending up to half of the web with the help of a hex and jeweller's saws, see Figure A.5. In the case of steel test beam SB-3, the induced initial damage in the bottom flange at the center of the beam was as a pair of symmetrically

placed holes with edge crack. The hole diameter is 0.5”, the center to center distance between the holes is 0.75”, and edge crack length are 0.25”, as shown in Figure A.6.

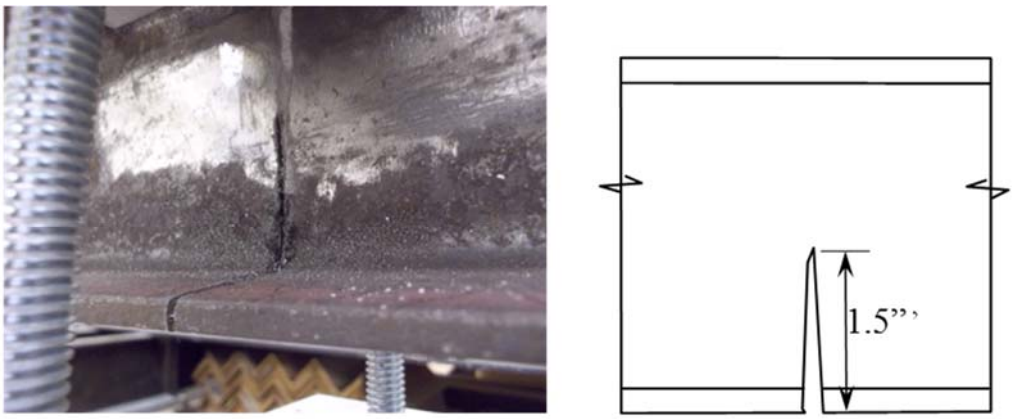

Figure A.5. Deliberately introduced crack in steel test beams SB-1 and SB-2.

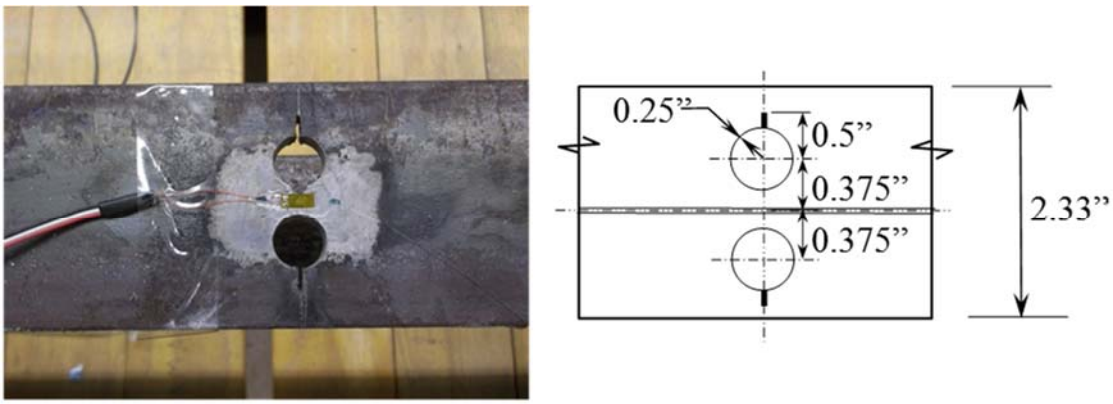

Figure A.6. Initial edge cracked holes in bottom flange of steel test beam SB-3.

APPENDIX B. DETAILS OF SUPPORTS, LOADING SYSTEMS AND CONTROLS FOR SHM

The main components of the cyclic loading system and controls are; the shaker, its control equipment and the support system which were assembled and calibrated together. The schematics of the system is shown in Figure B.1.

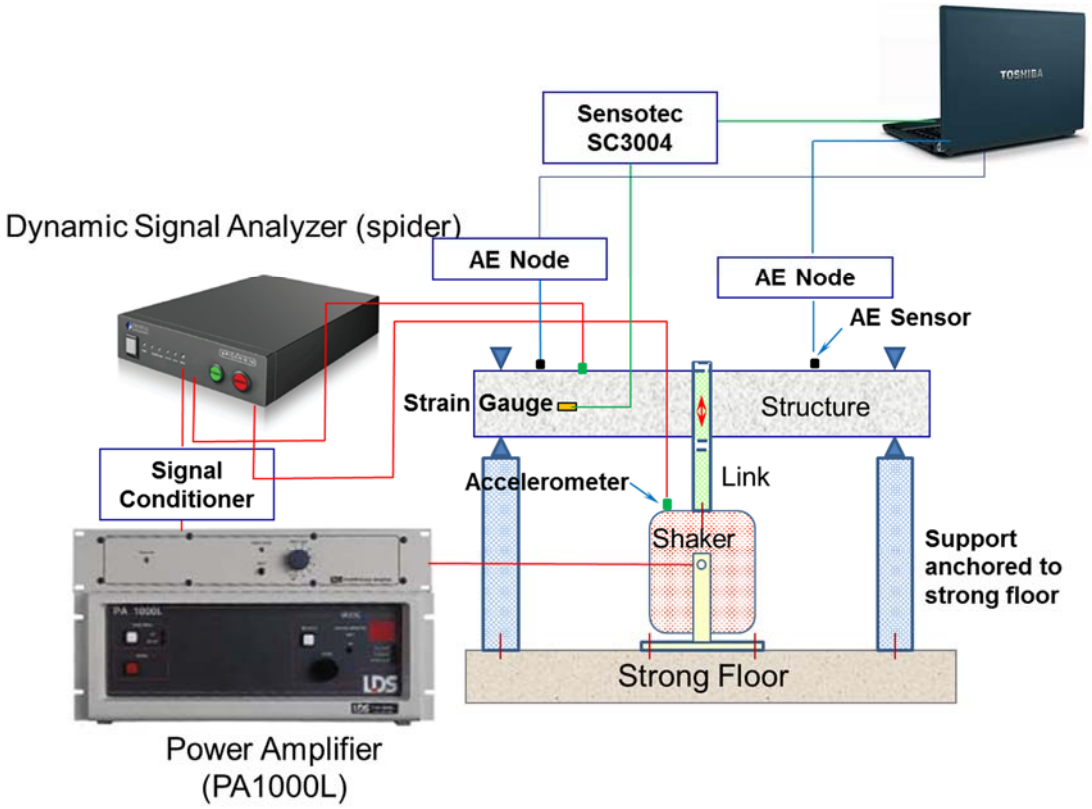

Figure B.1. Test Setup for Cyclic Loading.

The maker and model of the shaker is LDS V651 marketed by Bruel&Kjaer. The shaker was driven by a PA 1000L amplifier and a LDS FPS 10L field power supply. The support system and the link between the shaker and specimen were designed and fabricated to simulate essentially the three-point loading condition. Performance parameters of the mechanical shaker system are given in Table B-1.

Table B-1. Performance parameters of the shaker.

Parameter	Corresponding value
Sine Force (Peak)	364 lbs
Armature Resonance (fn)	3.8 kHz
Usable Frequency Range	5 Hz – 4 kHz
Velocity (sine peak)	55 inch/sec
Acceleration (sine peak)	73.7 g
Displacement (peak-peak)	1 inch

All components of the loading system was custom designed and erected and can easily be adjusted for any width, height and type of specimen. To provide support and transfer the applied force from the shaker to the specimen under test, the following custom designed and fabricated jigs and fixtures were used:

- The shaker link was fabricated out of plates, threads, bolts, nuts, washers and knife edged load application pieces (Figure B.2).
- The supports which were also fabricated out of plates, threads, bolts, nuts, washers and knife edges as in the shaker link (Figure B.3).
- The column supports were fabricated from rectangular pipes, plates, bolts, nuts and washers (Figure B.4).

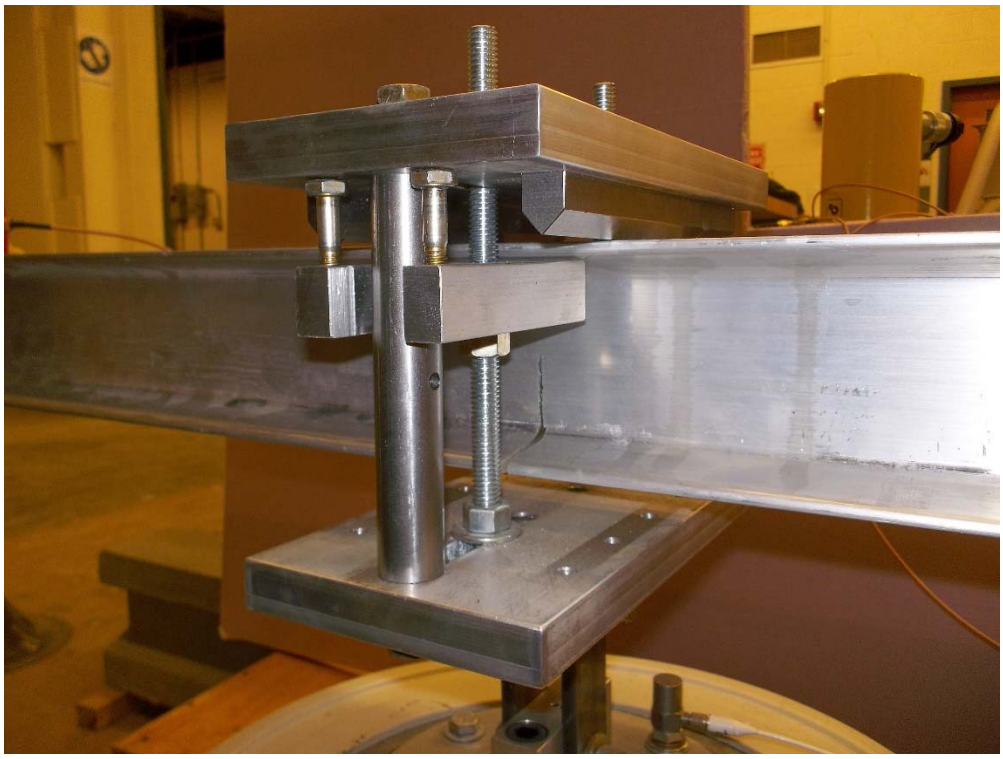

Figure B.2. Shaker link for the cyclic loading system.

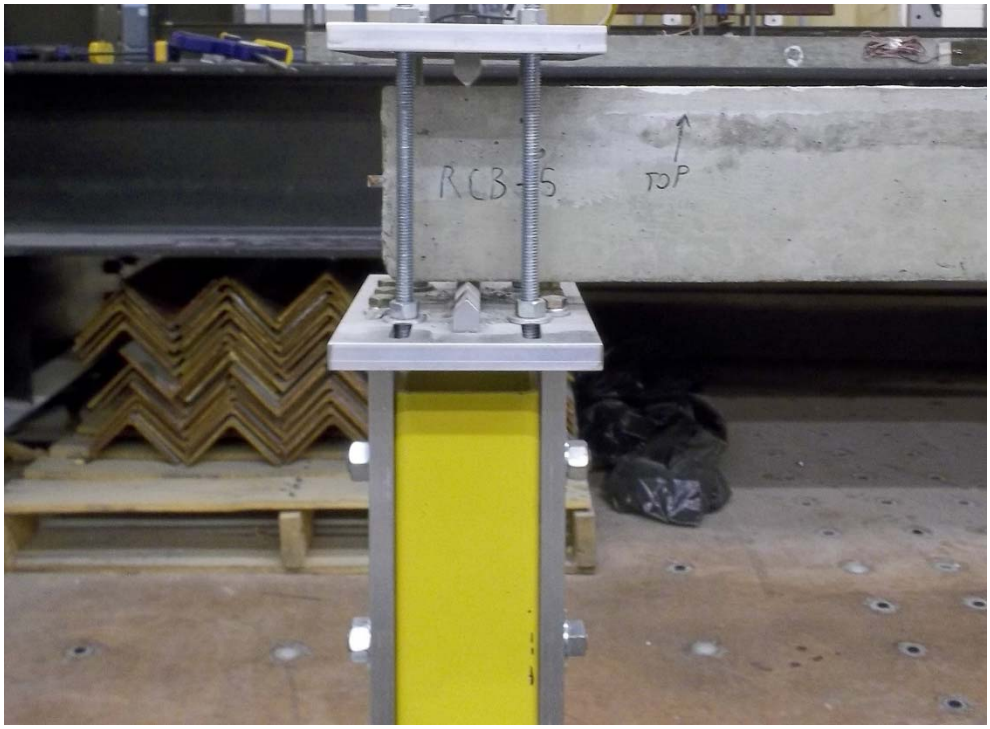

Figure B.3. Cyclic loading system support.

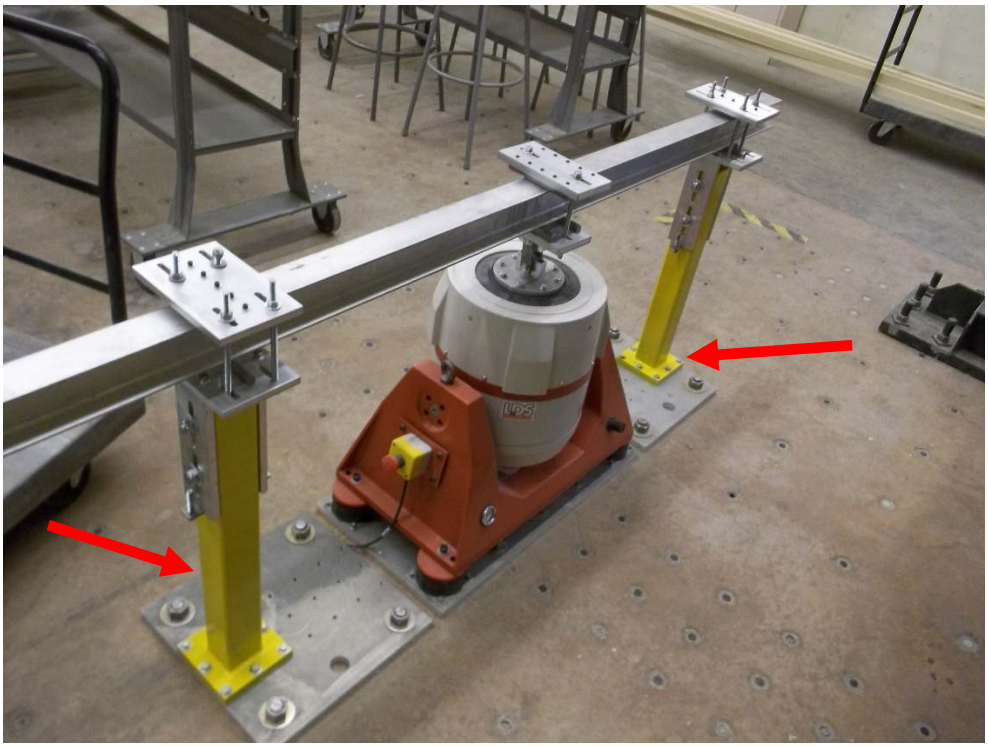

Figure B.4. Support columns for the cyclic loading system.

Unlike the steel and reinforced concrete beams, prestressed concrete beam was loaded quasi-statically. Loading configuration of prestressed concrete beam and test setup are shown in Figure B.5. Prestressed concrete beam PSCB3 used during SHM experiments is identical with the prestressed concrete beams PSCB1 and PSCB2 used in the repair stage.

For gathering the acoustic emission data, MISTRAS R15-α type sensor was used. Specifications of the sensor are given in Table B-2. The data acquisition system used during the experimental work is MISTRAS 1283 USB AE node, which is a compact and handy acoustic emission measurement system. The initial data processing of signals was undertaken using the AEWin software. Pictorial views of a R15-α type sensor and a 1283 USB AE node are shown in Figure B.6.

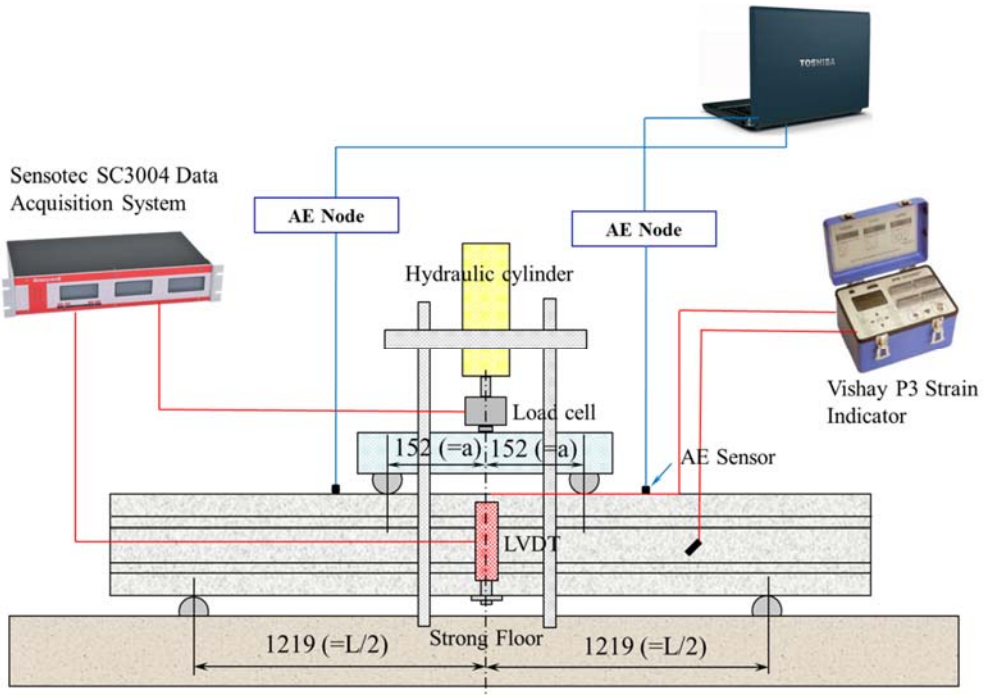

Figure B.5. Test setup for stage-1 prestressed concrete beam.

Figure B.6. R15-α type sensor (left) and 1283 USB AE Node (right).

Table B-2. Specifications of R15-α sensor.

Parameter	Corresponding value
Operating Frequency Range	50 – 400 kHz
Resonant Frequency	75 kHz
Peak Sensitivity	80 dB
Dimensions	19.05mm (dia.) x22.35mm (h)

During a test run, the system was triggered to record an acoustic emission hit waveform, whenever the threshold of 40 dB was exceeded. Temporal length of the recorded waveform was 1792 μs; 100 μs of which expires before the trigger kicks in. Sampling rate of the recorded acoustic emission signals were selected as 5 mbps. For peak definition time (PDT), hit definition time (HDT) and hit lockout time (HLT) values recommended by the manufacturers of the sensors were used, as shown in Table B-3.

Table B-3. PDT, HDT and HLT settings used during testing.

Material	PDT	HDT	HLT
Steel	1000	2000	20000
Concrete	50	200	300

Appropriate definition of PDT helps the system to properly identify the signal peak rise-time and peak amplitude. Correct HDT settings ensured that the system reports each signal as one and only one hit. Proper choice of settings for HLT avoids measurement errors during signal decay and increases data acquisition speed. All of the timing parameters used by the acoustic emission system are explained in detail below. Definitions of these parameters are specific to the current system and are consistent with user's manual of the manufacturer [98].

Peak Definition Time (PDT): Peak Definition Time (also known as Rise Time Out), is used for determining the true peak of an acoustic emission waveform. Using a PDT value shorter than it should be may cause false measurements. Graphical representation of this is shown in Figures B.7 and B.8.

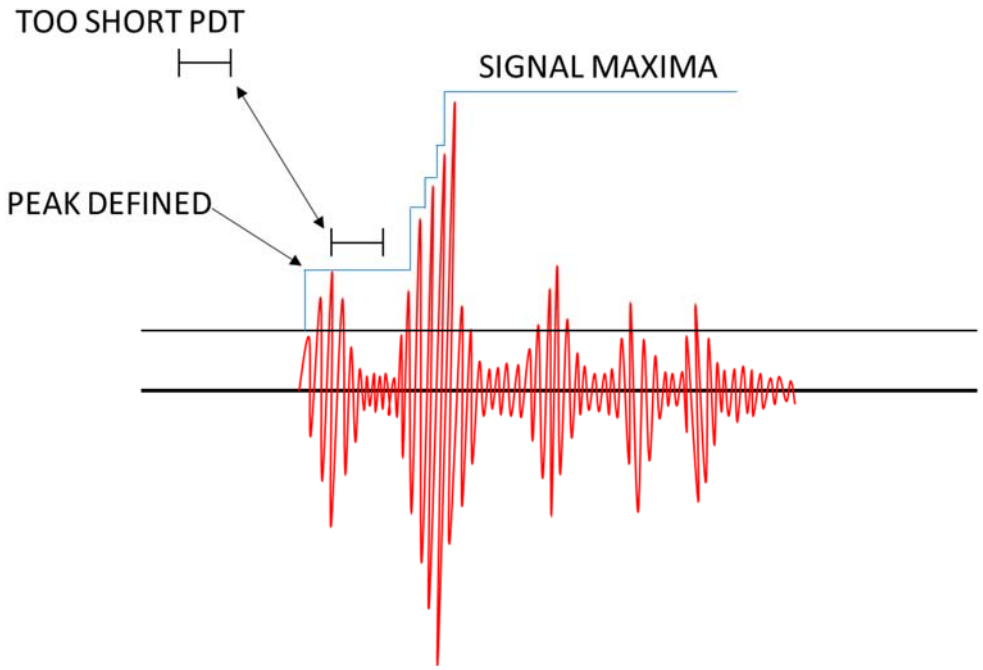

Figure B.7. False measurement of signal peak with a short PDT value.

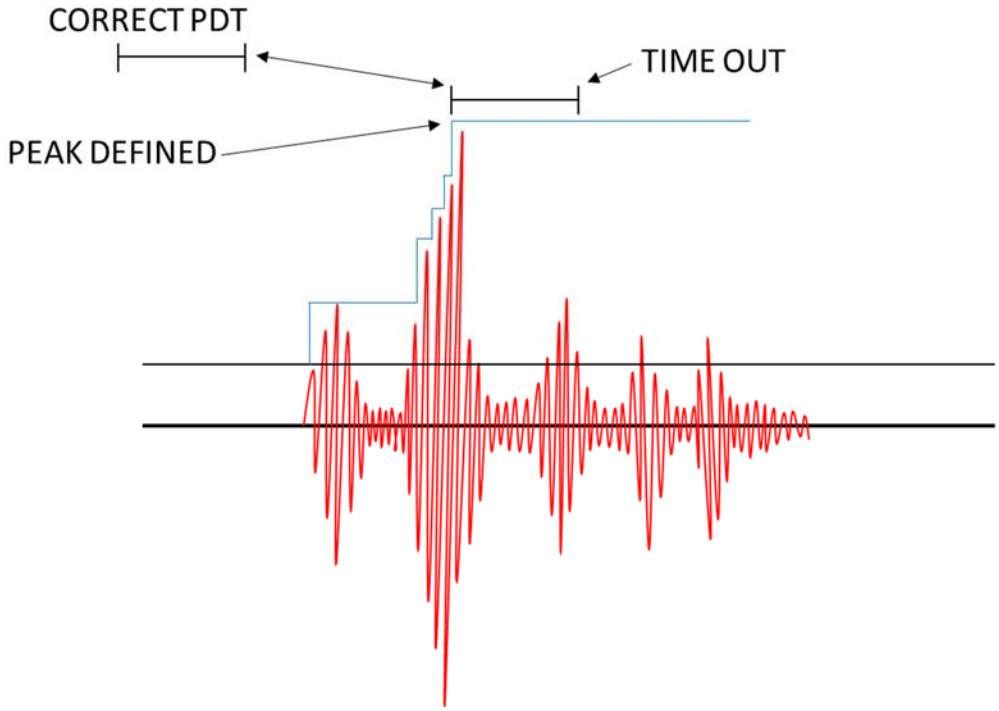

Figure B.8. Correct signal peak measurement with a reasonable PDT value.

Hit Definition Time (HDT): Hit Definition Time (also known as Single Channel Event Time Out), is used for determining the end of an acoustic emission hit, stop the measurement process, calculate the measurement parameters associated with that hit and store the data. Using a HDT value shorter than expected may cause the system to treat the single signal as separate multiple hits (Figure B.9). On the other hand, using a longer HDT may cause separate signals to be treated as a single hit. Figure B.10 shows correct signal hit end detection with a reasonable HDT value.

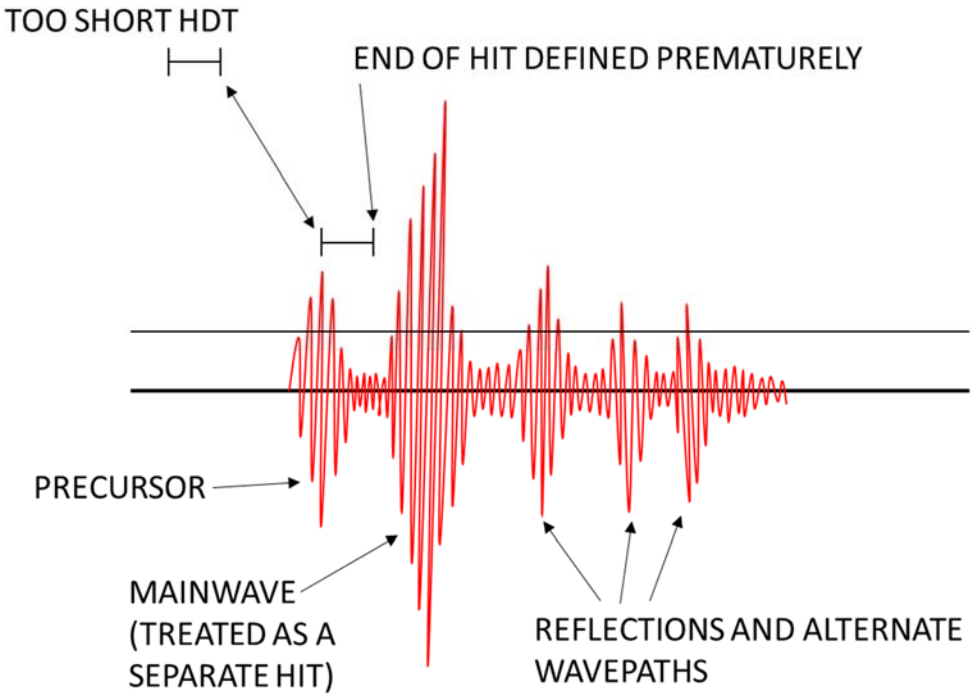

Figure B.9. False measurement of signal hit end with a short HDT value.

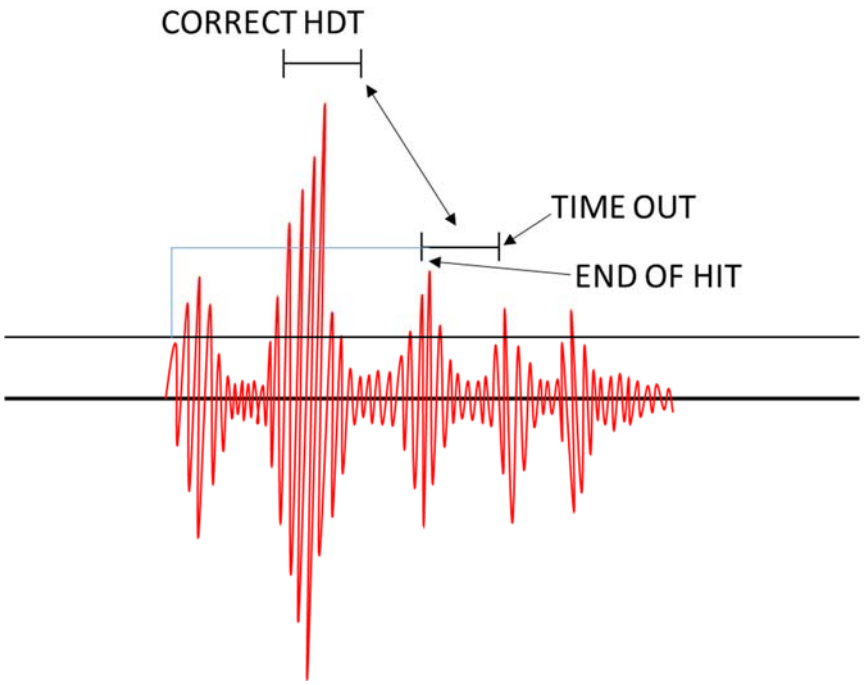

Figure B.10. Correct signal hit end measurement with a reasonable HDT value.

Hit Lockout Time (HLT): Hit Lockout Time (also known as Re-arm Time Out), is used for inhibiting the reflections and late arriving parts of the acoustic emission signals. Graphical representation of the correct use of the HLT is shown in Figure B.11.

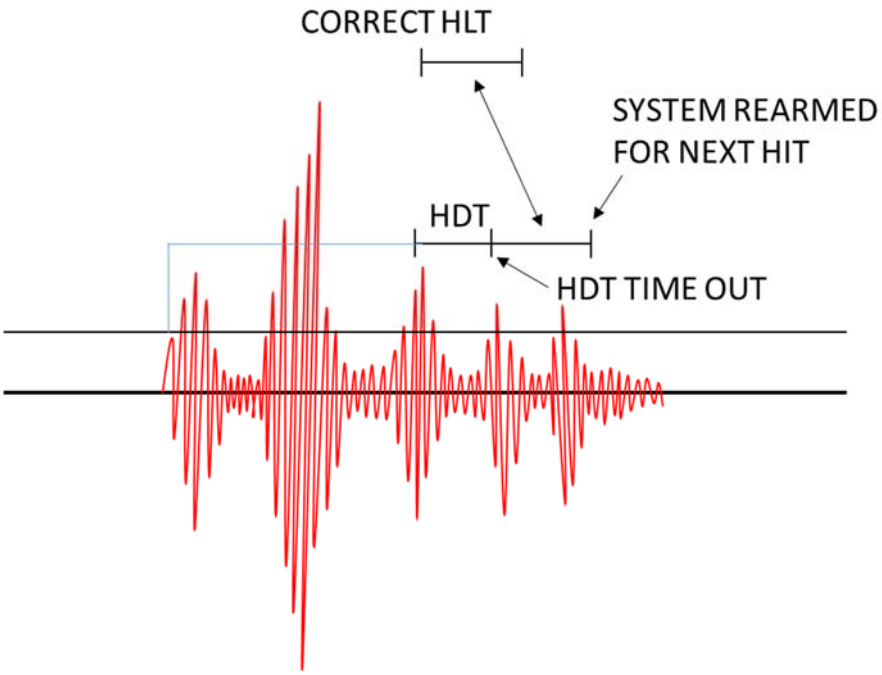

Figure B.11. Proper inhibition of the reflecting waves with a reasonable HLT value.

During the testing process, supplemental information was gathered from the critical locations of the test specimens. This was done by using accelerometers and strain gages during cyclic loading and by using LVDT's, load cells and strain gages during quasi-static load testing. Details of the strain gages, LVDT's and load cells are provided elsewhere [63]. Specifications of the accelerometers used are given in Table B-4.

Table B-4. Specifications of accelerometers.

Parameter	Corresponding value
Sensitivity (+ or – 10%)	10 mV/g
Measurement Range	+ or – 500g peak
Frequency Range (+ or – 10%)	1 to 10000 Hz
Resonant Frequency	> or = 70 kHz

APPENDIX C. AE SENSOR DISASSEMBLY PROCESS

The disassembly process comprised of, first, removal of the plate in the bottom of the sensor, see Figure C.1(a). In the intact sensor, the ceramic plate was glued to the sensor case and it was also attached to the bottom of the PZT sensor element. There are two electrodes attached to the sensor element one of which is attached to the bottom and the other one is attached to the top. There is a cable connected to the top electrode, the purpose of which is to feed the generated electric signals to the data acquisition system, see Figure C.1(b). The other end of the cable was soldered to the top part of the metallic sensor case, which itself filled with some type of epoxy as can also be seen in Figure C.1(b).

In order to find out if the red cable visible in Figure C.1(b) is attached to some type of circuit inside the epoxy, the sensor case was put into a bottle filled with methylene chloride. After a week, the epoxy was completely dissolved and the view was as shown in Figure C.1(c). After examining the sensor case and the residue in the bottle, it was found that there was nothing hidden inside the epoxy and the red cable was directly connected to the cable connector terminal mounted on the side of the sensor case. In order to make sure that no circuitry was hidden inside the sensor element, the element was cut into half and it was found that there was nothing but the piezoelectric crystal, as can be seen in Figure C.1(d).

(a) Bottom plate removed

(b) Removal of main element

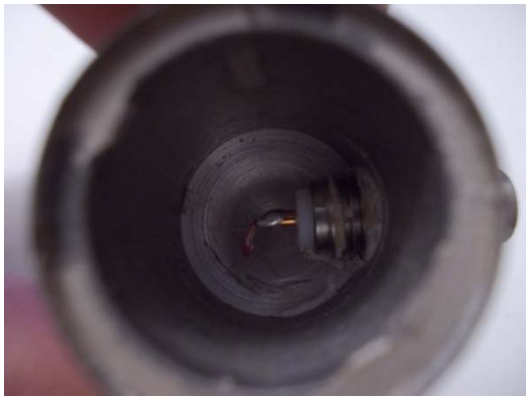

(c) After epoxy removal in base

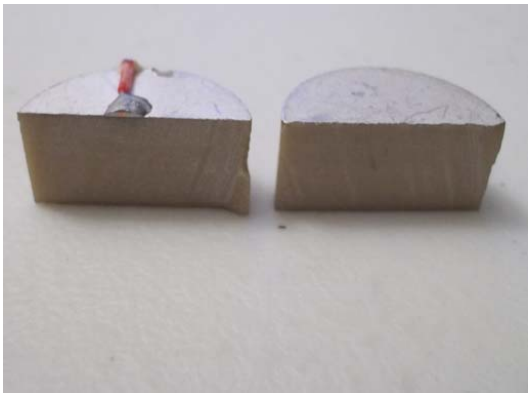

(d) Split view of sensor element

Figure C.1. Disassembly of Piezoelectric AE.

After this painstaking exploratory exercise, the true mechanical details of the acoustic emission sensor used were revealed leading to Figure C.2 showing the schematics of a R15-α type sensor. The whole sensor mechanism sits on a plate of Aluminium Oxide (Al_2O_3). The stainless steel sensor case and the sensor element are attached to the bottom plate. The sensor element is PZT-5H piezoelectric crystal with two electrodes, one attached to bottom and the other to top of crystal. To transfer the generated electrical signals, a cable is used one end of which is soldered to the top electrode of the sensor element and the other end is attached to the cable connector.

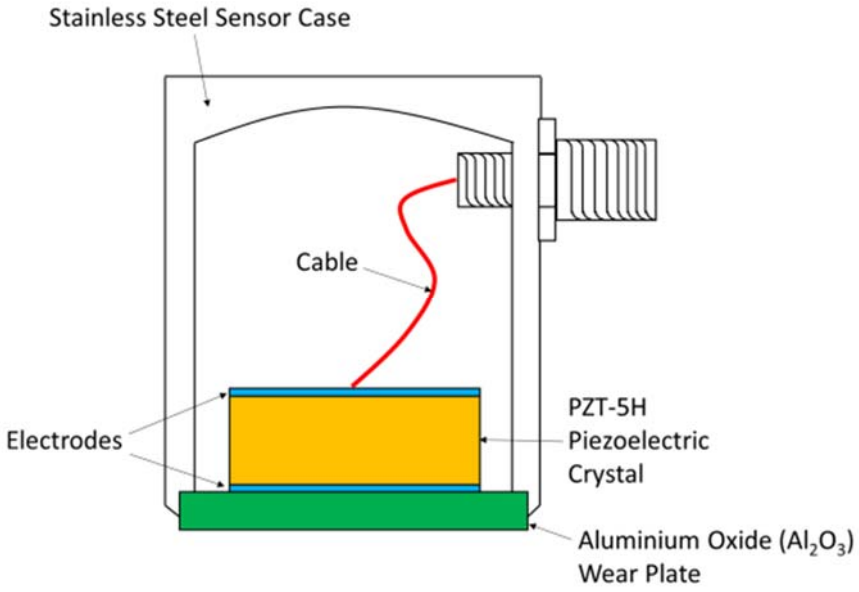

Figure C.2. Schematic of the R15-α acoustic emission sensor.

APPENDIX D. FABRICATION DETAILS OF THE TEST SPECIMENS FOR REMEDIAL MEASURES

Detailed design procedures for all the test beams can be found in the TDOT research report [63]. The details of test beams used were as follows:

- 18 rectangular reinforced concrete beam;
- 3 precast prestressed concrete I-section beams; and
- 4 steel beams of W-shape.

The dimension of two sets of reinforced concrete beams of length 3'-6" are shown in Figure D.1. The total weight of the reinforced concrete specimens were about 88 lbs. Twelve beams were deliberately over-designed in shear to enhance the possibility of flexural damage during testing and were designated as "flexural beams". The remaining six beams were designed without stirrups to ensure that these six beams undergo shear damage during testing and were termed as "shear beams". The reinforced concrete beams were proportioned using ACI-318 [66]. The stirrup spacing of flexural beams are shown in Figure D.2.

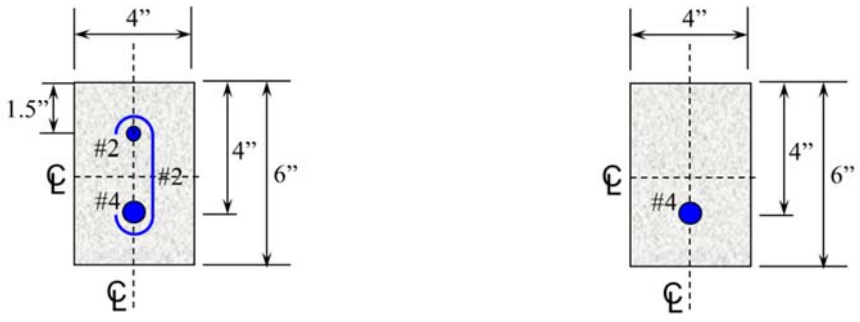

(a) Flexural beam (b) Shear beam

Figure D.1. Cross-sectional details of the reinforced concrete beams.

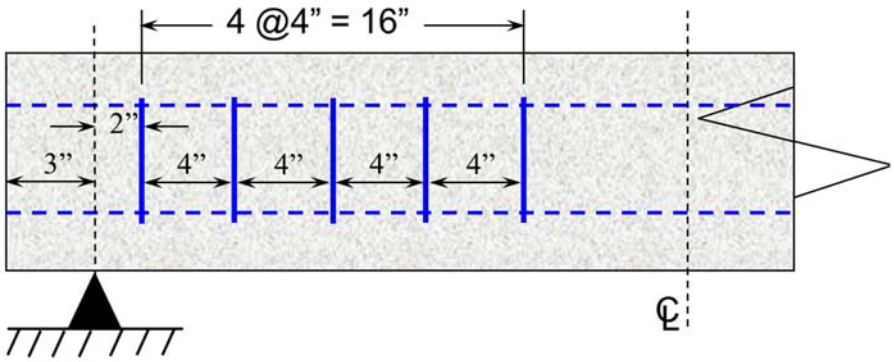

Figure D.2. Spacing of stirrups in flexural beams.

A standard concrete mix akin to what is often used by TDOT for bridge superstructure construction was the basis for the mix design of the reinforced concrete test specimens. The target compressive strength was chosen as 4 ksi. Fine sand was used as the fine aggregate and stone chips as coarse aggregate was ½” maximum. A view of the formwork with main steel in place is shown in Figure D.3.

Figure D.3. Forms for flexural and shear beams [63].

During pouring of the beams, 4” dia. x 8” long cylinders were also cast following standard procedures. On 28th day after pouring, the beams and cylinders were taken out of water and left for air drying. Thereafter, the cylinders were tested with a calibrated 500 kip Forney compression testing machine. The cylinders were tested as per the requirements of ASTM C39/C39M standard [94]. The results of compressive strength tests are given in Table D-1.

Table D-1. Concrete compressive testing results of reinforced concrete beams tested during second stage.

Cylinder ID	Failure load (lbs)	Compressive Strength (psi)
1	88860	7071.25
2	90940	7236.78
3	85940	6838.89
4	79170	6300.15
5	95190	7574.98
6	91910	7313.97
7	93020	7402.30
8	83400	6636.76
9	81370	6475.22
A	85740	6822.97
B	79290	6309.70
C	62510	4974.39
D	61800	4917.89
E	72570	5774.94
F	71150	5661.94
G	89520	7123.78
H	89140	7093.54
I	87490	6962.23

The details of all three prestressed concrete beams (PSCB1, PSCB2 and PSCB3) are given in Appendix-B. All steel beams used here were standard ASTM W6x12 section, the section properties of which are given in Table D-2. These beams were designated as SBC, SBI, SBII and SBIII. The lengths of those steel beams were 5’-6”. Limit capacities

of SBC, SBI, SBII and SBIII were calculated by following AISC provisions allowing for several flexural and shear limit states [97].

Table D-2. W6x12 properties from 2010 AISC Steel Manual [97].

$A =$	3.55	in^2	$k =$	0.53	in
$d =$	6.03	in	$T =$	4.50	in
$t_w =$	0.23	in	$I_x =$	22.10	in^4
$b_f =$	4.00	in	$I_y =$	2.99	in^4
$t_f =$	0.28	in			

In this study, the steel beams were considered to be damaged due to extensive corrosion. To simulate the resulting section loss, material was shaved off the beam surfaces (flanges and/or webs) of the beams SBI, SBII and SBIII by milling. The specimen SBC was left undamaged for control purposes. In the case of SBI, SBII and SBIII the target section losses caused by simulated corrosion were as follows:

- 15% of bottom flange of the steel beam SBI was shaved off.
- 15% of the web of the steel beam SBII was shaved off symmetrically from both sides.
- 15% of both the bottom flange and the web of the steel beam SBIII were shaved off.

A close-up view of the web of the steel beam SBII after milling is shown in Figure D.4. Due to manufacturing imperfections and flaws, shaving off exactly 15% material from the flanges and/or webs of the steel beams was found to be difficult. Therefore after the conclusion of the milling process, the weights and lengths of the beams were measured and the section losses were calculated by assuming the density of steel as 0.2836 lb/in^3. The

material loss of each beam was then estimated by comparing it with theoretical AISC values. Estimated flange and/or web losses of the steel beams SBI, SBII and SBIII are given in Table D-3.

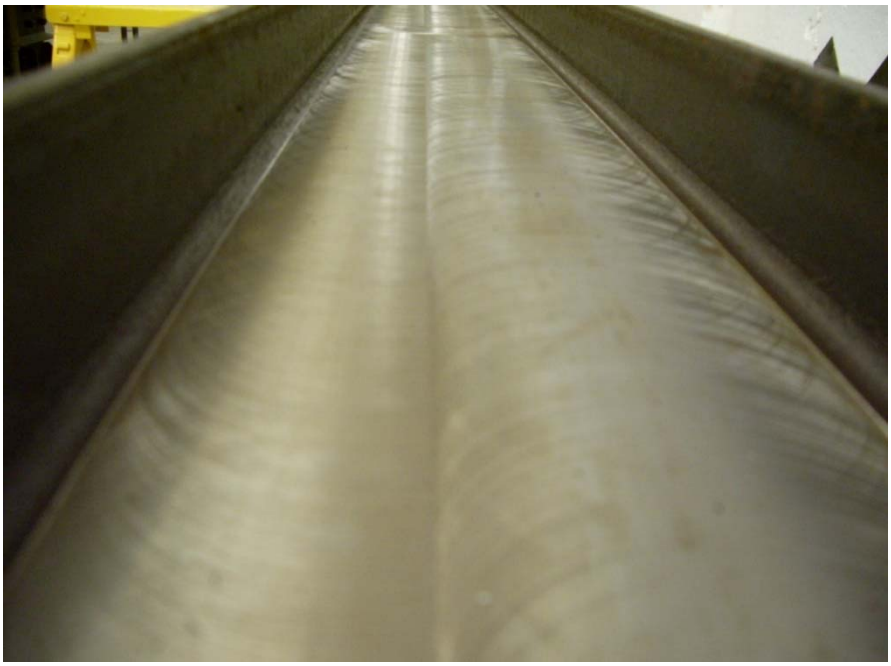

Figure D.4. A view of web of beam SBII after milling [63].

Table D-3. Actual amounts of shaved off material from the beams SBI, SBII and SBIII.

Beam ID	Calculated Cross-sectional Area (in^2)	% Weight Difference	Reduced Thickness (in)
SBC	3.55	-	No change
SBI	3.38	-4.73	0.238 (F)
SBII	3.38	-4.83	0.196 (W)
SBIII	3.24	-9.56	0.238/0.196 (F/W)

APPENDIX E. DETAILS OF THE QUASI-STATIC LOADING SYSTEM FOR REMEDIAL MEASURES

Laboratory setup used for all the test beams, except for the prestressed concrete beam PSCB3, can be seen in Figure E.1. Laboratory test setup for the specimen PSCB3 was described earlier in Appendix-A. Values of load configuration parameters *L* and *a*, as defined in Figure 3.2.1 are summarized for all test beams in Table E-1.

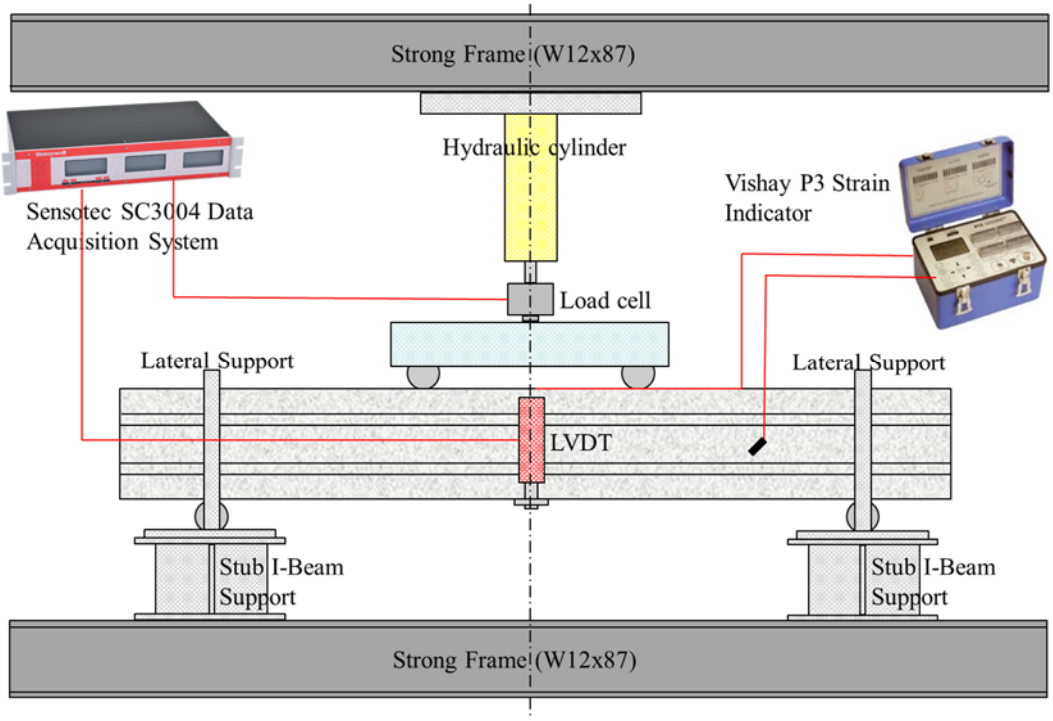

Figure E.1. Schematics of laboratory test setup for the stage-2 test beams.

Table E-1. Values of *L* and *a* for each specimen type.

Specimen Type	*L*	*a*
Reinforced Concrete Beams (shear)	3'-0"	12"
Reinforced Concrete Beams (flexural)	3'-0"	6"
Prestressed Concrete Beams	8'-0"	12"
Steel Beams	5'-0"	6"

As depicted in Figure E.1, supplemental test information like load, strain and displacement were recorded during the experiment at critical locations of the test beams by using:

- A 50 kip load cell.
- Linear variable differential transformers (LVDT).
- Strain gages (0.125”, 0.25” and 0.5”).

More details of those sensors devices can be found in the associated TDOT research report [63].

APPENDIX F. CHARACTERIZATION OF THE FRP PATCH MATERIALS

Currently the design and construction standards of traditional construction materials like steel, reinforced concrete and prestressed concrete are well established and matured. On the other hand, FRP composites are quite new in this arena and there has been no official design and construction standards available for this type of material, when these studies were undertaken. FRP composites comprise of a combination of two materials: high strength fibers and resins. Because of lack of manufacturing standards and wide variability of options for resin type and fiber material, fiber orientation, and curing conditions, mechanical properties of FRP composites is highly variable. Additionally, each FRP material is glued to the substrates with the help of an adhesive. There are various possibilities for the selection of the adhesive too. So, one has to heavily rely upon the minimum mechanical properties of the FRP material supplied by the manufacturers. The types and corresponding properties of FRP used in this study are summarized in Table F-1 as compared to typical structural steel. Of these only Sika CarboDur is reportedly specifically suited for concrete structures.

Table F-1. Basic mechanical properties of the FRP materials used.

Material	Density (lb/in3)	Tensile Strength (ksi)	Tensile Modulus (ksi)	Elongation %	Factory Thickness (in)
Grade 60 Steel	0.284	60	29000	10.00	Varies
Fibreglast Prepreg 3K	-	635	34900	1.95	0.012
SikaWrap Hex 230	0.064	624	34000	1.80	0.010
Sika CarboDur	0.058	449	23900	1.69	0.047
Newport LTC 4300	-	290	18700	1.44	0.010

As can be seen in Table F-1 above, only a limited number of physical and mechanical properties of the FRP materials are provided by the manufacturers. Additionally, no official standards for experimental procedures for determining mechanical properties of the FRP composites and adhesives could be identified. In this research work, experimental procedures specifically developed by the author as part of this study was used for determining needed supplemental mechanical properties of the adhesives [63].

The proposed experimental procedures were simple and easy to set-up and perform. To measure the shear stiffness and shear modulus of bond material, two simple steel plates were butt jointed with two FRP patches on two sides as cover plates, as shown in Figure F.1(a). The plates were pulled apart to obtain the load vs. displacement data which could be used to determine the shear stiffness of the adhesive treating the adhesive layer as shear springs, as illustrated in Figure F.1(b).

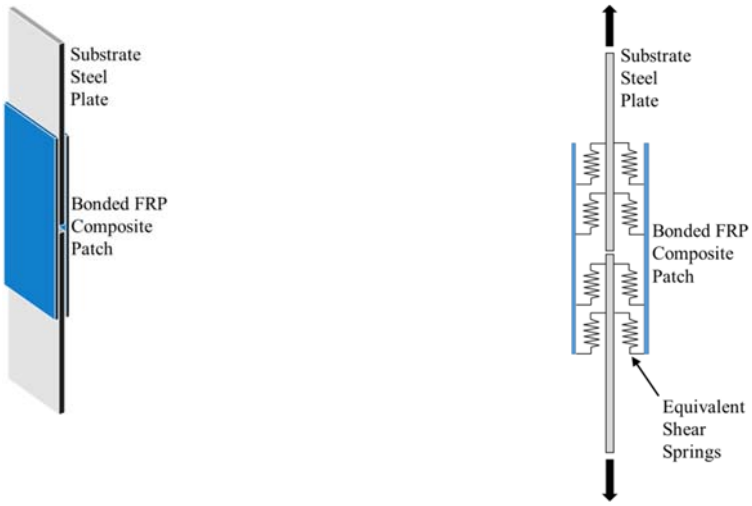

(a) Test specimen for shear (b) Spring theory for shear

Figure F.1. Test procedure to measure shear properties of adhesive.

Another simple test procedure was devised to determine the tensile properties of the adhesive. First, a short piece of an aluminium beam was cut into two creating two 'T' shaped aluminium sections. Then those two sections were glued together by their flange faces, first by bonding one face of FRP layer on flange faces of one tee and then by bonding the flange face of second tee piece on to the opposite face of the same FRP layer, as shown in Figure F.2(a). After curing, the specimens were pulled apart in the testing machine by applying tension force to the protruding webs, as shown in Figure F.2(b). The recorded load-displacement data was processed to determine the tensile properties of the adhesive.

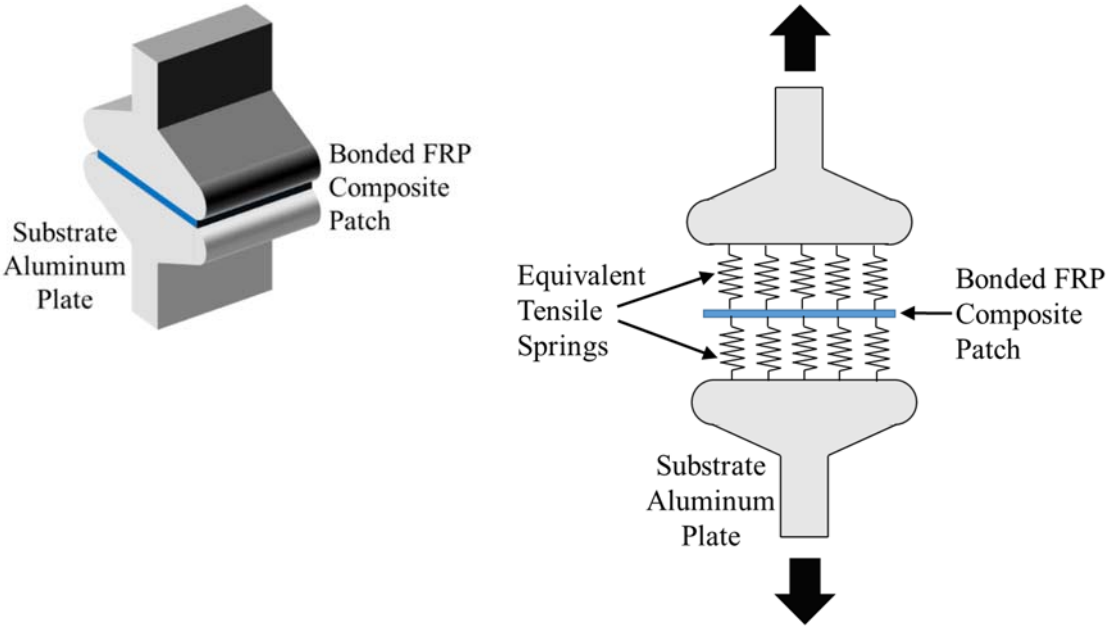

(a) Specimen for tension test (b) Spring theory for tension

Figure F.2. Testing scheme to measure tensile properties of adhesive.

In this document, only the details of the experimental work with Fibreglast Prepreg 3K FRP composite and the adhesive Fibreglast 1101 will be provided. Details of the other composites and adhesives can be found in another publication [63]. The shear and tensile

test specimens used for determining the mechanical properties of the Fibreglast 1101 adhesive is shown in Figure F.3 after testing.

(a) Shear test specimen (b) Tension test specimen

Figure F.3. Views of tests for tensile and shear properties of Fibreglast 1101 adhesive.

Fibreglast Prepreg 3K is a pre-impregnated FRP composite often qualified as prepreg. Such composites have two main components which are the fiber matrix and an incorporated resin system. Normally, prepregs do not require any additional adhesive. The composite is pressed against the substrate with uniform pressure and heat is applied causing the pre-impregnated resin inside the composite to melt and act as glue bonding the FRP to the substrate.

The expiry date of the Fibreglast Prepreg 3K was past and newer replacement could not be acquired. This was substituted with adhesive called Fibreglast 1101 to bond the substrate with the carbon fiber matrix. Fibreglast 1101 is a high strength structural adhesive

which is generally used to bond composites, metals and even common construction materials. Table F-2 shows the properties of this adhesive along with the other adhesives used in this study.

Table F-2. Properties of the adhesives.

Adhesive	G (ksi)	E (ksi)	τ_u (ksi)	σ_u (ksi)	k_v ($^{kip}/_{in^3}$)	k_u ($^{kip}/_{in^3}$)
Fibreglast 1101	0.068	12.390	0.180	0.518	2.823	1.665
SikaDur 330	0.441	0.770	0.362	1.010	72.73	8.77
SikaDur 30	16.002	23.886	1.594	0.867	75.76	34.25
LTC 4300	0.079	0.769	0.089	0.846	58.56	4.28

APPENDIX G. FRP PATCH DESIGN AND REPAIR PROCEDURE

In this section, only FRP patch design and repair procedure of the beam PSCB3 is covered in any detail. Details of design and repair procedure of other specimens can be found in another publication by the author [63]. Typical examples of repaired steel, "shear" reinforced concrete and "flexural" reinforced concrete beams are shown in Figures G.1 to G.3.

Figure G.1. Steel beam repaired with prepreg FRP composite.

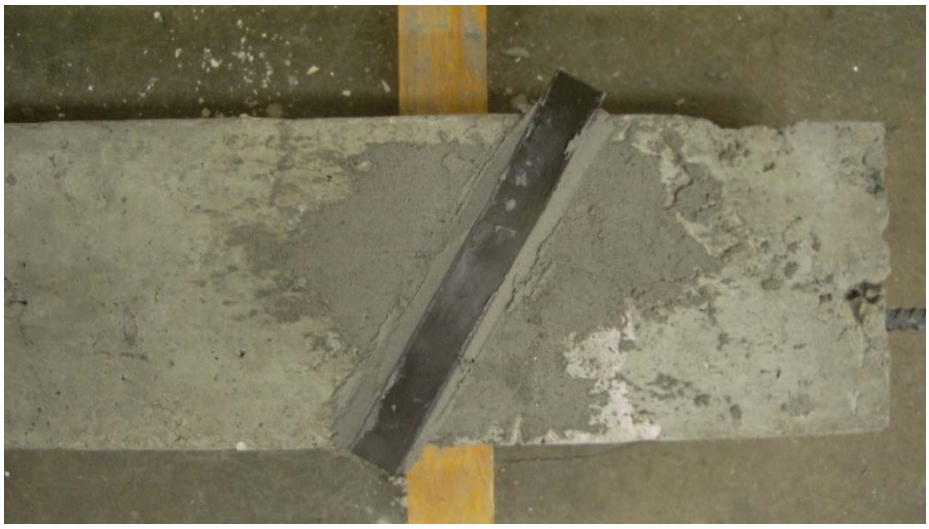

Figure G.2. Shear reinforced concrete beam repaired with FRP composite reinforcement.

Figure G.3. Flexural reinforced beam repaired with CarboDur patches.

By using the formulas developed in Chapter 3.3, patch repair of the beams damaged during the first loading stage was designed. For shear repair of the beam PSCB3, Fibreglast Prepreg 3K FRP composite was used. Bonding of the FRP to the specimen was accomplished using Fibreglast 1101 as adhesive. Data for the patches used to repair the two shear cracks appearing on each side of the same beam is summarized in Table G-1.

Table G-1. Details of shear patch design of the beam PSCB3.

Location	Configuration	Slope (α_p)	Design Force (V_p)	Required Width (w_p)	Provided Width
Web	U-Jacket	90°	13.30 kips	1.94”	15”

Fibreglast Prepreg 3K FRP is a ready-made resin impregnated system. But in the context of this research study, the adhesive Fibreglast 1101 was used to glue the composite to the damaged PSCB3 beam. Before starting with the repair process, the PSCB3 was flipped over to simulate the jacking up condition of the bridge superstructure in prototype applications. The surface of the specimen at the patch location was cleaned with a hard plastic brush to remove any loose particles and dust. Thereafter, latex gloves were worn to prevent contamination of the application surface. Using a sharp scissors, the accurately drawn patch areas on the composite fabric were cut out, as shown in Figure G.4. This was followed by mixing of the components of the adhesive Fibreglast 1101 by following manufacturer's recommendations. Since the adhesive starts to harden immediately after it is exposed to air, it can be mixed only after the specimen surface and the composite are ready to receive the patch. Using a spatula, the epoxy was applied in a uniform layer to the surface of the beam in the patch location. After removing the protective plastic membranes, the composite was properly positioned at the repair location and pressed into the adhesive layer with the help of a roller so that Fibreglast 1101 glue gets seeped into the composite matrix. Figure G.5 shows the bonded composite patch.

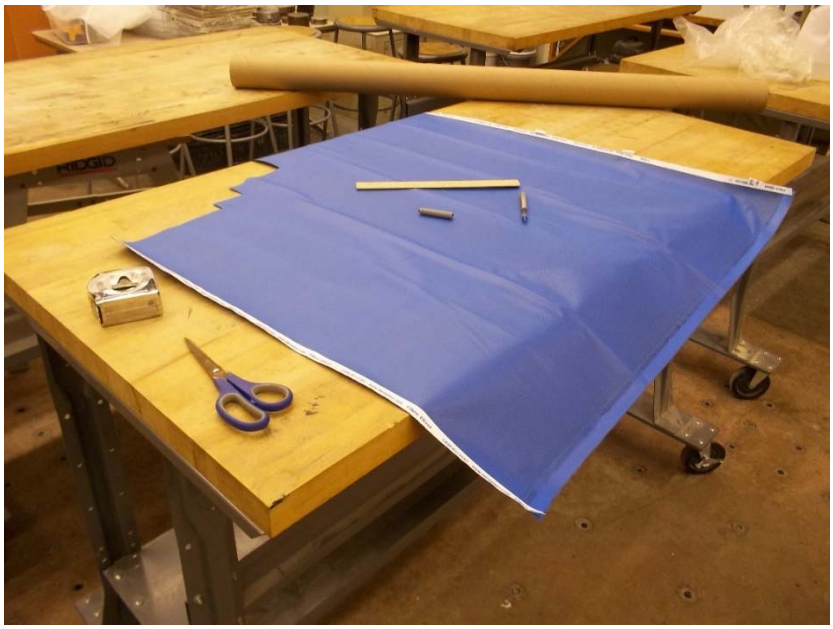

Figure G.4. Tools used to cut Fibreglast Prepreg 3K FRP Composite.

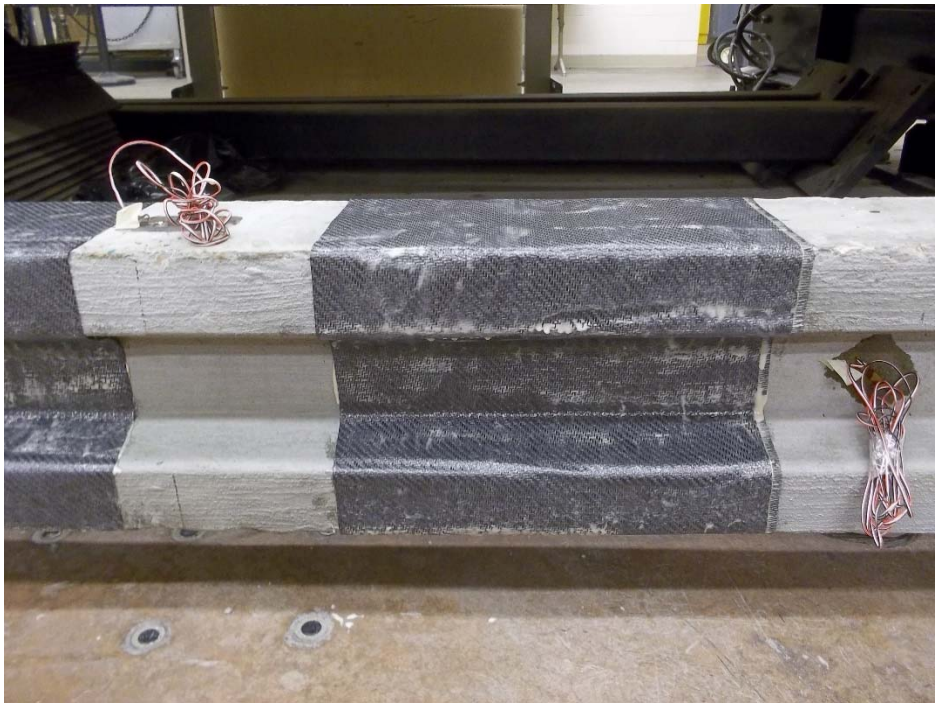

Figure G.5. View of bonded composite U-jacket repair of PSCB3 beam.

REFERENCES

[1] P. O. Moore, R. K. Miller and R. K. Hill, Nondestructive Testing Handbook, Volume 6, Acoustic Emission Testing, American Society for Nondestructive Testing, 2005.

[2] H. Dunegan and D. Harris, "Acoustic emission - a new nondestructuve testing tool," *Ultrasonics,* vol. 7, no. 3, pp. 160-166, 1969.

[3] M. Huang, L. Jiang, P. Liaw, C. Brooks, R. Seeley and D. Klarstrom, "Using acoustic emission in fatigue and fracture materials research," *Journal of the Minerals, Metals and Materials (JOM),* vol. 50, no. 11, pp. 1-14, 1998.

[4] R. E. Green Jr, "Basic wave analysis of acoustic emission," *Mechanics of nondestructive testing. Springer US,* pp. 55-76, 1980.

[5] J. Carlyle, "AE Testing the F-111 Aircraft, J.M. Report 127011," General Dynamics Corporation, Fort Worth, TX, 1987.

[6] M. Asty, "Acoustic emission source location on a spherical or plane surface," *NDT lnternational,* vol. 11, no. 5, pp. 223-226, 1978.

[7] P. Barat, P. Kalyanasundaram and B. Raj, "Acoustic emission source location on a cylindrical surface," *NDT&E International,* vol. 26, no. 6, pp. 295-297, 1993.

[8] A. Tobias, "Acoustic emission source location in two dimensions by an array of three sensors," *Non-Destructive Testing,* vol. 9, no. 1, pp. 9-12, 1976.

[9] D. Ozevin, Z. Li and Z. Heidary, "Early state damage detection of aluminum 7075-T6 plate based on acoustic emission," *Society of Photo-Optical Instrumentation Engineers (SPIE) Conference Series,* vol. 7983, p. 3, 2011.

[10] R. Mindlin, "Influence of Rotatory Inertia and Shear on Flexural Motions of Isotropic, Elastic Plates," *Journal of Applied Mechanics,* vol. 18, pp. 31-38, 1951.

[11] J. Jiao, C. He, B. Wu and R. Fei, "Application of wavelet transform on modal acoustic emission source location in thin plates with one sensor," *International Journal of Pressure Vessels and Piping,* vol. 81, p. 427–431, 2004.

[12] T. Kosel, I. Grabec and F. Kosel, "Intelligent Location of Simultaneously Active Acoustic Emission Sources: Part I," *Aircraft Engineering and Aerospace Technology,* vol. 75, pp. 11-17, 2003.

[13] T. Kosel, I. Grabec and F. Kosel, "Intelligent Location of Two Simultaneously Active Acoustic Emission Sources: Part II," *Aircraft Science and Technology,* vol. 9, no. 1, pp. 45-53, 2005.

[14] H. Bodine, R. Dawes, S. Henley and E. Hill, "Automatic Detection and Classification of Cracks in Complex Structures-Applying the Parametric Avalanche to Acoustic Emissions," *American Society for Nondestructive Testing, Proceedings of the ASNT Spring Conference,* pp. 115-117, 1995.

[15] H. Bodine, R. Dawes, S. Henley and E. Hill, "Detecting Crack Growth in Metal Structures using Temporal Processing," in *Proceedings of ANNIE'95: Artificial Neural Networks in Engineering*, Saint Louis, MO, 1995.

[16] C. Rovik, Classification of In-Flight Fatigue Cracks in Aircraft Structures Using Acoustic Emission and Neural Networks, Daytone Beach, FL: Thesis. Embry Riddle Aeronautical University, 1998.

[17] S. Vaughn, In-Flight Fatigue Crack Monitoring of an Aircraft Engine Cowling, Daytone Beach, FL: Thesis. Embry Riddle Aeronautical University, 1998.

[18] G. Swit, "Diagnostics of prestressed concrete structures by means of acoustic emission," in *In the Proceedings of 2009 8th International Conference on Reliability, Maintainability and Safety (ICRMS 2009)*, Chengdu, China, 2009.

[19] B. Schechinger and T. Vogel, "Acoustic emission for monitoring a reinforced concrete beam subject to four-point-bending," *Construction and Building Materials,* vol. 21, pp. 483-490, 2007.

[20] T. Ryan, R. Hartle, J. Mann and D. L.J., "Bridge Inspector's Reference Manual," U.S. Department of Transportation, Federal Highway Administration, Arlington, VA, 2006.

[21] J. S. Ahn and P. K. Basu, "Locally refined p-FEM modeling of patch repaired plates," *Composite Structures,* vol. 93, no. 7, pp. 1704-1716, 2011.

[22] T. Hassan, G. Horeczy, D. Svecova, S. Rizkalla, E. Shehata and D. Stewart, "Flexural Strengthening of Post-Tensioned Bridge Slab Using FRP," in *In Proceedings of the third Int. Conference on advanced composite materials for bridges and structures (ACMBS-III)*, Ottowa, Canada, 2000.

[23] J. Kasan and K. Harries, "Repair of Impact-damaged Prestressed Concrete Bridge Girders with Carbon Fiber Reinforced Polmers," in *In Proceedings of the Second Official International Conference of International Institute of FRP in Construction for Asia-Pacific Region*, Seoul, South Korea, 2009.

[24] A. Bassetti, P. Liechti and A. Nussbaumer, "Fatigue resistance and repairs of riveted bridge members," in *Third International Symposium on Fatigue Design, FD'98*, Espoo, Finland, 1999.

[25] T. Wipf, J. Rhodes and B. Kempers, "Effective Structural Concrete Repair-Volume 1 of 3: Repair of Impact Damaged Prestressed Concrete Beams with CFRP, No. Iowa DOT Project TR-428.," Iowa DOT, 2004.

[26] F. Russo, T. Wipf, F. Klaiber and R. Paradis, "Evaluation and Repair of Damaged Prestressed Concrete Girder Bridges," in *Mid-Continent Transportation Symposium Proceedings*, 2000.

[27] S. Luke, "The Use of Carbon Fibre Plates for the Strengthening of Two Metallic Bridges of a Historic Nature in the UK," *FRP Composites in Civil Engineering,* vol. 2, pp. 975-983, 2001.

[28] A. Shaat, D. Schnerch, A. Fam and S. Rizkalla, "Retrofit of steel structures using fiber-reinforced polymers (FRP): State-of-the-art," In Transportation research board (TRB) annual meeting. CD-ROM (04-4063), 2004.

[29] J. W. Gillespie, D. R. Mertz, W. M. Edberg, J. R. Demitz, K. Kasai and I. Hodgson, "Rehabilitation of steel bridge girders: large scale testing," in *Proceedings - American Society for Composites*, 1996.

[30] X. Liu, P. Silva and A. Nanni, "Rehabilitation of Steel Bridge Members with FRP Composite Materials," in *Proceedings of the CCC2001 Composites in Construction*, Porto, Portugal, 2001.

[31] M. Tavakkolizadeh and H. Saadatmanesh, "Repair of Cracked Steel Girders Using CFRP Sheets," in *Proceedings of the International Conference on Structural Engineering and Construction (ISEC-01)*, Honolulu, Hawaii, 2001.

[32] S. Shulley, X. Huang, V. Karbhari and J. Gillespie, "Fundamental Consideration of Design and Durability in Composite Rehabilitation Schemes for Steel Girders with Web Distress," in *Proceedings of the Third Materials Engineering Conference*, San Diego, California, 1994.

[33] W. Edberg, D. Mertz and J. Gillespie Jr., "Rehabilitation of Steel Beams Using Composite Materials," in *Proceedings of the Materials Engineering Conference, Materials for the New Millenium*, New York, NY, 1996.

[34] J. Gillespie, D. Mertz, W. Edberg, N. Ammar, K. Kasai and I. C. Hodgson, "Rehabilitation of Steel Bridge Girders Through Application of Composite Materials," in *Proceedings of the 28th International SAMPE Technical Conference*, Seattle, Washington, 1996.

[35] M. Abushaggur and A. El Damatty, "Testing of Steel Sections Retrofitted Using FRP Sheets," in *Proceedings of the Annual Conference of the Canadian Society for Civil Engineering*, Moncton, Nouveau-Brunswick, Canada, 2003.

[36] R. Sen, L. Liby and G. Mullins, "Strengthening Steel Bridge Sections Using CFRP Laminates," *Composites Part B: engineering,* vol. 32, no. 4, pp. 309-322, 2001.

[37] M. Tavakkolizadeh and H. Saadatmanesh, "Strengthening of Steel-Concrete Composite Girders Using Carbon Fiber Reinforced Polymers Sheets," *ASCE Journal of Structural Engineering,* vol. 129, no. 1, pp. 30-40, 2003.

[38] A.-H. Zureick, "Recommended Guide Specification for the Design of Externally Bonded FRP Systems for Repair and Strengthening of Concrete Bridge Elements," Transportation Research Board, 2010.

[39] K. A. Brewer, "AASHTO Maintenance Manual for Roadways and Bridges," American Association of State Highway and Transportation Officials (AASHTO), Washington, D.C., 2007.

[40] C. E. Bakis, "Guide for the design and construction of externally bonded FRP systems for strengthening concrete structures," American Concrete Institute (ACI), 2002.

[41] L. Hollaway, "Advances in adhesive joining of dissimilar materials with special reference to steels and FRP composites," in *Proceedings of the International Symposium on Bond Behaviour of FRP in Structures*, Hong Kong, China, 2005.

[42] T. C. Miller, M. J. Chajes, D. R. Mertz and J. N. Hastings, "Strengthening of a steel bridge girder using CFRP plates," *Journal of Bridge Engineering,* vol. 6, no. 6, pp. 514-522, 2001.

[43] M. Dawood, D. Schnerch, E. Sumner and S. Rizkalla, "Strengthening steel bridges with new high modulus CFRP materials," in *Third international conference on bridge maintenance, safety and management (IABMAS'06)*, Porto, Portugal, 2006.

[44] D. Schnerch, K. Stanford, E. Sumner and S. Rizkalla, "Bond behavior of CFRP strengthened steel bridges and structures," in *International Symposium on Bond Behaviour of FRP in Structures (BBFS 2005)*, Hong Kong, China, 2005.

[45] S. Miriyala, W. Tucker, T. Rockett and R. Brown, "Degradation of carbon reinforced polymer composites under galvanic coupling conditions," in *Proceedings of the 33rd*

AIAA/ASME/ASCE/AHS/ASC Structures, Structural Dynamics, and Materials Conference, Dallas, TX, 1992.

[46] M. Tavakkolizadeh and S. H., "Galvanic corrosion of carbon and steel in aggressive environments," *Journal of Composites for construction,* vol. 5, no. 3, pp. 200-210, 2001.

[47] T. West, Enhancement to the Bond Between Advanced Composite Materials and Steel for Bridge Rehabilitation, Newark, DE: Thesis. University of Delware, 2001.

[48] A. Brown, "The Corrosion of CFRP-to-Metal Couples in Saline Environments," in *Proceedings of the 2nd International Conference on Carbon Fibers*, London, England, 1974.

[49] D. Choqueuse, P. Davies, F. Mazeas and R. Baizeau, "Aging of composites in water: Comparison of five materials in terms of absorption kinetics and evolution of mechanical properties," in *ASTM Special Technical Publication STP 1302, Second Symposium on High Temperature and Environmental Effects on Polymeric Composites*, Norfolk, VA, 1997.

[50] T. Roberts, "Approximate Analysis of Shear and Normal Stress Concentrations in the Adhesive Layer of Plated RC Beams," *The Structural Engineer,* vol. 67, no. 12, pp. 229-233, 1989.

[51] A. S. H. Malek and M. Ehsani, "Shear and Normal Stress Concentrations in RC Beams Strengthened with FRP Plates," in *Second International Conference on Advanced Composite Materials in Bridges and Structures (ACMBS-II)*, Montreal, Canada, 1996.

[52] O. Gunes, A fracture-based approach to understanding debonding in FRP bonded structural members, Cambridge, MA: Dissertation. Massachusetts Institute of Technology, 2004.

[53] O. Buyukozturk, O. Gunes and E. Karaca, "Progress on understanding debonding problems in reinforced concrete and steel members strengthened using FRP composites," *Construction and Building Materials,* vol. 18, no. 1, pp. 9-19, 2004.

[54] B. Babjak, S. Szilvasi, A. Pedchenko, M. Hofacker, E. J. Barth, P. Volgyesi and A. Ledeczi, "Experimental Research Platform for Structural Health Monitoring," in *Advancement in Sensing Technology*, Berlin, Germany, Springer, 2013, pp. 43-68.

[55] S. Rao and B. Subramanyam, "Analysis of Acoustic Emission Signals using Wavelet Transformation Technique," *Defence Science Journal,* vol. 58, no. 4, p. 559–564, 2008.

[56] B. Barabara, "The mathematical microscope: Waves, wavelets, and beyond," in *A positron name Priscilla: Scientific discovery at the Fronteir*, Washington DC, National Academy Press, 1994, pp. 196-235.

[57] D. L. Donoho and J. M. Johnstone, "Ideal spatial adaptation by wavelet shrinkage," *Biometrika,* vol. 81, no. 3, pp. 425-455, 1994.

[58] J. C. Spall, J. L. Maryak and M. S. Asher, "Neural network approach to locating acoustic emission sources in non-destructive evaluation," *Journal of sound and vibration,* vol. 211, no. 1, pp. 133-143, 1998.

[59] K. Levenberg, "A Method for the Solution of Certain Non-Linear Problems in Least Squares," *Quarterly of Applied Mathematics,* vol. 2, p. 164–168, 1944.

[60] M. Hagan and M. Menhaj, "Training feedforward networks with the Marquardt algorithm," *IEEE Transactions on Neural Networks,* vol. 5, no. 6, pp. 989-993, 1994.

[61] Abaqus, Analysis User's Guide v6.13, Providence, RI: Dassault Systèmes, 2013.

[62] R. Kuhlemeyer and J. Lysmer, "Finite Element Method Accuracy for Wave Propagation Problems," *Journal of Soil Mechanics and Foundations Division,* vol. 99, no. 5, pp. 421-427, 1973.

[63] P. K. Basu, O. Yapar and J. McNutt, "Rapid Extension of Life of Deteriorating Bridge Superstructures," Strategic Research Program for Tenessee DOT, Nashville, TN, 2011.

[64] P. Colombi and P. Carlo, "An Experimental, Analytical and Numerical Study of the Static Behavior of Steel Beams Reinforced by Pultruded CFRP Strips," *Composites Part B: Engineering,* vol. 37, no. 1, pp. 64-73, 2006.

[65] O. Yapar, P. Basu, W. Seger, J. McNutt and N. Nordendale, "Local Repair of Precast Concrete Beams Using Bonded Composite Patch," in *PCI National Bridge Conference*, Nashville, TN, 2012.

[66] Building Code Requirements for Structural Concrete and Commentary (ACI 318M-11), American Concrete Institute (ACI), 2011.

[67] F. Vecchio and M. Collins, "The Response of Reinforced Concrete to In-Plane Shear and Normal Stress," University of Toronto, Toronto, Canada, 1982.

[68] E. Hognestad, N. Hanson and D. McHenry, "Concrete stress distribution in ultimate strength design," *American Concrete Institute (ACI) Journal Proceedings,* vol. 52, no. 12, pp. 455-480, 1955.

[69] M. Crisfield, "A fast incremental/iterative solution procedure that handles “snap-through”," *Computers and Structures,* vol. 13, no. 1, pp. 55-62, 1981.

[70] J. Lee and G. Fenves, "Plastic-damage model for cyclic loading of concrete structures," *Journal of Engineering Mechanics,* vol. 124, no. 8, pp. 892-900, 1998.

[71] J. Lubliner, J. Oliver, S. Oller and E. Onate, "A plastic-damage model for concrete," *International Journal of Solids and Structures,* vol. 25, no. 3, pp. 299-326, 1989.

[72] L. Kachanov, Introduction to continuum damage mechanics, Brookline, MA: Martinus Nijhoff Publishers, 1986.

[73] A. Mendelson, Plasticity: Theory and Application, Malabar, FL: Krieger Pub., 1983.

[74] H. Akita, H. Koide, M. Tomon and D. Sohn, "A practical method for uniaxial tension test of concrete," *Materials and Structures,* vol. 36, no. 6, pp. 365-371, 2003.

[75] A. Carpinteri and S. Invernizzi, "Influence of Damage on the Fractal Properties of Concrete Subjected to Pure Tension," *Materials and Structures,* vol. 34, no. 10, pp. 605-611, 2001.

[76] M. van Vliet, Size effect of tensile fracture in concrete and rock, Delft, Netherlands: Delft University of Technology, 2000.

[77] PCI Design Handbook Precast and Prestressed Concrete, Chicago, IL: Prestressed Concrete Institute (PCI), 2004.

[78] G. Cheok and W. Stone, "Performance of 1/3 Scale Model Precast Concrete Beam–Column Connections Subjected to Cyclic Inelastic Loads," NISTIR, Gaithersburg, MD, 1994.

[79] C. Moosbrugger, Atlas of Stress–Strain Curves, Novelty, OH: ASTM, 2002.

[80] Y. Obaidat, S. Heyden and O. Dahlblom, "The effect of CFRP and CFRP/concrete interface models when modeling retrofitted RC beams with FEM," *Composite Structures,* vol. 92, no. 6, pp. 1391-1398, 2010.

[81] W. Yeih, R. Huang, J. Chang and C. Yang, "A Pull-out Test for Determining Interface Properties Between Rebar and Concrete," *Advanced Cement Based Materials,* vol. 5, no. 2, pp. 57-65, 1997.

[82] H. Liebowitz and G. Sih, "Mathematical Theories of Brittle Fracture," Academic Press Inc., New York, NY, 1968.

[83] G. Irwin, "Plastic Zone Near a Crack and Fracture Toughness," in *Sagamore Research Conference*, Syracuse NY, 1961.

[84] R. Ripling and P. Crosley, "Crack Arrest Fracture Toughness of a Structural Steel (A36)," *Supplement to the Welding Journal,* pp. 65-74, 1982.

[85] J. Libby, Modern Prestressed Concrete, New York, NY: Van Nostrand Reinhold, 1977.

[86] A. Ayoub and F. Filippou, "Finite-element model for pretensioned prestressed concrete girders," *ASCE Journal of structural engineering,* vol. 136, no. 4, pp. 401-409, 2010.

[87] A. Arab, S. Badie and M. Manzari, "A methodological approach for finite element modeling of pretensioned concrete members at the release of pretensioning," *Engineering Structures,* vol. 33, no. 6, pp. 1918-1929, 2011.

[88] P. Okumus, M. Oliva and S. Becker, "Nonlinear finite element modeling of cracking at ends of pretensioned bridge girders," *Engineering Structures,* vol. 40, pp. 267-275, 2012.

[89] R. Taylor, FEAP Finite Element Analysis Program User Manual, Berkeley, CA: University of California at Berkeley, 2005.

[90] D. Mitchell, W. Cook, A. Khan and T. Tham, "Influence of high strength concrete on transfer and development length of pretensioning strand," *Prestressed Concrete Institute (PCI) Journal,* vol. 38, no. 3, pp. 52-66, 1993.

[91] A. Akhnoukh, Development of High Performance Precast/Prestressed Bridge Girders, Lincoln, NE: University of Nebraska-Lincoln, 2008.

[92] M. O'Callaghan and O. Bayrak, "Tensile Stresses in the End Regions of Pretensioned I-Beams at Release," Texas Department of Transportation, Austin, TX, 2008.

[93] G. Barnbrook, E. Dore, A. Jeffery, R. Keen, J. Parkinson, D. Sawtell, B. Shacklock and B. Spratt, Concrete practice, Cement & Concrete Association, 1975.

[94] ASTM, C39 - Standard Test Method for Compressive Strength of Cylindrical Concrete Specimens, ASTM, 2014.

[95] ASTM, ASTM C496 - Standard Test Method for Splitting Tensile Strength of Cylindrical Concrete Specimens, ASTM, 2011.

[96] AASHTO LRFD Bridge Design Specifications, American Association of State Highway and Transportation Officials (AASHTO), 2010.

[97] Steel Construction Manual, 14th Edition, American Institute of Steel Construction (AISC), 2010.

[98] Mistras, USB-AE Node and AEWin for USB Software User's Manual, Princeton Junction: Mistras Group Inc. Products and Systems Division, 2010.